THERMAL MANAGEMENT OF BATTERY MODULES USING PHASE CHANGE COMPOSITE AND LIQUID COOLED PLATES

Ph. D. Thesis

By

Vivek Saxena

(Roll No. 2001103003)

DEPARTMENT OF MECHANICAL ENGINEERING

INDIAN INSTITUTE OF TECHNOLOGY INDORE

December 2025

THERMAL MANAGEMENT OF BATTERY MODULES USING PHASE CHANGE COMPOSITE AND LIQUID COOLED PLATES

A THESIS

Submitted in partial fulfilment of the

requirements for the award of the degree

of

DOCTOR OF PHILOSOPHY

by

Vivek Saxena

(Roll No. 2001103003)

DEPARTMENT OF MECHANICAL ENGINEERING

INDIAN INSTITUTE OF TECHNOLOGY INDORE

December 2025

INDIAN INSTITUTE OF TECHNOLOGY INDORE

I hereby certify that the work which is being presented in the thesis entitled **Thermal Management of Battery Modules using Phase Change Composite and Liquid Cooled Plates** in the partial fulfilment of the requirements for the award of the degree of **DOCTOR OF PHILOSOPHY** and submitted in the **Department of Mechanical Engineering, Indian Institute of Technology Indore**, is an authentic record of my own work carried out during the time period from August 2020 to July 2025 under the supervision of **Dr. Santosh Kumar Sahu, Professor, Indian Institute of Technology Indore,** and **Dr. Shailesh Ishwarlal Kundalwal, Professor, Indian Institute of Technology Indore.**

The matter presented in this thesis has not been submitted by me for the award of any other degree of this or any other institute.

Vivek Saxena

18-12-2025

Signature of the student with date

(VIVEK SAXENA)

This is to certify that the above statement made by the candidate is correct to the best of my/our knowledge.

19.12.2025

Signature of Thesis Supervisor with date

(Dr. Santosh Kumar Sahu)

19.12.25

Signature of Thesis Supervisor with date

(Dr. Shailesh Ishwarlal Kundalwal)

Vivek Saxena has successfully given his Ph.D. Oral Examination held on **December 15, 2025**.

19.12.2025

Signature of Thesis Supervisor with date

(Dr. Santosh Kumar Sahu)

19.12.25

Signature of Thesis Supervisor with date

(Dr. Shailesh Ishwarlal Kundalwal)

ACKNOWLEDGEMENTS

I am deeply grateful to my advisors, **Prof. Santosh Kumar Sahu** and **Prof. Shailesh Ishwarlal Kundalwal**, Department of Mechanical Engineering, Indian Institute of Technology Indore, for their invaluable mentorship, unwavering support, and insightful guidance throughout my research. Their encouragement and constructive feedback have been instrumental in refining this work, and I sincerely appreciate the time and effort they invested in shaping my academic journey.

I extend my heartfelt appreciation to **Dr. Peichun Amy Tsai**, Department of Mechanical Engineering, University of Alberta, Canada, for her guidance and support during my research visit. The opportunity to work under her supervision was immensely rewarding, enriching my research experience and broadening my perspectives.

I am also thankful to my Ph.D. progress committee members, **Dr. Shanmugam Dhinakaran** and **Dr. Prabhat Kumar Upadhyay**, for their valuable insights and feedback, which significantly influenced the direction of my research. Additionally, I am indebted to **Prof. Suhas S. Joshi**, Director, IIT Indore, for facilitating numerous opportunities and providing financial support throughout my doctoral studies. I also appreciate the assistance extended by the Head of the Department, the DPGC convener, Faculty Members, and Staff at the Department of Mechanical Engineering, IIT Indore, whose timely help has been invaluable.

I sincerely acknowledge the financial support from the **Ministry of Education, Government of India**, through the prestigious **Prime Minister's Research Fellowship (PMRF)**, which enabled me to pursue my research work with dedication. My deepest gratitude goes to the **Anusandhan National Research Foundation (ANRF)** for awarding me the prestigious **Overseas Visiting Doctoral Fellowship (OVDF)**, allowing me to conduct part of my research at the University of Alberta, Canada. I also extend my thanks to the **Department of Mechanical**

Engineering, University of Alberta, for their support and hospitality during my time in Canada.

I am grateful to ANRF for providing International Travel Support for my participation in the ASME POWER 2022 Conference, USA. My appreciation also extends to the **American Society of Mechanical Engineers (ASME)** for recognizing my work with the Qualified Student Award at ASME POWER2022 conference. These opportunities have greatly contributed to the dissemination and impact of my research. The assistance of the staff at the **Workshop** and **Sophisticated Instrument Centre (SIC)**, IIT Indore, has been invaluable in facilitating my work. A special mention goes to **Mr. Arun Kumar Bhagwaniya** for his consistent support in the laboratory. I am also thankful to the **Central Library** staff at IIT Indore for their unwavering assistance throughout my research.

I am deeply indebted to my seniors, lab mates, and colleagues, including Dr. Avadhesh K. Sharma, Dr. Saurabh Yadav, Dr. Pushpanjay Singh, Dr. Rohit Kothari, Dr. Anuj Kumar, Dr. Jay Joshi, Dr. Pawan Sharma, Mr. Akhalesh Sharma, Dr. Pradeep Singh, Mr. Pradunmaya Dutta, Mr. Gaurav Sharma, Mr. Hari Chaurasia, Mr. Kartik, Mr. Hrishav Dey, and many others, whose collaboration, insightful discussions, and camaraderie have made this journey more enriching. A special note of gratitude to Dr. Rohit Kothari for his invaluable mentorship and guidance.

Above all, my deepest respect and heartfelt gratitude go to my **late grandfather, Shri Dwarka Prasad Saxena, late grandmother, Smt. Satyavati Saxena, my late mother, Smt. Sudha Saxena,** and **my father, Shri Brijesh Kumar Saxena**. Their love, sacrifices, and unwavering belief in me have been the foundation of my achievements. My father's enduring guidance and strength continue to inspire every step I take. This milestone is as much theirs as it is mine, for their constant support and encouragement have made it possible. A special acknowledgment to, **Vishal (my brother), Shraddha (my sister)**, their

support, in moments of doubt and determination alike, has been invaluable. I am equally grateful to my **extended family** for their blessings, steadfast encouragement and unwavering support.

Finally, my deepest appreciation is reserved for my **beloved wife, Neha Shrivastava.** Her patience, sacrifices, and unwavering faith in me have been the cornerstone of my perseverance, especially during my time away in Canada. Through every long distance, challenge, and sacrifice, she stood by me with grace and resilience. Her support has been my greatest strength, and I am forever grateful for her presence in my life. This journey has been made possible by the collective contributions of many individuals. I extend my sincerest gratitude to everyone who, in any way, has supported, guided, or encouraged me through this endeavour.

Finally, I would like to sign off with a quote that resonates deeply with my journey:

"The only impossible journey is the one you never begin." – *Tony Robbins*

Vivek Saxena

Dedicated to my family, whose love and support have been my greatest strength

ABSTRACT

This dissertation presents the theoretical and experimental investigations pertaining to the Phase Change Material (PCM) based passive and hybrid thermal management systems for electric vehicle battery modules. The objective of the present study is to analyse the performance of PCM based passive and hybrid thermal management systems for various applications, more specifically for battery modules of electric vehicles.

Initially, a theoretical model has been proposed to estimate the effective thermal conductivity (ETC) of open-cell metal foams (MFs) saturated with fluid or phase change materials (PCMs). These models incorporate realistic geometric characteristics (3-D) based on tetrakaidecahedron unit cell structures, incorporating different shapes of ligament and various shapes of node, orientation of ligament, geometry of MFs, coating thickness, and effect of materials. Among various models, the hexagonal-cell model featuring concave triprism ligaments and pyramidal nodes exhibits very good agreement with test data, with deviations below 3% for coated nickel and copper foams. The parametric study further highlights coating thickness as the most influential parameter, followed by the thermal conductivities of the coating material and the filler medium.

The next study proposes a 3-D computational fluid dynamics (CFD) model to analyse the thermal performance of MF-PCM composites integrated into a commercial prismatic lithium-ion battery. The effect of various parameters such as PCM thickness, discharge rate, porosity of MFs on the performance are analysed under steady, transient, and realistic driving conditions. Results demonstrate that the MF-PCM system significantly reduces peak battery temperatures and maintains thermal gradients within safe limits. A PCM thickness of 8 mm and a metal foam porosity of 0.95 are identified as optimal, which reduces the temperature rise by 56% compared to natural convection cooling; such arrangement exhibits reliable thermal buffering and stability for varied

range of loading conditions that demonstrate its suitability for practical electric vehicle applications.

In the subsequent study, a hybrid battery thermal management system (BTMS) is proposed that combines PCM with a lightweight, liquid-cooled cold plate. The system is evaluated under both continuous and melt-fraction-triggered intermittent cooling strategies. Realistic drive cycles such as Supplemental Federal Test Procedure (SFTP-US06), Urban Dynamometer Driving Schedule (UDDS), Worldwide Harmonized Light Vehicles Test Procedure (WLTP-class-3), Highway Fuel Economy Test (HWFET), along with rapid cyclic charging/discharging scenarios (4C–1C and 5C–1C), are used to assess performance. Unlike conventional designs, the proposed hybrid system effectively leverages the latent heat storage of PCM to passively stabilize temperatures and activates liquid cooling only when desired melt fraction is reached. The intermittent strategy enables complete coolant-free operation in three of the four drive cycles and achieves up to 83.9% energy savings during rapid charge-discharge cycles. The optimized zig-zag channel cold plate design results in improved PCM re-solidification, better thermal uniformity, a 52.9% weight reduction, and reduced hotspot formation, offering a lightweight and energy-efficient solution for practical BTMS integration.

In the last study, both experimental and numerical investigations have been carried out to analyse the passive PCM-based BTMS for cylindrical (18650) lithium-ion cells. Tests are conducted for various discharge rates (2C-5C), different PCMs (RT-24, RT-35, RT-38, RT-42, RT-47), at room temperature conditions. The 3-D numerical model exhibits good agreement with the test data, and the average deviation is found to be less than 5%. Here, the system with 4 mm PCM thickness is found to be the optimal condition that offers the best trade-off between temperature reduction, melt fraction utilization, and material efficiency. Among the tested PCMs, RT-35 exhibits superior thermal performance under moderate ambient conditions. Further, with the increase in the

convective heat transfer coefficients, the PCM re-solidification is found to improve, while it reduces the PCM melt fraction due to accelerated surface cooling, indicating a trade-off between enhanced cooling and uniform thermal distribution.

Keywords: *Battery Thermal Management System, Phase Change Composite, Effective Thermal Conductivity, Metal Foam, Rapid Discharging, Hybrid Cooling, Realistic Drive Cycles.*

TABLE OF CONTENT

LIST OF FIGURES

LIST OF TABLES

NOMENCLATURE

A_m	Mushy Zone Constant
a	Ligament's radius, m
BTMS	Battery thermal management system
HBTMS	Hybrid battery thermal management system
C	Inertial coefficient of the porous medium
C_p	Specific heat capacity, $J/kg{\cdot}K$
CC	Continuous cooling
CFD	Computational fluid dynamics
d_p	Pore size, m
d_l	Ligament diameter, m
ECM	Equivalent circuit model
ECh	Electrochemical
ETC	Effective thermal conductivity
EVs	Electric vehicles
e	node length, m
g	Acceleration due to gravity, m/s^2
HEVs	Hybrid electric vehicles
H	Enthalpy, J/kg
HWFET	Highway Fuel Economy Test
h	Heat transfer coefficient, $W/m^2.K$
I	Current, A
IC	Intermittent cooling
J	Total energy consumption
j	Current density, A/m^2
K	Thermal conductivity, $Wm^{-1}K^{-1}$
K_i	Thermal conductivity for ith layer, $Wm^{-1}K^{-1}$
L	Length of ligament, m
M	Permeability of porous medium, m^2
MF	Metal Foam
MSMD	Multiscale Multidomain
n	Coating thickness, m

OCV	Open circuit voltage, *V*
P	Pressure, *Pa*
PPI	Pores per inch
PCM	Phase change material
PCM_{lmp}	Phase change material with low melting range
PCM_{hmp}	Phase change material with high melting range
PBTMS	Passive battery thermal management system
$\dot{q}$	Volumetric Heat Generation Rate, W/m^3
Q	Total heat, *W*
R_e	Reynolds number
S	Source term in momentum equation
SOC	State of charge
SCP	Serpentine cold plate
T	Temperature
t	Time
U	NTGK model parameter
US06	Supplemental Federal Test Procedure
UDDS	Urban Dynamometer Driving Schedule
V	Voltage, *V*
$\vec{V}$	Velocity field, *m/s*
WLTP	Worldwide Harmonized Light Vehicles Test Procedure
Y	NTGK model parameter
ZCP	Zig-zag cold plate

Greek Symbols

α	Inclination angle for ligament (°)
β	Thermal expansion coefficient, *(1/K)*
β_1	Dimensionless parameters
β_2	Dimensionless parameters
γ	Volumetric Expansion Coefficient
δ	Thermal response time, *(s)*
ε	Porosity
ψ	Solid volume fraction
λ	Melt fraction

λ_1	Dimensionless parameters
λ_2	Dimensionless parameters
λ_3	Dimensionless parameters
ρ	Density, kg/m^3
φ	Electric potential, V
σ	Electrical conductivity, S/m
μ	Dynamic Viscosity, $Pa.s$
ω	Pore density (PPI)
Δ	Change

Subscripts

avg	Average
amb	Ambient
b	Battery
c	Coolant
cp	Cooling plate
eff	Effective
f	Fluid
g	Coating
i	Different layers
inf	Infiltrating
l	Liquid
max	Maximum
min	Minimum
mf	Metal Foam
O	Overall
ref	Reference
s	Solid
sur	Surface
Vol	Volume

Chapter 1

Introduction and Literature Review

1.1 General background

The rapid expansion of global population, industrial activity, and technological advancement has necessitated a sharp increase in energy demand; as per International Energy Agency (IEA), the demand is estimated to increase by 50% during 2020 to 2050 [1]. Despite significant progress in renewable energy technologies, fossil fuels are found to cater nearly 75% of the world's energy that contributes nearly 33 gigatons of CO_2 emission annually [2]. To meet the targets set by the Paris Agreement, particularly limiting global warming to below 2 °C, a significant effort needs to be made to reduce the CO_2 emissions through sustainable transportation technologies; wherein, the transportation sector contributes nearly 25% of global CO_2 emissions, primarily through gasoline and diesel-powered internal combustion engine (ICE) vehicles [3-4].

Electric vehicles (EVs) have emerged as an alternative to decarbonize transportation, improve air quality, and reduce reliance on fossil fuels. These battery-powered, zero-emission alternatives eliminate tailpipe pollution and have gained strong policy support worldwide. Several countries, such as Norway, UK, Germany, China, and India, have announced plans to phase out ICE vehicles by 2035–2040. India, under its Faster Adoption and Manufacturing of Hybrid and Electric Vehicles (FAME) initiative, aims for EVs to constitute 30% of the total vehicle by 2030 [5]. It may be noted that EVs primarily depend on battery modules as the source of power and these modules face intense thermal loads, especially during fast charging and high-power discharge events, with internal temperatures often surpassing 60 °C. Without effective heat dissipation system, this thermal buildup can accelerate battery degradation, reduce cycle life, and trigger safety hazards such as thermal

runaway [6-7]. Thus, thermal management is essential not only to extend battery life and maintain performance but also to ensure operational safety.

1.2 Battery technologies

Batteries in EVs store and supply electrical energy by converting chemical energy into electricity through electrochemical reactions. The EV batteries are classified in different categories such as lead-acid, nickel-metal hydride (NiMH), lithium-ion (Li-ion), and solid-state [8]. Among these, Li-ion batteries dominate due to their high energy density, longer lifespan, lightweight design, and fast charging/discharging capabilities [9]. These batteries offer higher efficiency, better charge retention, and lower self-discharge rates, which makes them suitable candidate for EV applications [10-11]; these are available in various form factors (cylindrical, prismatic, pouch) as shown in Fig. 1.1.

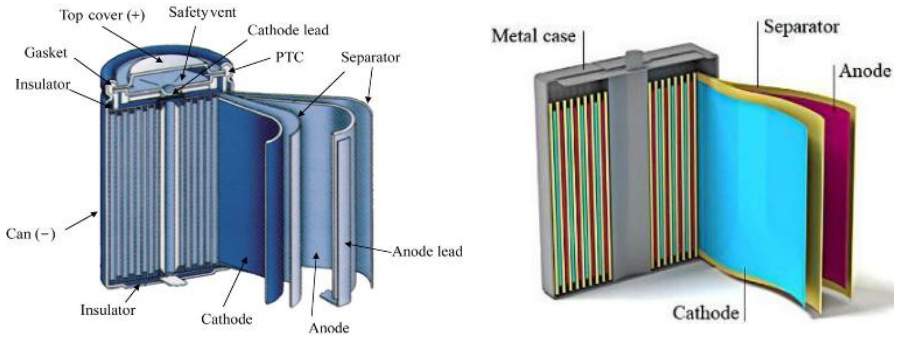

Cylindrical Li-ion cell Prismatic Li-ion cell

Figure 1.1: Commonly used Li-ion batteries

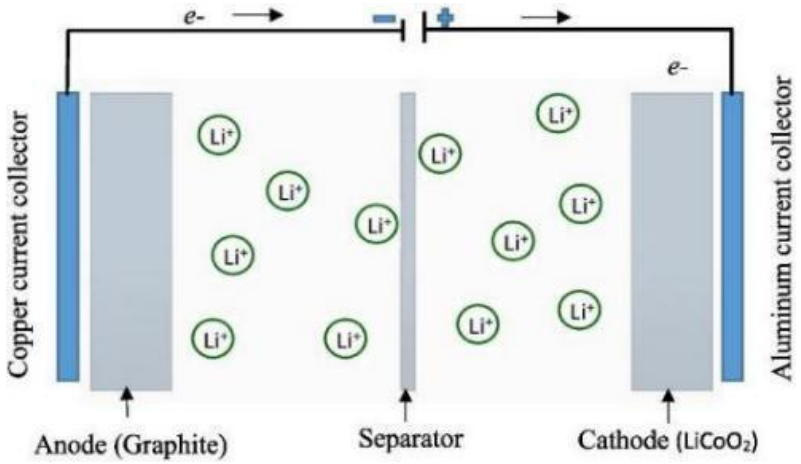

Figure 1.2: Components of Li-ion battery [12]

Lithium-ion batteries primarily consist of four key components: anode, cathode, electrolyte, and separator. These components and their configuration are illustrated in Fig. 1.2. The material composition and functional roles of each component in the Li-ion battery system are summarized in Table 1.1 [12]

Table 1.1: Components and electrochemical reactions for Li-ion battery

Components	Material	Purpose
Anode	Graphite	Stores lithium ions during charging and releases them during discharge
Cathode	Lithium metal oxides such as Lithium Cobalt Oxide ($LiCoO_2$), Lithium Iron Phosphate ($LiFePO_4$), Lithium Nickel Manganese Cobalt Oxide ($LiNiMnCoO_2$)	Releases lithium ions during discharge and stores them during charging.
Electrolyte	Lithium salt (typically $LiPF_6$) dissolved in organic solvents	Facilitates the transport of lithium ions between the anode and cathode.
Separator	Microporous polymer membrane	Prevents physical contact between electrodes while allowing ion flow

Charging and discharging of the battery

Figure 1.3 illustrates the working of the Li-ion batteries. During charging (energy storage), an external power source (battery charger) applies voltage, forcing lithium ions to migrate from the cathode to the anode through the electrolyte while electrons flow externally to the

anode. The lithium ions are intercalated into the graphite structure of the anode. While during discharging (energy release), the stored energy is released as lithium ions migrate from the anode to the cathode, generating an electrical current. The details of the reactions during charging and discharging are detailed in Table 1.2.

Table 1.2: Details of reactions during charging and discharging process

Stage	Anode	Cathode	Overall reaction
Charging	$xLi^+ + xe^- + C_6 \rightarrow xLiC_6$	$Li_xMO_2 \rightarrow xLi^+ + xe^- + MO_2$	$Li_xMO_2 + xC_6 \rightarrow xLiC_6 + MO_2$
Discharging	$xLiC_6 \rightarrow xLi^+ + xe^- + C_6$	$xLi^+ + xe^- + MO_2 \rightarrow Li_xMO_2$	$xLiC_6 + MO_2 \rightarrow Li_xMO_2 + xC_6$

where *x* denotes the number of lithium ions involved in the intercalation or deintercalation process, C_6 represent graphite, MO_2 represents the transition metal oxide in the cathode [13].

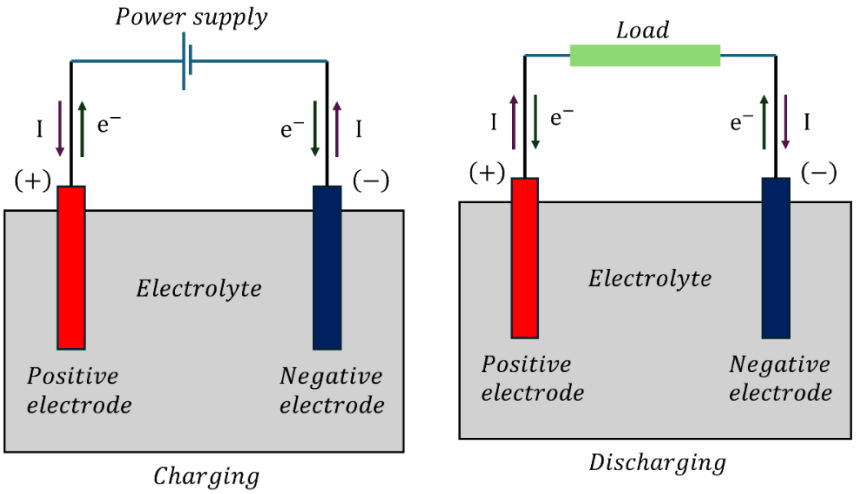

Cell under charging Cell under discharging

Figure 1.3: Working of Li-ion battery

1.3 Heat generation in batteries and its effects

1.3.1 Cause of heat generation in batteries

In a battery system, as current flows through various internal paths of the battery such as the electrode, electrolyte, separator, and current

collector, energy is dissipated due to resistance to ionic and electronic transport. In addition, the electrochemical reactions, which involve the transfer of lithium ions and electrons at electrode surfaces require driving voltage to overcome kinetic barriers, resulting in energy loss in the form of heat. During charging or discharging process, the transfer of lithium ions to (from) the system undergoes changes in internal energy and entropy; these thermodynamic processes can result in the absorption/release of heat, depending on the direction of the process and the specific properties of the electrode materials. Therefore, the heat generation in a lithium-ion cell arises due to various parameters such as interaction during charge transport, reaction kinetics, and thermodynamic properties. Also, the heat generation depends on various parameters such as charging or discharging (C-rate: the rate at which a battery is charged or discharged relative to its nominal capacity), temperature, state of charge (SOC), aging, and the design of the cell itself [7, 14]. The details of heat generation in battery modules are elaborated below.

1.3.2 The components of heat generation

The total heat generated within a lithium-ion battery during charging or discharging occurs due to various physical and chemical processes occurring inside the cell; this is illustrated in the Fig. 1.4 below.

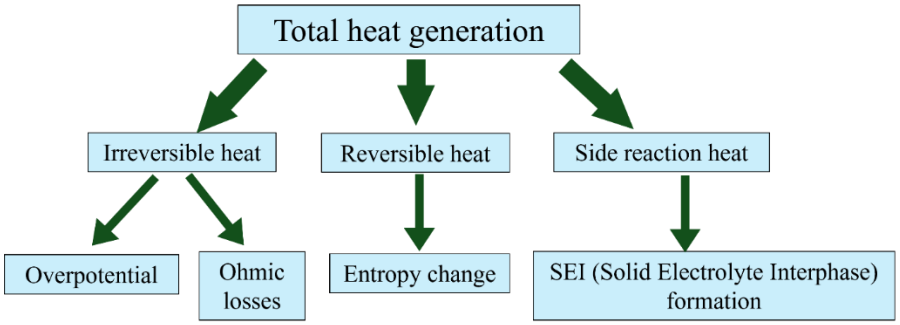

Figure 1.4: Components of heat generation in the battery

The heat sources can be broadly categorized into three main components:

$$Q_{charging/discharging} = A + B + C \tag{1.1}$$

Where, A, B and C denotes the heat generated due to irreversible, reversible and side reactions/degradation, respectively. During both charging and discharging, heat is produced due to energy losses associated with current flow, reaction kinetics, entropy changes, and degradation phenomena. This heat generation is captured by the widely accepted Bernardi equation and is defined as [12, 15, 16]:

$$\mathrm{Q_{charging/discharging}} = \mathrm{I(U - V)} - \mathrm{I}\left(\mathrm{T}\frac{\partial \mathrm{U}}{\partial \mathrm{T}}\right)_{\mathrm{soc}} \qquad (1.2)$$

Here, I, U, V, T, $\left(\frac{\partial U}{\partial T}\right)_{soc}$ and SOC is defined as charge/discharge current (A), open-circuit voltage (V), operating voltage (V), operating temperature (T), entropy coefficient (V/K) and state of charge of the battery, respectively. SOC refers to the percentage of a battery's remaining capacity relative to its maximum capacity. The details of various components of heat generation are detailed below.

A: Irreversible heat generation $[\boldsymbol{I(U - V)}]$

Ohmic (Joule) heating is the primary source of heat generation in Li-ion batteries which generates from internal resistance within the battery components. This resistance is usually found in various components such as electrode, electrolyte, current collector, and separator that restrict the flow of lithium ions and electrons. The magnitude of Joule heating increases significantly with higher charge/discharge rates such as fast discharging or rapid acceleration. In addition to Ohmic (Joule) heating, lithium-ion batteries generate heat from charge transfer and activation overpotential, which represent the extra voltage needed to overcome the kinetic and mass transport limitations at the electrode–electrolyte interfaces. Irreversible heat is always positive and is typically the dominant source of heat generation during high-current operation [7, 12-13, 16-18].

B: Reversible heat $[\left(IT\frac{\partial U}{\partial T}\right)_{soc}]$

This component is related to the thermodynamic entropy changes associated with the movement of lithium ions into and out of the electrode materials; the entropy of the system changes as lithium-ion intercalates into the electrode structure during charging or discharging. This component of heat generation depends upon the material, state of charge and operating temperature. The magnitude of reversible heat generation term depends on the magnitude of $\frac{\partial U}{\partial T}$ as below [7, 12-13, 16-18].

- When $\frac{\partial U}{\partial T} < 0$, the term becomes positive → heat is released (exothermic)
- When $\frac{\partial U}{\partial T} > 0$, the term becomes negative → heat is absorbed (endothermic)

C: Side Reaction Heat

In addition to the main sources of heat generation in a lithium-ion battery, certain quantity of heat generation takes place because of side reactions. These include the formation and thickening of the solid electrolyte interphase (SEI) layer, gas formation, degradation of electrode materials, and lithium plating. While the heat generation from these side reactions is usually low under normal operating conditions, it can be significant in aged cells or under stressful conditions [16, 18-19].

Heat generation during charging and discharging

It is observed that the amount and nature of heat generation inside a lithium-ion battery are not the same during charging and discharging process. The irreversible heat generation component (A) is always positive in the case of both charging and discharging process, while the reversible or entropic heat generation (B) varies during charging and discharging process. This component is related to the change in entropy that occurs as lithium ions move into or out of the electrodes. During

discharging, the entropy change often leads to the release of heat (exothermic), while during charging, especially when the battery is nearly full (high state of charge), the entropy change may cause the battery to absorb heat (endothermic). Because of this difference, the total heat generated is often higher during charging, particularly in the upper SOC range, where both resistance and entropy-related effects are more pronounced.

1.3.3 Possible harmful effects of heat generation

Excessive heat generation in lithium-ion batteries may lead to host of adverse effects that can significantly alter the performance, safety, and longevity. In the absence of effective heat removal mechanism, the rise in the internal temperature promotes electrochemical side reactions, such as electrolyte decomposition and degradation of the solid electrolyte interphase (SEI) layer; these reactions may lead to increase in the internal resistance, capacity fade, and performance degradation. Elevated temperatures also promote gas generation, which can result in cell swelling or leakage, especially in sealed configurations, and raises the risk of thermal runaway under high current loads.

In addition to these thermal effects, uneven heat distribution across battery cells and modules can create temperature gradients, resulting in non-uniform state of charges, localized over-charging/discharging, and non-uniform aging; all these factors reduce the reliability and service life of the battery system. Therefore, the main aim of the designer is to control the heat generation and maintain the temperature uniformity in the battery module which can ensure the safe, stable, and efficient operation of lithium-ion batteries. Also, the heat generation in battery modules is found to depend on the operating temperatures and is detailed in the next section.

1.4 Effect of operating temperature on thermal performance

Operating temperature plays a crucial role to access the performance, efficiency, lifespan, and safety of Li-ion batteries; it influences the electrochemical reaction kinetics, lithium-ion transport, internal resistance, and battery degradation mechanism [20-22]. In view of this, it is essential to maintain an optimal temperature range for the battery modules to ensure stable operation, maximize cycle life, and prevention of thermal runaway issues. The behaviour of Li-ion battery for different temperature ranges such as low, normal, and high, are discussed below.

1.4.1 Low-temperature operation (< 10 °C)

At lower temperature, battery performance is significantly affected due to reduced lithium-ion diffusion and increased internal resistance. The electrolyte becomes more viscous, reducing ion mobility and limiting charge transfer at the electrodes and leads to higher Ohmic losses, reduced power output, and lower charge acceptance. Also, the deposition of metallic lithium on the anode, can occur during charging, leading to irreversible capacity loss and potential short circuits. Alipour et al. [23] investigated the effect of operating temperature on a 20 Ah $LiFePO_4$ (LFP) pouch cells and reported that at -20 °C, the cell could not be discharged above 1C (The C-rate is a measure of the rate at which a battery is charged or discharged relative to its nominal capacity, for example, 1C rate indicates the battery is fully charged/discharged in one hour) due to a sharp voltage drop which may occur because of internal resistance; while, it is observed that discharge can be achieved up to 3C at -10 °C. Ramadass et al. [24] reported that the low-temperature, the operation can lead to significant reduction in capacity and power (often 30–40% below 0 °C) and significant non-uniformity in heat distribution. It is noted that the thermal gradient upto 10 °C can be observed across the cell surface, leading to uneven utilization of active materials and localized degradation. Zhang et al. [20] reported that lowering the

battery temperature from 20 °C to -20 °C results in the tenfold increase in internal resistance. Tippmann et al. [21] confirmed that the battery's stored energy and power output decreases due to reduced ion transport and increased lithium plating on the anode during charging; while at -40 °C, only 12% of the available capacity is recoverable compared to that at room temperature. Nagasubramanian [22] reported that at -40 °C, the energy and power densities of lithium-ion batteries are found to reduce by 5% and 1.25%, respectively, compared to their values at 20 °C.

1.4.2 Optimal temperature range (20 °C – 40 °C)

In general, the temperature range (20 °C – 40 °C) is recognized as optimal temperature range for Li-ion battery. In this temperature range, the electrochemical reactions occur efficiently, internal resistance remains minimal, lithium-ion transport is well-balanced enabling maximum energy efficiency with stable cycling and extended battery lifespan. It is argued that maximum capacity utilization and power efficiency are achieved in this temperature range, where the discharge rates can be achieved up to 3C with minimal voltage drop and temperature rise [23]. Tests conducted with battery Sony 18650 (18650 refers to cylindrical lithium-ion cell with 18 mm diameter and 65 mm long) exhibits strong capacity retention, (losing 30% of capacity after 800 cycles at room temperature) and stable impedance behaviour, while the longest cycle life is recorded (upto 1397 cycles) at a 1C discharge rate before losing its capacity by 20% [24]. In general, EVs utilize battery modules that includes multiple cells, which exhibit different characteristics such as internal resistance, capacity, and voltage; these behaviour leads to difference in charging and discharging characteristic resulting in non-uniform temperature profile within the module. Han [14] observed that in case of battery modules when the temperature difference between cells exceeds by 5 °C, the power output decreases by 10%, and thermal aging is accelerated by 25%. Therefore, in addition to the regulation of overall battery temperature, it is essential to control the

temperature gradient within the battery module. For EV applications, operating batteries within this optimal temperature range ensures maximum driving range, faster charging, and consistent power delivery.

1.4.3 High-temperature operation (> 45 °C)

At higher temperature (>45 °C), Li-ion batteries initially benefit due to the enhancement in reaction kinetics and reduced internal resistance, which leads to enhancement in power output, while for the sustained operation at this range leads to significant degradation in performance, reduces safety margins, and shortens the cycle life. Higher operating temperature accelerate side reactions such as SEI growth, electrolyte decomposition, and gas evolution, which leads to increase in internal resistance, loss of active lithium, and structural instability. In addition, Li-ion diffusion becomes non-uniform at higher temperature leading to localized heating, mechanical stress, and thermal gradients which can damage cell integrity. It has been argued that $LiFePO_4$ (LFP) pouch cells exhibits better performance at 50 °C under low C-rates, while they suffer power losses at higher discharge rates [23]. Figure 1.5 summarises the effect of operating temperature on the performance of Li-ion batteries.

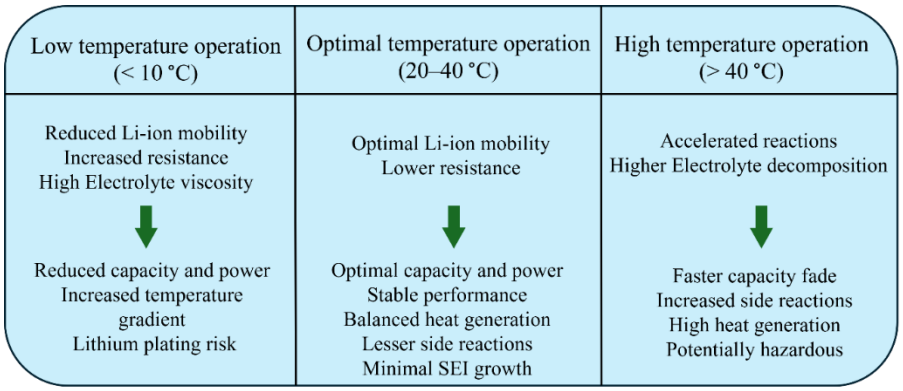

Figure 1.5: Effect of operating temperature on Li-ion battery performance

For 5C discharge at 50 °C, the surface temperature is found to reach to 82 °C; at this stage, the temperature approaches the boiling point of dimethyl carbonate (90.3 °C), a common electrolyte solvent and results

in the risk of solvent evaporation, gas generation, and potential thermal runaway. For Sony 18650 cells at 50 °C, nearly 60% capacity loss takes place after 600 cycles, while, at 55 °C, the capacity loss increases to 70% for 490 cycles [24]. Figure 1.5 summarises the effect of operating temperature on the performance of Li-ion batteries.

1.5 Thermal management techniques

As discussed in the previous section, excessive heat generation in lithium-ion batteries may lead to various adverse effects including reduced performance, safety, and longevity and the thermal runaway issues. In view of this, effective thermal management is essential to maintain the optimal operating temperature in batteries that can avoid overheating, improve performance, and extend the lifespan. The thermal management system (TMS) for batteries can be classified into three categories such as active system, passive system and hybrid system; the detail of components used for various thermal management techniques are shown in Fig. 1.6.

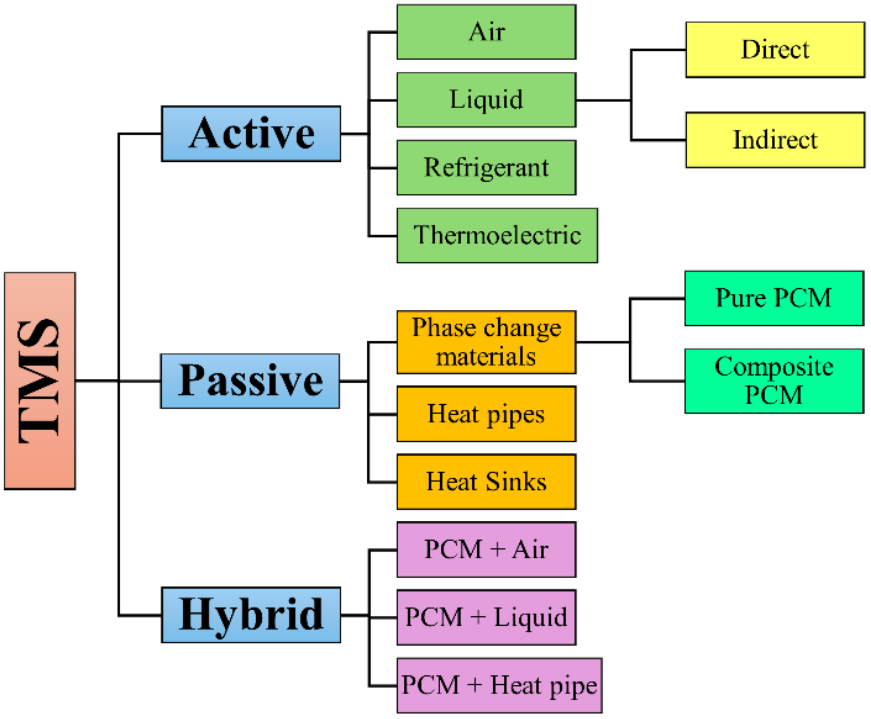

Figure 1.6: Classification of thermal management systems for batteries

1.5.1 Active techniques

Active thermal management techniques utilize external power to dissipate heat from systems. These techniques are widely used due to their simplicity, higher efficiency in controlling excess temperature in high power applications [7, 13, 17, 25]. The details are summarized below.

- *Air Cooling:* This technique utilizes forced airflow via fans or blowers to dissipate heat from the battery surface. It is simple, cost-effective, and commonly used in hybrid vehicles and small-scale battery modules.
- *Liquid cooling:* In this method, the coolant circulates through cold plates or cooling channels in direct or indirect contact with the cells; it offers superior heat removal capacity and is widely adopted in modern electric vehicles.
- *Vapor compression systems:* Such techniques use refrigerants in a closed-loop cycle to absorb the heat generated by battery modules; while, the technique needs higher power, it provides very good control on cooling and is used in high-performance EVs and stationary battery energy storage systems.
- *Spray and jet impingement cooling:* This technique involves the direct impingement of high-velocity coolant on battery surfaces and significantly enhances the localized heat transfer.

Figure 1.7 shows the schematic of air cooled, and liquid cooled active battery thermal management system.

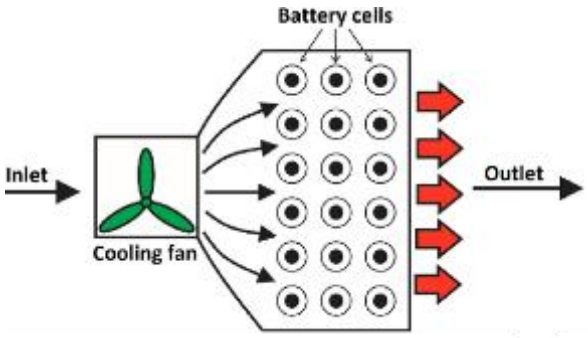

(a) Layout for air-cooled system

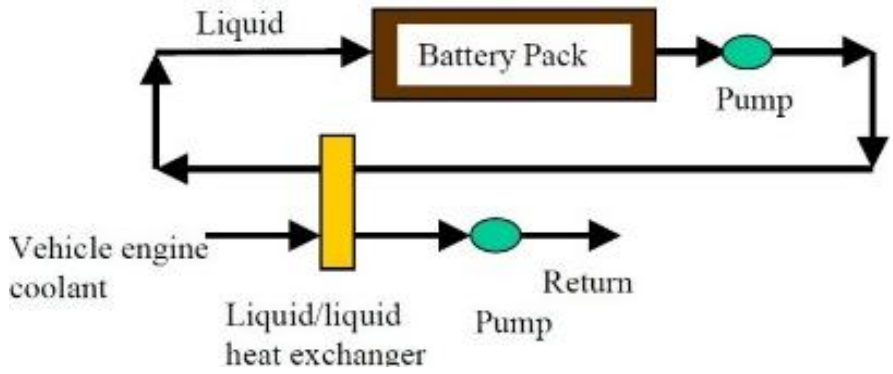

(b) Layout for liquid-cooled system

Figure 1.7: Active thermal management system [26]

1.5.2 Passive techniques

Passive thermal management techniques do not require external power and rely on natural heat dissipation processes such as conduction, convection, and radiation. These techniques are highly energy-efficient, reliable and simple in design; therefore, these techniques are widely used for compact, portable, or remote applications [7, 13, 17, 25]. The details of various passive techniques are summarized below.

- *Heat sinks:* These structures are made of various conducting materials in different configurations. These devices conduct heat due to multiple heat conducting paths. While, these devices are simple and less costly, their effectiveness is limited by ambient temperature and airflow.
- *Heat pipes: These devices* utilize phase change of liquid to rapidly spread heat away from high-temperature zones. These are compact and efficient devices for uniform distribution of temperature across the module.
- *Phase change materials (PCMs):* These materials change their phase after gaining heat energy from the hot surface and subsequently return to their original phase after cooling; these materials absorb and store excess during phase transition

(typically solid-to-liquid) and regulate the temperature of battery modules.

- *Radiative cooling surfaces:* These surfaces are used to emit heat through infrared radiation, these surfaces can be used in space applications or where convection is limited.

Figure 1.8 shows the heat sink and PCM based thermal management systems.

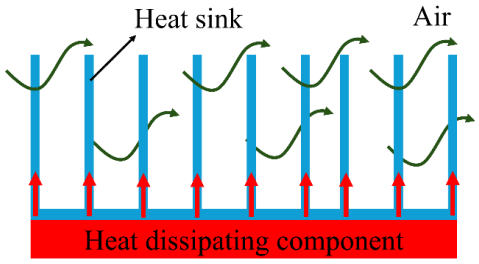

(a) Finned heat sink

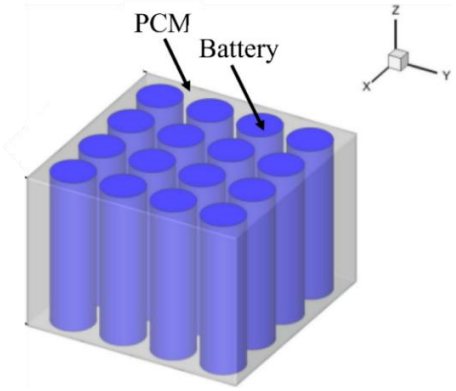

(b) PCM embedded with batteries

Figure 1.8: Passive thermal management system [27]

1.5.3 Hybrid techniques

Hybrid systems usually employ combination of both active and passive techniques to leverage their respective advantages; the details are elaborated below [7, 13, 17, 25]. Figure 1.9 shows the hybrid thermal management systems.

- *PCM + Air cooling:* In this configuration, the PCM absorbs excess heat during peak loads and reduces the thermal load on the air-cooling system, which helps to maintain a more uniform temperature distribution. Also, the airflow system prevents thermal buildup in the PCM and promotes the dissipation of residual heat to the surrounding.
- *PCM + Liquid cooling:* In this configuration, the PCM acts as a thermal buffer by absorbing heat loads, while the liquid cooling system enables continuous and efficient heat removal process.

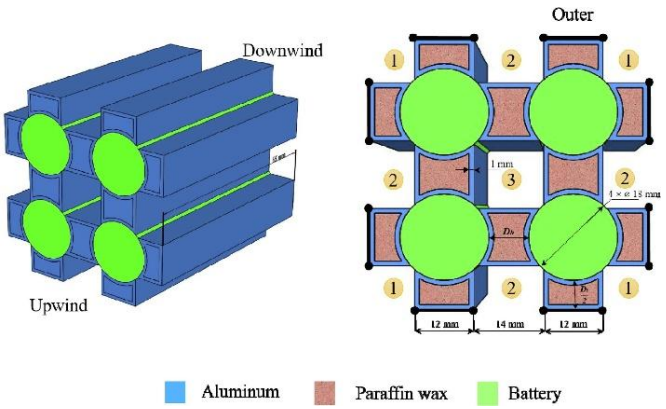

(a) PCM with forced air convection system by [28]

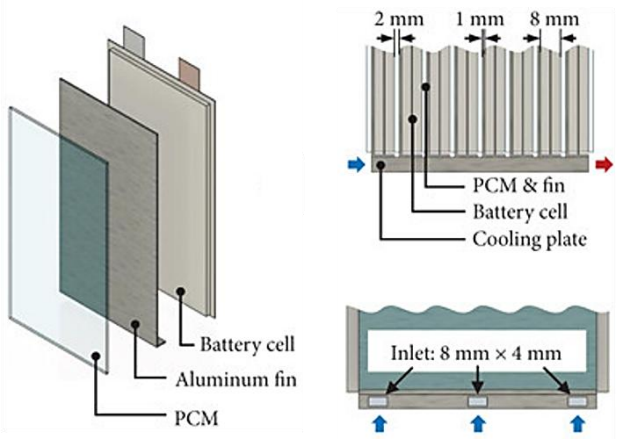

(b) PCM coupled with liquid cooling system by [29]

Figure 1.9: Hybrid battery thermal management system

The circulating coolant not only maintains the overall temperature of the battery pack but also helps to extract the heat stored in the PCM which

promotes faster solidification and enables the effective operation of thermal management system over extended cycles or under high thermal loads. The key features of passive, active, and hybrid thermal management strategies are comparatively summarized in Table 1.3.

Table 1.3: Comparison of different thermal management techniques

Features	Active Techniques	Passive Techniques	Hybrid Techniques
Power Requirement	Requires external power (fans, pumps, compressors)	No external power required	Moderate
Heat Removal Capacity	High; suitable for high-power, high-density systems	Moderate; best for low-to-medium power applications	High; handles transient and steady-state heat effectively
Complexity	High	Low	Moderate
Cost	Higher initial and operating costs	Low cost and minimal maintenance	Moderate; adds material cost but reduces operating expense
Reliability	Can be affected by mechanical or power failure	High; fewer moving parts	High
Size and Weight	Larger and heavier	Compact and lightweight	Moderate

Active cooling systems (such as liquid or air cooling) usually require auxiliary components including pumps, fans, compressors, heat exchangers, and piping, which substantially increase both the system volume and mass, typically contributing an additional 15–25 % to the total battery module weight. On the contrary, passive systems that

employ phase change materials (PCMs) or heat spreaders are compact in size as these systems eliminate moving parts and auxiliary units, leading to reduction in 5–8 % of the weight. Hybrid systems combine both techniques and therefore, exhibit better performance compared to passive systems with moderate increase in size and weight of the system.

1.6 Review of the literature

Extensive studies have been made to analyse the performance of various thermal management systems specifically for electric vehicle battery modules. These systems encompass a wide range of active, passive, and hybrid approaches. The relevant studies as reported by various researchers have been detailed below.

1.6.1 Active cooling techniques

Active cooling refers to a thermal management approach that relies on external energy input, typically provided by components such as fans or pumps, to dissipate heat from the system. In the case of battery modules, active cooling generally involves the flow of air or liquid around the cells to carry away excess heat and maintain temperature within safe operating limits. Yang et al. [30] reported the combined performance of PCM (n-eicosane) involving the air cooling for temperature control of 18650 batteries. The authors studied various PCMs with melting temperature of 28 °C, 35 °C and 42 °C and thickness varying between 1 mm to 5 mm; based on the analysis, the authors reported the optimum thickness as 2 mm for PCM melting point of 35 °C for effective thermal management. Li et al. [31] investigated a liquid cooled BTMS for a 12-cell prismatic $LiFePO_4$ module and evaluated the effect of cooling surface, number of inlet flow configurations and coolant flow direction. The optimal configuration, cooling from the inter-cell surface (Face A), with three inlets and alternating flow direction, achieved a maximum cell temperature of 303.6 K and a temperature difference of 2.3 K. Further analysis showed that increasing the single inlet mass flow rate to 1.2g/s, the peak temperature is found to reduce to 302.5 K while improving the temperature uniformity by 1.7 K. Huo et al. [32] analysed

a mini-channel cold plate-based BTMS for 5C discharging to examine the effects of channel number, flow direction, inlet mass flow rate, and ambient temperature on the performance. Results exhibit that the increase in the number of channels and the inlet flow rate significantly reduce the maximum battery temperature and optimal cooling is achieved with a flow rate of 5×10^{-4} kg/s.

Yan et al. [33] proposed a thermal management system involving mini-channel liquid cooling with air cooling; the authors analysed the temperature rise along the coolant flow direction in cylindrical Li-ion battery modules and reported that combining air cooling with optimized water flow rate (3×10^{-4} kg/s) reduced the maximum temperature and temperature difference by 2.22 K and 2.04 K, respectively. Li et al. [34] investigated the liquid cooling system involving copper tubes with silicon cold plates; the proposed configuration is found to outperform both natural and forced air cooling and found to maintain the maximum battery temperatures below 41.92 °C and temperature differences within 1.78 °C at a flow rate of 8 ml/s. The copper tubes are found to conduct heat away from the cold plates that significantly improve the cooling efficiency, especially at higher discharge rates; the system reduces the energy consumption by 47.4% compared to forced air convection.

Wang et al. [35] introduced a modular liquid-cooled BTMS to evaluate the effects of coolant flow rate and cooling configuration (serial vs. parallel) on the temperature control of battery modules. With the increase in the coolant flow rate, the thermal performance increases and attains a peak value; with further increase in coolant flow, the performance improvement is found to be minimal with increase in power consumption. Parallel cooling configurations exhibit superior performance compared to serial cooling configuration, lowering the maximum temperature and temperature difference by 7.55 °C and 6.74 °C, respectively at a 3C discharge rate. The optimal flow layout maintains a maximum temperature of 35.74 °C and a temperature difference of 4.17 °C. Zhao et al. [36] used a honeycomb-structured liquid cooling plate to enhance the heat dissipation performance of

prismatic lithium-ion batteries. The proposed dense hexagonal channels are found to significantly increase the heat exchange surface area. With 3 mm channel width, 6.8 mm hexagonal block spacing and an inlet velocity of 0.1 m/s, the system tends to maintain a maximum temperature of 302.5 K and temperature difference of 4.1 K.

Chen et al. [37] investigated the thermal performance of a hybrid BTMS using parallel mini-channel cold plates (PMCP) with three flow configurations such as I-type, Z-type, and U-type. Among the designs, symmetrical PMCP-I and PMCP-Z exhibit the superior performance compared to PMCP-U, while the symmetrical PMCP-I exhibits 43% and 61 % reduction in the maximum temperature difference (ΔT_{max}) and pumping power, respectively; on the contrary, PMCP-Z achieves the corresponding reductions of 19% and 66%, respectively.

1.6.2 Passive cooling techniques

Passive cooling is a thermal management technique that regulates temperature without the use of components such as fans or pumps. Instead, it relies on materials and design strategies that naturally absorb, store, or dissipate heat. Passive cooling is usually achieved through thermal conduction, natural convection, or the integration of heat-absorbing materials. This approach offers several benefits such as no external energy is needed for operation, silent operation, involves no moving parts, and requires minimal maintenance. Among various passive cooling approaches, the use of thermal energy storage materials such as Phase change materials (PCMs) has emerged as a promising solution for regulating temperature in battery systems.

PCMs for passive thermal regulation

PCMs are widely recognized for their high latent heat capacity and their ability to absorb and store thermal energy at nearly constant temperature during phase transition. This isothermal nature of phase transition allows PCMs to effectively mitigate temperature rise under thermally loaded condition, making them a promising solution for thermal management

in applications such as electronic devices, battery modules, and building energy systems [38]. With integration of PCM in thermal management modules, the PCM absorbs excess heat energy when the system temperature exceeds its melting point and later releases the stored energy during the cooling phase. This bidirectional heat exchange process provides a passive, energy-efficient, and reliable means of maintaining temperature within the desired operating range [39]. PCMs can be broadly categorized into three different categories: organic, inorganic, and eutectic (formed by mixing two or more components) each with distinct thermal and chemical characteristics. Among these, organic PCMs are most employed due to their favourable properties that include high latent heat capacity, chemical stability, lower supercooling, non-corrosiveness, long-term cycling reliability and ease of handling [40]. However, despite these distinct benefits, the practical integration of PCM in thermal management systems becomes difficult due to its inherently low thermal conductivity. Studies have demonstrated that PCMs can maintain battery temperature within safe operational limits by absorbing excess heat during high thermal loads.

Hussain et al. [41] numerically studied the effects of discharge rates (1C–5C), PCM type, ambient temperature, and heat transfer coefficients on the thermal performance of a prismatic Li-ion cell. They found that n-octadecane was most effective at 293 K and 300 K, while composite paraffin and RT-58 performed better at 313 K and 323 K. At 300 K, the proposed system reduced peak temperatures by 25.3 K and 19.5 K, and improved temperature uniformity by 5.3 K and 3.6 K at 5C and 4C, respectively. Zhao et al. [42] analyzed different PCM types (n-octadecane, n-eicosane, n-docosane) and the effect of PCM core size on the thermal management of 18650 batteries. The authors report that with the increase in the PCM core radius to 3.8 mm, the thermal management system can effectively maintain the peak temperatures below 50 °C. Wu et al. [43] investigated the influence of battery orientation on thermal performance for different combinations of PCMs with 18650-type cells. A horizontal arrangement configuration exhibits better temperature

uniformity (4.1 K) compared to the vertical configuration (5.7 K), as it helps to reduce heat accumulation in the solid PCM at the bottom.

Vashist et al. [44] demonstrated the role of PCM thickness in regulating cell temperatures; the author analysed three configurations (1.25 mm, 2.50 mm, and 5.00 mm) under discharge rates up to 3.5C. With 1.25 mm PCM layer, the thermal management module reduces the surface temperatures by 10.09 °C; while with thicker PCM layers, such as 2.50 mm and 5.00 mm, the melting process is delayed which indicates a slower thermal response.

Thermal conductivity enhancement in PCM

Researchers have proposed several techniques such as inclusion of metallic fins, metal foams, high thermal conductivity fillers and encapsulation to enhance the overall thermal conductivity of the PCM based thermal system [45]. Many times, the PCM thermal performance is improved with the inclusion of metallic fins. The fins act as passive conductors, increasing the heat transfer surface area and directs the heat away from localized hot spots, which improves the overall thermal response. The orientation and geometry of fins can also be tailored to meet specific application needs [46]. High thermal conductivity fillers also offer enhancement in performance, where various materials such as expanded graphite, metal particles, and carbon-based nanomaterials (e.g., carbon nanotubes and graphene) are dispersed within the PCM matrix. In some cases, the microencapsulation is also employed to improve thermal performance while also addressing practical concerns such as leakage and structural degradation. In this technique, the PCM is enclosed within thermally stable shells made of polymers or conductive materials [47]. However, these enhancement techniques exhibit certain limitations. The use of fins increases the system weight and occupies additional space, thereby reducing the available PCM volume and limiting design compactness. Additives (nanoparticles) can also lower the latent heat capacity of the composite PCM and may lead to issues such as sedimentation or agglomeration over time, affecting

long-term stability. Although microencapsulation effectively prevents the leakage and improves thermal cycling, it reduces the overall thermal storage capacity due to the presence of encapsulation material and introduces additional complexity in fabrication.

Another effective method to increase the thermal conductivity involves the integration of PCMs into porous structure such as Metal Foam (MF) [48]. These foams are characterized by porosity and pore density, typically measured in pores per inch (PPI). Porosity refers to the proportion of the foam's volume that consist of voids or empty space, which allows it to store a significant amount of PCM; a higher porosity indicates more available volume for PCM infiltration. Pore density, measured in PPI, refers to the number of pores present within one inch of the foam structure. It gives an indication of the pore size i.e., lower PPI corresponds to larger pores, while higher PPI means smaller, more closely packed pores. These interconnected networks create continuous conduction pathways that enhance thermal transport throughout the composite. In addition to improving heat transfer, porous structures provide structural support, capillary retention of the PCM during melting and reduce leakage [49]. Figure 1.10 illustrates copper-based open-cell foams with different pore densities.

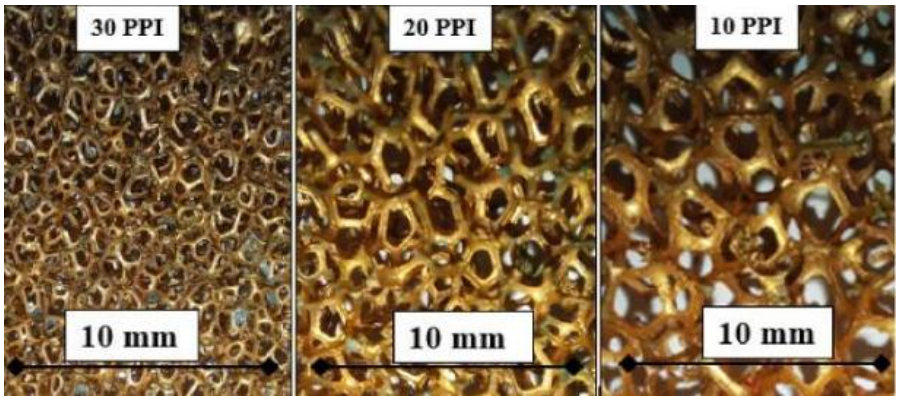

Figure 1.10: Open cell copper metal foams [49]

When saturated with PCM, the resulting MF-PCM composite addresses the typically low conductivity of PCM while enhancing thermal storage potential. To assess the performance of MF-PCM composite, an accurate estimation of thermophysical properties, particularly effective

thermal conductivity (ETC), becomes essential. Due to the intricate geometry of metal foams (Fig. 1.10), simplified 2D and 3D representations are commonly employed to model ETC of MFs saturated with PCM or fluid. Further enhancement of thermal conductivity has been achieved by coating open-cell metallic foams with high-conductivity materials. Petts et al. [50] reported the thermal conductivity of nickel foams coated with an ultra-thin layer of graphene and graphite to be 0.26 $Wm^{-1}K^{-1}$ to 1.7 $Wm^{-1}K^{-1}$, respectively, significantly higher than the base material. Hussain et al. [51] reported an increase of about 283% in the overall thermal conductivity of graphene coated nickel foam saturated with paraffin. These experimental studies demonstrated that coated MFs could achieve exceptional thermal properties and enhanced mechanical properties without increasing weight.

Studies on effective thermal conductivity modelling of MF-PCM composite

Calmidi and Mahajan [52] proposed a 2D theoretical model to estimate the effective thermal conductivity of metal foams saturated with fluid. Their model considers a 2D hexagonal-shaped structure with one node and two ligaments in the unit cell, assuming the shape of ligament and the node to be rectangle and square, respectively. The authors performed experiments with aluminium foams (ε_o = 0.90-0.97 and PPI = 5-40) infiltrated with air and water to validate their theoretical model. Bhattacharya et al. [53] extended the 2D model by considering circular nodes at the intersection of the ligaments, as shown in the Fig. 1.11.

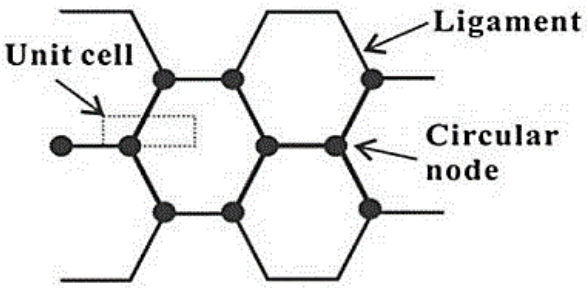

Figure 1.11: 2D unit cell of Calmidi and Mahajan [52]

The authors validated the theoretical models by fitting a dimensionless parameter called the area ratio ‘r’. Lafdi et al. [54] introduced a theoretical framework to account for the influence of surface coatings on metal foams. The study reveals that the addition of copper layer on carbon-based foams enhances the overall thermal conductivity compared to their uncoated counterparts; the proposed model exhibits good agreement with the test data. Chan et al. [55] proposed a theoretical model, based on the 2-D model of Calmidi and Mahajan [52], to predict the ETC of coated metal foams; the model, two empirical fitting parameters (r_s and r_g) are used to correlate the theoretical model with test data involving nickel and copper foams with graphene coatings. Paek et al. [56] proposed a 3-D cubic lattice configuration model to estimate the ETC of metal foams by following the initial approach suggested by Dul’nev [57]; the ETC is found to increase with the increase in the foam porosity. Edouard [58] proposed the cubic lattice model correlating the foam’s volume to that of a regular pentagonal dodecahedron. The ETC is estimated by analysing two limiting configurations such as slim foam (minimal node volume) and fat foam (dominant node volume). Later, Zenner and Edouard [59] proposed a model that employ a weighted arithmetic mean to bridge the slim and fat foam extremes. These models usually consider metal foams as periodic cubic frameworks which simplifies the mathematical treatment.

However, it is important to recognize that actual open-cell metal foams exhibit more irregular, stochastic geometries, which may limit the direct application of such idealized lattice-based models. To accurately represent the physical structure, numerous theoretical studies have been made that employ the tetrakaidecahedron geometry [60], also known as the Kelvin cell, to model ETC of MFs. This geometry is widely recognized as a close approximation of the natural structure formed during metal foam fabrication. During foaming, the Kelvin cell emerges when air bubbles are introduced into a molten metal slurry. These bubbles redistribute themselves within the liquid to minimize surface

energy, leading to a highly efficient spatial packing. As the bubbles stabilize, liquid metal accumulates at the junctions where the bubbles meet, forming interconnected strands and nodes that ultimately solidify into the foam structure [60-61]. The tetrakaidecahedron is composed of a combination of hexagonal and quadrilateral (square) faces (Fig. 1.12). Ligaments are the thin metal struts connecting these faces, while nodes form at the junctions where multiple ligaments intersect, appearing as slightly thickened regions.

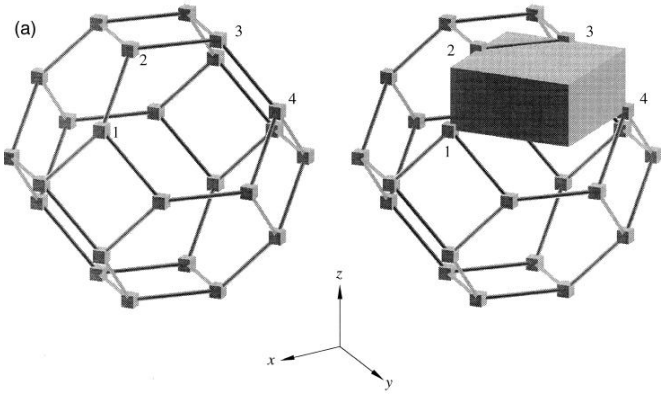

Figure 1.12: Tetrakaidecahedron structure [61]

This geometry accurately captures the topology of real open-cell metal foams and offers a logical basis to predict the thermal behaviour compared to simplified cubic or dodecahedral models. Boomsma and Poulikakos [61-62] proposed a theoretical model based on the tetrakaidecahedron structure to evaluate the ETC of MFs. The authors proposed a three-dimensional representative volume element featuring a hexagonal geometry derived from the Kelvin cell framework; the authors introduced a dimensionless fitting parameter "e" defined as the ratio of the edge length of a node to the length of a ligament to correlate the theoretical model with the test data of Calmidi and Mahajan [52]. Dai et al. [63] extended the Boomsma Poulikakos [61-62] model by incorporating the influence of ligament orientation on thermal transport, which aims to represent the directional conduction pathways within the foam matrix; these models usually consider a constant value of fitting parameter "e" to correlate the theoretical model with the test data. Yang et al. [64] argued that the structural dimensions of metal foams vary with

porosity, and therefore assumption of fixed value of geometric parameter may reduce the accuracy of the solution. In view of this, the authors proposed the model by incorporating a dimensionless parameter that is a function of porosity that enables a more adaptable and physically representative framework to predict ETC for a wide range of foam structures. Yao et al. [65] improved the earlier model by incorporating concave triprism shaped ligament and pyramidal structure, which is the realistic MF structure. Wu and Huang [66], further proposed a theoretical model employing the pentagonal dodecahedron geometry by incorporating various parameters such as the shape, hollowness, and inclination of the ligament.

It is evident from the literature that because of the more realistic representation of the MFs, compared to other structures, the tetrakaidecahedron structure is widely used for the analysis. Several models have been developed to estimate the ETC of uncoated MFs saturated with fluids or PCM. These models, while effective for uncoated systems, are unable to predict the influence of surface coatings on the ETC. Conversely, limited two-dimensional models have been proposed to address the effect of coating thickness of metal foams on the ETC. The summary of various models is elaborated in the Table 1.4.

Table 1.4: Summary of effective thermal conductivity models for MFs saturated with PCM or Fluid

Author	Analysis	Unit cell description and Geometry	MF coating	Ligament orientation	Remark
Calmidi and Mahajan [52]	2D	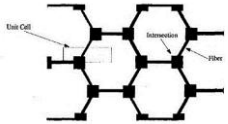 Hexagonal cell - square nodes	No	No	▪ Semi-analytical 2D model. Hexagonal honeycomb structure with square nodes. Value of fitted parameter, r = 0.09. Unrealistic representation of MFs.
Bhattacharya et al. [53]	2D	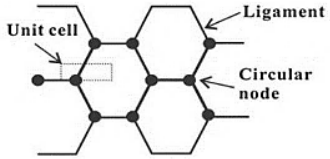 Hexagonal unit cell with circular node	No	No	▪ Semi-analytical 2D model. Hexagonal honeycomb structure with circular nodes. Value of fitted parameter, r = 0.19. Unrealistic representation of MFs.
Paek et al. [56]	3D	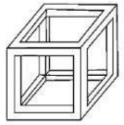 Cubic cell	No	-	▪ Semi-analytical 3D model. Twelve cubic ligaments without any node. The model exhibits better agreement with the test data.

Edouard [58]	3D	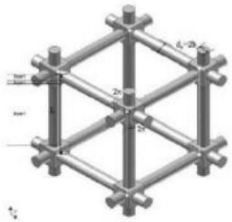 Cubic cell	No	-	▪ Semi-analytical 3D model. Modified cubic geometry and unrealistic representation of MFs.
Zenner and Edouard [59]				-	▪ Twelve cylindrical ligaments in the unit cell with nodes. Model exhibits an improvement over the previous model. Unrealistic representation of MFs.
Boomsma and Poulikakos [61], [62]	3D	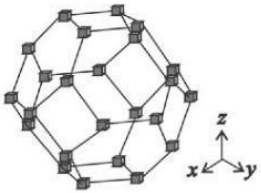 Tetrakaidecahedron cell	No	No	▪ 3D semi-analytical model based on tetrakaidecahedron structure. Cylindrical ligaments and cubic nodes. Value of fitted parameter, $e = 0.339$. More realistic representation of MFs.
Dai et al. [63]	3D		No	Yes	▪ 3D semi-analytical model. Cylindrical ligaments and cubic nodes considering the orientation of the ligament. Value of fitted parameter, $e = 0.198$. ▪ More realistic representation of MFs.
Yang et al. [64]	3D		No	Yes	▪ 3D semi-analytical model. Cylindrical ligaments and cubic nodes considering the orientation of the ligament. Improvement over previous model as fitted parameter is expressed as function of porosity of MF.

Yao et al. [65]	3D	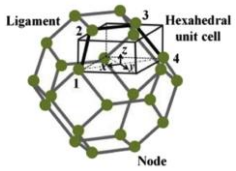 Tetrakaidecahedron cell	No	Yes	▪ Tetrakaidekahedron structure with concave triprism ligament and pyramidal node. ▪ More realistic representation of node, ligament and metal foam geometry, eliminates the requirement of empirical parameter.
Lafdi et al. [54]	2D	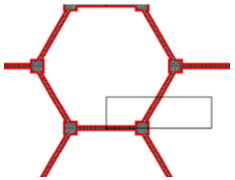 Hexagonal Unit cell with square nodes	Yes	No	▪ Semi analytical 2D model. ▪ Hexagonal honeycomb structure with square nodes. ▪ The model is validated for copper coated carbon foams for a porosity of 0.97. ▪ Unrealistic representation of MFs.
Chan et al. [55]	2D	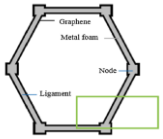 Hexagonal Unit cell with square nodes	Yes	No	▪ Semi analytical 2D model. ▪ Hexagonal honeycomb structure with square nodes. ▪ Two dimensionless parameters have been used to validate with experimental results. ▪ Unrealistic representation of MFs.

Studies based on MF-PCM composites

Numerous studies have been made that analyse the effect of MF-PCM composite on the performance of thermal management system. Huang et al. [67] studied PCM-based cooling for a 25-cell 18650 Li-ion battery pack under constant discharge conditions. The addition of metal foam in PCM maintained the temperature gradient below 1 °C for the porosity value of 94%. However, the impact of metal foam pore density (pores per inch, PPI) on the performance was not specifically analyzed by the authors; the findings indicate that thermal conductivity beyond a certain threshold shows diminishing returns on thermal performance. It has been argued that porosity value of 94% offers the best balance between temperature reduction and uniformity, optimizing thermal management performance. Alipanah and Xianglin [68] numerically analyzed a range of PCMs and MF-PCM composites under various values of heat flux conditions (q" = 400, 600, and 800 W/m²) for simulated battery discharging condition. PCMs with higher thermal diffusivity are found to maintain lower battery temperatures, while metal foam integration significantly enhanced thermal performance. Gallium and octadecane based PCMs involving Al foam exhibit better heat storage capacity compared to pure octadecane. Li et al. [69] examined the thermal performance of copper MF with PCM (RT 44HC) in a prismatic Li-ion battery pack for varied range of porosity values (0.90, 0.95, and 0.97) and is shown in Fig. 1.13.

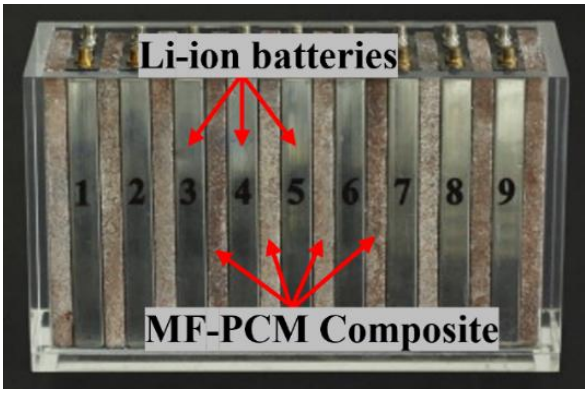

Figure 1.13: Battery pack integrated with MF-PCM composite, adopted from Li et al. [69]

At higher PPI, the MF increases cell temperature due to reduced pore size, although the composite still maintains better thermal uniformity than air convection cooling. Li and Barnes [70] investigated a 19.5 Ah prismatic $LiFePO_4$ cell integrated with aluminum and carbon foams integrated with PCM for different C-rates (1–5) and varied range of environmental temperatures (4 °C, 20 °C, and 35 °C). It has been observed that at 3C discharge, the average battery surface temperature could rise by 25 °C, with significant temperature variations of up to 17 °C across the surface; while, with foam and PCM combination, the temperature is maintained within the limits and the foam-PCM combination consistently performed better under all test conditions. Heyhat et al. [48] analyzed the thermal behavior of PCM embedded with MF for an 18650 Li-ion battery for heat rejection rates of 4.6 W and 9.2 W. The MF-PCM combination demonstrated superior thermal performance with lowering the mean battery temperature by 4 K and 6K at 4.6 W and 9.2 W, respectively, while changes in porosity from 95% to 85% had minimal effect. Kursun et al. [71] explored how outer container geometry affects the battery cooling when used with MF-PCM. Among the five tested geometries, a triangular container design achieved the lowest battery temperatures, reducing them by 14.42% compared to circular enclosures.

Studies based on PCM coupled with fins

Sun et al. [72] studied the effect of different fin shapes such as cylindrical and longitudinal for the thermal management of cylindrical (26650 type) cells. The authors used a cylindrical heating element to mimic the thermal behavior of the battery; it is observed that the addition of fins can increase the working time of the batteries at the optimum temperature. In another study [73], a novel arc-shaped fin was embedded with PCM and the enhancement in working time was found to be 157%, 189%, and 238% for ambient temperature of 20 ºC, 30 ºC, and 40 ºC, respectively. Choudhari et al. [74] studied the effect of various fin shapes such as triangular, rectangular, “I”, and “T” embedded with PCM

on the thermal performance of system involving an 18650-type cell (Fig. 1.14). The optimized PCM module with a 26 mm PCM thickness and 4 fins is found to reduce the battery temperature by 2.38% and 9.28% at 2C and 3C, respectively. The "I" shaped fin exhibits the best efficiency and triangular fins shows the least efficiency. Later on, the authors [75] analyzed a 5×5 battery pack for various configurations of fins with PCM; with the increase in heat transfer coefficient from 5 W/m^2K to 25 W/m^2K, the average cell temperature and melt fraction is found to decrease by 19.79 ºC and 66%, respectively.

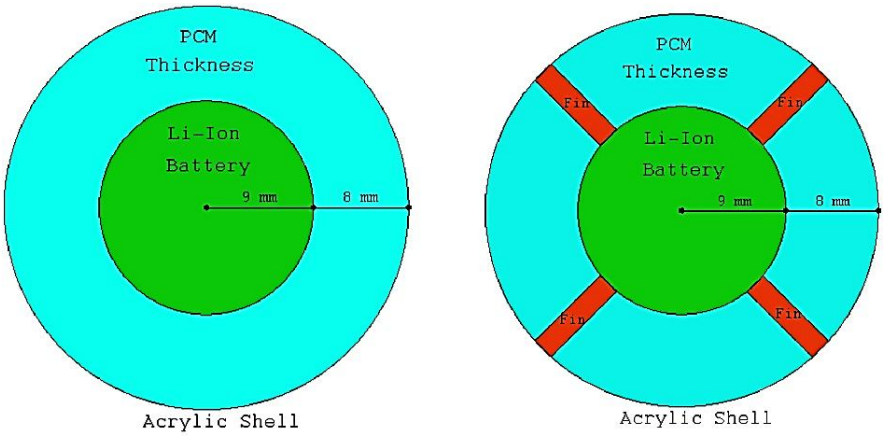

Figure 1.14: Cell in PCM-Fin arrangement by Choudhari et al. [74]

Ambekar et al. [76] conducted two-dimensional (2D) thermal analysis of various cylindrical cell configurations involving different fin arrangements for a range of discharge rates (1C to 3C). While the fins enhance the thermal conductivity, excessive number of fins could reduce the available PCM volume, leading to reduced heat absorption capacity. Further, the inclined fin arrangement is found to be most effective in regulating cell temperature, offering an optimal balance between heat dissipation and PCM utilization. Zare et al. [77] incorporated internal and external fins into a PCM coupled cylindrical battery system, and the best thermal performance was achieved with four internal-external fins; for such cases, the surface temperatures are reduced by 9.90 K (3C) and 17.45 K (5C) with 11.11% improvement in heat storage capacity. Li et al. [78] studied dual-PCM configuration to enhance adaptability across varying environmental conditions; the dual PCM configurations were

found to reduce overall battery temperature and temperature gradient across all discharge rates compared to the system that incorporate individual PCMs (single PCM at a time). Such systems are found to maintain the battery temperatures within 29.87 °C – 39.41 °C for 1C-5C discharge rates at 25 °C ambient temperature. Wang et al. [79] studied the effect of different fin types and found that four longitudinal fins demonstrate optimal cooling with reduction in battery temperature from 36.9 °C to 34.2 °C, the detail of their configuration is shown in Fig. 1.15.

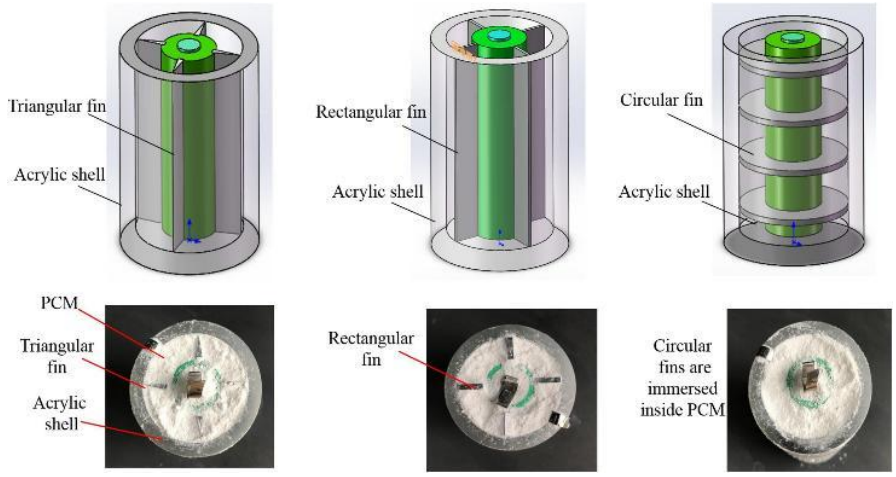

Figure 1.15: Various fin arrangements with PCM by Wang et al. [79]

For this configuration, the circular fin arrangement provides a larger effective contact area with the PCM compared to the corresponding longitudinal fin design, which enhances the radial heat conduction from the battery surface [79]. However, performances of such systems are found to depend on various parameters such as number of fins, their dimensions, thickness, and spacing. It has been argued that the number of fins enhances heat dissipation, while excessive number of fins may reduce the overall efficiency due to reduced PCM volume. For the optimized condition of PCM-finned configurations, the rise in the temperature is limited to 29.1 °C and the difference in the temperature is found to be 1.8 °C at 1C that ensures the better thermal uniformity [79].

Studies based on PCM enhanced with nanoparticles

Numerous studies have evaluated the effect of nano-enhanced PCMs (NePCMs) on the performance of battery thermal management systems. Bais et al. [80] analyzed the thermal performance of NePCM by incorporating Al_2O_3 nanoparticles into RT-42 across a range of concentrations (0.5% to 5% by weight), with a fixed PCM thickness of 4 mm. It was observed that increasing the nanoparticle concentration led to a rise in battery temperature, likely due to the reduction in the latent heat capacity of the composite. Balaji and Akula [81] investigated the effect of addition of expanded graphite to the PCM (Eicosane) embedded with fins; the addition of fins and expanded graphite is found to reduce PCM temperature, enhance the temperature uniformity and operating time. The best performance is reported by 260 fin system with maximum reduction in peak temperature by 17.5 °C (2C), 20.5 °C (3C), 22.7 °C (4C). The summary of various studies is elaborated in the Table 1.5.

Table 1.5: Overview of studies on PCM integration with fins, additives, and MFs

Author	Analysis details	Investigation parameters	Remark
Choudhari et al. [74]	Investigation: Numerical Battery: Cylindrical (18650) PCM: Paraffin RT-42 Discharge rate: 1-3 C	Effects of PCM thickness, fin structures (rectangular, triangular, trapezoidal, I and T shapes) and heat transfer coefficient.	▪ Proposed optimum parameters: PCM thickness of 26 mm, number of fins 4 and heat transfer coefficient 15 W/m^2. Only tested for single cell with one PCM type and only for discharging. Does not consider the effect of ambient temperature ▪ Proposed system could be bulkier with reduced energy density of battery pack.
Choudhari et al. [75]	Investigation: Numerical Battery: Cylindrical (18650) PCM: RT44HC Discharge rate: 1-3 C	Tested four fin configurations in the battery pack's central region. Effect of rest time between charge and discharge; cyclic charging-discharging operation.	▪ Proposed to place fins at the central region only to get better performance (Type 4). ▪ Only tested with single PCM and does not consider the effect of ambient temperature
Hussain et al. [41]	Investigation: Numerical Battery: Prismatic (14.6 Ah) PCM: n-octadecane, RT-58, composite paraffin Discharge rate: 1-5 C Harsh thermal loading conditions on the battery	Effects of ambient temperature, discharging rate, and heat transfer coefficients. Selection of optimum PCM. Analysis under harsh thermal loading conditions.	▪ n-octadecane is effective at 293 K and 300 K, while composite PCM (paraffin + EG) and paraffin RT-58 perform better at 313 K and 323 K. ▪ Proposed system lowers the maximum temperature by 25.3 K at 5C and 19.5 K at 4C at 300 K ambient temperature. Lacks the optimization study for PCM thickness. Not tested for cyclic operation.

Kursun et al. [71]	Investigation: Numerical Battery: Cylindrical PCM: RT-42 Metal foam: Copper Discharge rate: 1-3 C	Effect of outer container geometry with PCM-MF composition; Effects of external heat transfer coefficient, PCM amount, and porosity of Metal foam.	▪ Triangular container reduced battery temp. by 14.42%. 2D simulations, single PCM type and single discharging conditions. Lacks the analysis on different ambient temperature
Balaji & Akula [81]	Investigation: Experimental & Numerical Battery: Cylindrical PCM: Eicosane Discharge rate: 2-4 C	Effect of addition of fins to the PCM. Influent of expanded graphite. Combined effect of PCM and expanded graphite.	▪ Best performance is reported by 260-fin system; maximum reduction in peak temp. by 17.5 °C (2C), 20.5 °C (3C), 22.7 °C (4C). Not investigated the effect of ambient temperature and different PCM type.
Li et al. [78]	Investigation: Numerical Battery: Cylindrical (18650) PCM: Paraffin, OP35E Discharge rate: 1-5 C	Influent of C rate in battery temperature. Effect of ambient temperature. Effect of using dual PCMs with fin. Optimization of fin with PCM arrangement	▪ The asymmetric fins reduced temperature rise by 42.76% at high ambient conditions. Reported temperature range between 29.87 °C and 39.41°C for 1C–5C discharge rates at 25 °C ambient temperature. The proposed system could require a complex manufacturing.
Vashist et al. [44]	Battery: Cylindrical (18650) PCM: Capric acid Discharge rate: 1-3.5 C	Effect of discharge rate. Analysis on thickness of PCM. PCM thickness optimization	▪ Proposed a 1.25 mm PCM layer that reduced surface temperatures by 10.09 °C at 3.5C discharge rate. (1.25 mm, 2.50 mm, 5.00 mm), 35–40 °C up to a discharge rate of 3.5C. ▪

1.6.3 Hybrid cooling technique

A hybrid thermal management system usually combines both active and passive cooling techniques to regulate battery temperature. In such a case, the hybrid system utilizes the strengths of each method and enhances cooling performance, improves energy efficiency and thermal stability under varying operating conditions. In view of this, numerous studies have been made to analyze the performance of various hybrid cooling techniques and are discussed below.

Mousavi et al. [82] investigated a mini-channel cold plate (MCP) with PCM (n-eicosane) for thermal management of prismatic batteries under pulse and constant thermal loading conditions. The orientation of battery modules is found to significantly influence the performance of BTMS. Compared to MCP, the hybrid MCP is found to lower maximum battery temperatures by 0.06 K, 1 K, and 10.35 K at heat loads of 100, 200, and 400 kW/m³, respectively. Yang et al. [83] proposed an innovative honeycomb-shaped BTMS involving hexagonal cooling plate with PCM for 18650 cylindrical cells. Compared to a rectangular cooling plate, the hexagonal design is found to reduce the peak temperature, temperature gradient, and pressure drop by 0.36 K, 2.3 K, and 4.37 Pa, respectively, at an inlet flow rate of 0.001 kg/s. Akbarzadeh et al. [84] analyzed the thermal behavior of a 48V Li-ion battery module involving liquid-cooled aluminum plate with PCM. The hybrid cooling approach is found to reduce pumping power by 40% compared to conventional liquid cooling and maintains an average temperature of 3.5 °C lower compared to standard aluminum cooling plate. Xu et al. [85] examined the hybrid BTMS involving PCM, liquid cooling, and expanded graphite to enhance thermal management in high C-rate charge-discharge cycles. Integration of EG with PCM improves the temperature control, but the benefits plateau beyond 9% EG concentration. It is observed that in case of pure PCM systems, the increase in the battery spacing significantly increases the battery temperature, while the addition of EG reduces this temperature. The study identified RT44HC as a suitable PCM due to its higher melting temperature, which effectively dissipates heat under

harsh conditions. While the EG content of 3%, battery spacing of 3 mm and coolant velocity of 0.01 m/s is considered as the best combination for balancing cooling performance, cost, and system weight. Zheng et al. [86] and Wang et al. [87] demonstrated the benefits of wavy, microchannel cold plates integrated with PCM that achieves temperature reductions and uniformity. PCM layer of 1 mm thickness is identified as optimal condition which lowers the temperature difference by 3.56 °C while maintaining high energy density and PCM utilization efficiency. While, the coolant flow rate increases heat dissipation, it reduces temperature uniformity. Further, the authors report that the coolant inlet temperature should be close to the battery pack and PCM phase change temperature to balance heat dissipation and temperature uniformity. Under pulsed heat loads, the hybrid wavy microchannel cold plate is found to reduce the maximum temperature by 2.3 K and the temperature difference by 0.5 K compared to wavy microchannel cold plate. Additionally, the hybrid case is found to reduce system weight by 45%, significantly improving energy efficiency for EV applications. Liu et al. [88] investigated mini-channel cold plates with PCM at both single-cell and pack levels and analyzed the effects of coolant flow rate, inlet temperature, and PCM thickness on the thermal performance. In single-cell tests, a 3-channel MCP with a 5 mm PCM layer is found to lower the battery temperature from 64.45 °C to 42.83 °C (33.55% reduction) at 2C discharge. The hybrid system exhibits superior performance compared to single-side PCM cooling and requires 13 times less energy compared to MCP-only cooling to achieve similar thermal regulation. Lee et al. [89] analyzed the hybrid system using PCM to improve the heat dissipation during fast charging and battery preheating in cold environments, Fig. 1.16 provides an overview of their configuration. Parametric optimization results in 35.2% reduction in liquid cooling duration compared to conventional BTMS. During 3C fast charging at room temperature, the system limits the maximum battery temperature to 39.3 °C. Among various configurations, a double-layer pouch combining pure PCM and PCM composite with copper foam is found to exhibit the best performance. A PCM layer of 1 mm is found to offer

optimal thermal control, the heat transfer rate is found to enhance with the addition of 1 mm graphite fins to the system.

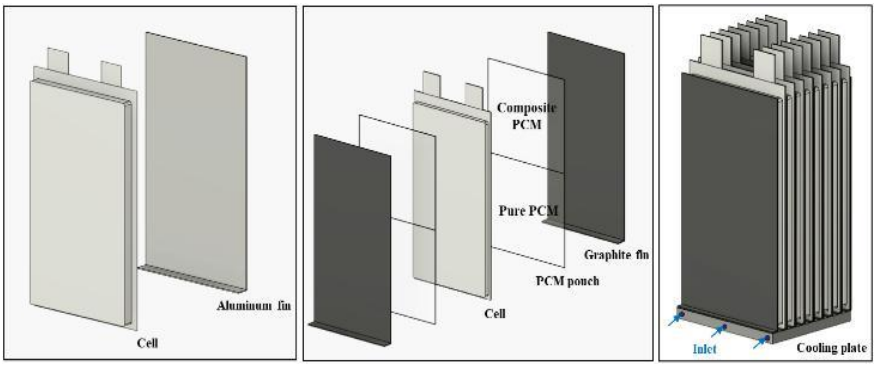

Figure 1.16: Cold plate coupled with PCM; from Lee at al. [89]

An et al. [90] proposed a novel capillary/honeycomb configuration involving bionic cooling channels and honeycomb cold plates. The system enhances the contact with the battery surface, reduces PCM degradation and improves efficiency by 14.11 %. The honeycomb design is found to provide uniform cooling, while capillary channels and diagonal inlet/outlet layout further enhances the heat exchange with minimal pressure drop. Liu et al. [91] proposed liquid cooling and PCM with a honeycomb structure to enhance heat dissipation in lithium-ion pouch cells. The author compared the performance of various cooling methods such as air PCM, and liquid-PCM cooling methods. Compared to other methods, the liquid-PCM system is found to offer superior performance, and the optimal result is obtained at a flow rate of 0.06 m/s and 36 °C coolant inlet temperature. Hybrid cold plates with Z-type parallel channels [92] offer another strategy for enhancing BTMS efficiency. This study introduces a hybrid liquid cold plate incorporating Z-type channels, a PCM/aluminum foam composite. The best design is found to reduce weight by 53% and maintain the thermal control below 40 °C. The delayed cooling approach improves energy efficiency and reduces power use by 90% at 1C and more than 50% at 2C. At 3C, small PCM block design (D8) is found to outperform larger blocks (D1) which reduce power by 85% and make them ideal for high-load scenarios. The key findings from the studies are summarized in Table 1.6.

Table 1.6: Summary of existing literature using PCM in hybrid thermal management system

Author	Details	Cooling methodology	Investigation parameters	Remark
Xu et al. [85]	Cylindrical (21700), 3Ah capacity, Numerical (3D)	Hybrid (PCM with liquid cooling)	PCM: RT28HC, RT35HC, RT44HC. EG content: 0-30%. Coolant velocity: 0.01-0.05 m/s.	▪ Not tested with realistic drive cycles. ▪ Battery temperature reaches more than 100 °C during cyclic operations with pure PCM. ▪ Continuous coolant flow is required. Proposed system with PCM thickness of 3 mm with 3% EG with a coolant velocity of 0.01 m/s.
Zheng et al. [86]	Cylindrical (21700), 4Ah capacity, Numerical (3D)	Hybrid (PCM with liquid cooling)	PCM: OP44E; PCM thickness: 1-4 mm. Coolant flow rate: $1\text{-}4\times10^{-3}$ kg/s. Inlet coolant temperature: 20-40 °C	▪ 1 mm PCM layer reduces temperature difference by 3.56 °C while keeping peak battery temperature below 50 °C. ▪ Not tested with realistic drive cycle data. Evaluation has been made under single discharge rate. System could be bulkier with compromise on battery pack energy density; the system needs continuous coolant flow rate.
Wang et al. [87]	Cylindrical (18650) 2.2Ah capacity Numerical (3D)	Hybrid (PCM with liquid cooling)	PCM: RT44HC. PCM thickness: 2-4 mm. Number of micro-channels: 4-6	▪ Not tested with realistic drive cycles. Evaluation under constant discharge rate and pulsed heat generation case. ▪ Continuous coolant flow is required and pumping power of the system needs to be evaluated.

Qiu et al. [93]	Cylindrical (18650) 3.2Ah capacity Numerical (3D)	Hybrid cooling (PCM with liquid cooling)	PCM: Paraffin (85%) + EG (15%). Cooling channel diameter: 2-5 mm. Coolant velocity: 0.1-0.7 m/s.	▪ Proposed optimal conditions involving pipe diameter of 3.875 mm, velocity 0.4m/s with coolant start delay of 537.5s. ▪ Not tested with realistic drive cycles. The delayed cooling scheme fails to meet the optimum battery temperature range. Evaluation has been made under constant discharge rate and needs continuous coolant flow rate for operation.
Liu et al. [88]	Prismatic 40Ah capacity Numerical (3D)	Only PCM, Only Cold plate (liquid cooling), Hybrid (PCM with liquid cooling)	PCM: Paraffin wax. Inlet coolant velocity:0.01-0.1 m/s. Number of cooling channels: 2-4. Impact of various cooling schemes	▪ 5 mm PCM layer reduces the temperature from 64.45 °C to 42.83 °C (33.55% reduction). Not tested with realistic drive cycles. The design of hybrid system could increase the weight and decrease the pack energy density. ▪ Evaluation has been done only under constant discharge rate, and it needs continuous coolant flow rate.
Lee et al. [89]	Prismatic 16Ah capacity Experimental-Numerical (3D)	Hybrid cooling (PCM and liquid cooling plate with plate fin)	PCM: n-eicosane. Metal foam: 0.92 porosity. PCM thickness: 0.25-1.5 mm. Ambient temperatures: 25-35 °C	▪ Reported a maximum battery temperature and gradient of 39.3 °C and 3 °C, for 3C discharge. ▪ Not tested with realistic drive cycles. ▪ The proposed system could require high initial cost to set up. Evaluation under constant discharge rate. Continuous coolant flow is required.

Z An et al. [90]	Prismatic 15Ah capacity Experimental-Numerical (3D)	Hybrid cooling (PCM with liquid cooling)	PCM: Composite PCM with 6% EG. Shapes cellular metal matrix sink: circular, square, honeycomb. Various cooling channel configurations.	▪ For 3C discharge at 40 °C ambient, maximum battery temperature is limited to 45.16 °C using the honeycomb structure. ▪ Not tested with realistic drive cycles. Complicated design of the proposed system. Evaluated under constant discharge conditions.
Liu et al. [91]	Prismatic 60Ah capacity Numerical (3D)	Only PCM, Hybrid cooling (PCM with liquid cooling)	PCM: Paraffin, Honey-comb shaped cooling channel. Coolant flow rate: 0.02-0.1 m/s. Coolant inlet temperature: 30-40 °C.	▪ Not tested with realistic drive cycles. Complicated design of the cooling channels. ▪ Evaluated under constant discharge conditions. Continuous flow of the coolant required for the system.

1.7 Objectives and scope of present study

Extensive studies have been made to analyse the performance of battery modules by employing various methods such as active, passive and hybrid cooling techniques. These studies have been made through theoretical, numerical, and experimental investigations. These studies are found to employ different types of PCMs, thermal conductivity enhancers for passive cooling systems, while different coolant flow paths and number of coolant channels are used to analyse thermal performance of battery modules in case of hybrid thermal management systems. However, certain issues need to be taken care during thermal management of battery modules for various operating conditions; some of these are detailed below.

a) In the case of composite PCM systems involving metal foams (MFs), the theoretical studies have been proposed to predict the effective thermal conductivity (ETC) of uncoated MFs using 2-D models. Efforts should be made to propose three-dimensional (3D) theoretical models to estimate the overall thermal conductivity of both externally coated and uncoated open cell MFs saturated with fluids/PCMs.
b) The effect of various parameters of MF such as geometry (hexagonal and square), type of material, porosity, ligament behaviour (shape, orientation), shape of node, external coating thickness, and filler materials (fluid, PCM) on the thermal conductivity of the MF-PCM composite needs to be analyzed.
c) Existing studies that incorporate MF-PCM composite for the thermal management of battery modules are reported for lower discharge rates (1C to 2C), and steady thermal loading conditions involving 2D numerical models. Therefore, efforts need to be made to propose 3-D models to analyse performance of battery thermal management system for various conditions such as steady (higher C-rates) and dynamic thermal loading,

realistic drive cycles, thermal abusive conditions (internal and external short circuit tests).

d) Also, efforts need to be made to analyse the effect of PCM thickness, PCM type, ambient condition, discharge rates, MF porosity on the performance of PCM composite based battery thermal management system.
e) It may be noted that the existing hybrid thermal management system involving PCM with cold plates employs conventional designs that lacks the maximum utilization of PCM and require continuous coolant flow to maintain the performance, leading to higher energy consumption and a corresponding reduction in overall system efficiency. Therefore, effort should be made to develop an efficient hybrid thermal management system using PCM and liquid cooling channels and analyse the effect of various configuration of cooling channels, coolant temperature, coolant flow velocity on the thermal performance.
f) Further studies are required to analyse the performance of hybrid thermal management system employing commercial realistic drive cycles, cyclic charging-discharging operations and rapid battery discharging.

The present work is aimed to address the above-mentioned issues associated with performance enhancement of PCM composite based thermal management systems for electric vehicle battery modules. Here, efforts have been made to predict the effective thermal conductivity of both externally coated and uncoated open cell MFs saturated with fluids/PCMs by employing 3-D models. Numerical investigations have been made to evaluate the effect of various parameters such as porosity, PCM thickness, discharge rates, and realistic drive cycles on the thermal performance of MF-PCM composites coupled with prismatic batteries. In addition to this, an advanced hybrid thermal management system is developed involving PCM and liquid cooling with cold plates. The study addresses the effect of various parameters such as cooling channel design, coolant flow, inlet temperature, flow velocity on the

performance of thermal management system under cyclic charging and discharging conditions. Also, tests are performed with 18650 cylindrical Li-ion cells under various discharge rates ranging from 2C to 5C at room temperature; subsequently, the numerical results are validated with the test data. The organization of the thesis is as follows:

Chapter 1: This chapter discusses the heat generation in lithium-ion batteries and its performance at various operating temperatures. A detailed review of the literature on various passive and hybrid battery thermal management techniques, that utilize phase change materials (PCMs), has been discussed. Subsequently, the scope of present investigation has been highlighted.

Chapter 2: In this chapter, a three-dimensional (3D) theoretical model has been proposed to estimate the effective thermal conductivity (ETC) of both coated and uncoated open-cell metal foams saturated with fluids or PCMs. Also, the chapter discusses the effect of various parameters of MF such as geometry (hexagonal and square), type of material, porosity, ligament behaviour (shape, orientation), shape of node, external coating thickness, and filler materials (fluid, PCM) on the thermal conductivity of the MF-PCM composite.

Chapter 3: This chapter reports a comprehensive numerical investigation on the performance of PCM based thermal management schemes with battery modules. Initially, efforts have been made to analyse the effectiveness of MF-PCM composites to enhance the thermal regulation under high discharge rates; later on, the analysis has been extended to estimate the performance of hybrid thermal management system involving PCM with liquid cooling under realistic operational conditions.

Chapter 4: This chapter reports both experimental and numerical study on the performance of cylindrical 18650 lithium-ion cells using various PCM based thermal management systems. The effects of PCM type,

PCM thickness, PCM filling volume, ambient temperature, and heat transfer coefficients on thermal performance are analysed; the optimal design conditions are proposed based on the analysis.

Chapter 5: This chapter summarizes the conclusions obtained from the research work presented in the thesis. The chapter also outlines potential directions for future investigations on this topic.

Chapter 2

Theoretical model for effective thermal conductivity of open cell coated metal foams saturated with fluid/Phase change material

2.1 General background

Phase change materials (PCMs) are widely used for thermal energy storage and passive battery thermal management systems due to their high latent heat capacity and temperature-regulating capabilities. However, the low thermal conductivity of PCMs limits the rate of heat transfer, leading to slower thermal response and reduced system efficiency. Therefore, various approaches such as high-conductivity additives, fins, porous media, and metal foams have been incorporated to enhance the effective thermal conductivity of PCM systems. Among various approaches, open-cell metal foams (MFs) have shown considerable promise due to their high porosity, interconnected structure, and relatively good thermal conductivity. The MFs, impregnated with PCM, significantly improve thermal conductivity due to enhanced solid–solid conduction pathways, and lead to uniform melting/solidification and better heat distribution. Further, studies have demonstrated that uniform deposition of thin layers of high-thermal-conductivity materials onto metal foams can substantially improve their effective thermal conductivity (ETC). These coated metal foams offer various advantages such as enhanced thermal conductivity and improved mechanical and chemical stability, without significant increase in weight or reducing porosity. These advantages motivate designers to consider the use of coated MFs for thermal management applications.

It may be noted that only limited studies have been made that employ a two-dimensional (2-D) approximation to predict ETC of coated MFs, while various 3-D theoretical models have been proposed

by different researchers to predict the ETC of uncoated MFs saturated with fluid/PCM. In general, tetrakaidekahedron structure with different geometries (hexagon and square) is used to represent the MFs during analysis. The incorporation of various geometries (hexagon and square) in the model may provide different prediction results, which may be due to the number of heat-conducting paths and thermal resistance of the element and the shape of the skeleton and node. A comprehensive study incorporating the different shapes of MF geometry, ligament, and node is not available in the literature.

Therefore, in the present investigation, a 3D model involving a thin coating layer over the metal foam based on the tetrakaidecahedron structure is proposed to predict the effective thermal conductivity. The present study incorporates two different shapes of metal foam structure, namely, hexagonal and square, for the analysis. In the case of hexagonal structure, variation in the shape of ligament and nodes has also been considered for the analysis. In addition to this, the effect of ligament orientation in the MF geometry has been considered. The dimensionless parameters representing the ratio of length of the edge of node to the ligament length is expressed as the function of the overall porosity of the MF. The models are validated with the available test data for both coated and uncoated MFs, various materials of MFs such as (Aluminium, Copper, Nickel) saturating medium (air, water, paraffin wax), porosity range (0.9-0.98), PPI (5-40) and externally coated material (Graphene) and with the widely used existing theoretical models.

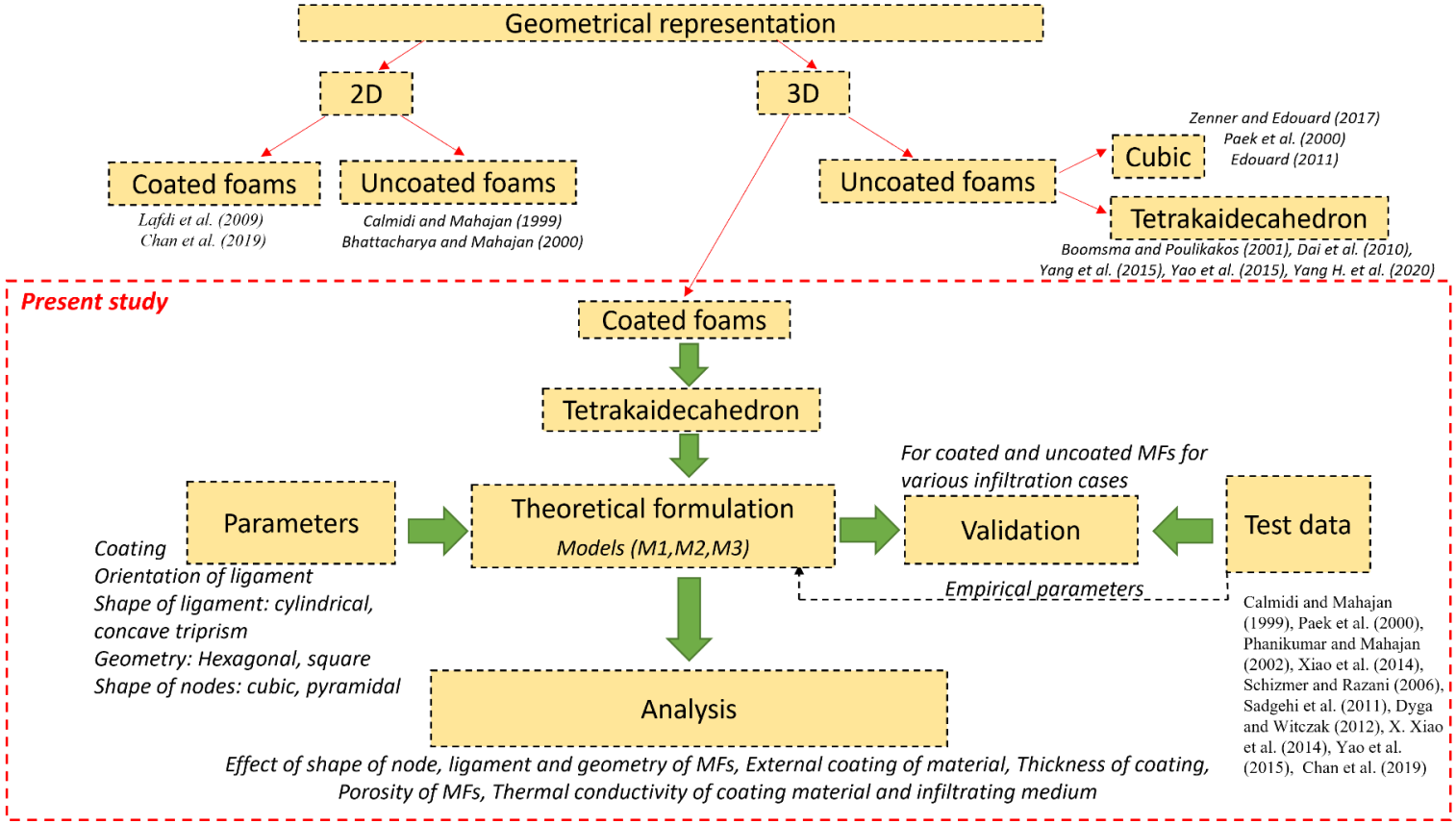

Figure 2.1: Model development and analysis for the Effective thermal conductivity

2.2 Mathematical modeling

The present study is based on the volume averaging technique to determine the ETC using the tetrakaidecahedron structure (Fig. 2.2(a)). A unit cell is constructed as a representative element, and it contains the coated MF and infiltrating medium as constituents. The unit cell is divided into certain layers, and the contribution of MF and filling medium in the ETC is assessed for each layer. Subsequently, the sliced layers are assumed to be connected in series, and ETC is obtained based on Fourier's law of heat conduction [52, 61-63, 65]. Here under are the assumptions taken in the analysis [55]:

- The porosity of the MF and the coating thickness are uniform.
- Heat transfer is through conduction only.
- The thermophysical properties are assumed to be temperature-independent.
- Thermal resistance due to contact between phases is negligible, and thermal equilibrium is maintained.

Several researchers have employed the local thermal equilibrium (LTE) assumption while applying the volume averaging technique. Vafai et al. [94] conducted an in-depth analysis on the conditions under which LTE holds and found that its validity diminishes in packed bed systems with high Reynolds and Darcy numbers, where fluid and solid phases exhibit notable temperature differences.

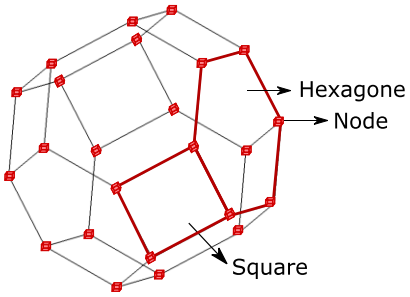

(a) Tetrakaidekahedron structure

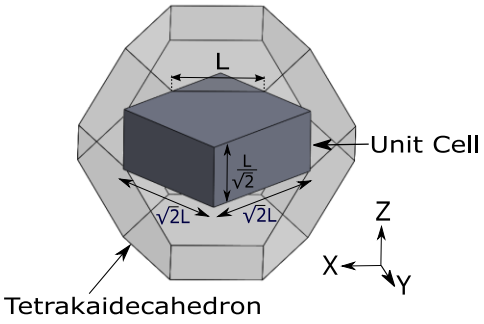

(b) Unit cell using the hexagonal geometry of MF

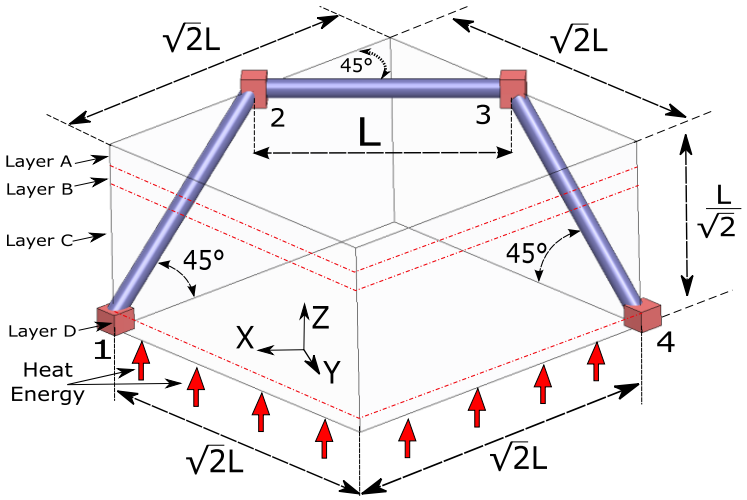

(c) Ligaments and node arrangement inside the unit cell

Figure 2.2: Schematic of the unit cell

Conversely, the LTE assumption remains appropriate in scenarios involving stagnant or very slowly moving fluids, characterized by low Reynolds and Darcy numbers [61-62]. In the present work, since convective effects are neglected and the metal foam is saturated with a stationary medium, the LTE assumption is deemed applicable. Similar considerations have been made in studies involving flow through porous media with low permeability, where thermal equilibrium between phases is more likely to persist.

2.2.1 Theoretical modeling using the Hexagonal geometry

Model M-1: Cylindrical ligament and cubic nodes of MF

Figure 2.2(b) illustrates the representative unit cell derived from the hexagonal configuration of the tetrakaidecahedron geometry. This unit cell encompasses all key geometrical characteristics of the original structure and is therefore suitable for evaluating the effective thermal conductivity. The model assumes cylindrical ligaments and cubic nodes, where the nodes are formed at the intersections of the ligaments. Figure 2.2c displays the spatial arrangement of ligaments and nodes within the unit cell, under the assumption of one-dimensional heat flow. For simplification, the coating layer is not depicted in Figure 2.2(c); however, the coating thickness on the metal foam is highlighted by the

red boundary in Figure 2.3. Figures 2.3 and 2.4 present the layered structure and top view of the unit cell, respectively. The geometric parameters include L (distance between the centers of two nodes), a (ligament radius), r (edge length of the node), and n (coating thickness).

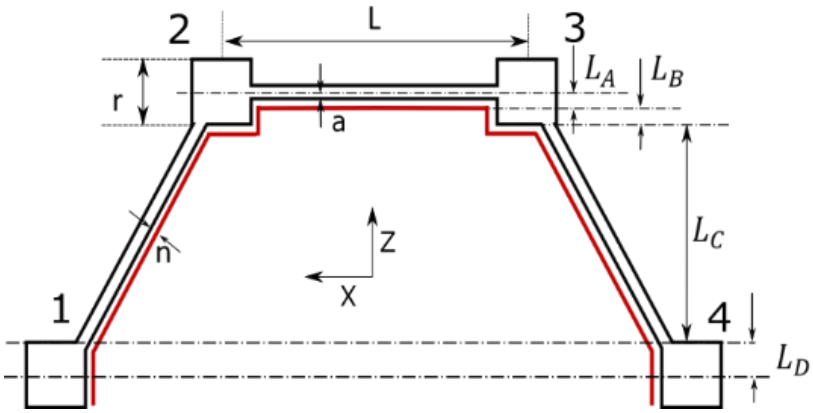

Figure 2.3: Layers in the unit cell

Since ligaments and nodes are shared among adjacent cells in the tetrakaidecahedron network, only the fraction contained within the defined unit cell is considered in the ETC calculations.

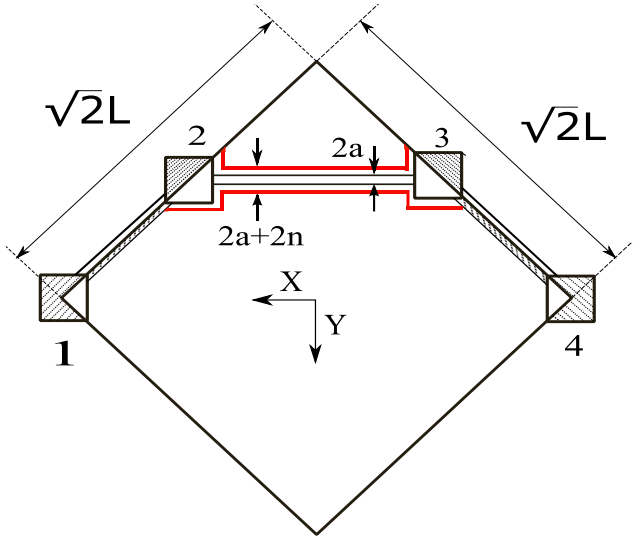

Figure 2.4: Top view of the unit cell

From the geometry of the unit cell and the angle between the ligaments, the length, height and width of the cell is $\sqrt{2}$L, $\frac{\sqrt{2}}{2}$L and $\sqrt{2}$L, respectively, and the entire unit cell volume is found to be $\sqrt{2}L^3$. Further, four layers are created along the z-direction, namely A, B, C and D with

their respective thickness of L_A, L_B, L_C, L_D, keeping the total height of all the layers equal to the height of the unit cell. The thickness for the layers is given as:

$$L_A = n + a \tag{2.1}$$

$$L_B = \left(\frac{r}{2}\right) - a - n \tag{2.2}$$

$$L_C = \left(\frac{\sqrt{2}}{2}\right) L - r \tag{2.3}$$

$$L_D = \frac{r}{2} \tag{2.4}$$

The volume of each component associated with different layers is needed to estimate the ETC. For layer A, one can estimate the volume of various parameters ($V_{t_A}, V_{mf_A}, V_{g_A}$) as below. Here, V_t represents the total volume of the layer, V_{mf} and V_g denote the volume of metal foam and the coating volume present in that layer, respectively. These values for Layer A are calculated:

$$V_{t_A} = 2L^2(a + n) \tag{2.5}$$

$$V_{mf_A} = r^2 a + (L - r)\frac{\pi}{2}a^2 \tag{2.6}$$

$$V_{g_A} = \frac{\pi}{8}(L - r - 2n)(8an + 4n^2) + 4nr(a + n) \tag{2.7}$$

Utilizing this technique, the values V_t, V_{mf}, V_g are calculated for layer B, C and D.

For layer B:

$$V_{t_B} = 2L^2\left(\frac{r}{2} - a - n\right) \tag{2.8}$$

$$V_{mf_B} = r^2\left(\frac{r}{2} - a - n\right) \tag{2.9}$$

$$V_{g_B} = 4nr\left(\frac{r}{2} - a - n\right) \tag{2.10}$$

For Layer C:

$$V_{t_C} = 2L^2\left(\frac{L}{\sqrt{2}} - r\right) \tag{2.11}$$

$$V_{mf_C} = \pi a^2\left(L - \sqrt{2}r\right) \tag{2.12}$$

$$V_{g_C} = \frac{\pi}{4}(8an + 4n^2)\left(L - \sqrt{2}r - 2\sqrt{2}n\right) + rn(r + 2n) \tag{2.13}$$

For Layer D:

$$V_{t_D} = 2L^2\left(\frac{r}{2}\right) \tag{2.14}$$

$$V_{mf_D} = \frac{r}{2} \tag{2.15}$$

$$V_{g_D} = \frac{r^3}{4} \tag{2.16}$$

Following dimensionless parameters are introduced for simplification:

$$\lambda_1 = r/L,\ \lambda_2 = a/L \text{ and } \lambda_3 = n/L \tag{2.17}$$

The volume fraction of different components in each layer can be estimated as:

$$\psi_{X_y} = \frac{V_{s_{layer}}}{V_{t_{layer}}} \tag{2.18}$$

Here, X represents the metal foam/coating and y represents different layers. The volume fractions for each layer are calculated as follows:

For layer A

$$\psi_{mf_A} = \left(\frac{{\lambda_1}^2\lambda_2}{2(\lambda_2 + \lambda_3)}\right) + \left(\frac{(1 - \lambda_1)\pi{\lambda_2}^2}{4(\lambda_2 + \lambda_3)}\right) \tag{2.19}$$

$$\psi_{g_A} = \left(\frac{\frac{\pi}{8}(1 - \lambda_1 - 2\lambda_3)\left(8\lambda_2\lambda_3 + 4{\lambda_3}^2\right) + 4\lambda_3\lambda_1(\lambda_2 + \lambda_3)}{2(\lambda_2 + \lambda_3)}\right) \tag{2.20}$$

Layer B

$$\psi_{mf_B} = \frac{{\lambda_1}^2}{2} \tag{2.21}$$

$$\psi_{mf_B} = 2\lambda_1\lambda_3 \tag{2.22}$$

Layer C

$$\psi_{mf_C} = \frac{\pi}{\sqrt{2}}{\lambda_2}^2 \tag{2.23}$$

$$\psi_{g_C} = \left(\frac{\pi(2\lambda_2\lambda_3+{\lambda_3}^2)(1-\sqrt{2}\lambda_1-2\sqrt{2}\lambda_3)+{\lambda_1}^2\lambda_3+2{\lambda_3}^2\lambda_1}{\sqrt{2}(1-\sqrt{2}\lambda_1)}\right) \tag{2.24}$$

Layer D

$$\psi_{mf_D} = \frac{{\lambda_1}^2}{4} \tag{2.25}$$

$$\psi_{g_D} = \lambda_1\lambda_3 \tag{2.26}$$

The overall porosity (ε_o) of metal foam is evaluated as ratio of void volume to total volume:

$$\varepsilon_o = 1 - \frac{V_{mf} + V_{coating}}{V_{unit\ cell}} \tag{2.27}$$

Using Eqs. (2.19-2.26) and after simplification, the following expression is obtained:

$$A{\lambda_2}^2 + B\lambda_2 + C = 0 \tag{2.28}$$

where

$$A = \frac{\pi}{2}\left(3 - \left(1 + 2\sqrt{2}\right)\lambda_1\right) \tag{2.29}$$

$$B = \left(\pi\lambda_3\left(3 - \left(1 + 2\sqrt{2}\right)\lambda_1 - \left(2 + 4\sqrt{2}\right)\lambda_3\right) - 4\lambda_1\lambda_3\right) \tag{2.30}$$

$$C = \left(\frac{\pi}{2}{\lambda_3}^2\left(3 - \left(1 + 2\sqrt{2}\right)\lambda_1 - \left(2 + 4\sqrt{2}\right)\lambda_3\right) + \left(\frac{\lambda_1}{2} - \lambda_3\right)\left(4\lambda_3\lambda_1 + {\lambda_1}^2\right) + 2\lambda_1\lambda_3(\lambda_1 + \lambda_3) + \frac{{\lambda_1}^3}{4} - (1 - \varepsilon_o)\sqrt{2}\right) \tag{2.31}$$

Using Eqs. 2.28-2.31, the positive root can be expressed as:

$$\lambda_2 = \frac{\left(4\lambda_1\lambda_3 - \pi\lambda_3\left(3 - \left(1+2\sqrt{2}\right)\lambda_1 - \left(2+4\sqrt{2}\right)\lambda_3\right)\right)}{2\left(\frac{\pi}{2}\left(3 - \left(1+2\sqrt{2}\right)\lambda_1\right)\right)}$$

$$+$$

$$\frac{\sqrt{\begin{array}{c}\left(\pi\lambda_3\left(3-\left(1+2\sqrt{2}\right)\lambda_1-\left(2+4\sqrt{2}\right)\lambda_3\right)-4\lambda_1\lambda_3\right)^2- \\ 4\left(\frac{\pi}{2}\left(3-\left(1+2\sqrt{2}\right)\lambda_1\right){\lambda_2}^2\right) \\ \left(\left(\frac{\pi}{2}{\lambda_3}^2\left(3-\left(1+2\sqrt{2}\right)\lambda_1-\left(2+4\sqrt{2}\right)\lambda_3\right)\right)+\left(\frac{\lambda_1}{2}-\lambda_3\right)\left(4\lambda_3\lambda_1+{\lambda_1}^2\right)+2\lambda_1\lambda_3\left(\lambda_1+\lambda_3\right)+\frac{{\lambda_1}^3}{4}-(1-\varepsilon_o)\sqrt{}\right.\end{array}}}{2\left(\frac{\pi}{2}\left(3-\left(1+2\sqrt{2}\right)\lambda_1\right)\right)} \quad (2.32)$$

Here, λ_1 and λ_3 are the empirical parameters and ε_o is the porosity of the metal foam. The volume-averaged thermal conductivity can be expressed as

$$K_n = \psi_{mf_n} K_s + \psi_{g_n} K_g + \left(1 - \psi_{mf_n} - \psi_{g_n}\right) K_f \quad (2.33)$$

The volume-averaged thermal conductivity approach is a first-order estimation method that accounts for the contribution of each constituent material based on its volume fraction. This method assumes conduction as the dominant mode of heat transfer, while neglecting the effects of convection and radiation. It has been widely applied to predict the effective thermal conductivity of systems such as packed beds of spheres and uncoated metal foams [55, 61-63, 95]. In this approach, the thermal conductivity of each material is weighted by its corresponding volume fraction, and the resulting products are summed to determine the overall thermal conductivity of a given layer. This equation is applied to all the layers except layer C. For Layer C, an inclination factor is applied to account for the orientation (α) and the value of α is taken as 45º (Eq. 2.34) [63], [65]. In such case, the thermal conductivity of layer C can be expressed:

$$K_C = \left(\psi_{mf_c} K_s + \psi_{g_c} K_g\right) \cos^2 \alpha + \left(1 - \psi_{mf_c} - \psi_{g_c}\right) K_f \quad (2.34)$$

After estimating the thermal conductivity of each layer, the ETC is determined using Fourier's law of heat conduction, assuming the layers are thermally connected in series:

$$K_{eff} = \frac{L_A + L_B + L_C + L_D}{\left(\frac{L_A}{K_A} + \frac{L_B}{K_B} + \frac{L_C}{K_C} + \frac{L_D}{K_D}\right)} \tag{2.35}$$

Model M-2: Concave triprism ligament and pyramidal node of MF

Yao et al. [65] highlighted the significant influence of ligament and node geometry on the effective thermal conductivity (ETC) of metal foams. Through scanning electron microscopy (SEM) analysis, they observed that the actual ligament and node structures could be approximated as concave triprism and pyramidal forms, respectively. The study suggested that these geometries adhere to Plateau's law and are representative of the natural morphology developed during the foaming process. Since ETC is strongly dependent on both the shape and volume of the solid matrix, a more accurate geometric representation can improve the reliability of predictive models. In light of this, the present model (M-2) adopts concave triprism ligaments and pyramidal nodes to estimate the ETC of coated metal foams, a configuration not previously addressed in the literature. Kanaum et al. [96] earlier provided estimates of the volume associated with concave triprism ligaments and node regions in their work. Following their model, the volumes of the ligament and nodes are estimated as follows:

$$V_{ligament} = 2\pi {a_2}^2 L\left(\frac{1 + {a_1}^2}{15{a_1}^2}\right)(15 - 80a_3 + 128{a_3}^2) \tag{2.36}$$

$$V_{node} = \frac{1}{3}\pi {a_2}^3\left(\frac{1 + {a_1}^2}{{a_1}^2}\right)\left[1 - 4{a_3}^2\left(1 - \left(\frac{a_2}{L}\right)^2\right)\right]^2 \tag{2.37}$$

Here, a_1, a_2 and a_3 denote the cross-section shape, size, and longitudinal curvature, respectively, while L denotes the length of the ligament (Figs. 2.5 and 2.6). The influence of a_1 on the ETC is not significant (please refer to Fig. 4 in Ref. [65]) and to represent concave triprism structure, its range lies between $2 \leq a_1 \leq 3$.

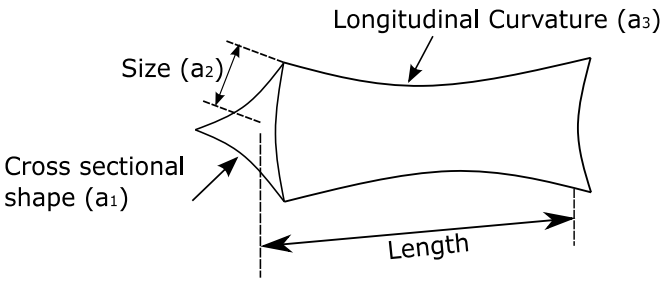

Figure 2.5: Schematic diagram of the ligament

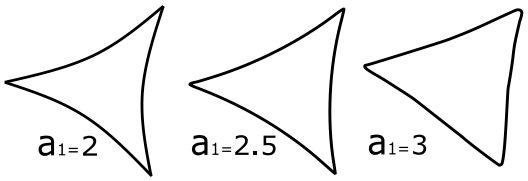

Figure 2.6: Shape of ligament for various values of a_1

In view of this, for the present study the value of a_1 is kept as 2.01 [65-66]. The parameter a_3, the longitudinal curvature effects of the ligament, exhibits negligible influence on the ETC, therefore, assumed to be zero in this investigation. Previous researchers [65-66] have used similar assumptions to estimate ETC for uncoated metal foams for triprism ligament and pyramidal node. The present model's unit cell is the same as the previous model (M-1), with the difference in the shape of ligament and node. Fig. 2.7(a) shows the unit cell for the present model (M-2), for simplicity, the nodes are represented by the circular dots and the ligament by thick lines. Fig. 2.7(b) depicts the concave triprism ligament structure with a coating of thickness 'n'.

In order to incorporate the external coating of the material, a_2 is replaced as $a_{2'} = (a_2 + n)$ in Eq. 2.36-2.37. In this case total three layers (A, B, C) are formed; for the first layer (A) and the last layer (B), the thickness is calculated by projecting the height of a_2 on the x-z plane (Fig. 2.7 (a-b)).

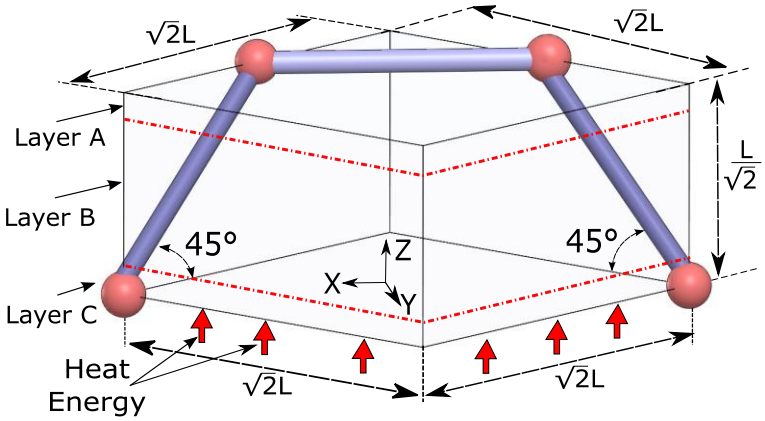

(a) Layers in the unit cell

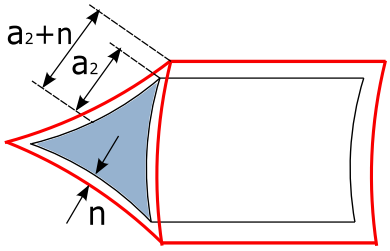

(b) Coated ligament

Figure 2.7: Description of the unit cell and ligament

The thickness of layer C is calculated by subtracting the thickness of A and B from the projected height of the inclined ligament. While calculating the volume of coating, the volume of uncoated metal foam is subtracted from the combined volume of metal foam and coating material. This approach has been adopted to calculate the volume for every layer. The length of the layers can be expressed as:

$$L_A = L_C = \frac{\sqrt{2}}{2} a_{2'} \tag{2.38}$$

$$L_B = \frac{\sqrt{2}}{2} L - \sqrt{2} a_{2'} \tag{2.39}$$

Following dimensionless parameters are introduced for the analysis

$$\beta_1 = \frac{a_2}{L} \tag{2.40}$$

$$\beta_2 = \frac{n}{L} \tag{2.41}$$

At this juncture, the volume of constituents in different layers is estimated, and subsequently, the volume fraction is estimated by using Eq. (2.18). The detailed procedure for estimation of volume and volume fractions for layer A is shown in Eqs. 2.42(a-e). Following the same procedure, the volumes for layer B and C are estimated, and finally the volume fractions are calculated.

Layer A

$$V_{t_A} = \sqrt{2}L^3(\beta_2 + \beta_1) \tag{2.42a}$$

$$V_{mf_A} = \pi\left({\beta_1}^2(1 - 2\beta_1) + \frac{2}{3}{\beta_1}^3\right)\left(\frac{1 + {a_1}^2}{{a_1}^2}\right)L^3 \tag{2.42b}$$

$$V_{g_A} = \pi\left(4\beta_2(1 - 2\beta_1)(\beta_1 + \beta_2) + \frac{2}{3}\left(8{\beta_2}^3 + 6\beta_2{\beta_1}^2 + 12\beta_1{\beta_2}^2\right)\right)\left(\frac{1+{a_1}^2}{{a_1}^2}\right)L^3 \tag{2.42c}$$

$$\psi_{mf_A} = \frac{\pi\left({\beta_1}^2(1-2\beta_1)+\frac{2}{3}{\beta_1}^3\right)\left(\frac{1+{a_1}^2}{{a_1}^2}\right)}{\sqrt{2}(\beta_2+\beta_1)} \tag{2.42d}$$

$$\psi_{g_A} = \frac{\pi\left(4\beta_2(1-2\beta_1)(\beta_2+\beta_1)+\frac{2}{3}\left(8{\beta_2}^3+6\beta_2{\beta_1}^2+12\beta_2{\beta_1}^2\right)\right)\left(\frac{1+{a_1}^2}{{a_1}^2}\right)}{\sqrt{2}(\beta_2+\beta_1)} \tag{2.42e}$$

Layer B

$$\psi_{mf_B} = \frac{\pi\left({\beta_1}^2(1 - 2\beta_1)\right)\left(\frac{1 + {a_1}^2}{{a_1}^2}\right)}{\frac{\sqrt{2}}{2} - \sqrt{2}(\beta_2 + \beta_1)} \tag{2.43a}$$

$$\psi_{g_B} = \frac{4\pi\left({\beta_2}^2 + \beta_2\beta_1\right)(1 - 2\beta_1)\left(\frac{1 + {a_1}^2}{{a_1}^2}\right)}{\frac{\sqrt{2}}{2} - \sqrt{2}(\beta_2 + \beta_1)} \tag{2.43b}$$

Layer C

$$\psi_{mf_C} = \frac{\frac{\pi}{3}\left({\beta_1}^3\right)\left(\frac{1 + {a_1}^2}{{a_1}^2}\right)}{\sqrt{2}(\beta_2 + \beta_1)} \tag{2.44a}$$

$$\psi_{gc} = \frac{\frac{\pi}{3}\left(8{\beta_2}^3 + 6\beta_2\beta_1(\beta_1 + 2\beta_2)\right)\left(\frac{1+{a_1}^2}{{a_1}^2}\right)}{\sqrt{2}(\beta_2 + \beta_1)} \qquad (2.44b)$$

Utilizing Eqs. 2.27, 2.42-2.44, one can obtain:

$$-5{\beta_1}^3 + 3{\beta_1}^2(1 - 6\beta_2) + 12\beta_1\left(\beta_2 - {\beta_2}^2\right) + 20{\beta_2}^2 - \frac{(1-\varepsilon_o)\sqrt{2}}{\pi\left(\frac{1+{a_1}^2}{{a_1}^2}\right)} = 0 \qquad (2.45)$$

Eq. 2.45 is a higher-order polynomial equation of β_1 and iteration method is used to find the positive root β_1. Here, β_2 denote the empirical parameter and ε_o is the porosity of metal foam. Following this, the thermal conductivity of various layers (A, C) and B is calculated by using Eq. 2.33 and Eq. 2.34, respectively. Finally, the effective thermal conductivity is calculated using Eq. 2.46.

$$K_{eff} = \frac{L_A + L_B + L_C}{\left(\frac{L_A}{K_A} + \frac{L_B}{K_B} + \frac{L_C}{K_C}\right)} \qquad (2.46)$$

2.2.2 Theoretical modeling using the Square geometry

Model M-3: Cylindrical ligament and cubic nodes of MF

Numerous investigations have employed the tetrakaidecahedron structure to evaluate effective thermal conductivity, emphasizing the importance of geometric configuration on thermal transport. In the current model (M-3), a square-based unit cell (Fig. 2.8) is derived from the tetrakaidecahedron structure, featuring cylindrical ligaments and cubic nodes (Fig. 2.9). This specific configuration has not been previously reported in the literature.

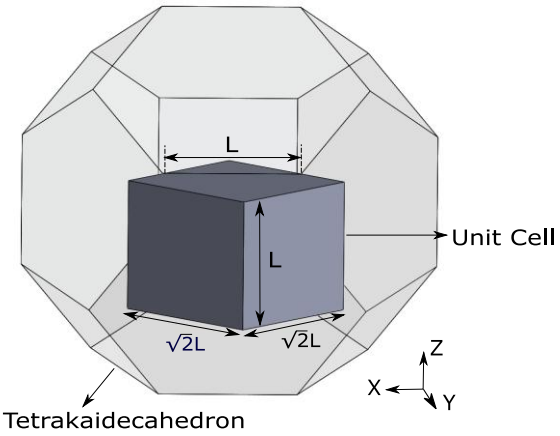

Figure 2.8: Unit cell using square geometry of MF

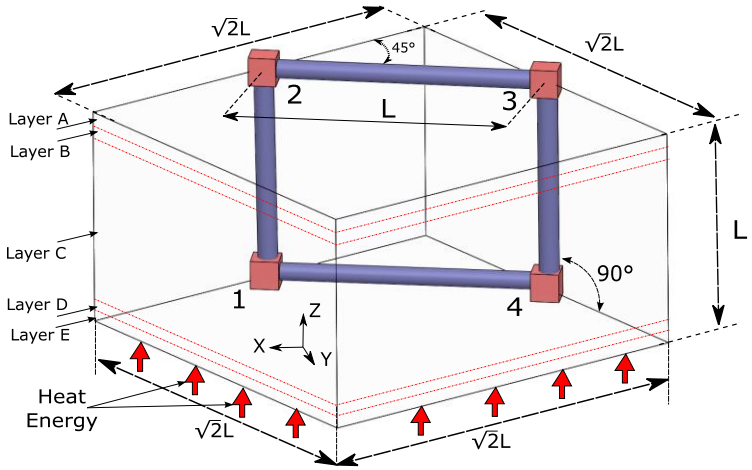

Figure 2.9: Ligaments and nodes arrangement

Existing square-geometry models typically assume a periodic structure with twelve ligaments and four nodes, whereas the present model is based on the tetrakaidecahedron structure and incorporates only four ligaments and nodes. The ligament length, radius, and edge are the same as considered in model M-1; while the height of the unit cell is equal to the length of the ligament. In this configuration, the length, height, and width of the unit cell are $\sqrt{2}L$, L and $\sqrt{2}L$, respectively, resulting complete volume as $2L^3$. In this model, because of the perfect alignment of ligaments, there is no inclination along the z-axis.

Figures 2.10 and 2.11 show the layers for this geometry and the top view of the unit cell with external coating. Here, the unit cell is sliced into five layers. The length of the individual layers can be calculated following the procedure explained earlier in model M-1.

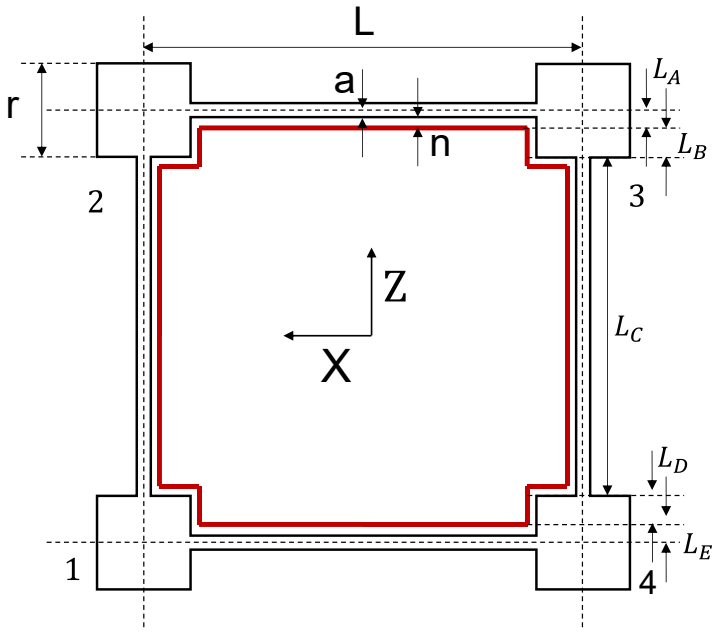

Figure 2.10: Various layers for square geometry

The length of layers can be stated as:

$$L_A = L_E = a + n \tag{2.47a}$$

$$L_B = L_D = \frac{r}{2} - a - n \tag{2.47b}$$

$$L_C = L - r \tag{2.47c}$$

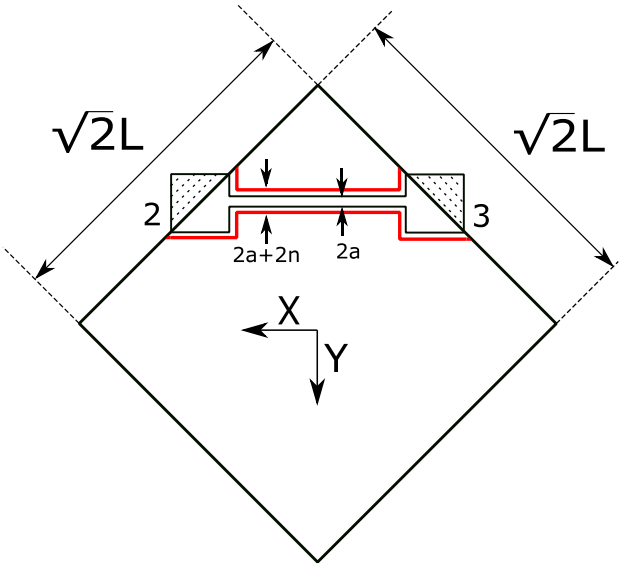

Figure 2.11: Top view of the unit cell

The volumes and volume fractions of Layers A and E, and of B and D, are identical due to their equal heights.

Layer A's total volume, metal foam volume, and coating may be written as:

$$V_{t_A} = 2L^2(a+n) \tag{2.48a}$$

$$V_{mf_A} = \frac{\pi}{2}(L-r)a^2 + r^2 a \tag{2.48b}$$

$$V_{g_A} = \frac{\pi}{2}(L-r-2n)(2an+n^2) + 4nr(n+r) \tag{2.48c}$$

For layer B

$$V_{t_B} = 2L^2\left(\frac{r}{2} - a - n\right) \tag{2.49a}$$

$$V_{mf_B} = r^2\left(\frac{r}{2} - a - n\right) \tag{2.49b}$$

$$V_{g_B} = 4nr\left(\frac{r}{2} - a - n\right) \tag{2.49c}$$

For layer C

$$V_{t_C} = 2L^2(L-r) \tag{2.50a}$$

$$V_{mf_C} = \pi a^2(L-r) \tag{2.50b}$$

$$V_{g_C} = \pi(L-r-2n)(2an+n^2) + (2r^2 n) \tag{2.50c}$$

Since cylindrical ligaments and cubic nodes are considered in this square model, the dimensionless parameters used in M-1 have been considered for simplification. The following are the volume fractions for the various layers:

Layer A

$$\psi_{mf_A} = \left(\frac{(1-\lambda_1)\pi{\lambda_2}^2}{4(\lambda_2+\lambda_3)}\right) + \left(\frac{{\lambda_1}^2\lambda_2}{2(\lambda_2+\lambda_3)}\right) \tag{2.51}$$

$$\psi_{g_A} = \left(\frac{\frac{\pi}{2}(1-\lambda_1-2\lambda_3)\left(2\lambda_2\lambda_3+{\lambda_3}^2\right) + 4\lambda_3\lambda_1(\lambda_2+\lambda_3)}{2(\lambda_2+\lambda_3)}\right) \tag{2.52}$$

The volumes and volume fractions for the remaining layers are estimated using the same procedure:

Layer B

$$\psi_{mf_B} = 2\lambda_1\lambda_3 \tag{2.53}$$

$$\psi_{mf_B} = \frac{\pi}{2}{\lambda_2}^2 \tag{2.54}$$

Layer C

$$\psi_{mf_C} = \frac{\pi}{2}{\lambda_2}^2 \tag{2.55}$$

$$\psi_{gc} = \left(\frac{\pi\left(2\lambda_2\lambda_3 + {\lambda_3}^2\right)(1-\lambda_1-2\lambda_3) + 2{\lambda_1}^2\lambda_3}{2(1-\lambda_1)}\right) \tag{2.56}$$

Using Eqs. 2.27, 2.48-2.56, Eq. 2.57 gives us a quadratic equation of the kind, and the coefficients are reported as:

$$P{\lambda_2}^2 + Q\lambda_2 + R = 0 \tag{2.57}$$

$$P = 2\pi(1-\lambda_1) \tag{2.58a}$$

$$Q = (4\pi\lambda_3(1-\lambda_1-2\lambda_3) - 8\lambda_3\lambda_1) \tag{2.58b}$$

$$R = \left(2{\lambda_1}^2 + 8\lambda_3\lambda_1\right)\left(\frac{\lambda_1}{2} - \lambda_3\right) + 2\pi{\lambda_3}^2(1-\lambda_1-2\lambda_3) + 8\lambda_1\lambda_3(\lambda_1+\lambda_3) + 2{\lambda_1}^2\lambda_3 - (1-\varepsilon_o)*2 \tag{2.58c}$$

The positive root is:

$$\lambda_2 = \frac{\left(8\lambda_3\lambda_1 - 4\pi\lambda_3(1-\lambda_1-2\lambda_3)\right)}{4\pi(1-\lambda_1)} + \frac{\sqrt{\begin{matrix}(4\pi\lambda_3(1-\lambda_1-2\lambda_3)-8\lambda_3\lambda_1)^2 - \\ 8\pi(1-\lambda_1)\left(2\pi{\lambda_3}^2(1-\lambda_1-2\lambda_3)+8\lambda_1\lambda_3(\lambda_1+\lambda_3)+2{\lambda_1}^2\lambda_3-2(1-\varepsilon_o)\right)\end{matrix}}}{4\pi(1-\lambda_1)} \tag{2.59}$$

In this case, the orientation effect is absent, and the thermal conductivity for each layer is calculated by using Eq. (2.33). Following this, the effective thermal conductivity is estimated:

$$K_{eff} = \frac{L_A + L_B + L_C + L_D + L_E}{\left(\frac{L_A}{K_A} + \frac{L_B}{K_B} + \frac{L_C}{K_C} + \frac{L_D}{K_D} + \frac{L_E}{K_E}\right)} \tag{2.60}$$

2.3 Validation of the numerical models

The current models (M-1 and M-2) have been validated by reducing them to the limiting case of uncoated metal foams. Model M-1, based on hexagonal geometry with cylindrical ligaments and cubic nodes, has been benchmarked against the theoretical model developed by Dai et al. [63]. Similarly, Model M-2, which incorporates a hexagonal configuration with concave triprism ligaments and pyramidal nodes, has been validated using the theoretical model proposed by Yao et al. [65]. These references were selected due to their strong agreement with experimental data for uncoated metal foams. A similar validation approach has also been adopted in previous studies . The proposed model based on square geometry (M-3) has been validated for both coated and uncoated foams using the existing experimental test data from the literature. The validation process and results are discussed in detail:

Reduction of model M-1 to Dai et al. [63] model

The parameter λ_3 (Eq. 2.28) represents the presence of a coating on the metal foam. As $\lambda_3 \rightarrow 0$, the value of λ_2 reduces to:

$$\lambda_2 = \left(\frac{2\left(\sqrt{2}(1-\epsilon_o) - \frac{3}{4}{\lambda_1}^3\right)}{\pi\left(3 - \left(1+2\sqrt{2}\right)\lambda_1\right)} \right)^{0.5} \tag{2.61}$$

Here, Eq. 2.61 is similar to the solution given by Dai et al. [63], which is an improvement over Boomsma's original model [61] for uncoated metal foams saturated with fluid. Utilizing Eq. 2.61, the final expression for the ETC of uncoated MFs can be obtained (please see Eq.12-13 in Ref. [63])

Reduction of model M-2 to Yao et al. [65] model

The parameter β_2 accounts for the coating of external material, for $\beta_2 \rightarrow 0$, Eq. 2.45 reduces to Eq. 2.62 (β_1 represents λ_1 in the original model by, please see Eq. 15 in Ref. [65]). Here, Eq. 2.62 is similar to the solution provided by Yao et al. for uncoated metal foams saturated with

fluid/PCM. Using Eq. 2.61, the final expression for ETC of uncoated MFs can be obtained (please see Eq.18-22 in Ref. [65]).

$$-5{\beta_1}^3 + 3{\beta_1}^2 - \frac{(1-\varepsilon_o)\sqrt{2}}{\pi\left(\frac{1+{a_1}^2}{{a_1}^2}\right)} = 0 \qquad (2.62)$$

This shows that the reduced present models (M-1 & M-2) are an extension of the existing models and are capable of predicting ETC for uncoated MFs saturated with fluid/PCM.

Reduction of the square model (M-3)

Following the similar procedure, substituting $\lambda_3 \rightarrow 0$, in Eqns. 2.47-2.60; the quadratic Eq. 2.57 having coefficients from Eqs. 2.58 reduces to:

$$\lambda_2 = \left(\frac{\left(2(1-\epsilon_o) - {\lambda_1}^3\right)}{2\pi(1-\lambda_1)}\right)^{0.5} \qquad (2.63)$$

The proposed model can estimate the effective thermal conductivity for uncoated metal foams saturated with fluids or PCMs. To validate the reduced form of Model M-3, experimental data from various studies involving copper and aluminium foams, with porosities ranging from 0.90 to 0.98 and pore densities between 5 and 40 PPI, have been employed. Additionally, the predictions of the reduced Model M-3 have been compared with those of several well-established theoretical models commonly referenced for uncoated metal foams, allowing for a comprehensive assessment of its accuracy and applicability.

Figures 2.12 to 2.15 present a comparison between the predictions of the proposed model and both experimental data and existing theoretical models, including those by Calmidi and Mahajan [52], Paek et al. [56], Boomsma and Poulikakos [61], [62], Yang et al. [64], Yao et al. [65] , Phanikumar and Mahajan [97], Schmierer et al. [98], Sadgehi et al. [99], Witczak and Dyga [100], Yang X. et al. [101], and Xiao et al. [102]. These comparisons include uncoated aluminum foams saturated with air, and uncoated copper foams saturated with air, water, and PCM. Experimental observations show that ETC decreases with increasing

porosity, attributed to the reduction in the solid metal fraction. Copper foams consistently exhibit higher ETC than aluminum foams at the same porosity and with the same saturating medium, due to copper's higher intrinsic thermal conductivity. The reduced square model (M-3) shows good agreement with the experimental data, indicating its reliability for predicting ETC in uncoated metal foam systems. The three-dimensional model developed by Boomsma and Poulikakos [61-62] consistently overpredicts the effective thermal conductivity across the entire porosity range for both copper and aluminium foams.

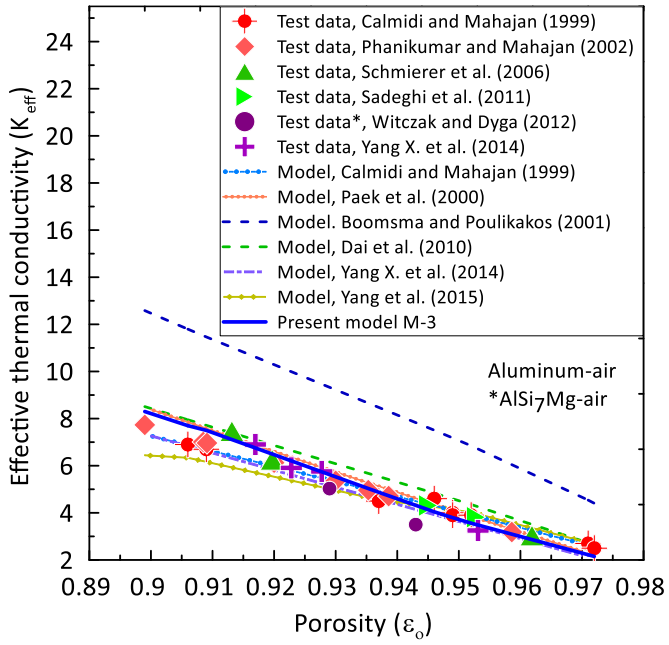

Figure 2.12: ETC for aluminium foam with air

In contrast, the models proposed by Dai et al. [63] and Yang et al. [64] demonstrate improved accuracy, attributable to their consideration of ligament orientation and the incorporation of a porosity-dependent empirical parameter, respectively. While the model by Paek et al. [56] shows reasonable agreement with experimental results, it is based on an idealized cubic lattice, which does not realistically represent the microstructure of metal foams. Several other models rely on two-dimensional assumptions and neglect the influence of the saturating medium, thereby limiting their predictive capabilities. The present reduced square model (M-3) offers better accuracy than the previously discussed models. Aligning with earlier findings [64] that foam

geometry varies with porosity, the current model introduces the geometric factor λ_1 as a function of porosity, enhancing its adaptability and predictive performance. In contrast to earlier theoretical models [52, 61-63] which assume a constant value of λ_1, the present reduced square model (M-3) introduces λ_1 as a variable dependent on porosity.

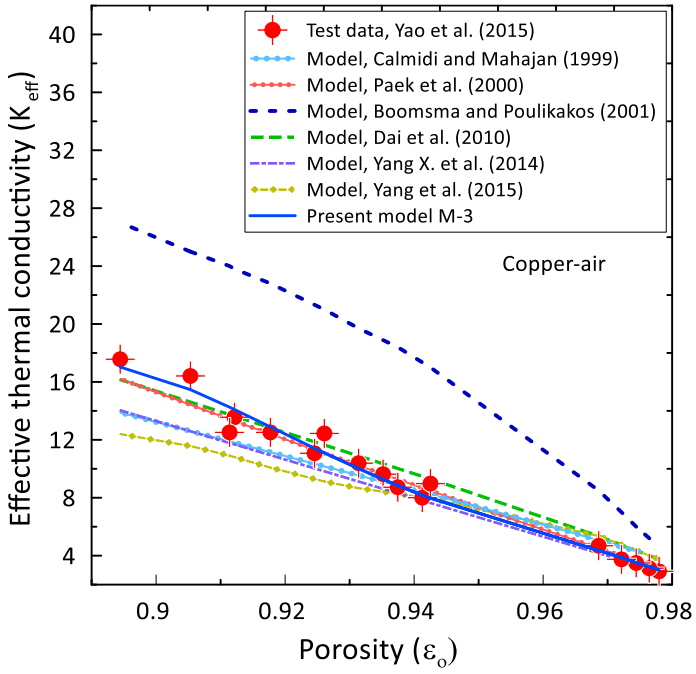

Figure 2.13: ETC for copper foam with air

The use of a fixed λ_1 often results in a ratio of node edge length to ligament diameter (r/2a) falling below unity, thereby violating a fundamental geometric assumption noted during model formulation [64]. In this study, λ_1 has been calibrated specifically for square geometry using available experimental data, yielding a third-order polynomial expression as a function of porosity. This approach aligns with the methodology adopted by previous researchers. The resulting fitted relationship is: $\frac{r}{L} = -252.99{\varepsilon_O}^3 + 692.45{\varepsilon_O}^2 - 633.89\varepsilon_O + 194.59$. The model exhibits a fitting error of less than 1%, confirming its high reliability. Table 2.1 presents a detailed comparison between model predictions and experimental results. The average, maximum and minimum relative deviations are depicted for present reduced model (M-3) and other theoretical models.

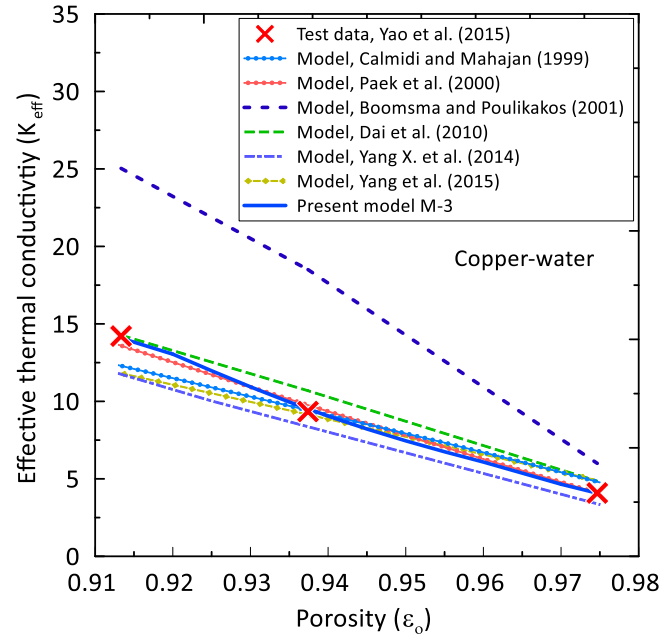

Figure 2.14: ETC for copper foam with water

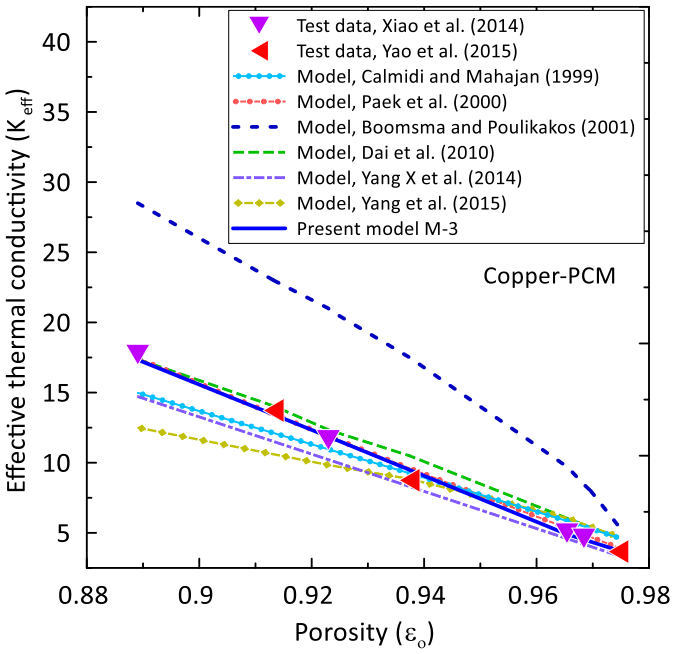

Figure 2.15: ETC for copper foam with PCM

Here, the relative deviation between the different theoretical models with the existing test data is given by:

$$\text{Relative Deviation} = \left| \frac{K_{eff_{predicted}} - K_{eff_{experimental}}}{K_{eff_{experimental}}} \right| \qquad (2.64)$$

It should be noted that the predictions obtained from the reduced square model clearly justify that the model can predict the data for uncoated

infiltrated metal foams and can be extended further to calculate coated metal foams' ETC.

The experimental data reported by Chan et al. [55] have been employed to validate the proposed models M-1, M-2, and M-3 for coated metal foams. This dataset includes measurements from graphene-coated copper and nickel foams saturated with air, PCM. In their 2D model, Chan et al. defined the dimensionless coating thickness as the ratio of coating thickness to node thickness, with fitted values ranging from 0.004 to 0.005. In the present work, the coating thickness is characterized using two non-dimensional parameters, λ_3 and β_2, defined as the ratio of coating thickness to ligament length. Consistent with earlier studies, the values of have been determined through curve fitting to match experimental results for both copper and nickel foams. The fitted parameters and corresponding details are summarized in Table 2.2.

Table 2.1: The relative deviations from the present model (M-3) against the existing experimental test data for uncoated MFs

Sample	Experimental data source	Present reduced model M-3			Boomsma and Poulikakos [61]	Dai et al. [63]	Yang et al. [64]	Calmidi Mahajan [52]	Paek et al. [56]	Yang X. et al. [101]
		Max	Avg	Min	Average	Average	Average	Average	Average	Average
Al-air	Calmidi and Mahajan [52]	17.74%	9.80%	2.37%	75.22%	12.14%	5.01%	3.24%	9.11%	9.13%
	Paek et al. [56]	5.9%	1.01%	9.68%	85.33%	21.35%	21.61%	8.95%	10.83%	7.02%
	Phanikumar and Mahajan [97]	15.26%	4.55%	0.07%	71.63%	13.2%	11.08%	3.50%	7.18%	5.20%
	Sadeghi et al. [99]	11.63%	8.6%	5.22%	64.45%	10.65%	11.65%	3.77%	4.60%	7.65%
	Xiao et al. [102]	10.5%	7.19%	1.77%	115.18%	18.85%	16.14%	14.70%	19.80%	9.80%
	Schmierer and Razani [98]	8.06%	4.15%	0.42%	75.16%	12.36%	6.78%	10.68%	4.5%	12.09%
$AlSi_7Mg$-air	Dyga and Witczak [100]	5.87%	3.89%	1.94%	67.63%	11.84%	8.18%	13.98%	12.37%	17.43%
Al-water		7.19%	4.63%	2.05%	94.86%	16.08%	9.56%	17.83%	23.54%	24.28%
	Xiao et al. [102]	24.05%	18.85%	12.26%	127.36%	33.90%	23.25%	28.06%	30.02%	9.16%
Copper-air	Yao et al. [65]	13.89%	5.38%	0.128%	69.14%	13.12%	21.79%	15.41%	6.41%	9.93%
Copper-water		12.61%	6.83%	2.61%	64.92%	11.12%	12.98%	16.43%	7.94%	10.16%
Copper-PCM		3.36%	2.71%	2.30%	73.81%	16.69%	15.56%	11.07%	3.20%	15.37%
	Xiao et al. [102]	14.19%	7.71%	1.28%	75.95%	12.84%	18.60%	14.34%	6.06%	9.71

Table 2.2: Parameters used for validating present models for coated MFs [55]

Type	Material	Thermal Conductivity ($W.m^{-1}.K^{-1}$)
Metal foam	copper ($PPI = 12.7, \varepsilon_o = 0.95, 0.98$)	398
	nickel ($PPI = 12.7, \varepsilon_o = 0.90, 0.95, 0.98$)	91.4
Infiltrating medium	Air	0.0265
	PCM_{lmp} (Low melting point Paraffin, 38ºC-41 ºC)	0.2
	PCM_{hmp} (High melting point Paraffin, 58ºC-62 ºC)	0.305
Coating material	Graphene	3000
Fitted dimensionless parameters	For copper foams λ_3 (Model $M-1$ and $M-3$) $= 0.0004$ β_2 (Model $M-2$) $= 0.0004$	-
	For nickel foams λ_3 (Model $M-1$ and $M-3$) $= 0.0006$ β_2 (Model $M-2$) $= 0.0006$	-

2.4 Results and discussion

2.4.1 Comparison of proposed models

The current predictions for coated metal foams saturated with fluid have been evaluated against the experimental data provided by Chan et al. [55]. In their study, tests were conducted on graphene-coated copper and nickel foams using air and PCM as the infiltrating media. Chan et al. [55] also proposed a two-dimensional model to estimate the effective thermal conductivity (ETC) of coated metal foams, which they validated using their experimental results. The model employed two dimensionless fitting parameters, 'r_s' and 'r_g', which were adjusted to

minimize the average deviation between the model predictions and the measured data. In this study, the proposed models (M-1, M-2, and M-3) are compared with the same experimental dataset to assess their accuracy in predicting ETC for graphene-coated foams. The comparative analysis is presented in detail below.

Comparison for graphene coated nickel foam

Here, λ_1 (for models M-1 and M-3), and β_1 (for model M-2) are expressed as functions of the overall porosity of the metal foam by calibrating with the test data. The fitted polynomial functions for M-1, M-2 and M-3, along with the average value of $\frac{r}{2a}$ for M-1 and M-3 and porosity range for the available experimental data have been tabulated in Table 2.3. A third-order polynomial is selected by the trial-and-error method to minimize the deviations.

Table 2.3: Porosity-dependent dimensionless parameter for nickel foams

Metal foam	MF Geometry	r/L	r/2a	Test data [55] porosity Range
Nickel	Hexagonal (M-1)	$\frac{r}{L} = 874.0487{\varepsilon_o}^3 - 2479.6755{\varepsilon_o}^2 + 2339.2118\varepsilon_o - 733.3613$	5.09	$0.98 \geq \varepsilon_o \geq 0.90$
	Hexagonal (M-2)	$\frac{a_2}{L} = 50{\varepsilon_o}^3 - 145.33{\varepsilon_o}^2 + 140.03\varepsilon_o - 44.661$	-	
	Square (M-3)	$\frac{r}{L} = -607.0649{\varepsilon_o}^3 + 1657.8931{\varepsilon_o}^2 - 1511.7574\varepsilon_o - 460.8176$	4.10	

In case of both the models (M-1 and M-3), for the complete range of porosity, the condition of $\frac{r}{2a} \geq 1$ has been satisfied, i.e., the node is assumed to be greater than the ligament.

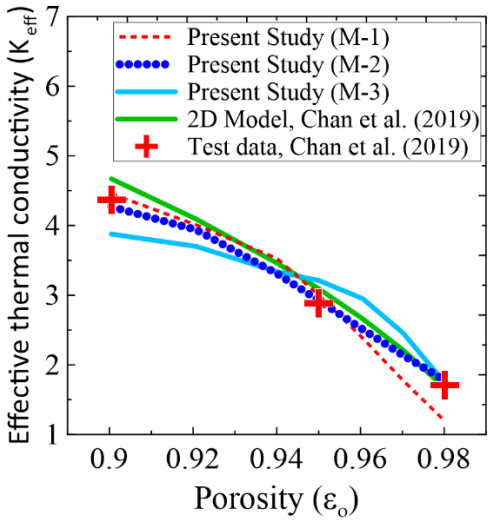

(a) Graphene coated nickel foam saturated with air

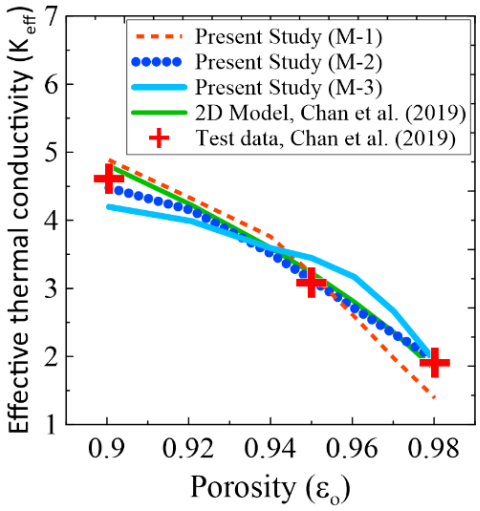

(b) Graphene coated nickel foam saturated with PCM_{lmp}

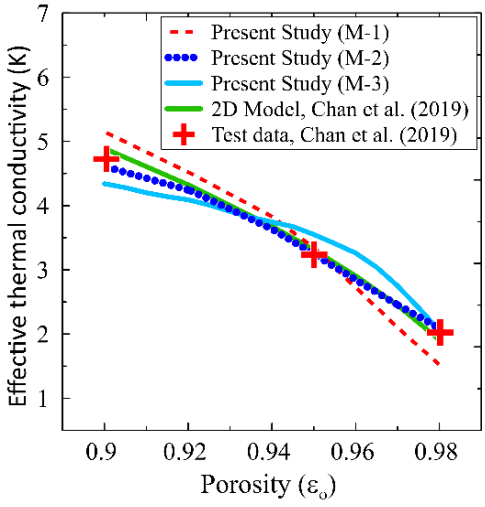

(c) Graphene coated nickel foam saturated with PCM_{hmp}

Figure 2.16: ETC for graphene coated nickel foam

Further, for the nickel foams the best fitted value of λ_3 and β_2 is taken as 0.0006. Figs. 2.16 (a-c) depict the comparison of present predictions

with the test data and 2D model result of Chan et al. [55]. The authors considered the fitting value of 'r_s' and 'r_g' as 0.1 and 0.005, respectively, for the nickel foam to compare the 2-D model with their test data. The effective thermal conductivity of various composite systems, including metal foams infiltrated with PCM_{lmp} (a paraffin-based PCM with a melting range of 38–41 °C), PCM_{hmp} (melting range of 58–62 °C), and air. Results consistently show that ETC decreases with increasing porosity, attributed to the reduction in the volume fraction of metal as porosity increases, thereby diminishing the dominant heat-conducting pathway within the foam structure, as depicted in Fig. 2.16. Fig. 2.16(a) compares the model predictions with experimental data for graphene-coated nickel foams (ε_o = 0.90–0.98, 12.7 PPI) saturated with air.

For the air-saturated nickel foam, the average deviation between model predictions and experimental results is 12.01% for M-1, 2.61% for M-2, and 8.15% for M-3. In contrast, the 2D model developed by shows a deviation of 5.36%, indicating a reasonable fit. Figs. 2.16(b) and 2.16(c) present the corresponding results for nickel foams saturated with PCM_{lmp} and PCM_{hmp}, respectively. Notably, across all porosities, MF-PCM composites incorporating PCM_{hmp} exhibit higher ETC values compared to those using PCM_{lmp}. This can be linked to the typically greater thermal conductivity of high-melting-range paraffins and their more stable phase behaviour, which enhance heat transfer characteristics in the composite.

For MF-PCM_{lmp}, the deviations between model predictions and test data are 12.45% (M-1), 2.5% (M-2), and 7.38% (M-3), while for MF-PCM_{hmp}, the deviations are 12.37%, 1.98%, and 6.48%, respectively. Comparatively, the 2D model shows deviations of 4.59% for PCM_{lmp} and 2.74% for PCM_{hmp}. These results suggest that Model M-2, which incorporates realistic ligament and node geometries, provides the closest agreement with experimental findings across all tested conditions.

Comparison for graphene coated copper foam

In this section, the proposed models are evaluated against available experimental data for graphene-coated copper foams with porosity values ranging from 0.95 to 0.98 and a pore density of 12.7 PPI, infiltrated with air, PCM_{lmp}, and PCM_{hmp}. For copper foams, the existing 2D theoretical model employs constant values of the dimensionless parameters, 'r_s' and 'r_g' as 0.11 and 0.004, respectively. However, in the present work, the non-dimensional coating parameter, expressed as a function of porosity, has been recalibrated specifically for copper foams using the corresponding experimental dataset. As in the previous case with nickel foams, the fitted values of key parameters used for validation are summarized in Table 2.4. The optimal fitted values for λ_3 and β_2 for copper foam are both determined to be 0.0004.

Table 2.5 presents the prediction results for graphene-coated copper foams saturated with air, PCM_{lmp}, and PCM_{hmp}. Interestingly, for copper foams, all three models (M-1, M-2, and M-3) demonstrate improved accuracy compared to their performance with nickel foams. For air-saturated copper foams, the average deviations between the predicted and experimental ETC values are 4.04% for M-1, 1.33% for M-2, and 1.28% for M-3. In the case of copper foams infiltrated with PCM_{lmp} and PCM_{hmp}, Model M-1 shows deviations of 4.86% and 5.66%, respectively. In contrast, Model M-3 achieves better agreement, with deviations of 1.01% for PCM_{lmp} and 1.52% for PCM_{hmp}. These results suggest that the models, particularly M-3, offer reliable predictions for coated copper foam composites across various saturating.

For Model M-2, the deviation between predicted values and experimental data remains below 2% for graphene-coated copper foams saturated with both PCM_{lmp} and PCM_{hmp}. In comparison, Chan's 2D model [55] yields deviations of 4.03%, 4.56%, and 5.04% for air, PCM_{lmp}, and PCM_{hmp}, respectively, when applied to graphene-coated copper foams.

Table 2.4: Porosity-dependent dimensionless parameter for copper foams

Metal foam	MF Geometry	r/L	r/2a	Test data [55] porosity Range
Copper	Hexagonal (M-1)	$\frac{r}{L} = -4198.21{\varepsilon_o}^3 + 11988.38{\varepsilon_o}^2 - 11415.6\varepsilon_o + 3625.174$	2.03	$0.98 \geq \varepsilon_o \geq 0.95$
	Hexagonal (M-2)	$\frac{a_2}{L} = -7.622{\varepsilon_o}^3 + 22.161{\varepsilon_o}^2 - 22.03\varepsilon_o + 7.54$	-	
	Square (M-3)	$\frac{r}{L} = -1099.98{\varepsilon_o}^3 + 3126.785{\varepsilon_o}^2 - 2966.88\varepsilon_o + 940.0516$	2.42	

Among the present models, M-1 and M-3 show good agreement with experimental results, while M-2 demonstrates exceptional accuracy. Overall, predictions from the present 3D model (M-2) surpass the accuracy of the 2D model for both nickel and copper-based coated metal foams. Additionally, the thermal conductivity values observed for graphene-coated copper foams are consistently higher than those for nickel foams across all cases, likely due to copper's thermal conductivity being approximately 4.2 to 4.5 times greater than that of nickel.

Table 2.5: Comparison of present models with experimental test data [55] for graphene-coated copper foams

Cases		Test data (I) (K_{eff})	2D model (II) (K_{eff})	Present models (K_{eff})			Average Deviations			
				M-1 (III)	M-2 (IV)	M-3 (V)	I-II	I-III	I-IV	I-V
Copper-air	ε_o= 0.95	6.83	7.11	6.80	6.84	6.75	4.03%	4.04 %	1.33 %	1.28 %
	ε_o= 0.98	3.92	3.76	3.49	3.98	3.67				
Copper-PCM_{lmp}	ε_o= 0.95	7.01	7.25	7.11	7.05	7.013	4.56%	4.86 %	1.08%	1.01 %
	ε_o= 0.98	4.14	3.90	3.69	4.19	3.89				
Copper-PCM_{hmp}	ε_o= 0.95	7.10	7.33	7.29	7.18	7.17	5.04%	5.66 %	1.35 %	1.52 %
	ε_o= 0.98	4.28	3.99	3.80	4.31	4.02				

The variation in effective thermal conductivity with increasing porosity is observed to follow an approximately linear trend. For a fixed porosity, ETC is highest for PCM_{hmp}, followed by PCM_{lmp} and air, which corresponds to the descending order of thermal conductivity of the infiltrating media. Among the proposed models, M-2 consistently demonstrates the highest level of accuracy. This improved performance is likely due to its more realistic geometric representation of the metal foam structure. Model M-2 shows excellent agreement with the experimental data across all types of infiltrating media and both copper and nickel foams. A summary of the maximum, minimum, and average deviations between the model predictions and experimental results is provided in Table 2.6.

Because of the excellent agreement between M-2 and test data, the analysis has been extended to explore the effect of infiltrating medium, coating material and coating thickness on the ETC of the composite. The theoretical model M-2 and the data for graphene coated copper foams infiltrated with PCM_{lmp} have been used for this investigation (section 2.4.2 to 2.4.4). Since the metal foams exist for a wide range of porosity values, the range selected for the analysis is ($0.70 \leq \varepsilon_o \leq 0.98$).

Table 2.6: Deviation results from the experimental data of Chan et al. [55]

MF-Composite	3D Hexagonal Model (M-1)		3D Hexagonal model (M-2)		3D Square Model (M-3)	
	Range	Average	Range	Average	Range	Average
Nickel-Air	1.19 % - 30.09 %	12.01 %	1.31 % - 4.15 %	2.61 %	1.89 % - 11.31 %	8.15 %
Nickel-PCM_{lmp}	4.33 % - 27.06 %	12.45 %	1.40 % - 3.23 %	2.51 %	1.34 % - 11.85 %	7.38 %
Nickel-PCM_{hmp}	3.22 % - 25.22 %	12.37 %	0.19 % - 3.16 %	1.98 %	1.51 % - 10.81 %	6.48 %
Copper-Air	0.26 % - 7.82 %	4.04 %	0.48 % - 2.18 %	1.33 %	1.03 % - 1.53 %	1.28 %
Copper-PCM_{lmp}	1.56 % - 8.15 %	4.86 %	0.6% - 1.56%	1.08%	0.21 % - 1.65 %	1.01 %
Copper-PCM_{lmp}	2.81 % - 8.51 %	5.66 %	0.48 % - 2.22 %	1.35 %	1.14 % - 1.9 %	1.52 %

2.4.2 Effect of coating thickness on overall thermal conductivity

Figure 2.17 illustrates the effect of coating thickness on the ETC of open-cell infiltrated metal foams. The increase in coating thickness has been depicted by the increase in the value of β_2. The enhancement in the ETC is illustrated with respect to uncoated metal foams i.e., for $\beta_2 = 0$.

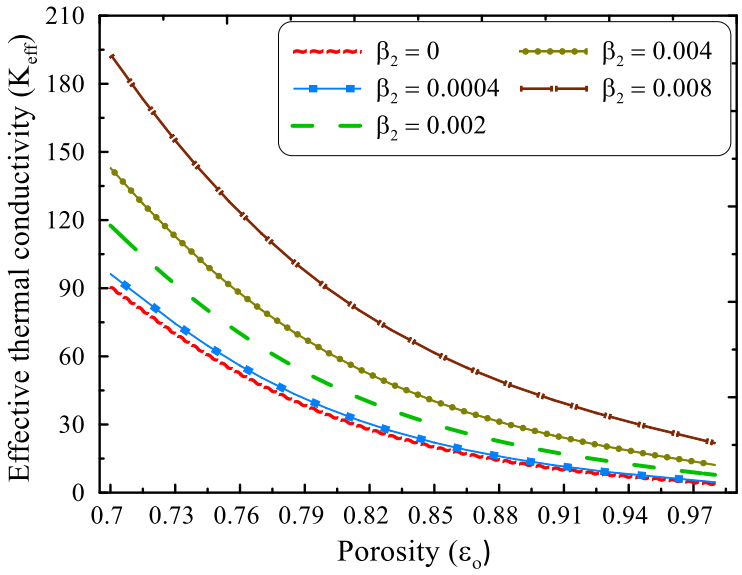

Figure 2.17: Effect of coating thickness on the ETC

The average percentage increase in the ETC relative to uncoated metal foams is calculated to be 10.83%, 54.05%, 109.31%, and 226.07% for β_2 = 0.0004, 0.002, 0.004 and 0.008 respectively, across the porosity range of 0.70 to 0.98. These results highlight the effectiveness of applying a high-conductivity coating to metal foams as a strategy to enhance ETC. The improvement is primarily attributed to two factors: the increased surface area introduced by the coating and the inherently higher thermal conductivity of the coating material compared to the base metal foam and the infiltrating medium. As the coating thickness increases, the fractional solid volume also rises, thereby strengthening the heat conduction pathway through the solid matrix. For a low porosity value ε_o = 0.70, the corresponding increases in ETC are 6.31%, 29.95%, 57.90%, and 113.20%, while at high porosity ε_o = 0.98, the enhancements rise significantly to 20.91%, 107.15%, 221.80%, and 475.28%, respectively, for β_2 = 0.0004, 0.002, 0.004 and 0.008. These

trends indicate that the relative increase in ETC is more pronounced at higher porosity levels, although the absolute influence of the coating becomes less dominant as porosity increases.

2.4.3 Effect of thermal conductivity of infiltrating medium

An important aspect to investigate is the influence of the infiltrating medium on the ETC of the composite. Fig. 2.18 shows how changes in the thermal conductivity of the infiltrating medium affect the overall ETC of the MF–PCM composite. As the thermal conductivity of the infiltrating material increases, a noticeable enhancement in the composite's ETC is observed.

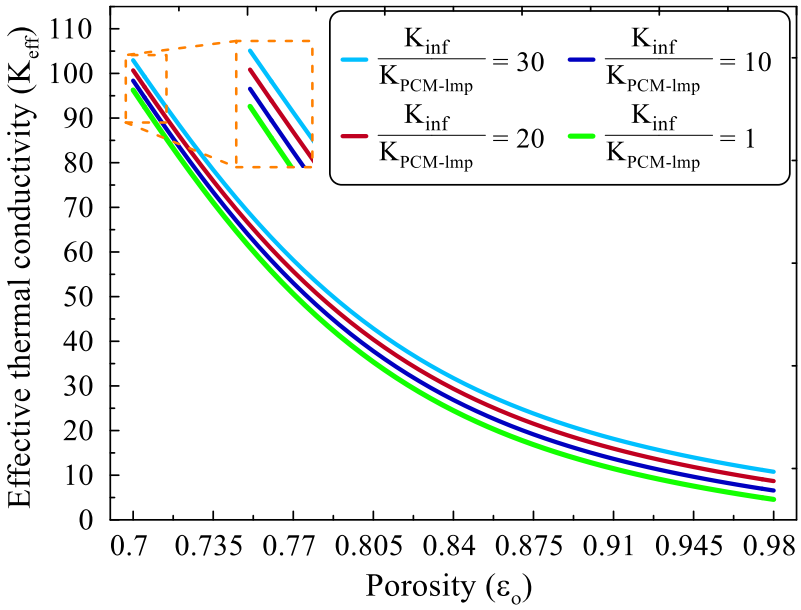

Figure 2.18: Effect of thermal conductivity of infiltrating medium on the ETC

This trend highlights the role of the fluid phase in contributing to the overall heat transfer, especially in highly porous structures where the fluid occupies a significant volume fraction. Here, K_{inf} denotes the arbitrary thermal conductivity of infiltrating medium, and $K_{PCM-lmp} = 0.2\ W.m^{-1}.K^{-1}$ denotes the thermal conductivity of low melting point paraffin. The increase in the thermal conductivity of infiltrating medium enhances the overall thermal conductivity of the composite. The average percentage increase in the ETC is found to be 13.45%, 27.59% and

41.30% for $\frac{K_{inf}}{K_{PCM-lmp}}$ of 10, 20, and 30, respectively for 0.7< ε_o <0.98. The absolute increase in ETC is 2.18%, 4.57%, and 6.92% for $\frac{K_{inf}}{K_{PCM-lmp}}$ = 10, 20, and 30, respectively at ε_o = 0.70; while for ε_o = 0.98 the increment is 43.42%, 89.60%, and 135.16%, respectively. Here, the percentage enhancement in the ETC increases with the increase in the thermal conductivity of infiltrating medium; the effect is more pronounced at higher values of porosity. For a lower value of porosity, the solid fractional volume is more and has a major contribution to the ETC. In contrast, the solid fractional volume decreases for higher porosity, and the effect of infiltrating medium becomes significant; thus, more enhancement is observed for a higher porosity value.

2.4.4 Effect of thermal conductivity of externally coated material

The influence of the coating material's thermal conductivity on the ETC of the MF composite is illustrated in Fig. 2.19. Here, K_g and K_s denote the thermal conductivity of coating material and MF, respectively. The ETC of MF-composite is found to increase with the increase in K_g. The average increase in the ETC is 1.42%, 5.68%, 12.72%, and 19.70% for $\frac{K_g}{K_s}$ = 2, 5, 10, and 15, respectively for 0.7< ε_o<0.98. The absolute increase in ETC is about 0.85%, 3.39%, 7.51%, 11.52% (at ε_o = 0.70) and 2.70%, 10.81%, 24.29%, and 37.72% (at ε_o = 0.98), respectively for $\frac{K_g}{K_s}$ = 2, 5, 10, and 15. Again, the percentage increase in ETC due to the increase in thermal conductivity of coating material is more for higher values of porosity. It can be observed that with the increase in the $\frac{K_g}{K_s}$ ratio, the ETC of the composite increases irrespective of the porosity value. For the same volume fraction of the coating solid region, a higher thermal conductivity value of the material promotes more heat conduction through the solid region. Therefore, a coating material with a thermal conductivity significantly higher than that of the metal foam should be preferred for maximizing ETC enhancement.

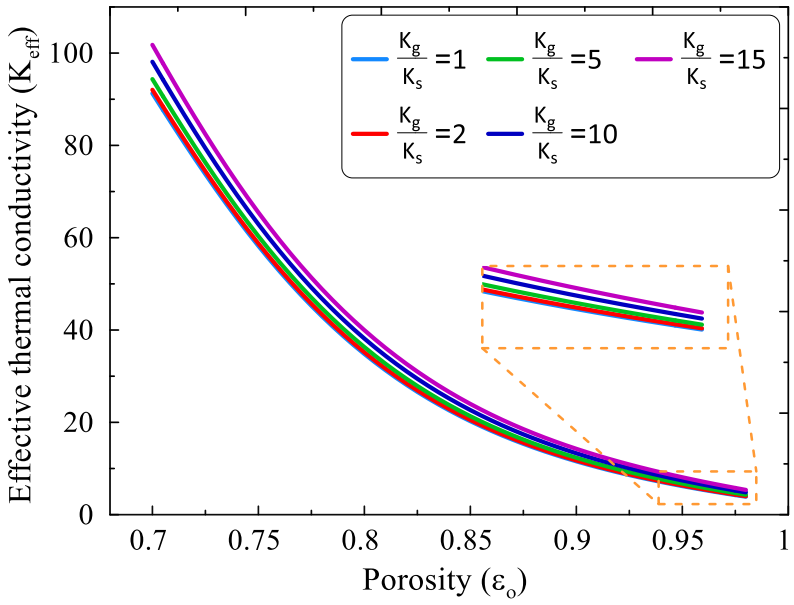

Figure 2.19: Effect of thermal conductivity of coating material on the ETC

The effect of various parameters such as coating thickness, thermal conductivity of coating material and infiltrating medium on ETC of MF-composite for a varied range of porosity has been discussed. The percentage enhancement in ETC increases with porosity for the increase in the values of thermal conductivity of coating material and infiltrating medium, while the percentage increase is more significant when the coating thickness is increased. Based on this, the designer needs to make a choice to develop better MF-composite while keeping other factors such as long-term effect of coating material, cost of coating and feasibility of coating process.

2.5 Concluding remarks

Here, a one-dimensional conduction approach has been proposed to estimate the ETC of coated metal foams saturated with fluid/PCM by considering the three-dimensional configuration. Two different metal foam geometries adopted from the tetrakaidecahedron structure, namely hexagonal and square, involving different shapes of ligaments (cylindrical, concave triprism) and nodes (cubic, pyramidal), have been considered for the analysis. The accuracy of the solution obtained from various models has been discussed in this chapter.

Among the models investigated, the model M-2, based on the hexagonal geometry involving concave triprism ligament and pyramidal nodes, exhibits excellent agreement with test data for all the cases. The average deviation between the model and test data is found to be less than 3% for nickel foams and less than 2% for copper foams. The higher degree of accuracy associated with M-2 may be attributed to the relatively more realistic representation of metal foam structure. For graphene-coated nickel foams, the average deviation between theoretical prediction and the test data for models M-1, M-2 and M-3 are found to be 12.27%, 2.36%, and 7.33%, respectively; whereas, for graphene-coated copper foams, the corresponding deviations are 4.85%, 1.25%, and 1.27%, respectively. The ETC of MF-composite is found to increase with the coating thickness, the thermal conductivity of coating material and infiltrating medium. Among these, the percentage enhancement is most pronounced with an increase in coating thickness, compared to increases in the thermal conductivity of the coating material or the infiltrating medium.

This theoretical study demonstrates that the geometric configuration, ligament shape, and node shape significantly affect the ETC of MF composite systems for both coated and uncoated foams. These findings can support the design of advanced thermal management systems for various applications.

Chapter 3

Numerical Investigation of Passive and Hybrid Battery Thermal Management Using Metal Foam–PCM and Liquid-Assisted PCM Systems

3.1 General background

Thermal management of Lithium-Ion Batteries (LIBs) plays a crucial role in the design and operation of LIB modules, especially under the demanding thermal loads that are frequently encountered in EV applications. Excessive temperature and non-uniform thermal distribution play a significant role in accelerating cell degradation, reducing cycle life, and increasing the risk of thermal runaway. Passive thermal management systems based on phase change materials (PCMs) have received significant attention due to their ability to regulate temperature through latent heat absorption during melting. However, the low thermal conductivity of most PCMs limits their effectiveness in heat removal, especially under high C-rate discharges or cyclic operations. Among the various approaches, systems combining PCMs and metal foams (MFs) have received significant attention due to various advantages: PCMs regulate temperature via latent heat absorption during melting, while MFs enhance heat transfer by providing conductive pathways. When MF-PCMs are used to regulate the temperature of battery modules, numerous design parameters involving PCM thickness, foam porosity, and discharge rates need to be optimized under dynamic and extreme conditions, which are not extensively reported in the literature.

While passive thermal management is simple and reliable, its thermal regulation capacity is limited due to high thermal loads, inadequate heat storage capacity, and elevated ambient temperatures. Hybrid battery thermal management systems, which combine PCMs with active liquid

cooling, offer a promising alternative by enhancing heat removal and extending the safe operating range of the battery.

However, existing hybrid thermal management systems often suffer from increased complexity, size, and weight. Common configurations, such as PCM interlayers paired with bottom-mounted liquid-cooled plates, compromise spatial efficiency and increase manufacturing challenges. Moreover, many hybrid systems depend on continuous coolant circulation to maintain performance, resulting in significant energy consumption and reduced overall system efficiency, which limits their suitability for real-world EV applications.

An overview of the overall investigation framework, outlining the passive (MF–PCM) and hybrid (PCM + liquid-cooled) systems along with the key parameters studied, is presented in Figure 3.1. In this chapter, a three-dimensional (3D) numerical framework is initially proposed that includes both cell-level and battery pack-level behaviour of MF–PCM composites under various conditions, such as steady-state, dynamic, and extreme thermal environments, and evaluates their performance for a range of PCM thicknesses, foam porosities, and discharge rates.

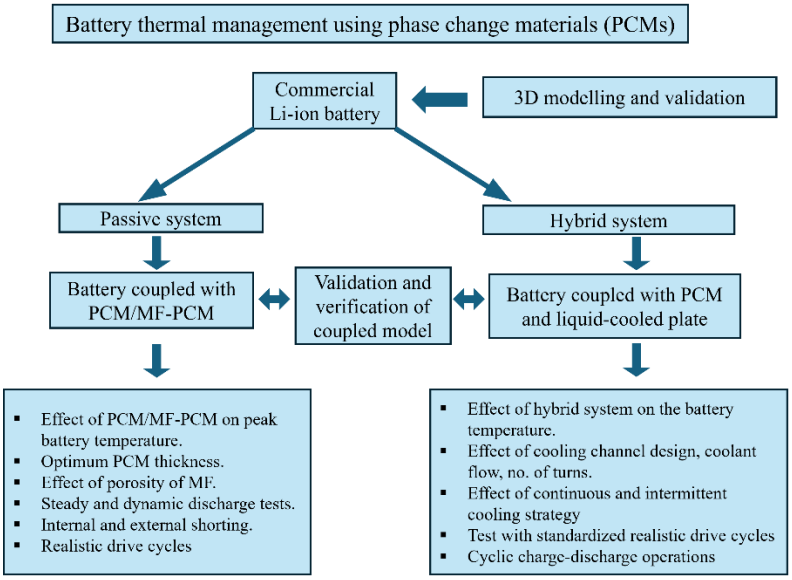

Figure 3.1: Overview of the PCM–battery thermal management framework

Subsequently, the study presents a 3D numerical analysis of a compact hybrid thermal management configuration that strategically integrates PCM with a liquid cooling system to improve heat dissipation and minimize structural complexity and energy usage. Together, these two studies aim to provide comprehensive insight into the thermal behaviour of LIBs under realistic and demanding operational scenarios, while offering practical design strategies for future thermal management systems.

3.2 Analysis of Li-ion battery under high discharge rate embedded with metal foam phase change composite.

While numerous studies have assessed PCM-based battery thermal management systems, most have been limited to simplified conditions, particularly constant current discharge scenarios. There is a lack of comprehensive studies that evaluate PCM based systems under more realistic and dynamic operating conditions, such as rapid charge-discharge cycles, thermal abuse scenarios, and realistic drive cycles that reflect normal and high-performance EV operations. This study presents a detailed 3D numerical investigation of a LIB module integrated with copper metal foam-PCM composites. The model explores the influence of PCM thickness, MF porosity, and discharge rate on the thermal response of the cells. A broad range of thermal loading scenarios is considered, including steady and dynamic high-rate charging and discharging, thermal abuse conditions such as internal and external shorting, and realistic drive cycles representing both standard and aggressive driving behaviours. Key performance metrics such as average temperature, maximum temperature, and temperature gradient within the battery cells are analysed. The objective of this investigation is:

- To develop a three-dimensional (3D) numerical model of a commercial lithium-ion battery integrated with a PCM embedded in MF for thermal management applications.

- To analyze the effects of PCM thickness, battery discharge rate, and MF porosity on cell temperature profiles.
- To evaluate thermal performance under various operating conditions, including continuous rapid discharge (4C and 5C), time-varying constant current charge/discharge, realistic drive cycles and thermal abuse scenarios such as external and internal shorting.

3.2.1 Numerical modeling

Geometry and computational domain

To study the passive BTMS, a large format prismatic Li-ion battery, model: EIG-ePLB C020 (Li[Ni-CoMn$_2$]O$_2$ cathode and graphite anode) is considered for the analysis [103]. The schematic and computational domain of a single cell are shown in Fig. 3.2. Fig. 3.2(a) shows the active zone and the tab in the cells; the active zone, considered to be homogeneous, is responsible for the heat generation. Fig. 3.2(b) illustrates the cell domain, the PCM domain, and the mesh generated for the numerical solution. In general, an external acrylic shell is used to cover the PCM embedded battery module; however, to reduce the complexity of the problem, it is not considered in the present investigation.

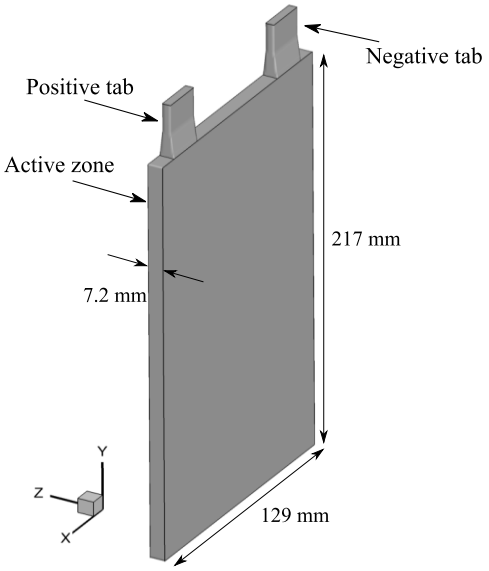

(a) Schematic of the cell

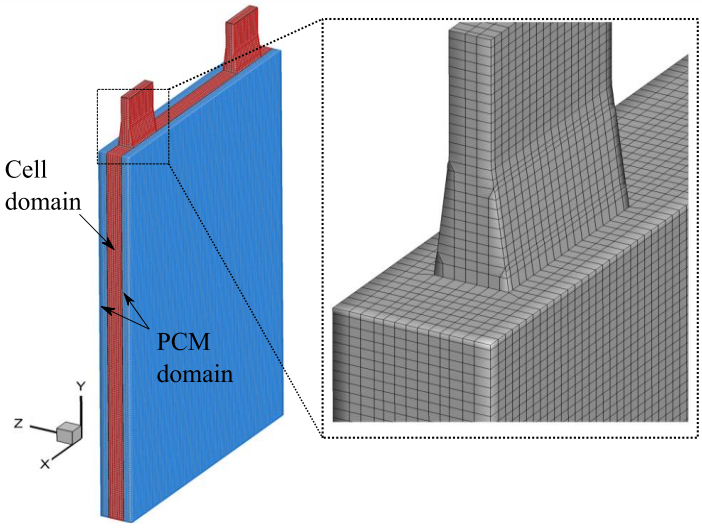

(b) Computational domain and mesh

Figure 3.2: Description of the cell and computational domain

The details and specifications of the commercial Li-ion battery have been tabulated in Table 3.2.1.

Table 3.2.1: Battery specifications [103-104]

Name and make	ePLB C020 Li-ion polymer battery, Make: EIG corporation (South Korea)
Form factor and chemistry	Prismatic, Cathode: $Li[Ni - CoMn_2]O_2$ Anode: graphite
Length, width, thickness weight	216±1 mm, 130±1 mm, 7.2±0.2 mm, approx. 410gms
Nominal Voltage and capacity	3.65 Volts, 20 Ah
Energy density and specific energy	365 $Wh.L^{-1}$, 180 $Wh.kg^{-1}$
Charging method with cutoff	CC/CV, 2.5 Volts (discharge), 4.2 Volts (charge)
Maximum discharge rate: continuous	5C

The cell model

A variety of battery models are reported in the literature for thermal analysis such as constant heat flux models and uniform volumetric heat generation approaches [68, 74, 103]. While these simplified models can capture the general thermal response of a battery under specific operating conditions, they lack the capability to represent the intricate coupling between electrochemical and thermal phenomena. As a result, their predictive accuracy becomes limited, particularly under dynamic or high-stress scenarios. Accurate thermal modeling is essential for understanding the temperature evolution of LIBs across a wide range of real-world applications.

To address the limitations, researchers have developed more advanced frameworks that couple electrochemical and thermal processes to capture the complex behaviour of lithium-ion batteries under realistic operating conditions. These models fall under the broader category of Multi-Scale Multi-Domain (MSMD) modeling approaches, which are designed to simulate the interplay of physical phenomena occurring across multiple length and time scales within a battery system, ranging from particle-level electrochemical reactions to cell and pack-level thermal gradients and electrical dynamics. Prominent among these MSMD approaches are the Equivalent Circuit Model (ECM) [105], the NTGK (Newman–Tiedemann–Gu–Kim) model [106], and Newman's pseudo-two-dimensional (P2D) model [107]. These models vary in complexity and fidelity.

The ECM simplifies the battery's internal behaviour using an equivalent electrical circuit, where the open-circuit voltage (OCV), internal resistance, and dynamic response are modelled using voltage sources, resistors, and resistor–capacitor (RC) pairs, respectively. The ECM uses the state of charge (SOC) and temperature as inputs to compute these electrical parameters, offering a balance between computational efficiency and physical realism. Due to its adaptability and low computational cost, the ECM is widely employed for simulating both individual cells and battery packs, including solid-state and

conventional LIBs. In contrast, the NTGK model determines the volumetric current transfer rate based on the potential difference between electrodes, with polarization behaviour described using empirical polynomial functions. These functions are typically derived from experimental discharge profiles by curve fitting to determine key coefficients. Meanwhile, Newman's P2D model provides a more detailed framework by incorporating Li-ion intercalation/deintercalation in solid particles, electrochemical reaction kinetics at particle surfaces, and transport phenomena in the electrolyte using concentrated solution theory.

All three models have been successfully integrated into commercial simulation platforms such as ANSYS Fluent [108] and COMSOL Multiphysics [109], allowing for two-dimensional and three-dimensional Multiphysics simulations of battery cells and packs. These integrations enable comprehensive thermal–electrochemical modeling, including spatially resolved heat generation, SOC evolution, and performance degradation making them valuable tools for battery management system design and thermal optimization in electric vehicle applications.

Governing equations

In the present study, the cell behaviour is modelled using the ECM approach, which effectively captures the transient electrochemical and thermal response of the battery. In reality, the active part of the cell consists of multiple layers of cathode, anode, electrolyte, and separator. The ECM model offers a very accurate thermal modeling of LIBs by considering a homogeneous active zone while carefully defining the cell material properties. As shown in Fig. 3.3, the ECM consists of a voltage source representing the OCV, a series resistor for internal ohmic losses, and one or more RC pairs to account for dynamic voltage changes during charge and discharge. This configuration enables the simulation of realistic thermal loading conditions while maintaining computational efficiency in full 3D battery pack simulations. The battery's thermal and

electrical fields are solved at the cell scale in the computational fluid dynamic (CFD) domain, by discretizing the following differential equations governing these fields based on conservation principles [104, 110]:

$$\frac{\partial \rho_b C_{p_b} T_b}{\partial t} = \nabla.(k_b \nabla T_b) + \dot{q}_{total} \tag{3.1}$$

$$\nabla.(\sigma_+ \nabla \varphi_+) = -(j_{ECh} - j_{short}) \tag{3.2}$$

$$\nabla.(\sigma_- \nabla \varphi_-) = j_{ECh} - j_{short} \tag{3.3}$$

Equation (3.1) represents energy conservation for the battery depicting temperature change due to heat generation and thermal conduction. Equations (3.2) and (3.3) are the governing conservation equations for the positive and negative current fluxes, respectively, and relate the divergence of electric current density in the battery to the electrical current.

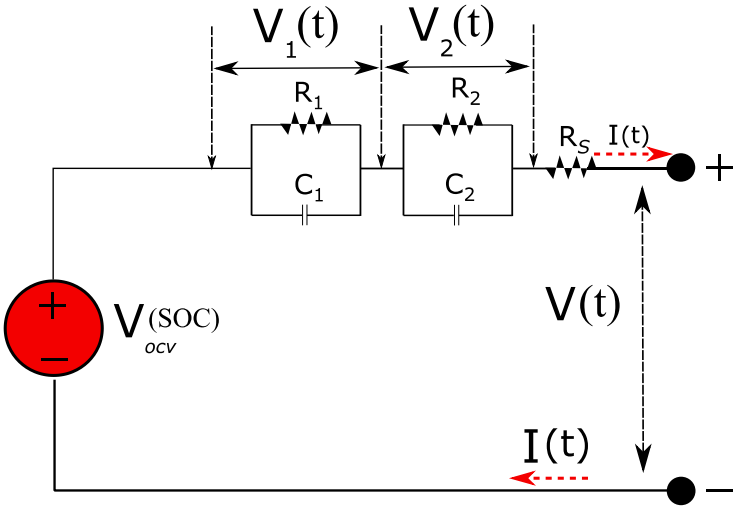

Figure 3.3: Equivalent circuit model (ECM)

Here, ρ_b, C_{p_b}, T_b, k_b denote the density, specific heat, temperature, and thermal conductivity of the battery. σ_+ and σ_- denote the electrical conductivities, φ_+ and φ_- represent the phase potentials for the positive and negative electrodes, respectively. j_{ECh} and j_{short} is the volumetric current transfer rates due to electrochemical reactions and shorting conditions.

During the charging and discharging processes, significant heat generation occurs in the battery, expressed as [104, 110]:

$$\dot{q}_{total} = \dot{q}_{irreversible} + \dot{q}_{reversible} + \dot{q}_{short} + \dot{q}_{abuse} \quad (3.4)$$

The total heat generated ($\dot{q}_{total}$) is conserved, including contributions from reversible heat ($\dot{q}_{reversible}$, due to entropy changes during the chemical reaction), irreversible heat ($\dot{q}_{irreversible}$, due to the internal resistance of the cell), and heat generated due to shorting and thermal abusive conditions. Under the normal operating conditions of the battery the last two terms in Eqn. 3.4 accounting for heat from shorting and abusive conditions remain zero.

The electrochemical reactions inside the battery are not fully efficient, and the associated energy losses are released as heat ($\dot{q}_{ECh}$). Additionally, there is resistance to the flow of the electrons leading to heat generation ($\dot{q}_{ohmic}$). Therefore, based on the definitions, the irreversible heat generation is defined as follows :

$$\dot{q}_{irreversible} = \dot{q}_{ECh} + \dot{q}_{ohmic} \quad (3.5)$$

$$\dot{q}_{irreversible} = I(V_{ocv} - V) + \sigma_{+}|\nabla\varphi_{+}|^2 + \sigma_{-}|\nabla\varphi_{-}|^2 \quad (3.6)$$

In Eqn. (3.6), $I(V_{ocv} - V)$ represents the battery overpotential, defined as the difference between the voltage across the battery terminals, V, and the open circuit voltage,V_{ocv}. The reversible heat ($\dot{q}_{reversible}$) involves heating effects that are due to the entropy change of the electrochemical reactions in the battery. This heat does not result from energy loss like the irreversible one, but from the thermodynamic nature of the reactions, expressed as:

$$\dot{q}_{reversible} = \dot{q}_{entropy} = -IT\frac{\partial V_{ocv}}{\partial T} = -T\Delta S\frac{I}{nF} \quad (3.7)$$

where the entropy changes as

$$\Delta S = -\frac{\partial \Delta G}{\partial T} = -nF\frac{\partial V_{ocv}}{\partial T} \quad (3.8)$$

and the Gibbs energy change is expressed as

$$\Delta G = -nFV_{ocv} \tag{3.9}$$

Here, I is the current, T is temperature, $\frac{\partial V_{ocv}}{\partial T}$ is the temperature derivative depicting sensitivity towards temperature change, V_{ocv} is the open circuit voltage (OCV), n is the charge number, ΔS is the entropy change, F is the Faraday constant (in C/mol), and ΔG is the Gibbs energy change (in J/K.mol).

The electrochemical sub-model determines the volumetric current density (j) through the interaction between the battery scale and the subscale model. The temperature equation is solved simultaneously by generating a source term for the heat transfer equation. The following equations are used to evaluate the voltage at the terminals as [104], [110]:

$$V(t) = V_{OCV}(soc) - V_1 - V_2 - R_s(soc)\, I(t) \tag{3.10}$$

$$\frac{\partial V_1}{\partial t} = -\frac{1}{R_1(soc)C_1(soc)} V_1 - \frac{1}{C_1(soc)} I(t) \tag{3.11}$$

$$\frac{\partial V_2}{\partial t} = -\frac{1}{R_2(soc)C_2(soc)} V_2 - \frac{1}{C_2(soc)} I(t) \tag{3.12}$$

$$\frac{d(SOC)}{dt} = \frac{I(t)}{3600 Q_{ref}} \tag{3.13}$$

The open circuit voltage, resistor resistances, and capacitor capacitances for a particular battery all depend on the battery's state of charge (SOC). Equations 3.10-3.13 account for the evaluation of the overall battery voltage, including the effects of open-circuit voltage, internal resistance, and series resistance, which are influenced by SOC and current. These functions R_s, R_1, C_1, R_2, C_2, and V_{OCV} can be represented by higher-order polynomials. In general, the ECM model provides numerical solutions with significant parametric flexibility, yielding results that accurately fit test data. The I-V performance data of the cell under different discharge conditions are used to estimate the parameters, which are then utilized to express various modeling parameters such as R_s, R_1, C_1, R_2, C_2, and V_{OCV} as functions of SOC as is presented in Table 3.2.

Similar approaches have been adopted in previous studies. Assuming uniform heat generation and normal charge/discharge conditions, the current density and the heat source term are computed as follows [104, 110]:

$$j_{ECh} = I\frac{Q_{nominal}}{Q_{ref}Vol} \tag{3.14}$$

$$\dot{q}_{total} = j_{ECh}\left[V_{ocv} - V - T\frac{dU}{dT}\right] + \sigma_{+}|\nabla\varphi_{+}|^2 + \sigma_{-}|\nabla\varphi_{-}|^2 \tag{3.15}$$

Here, $Q_{nominal}$ is nominal charge capacity, Q_{ref} is the reference charge capacity, Vol is volume of battery. Equation 3.15 denotes the total heat generation in the cell and includes irreversible and reversible parts.

Table 3.2: The fitted parameters as the function of SOC of battery [104, 110]

$$V_{OCV} = 3.5 + 0.35SOC - 0.0178SOC^2 + 0.3201SOC^3 - 1.031\exp(-80SOC) \tag{3.16a}$$

$$R_s = 0.07446 + 0.5\exp(-24.37SOC) \tag{3.16b}$$

$$R_1 = 0.002 + 0.3208\exp(-29.14SOC) \tag{3.16c}$$

$$C_1 = 703.6 - 752.9\exp(13.51SOC) \tag{3.16d}$$

$$R_2 = 0.002 + 6.604\exp(155.2SOC) \tag{3.16e}$$

$$C_2 = 4475 - 6056\exp(27.12SOC) \tag{3.16f}$$

PCM embedded with Metal Foam model

The most widely utilized enthalpy-porosity formulation [111] adopted to model the melting behaviour of the PCM. To account for the presence of porous media in the domain, pressure losses due to inertia and viscosity are incorporated into the momentum equation. Natural convection is approximated using the Boussinesq method with fluid as

incompressible and Newtonian. In Boussinesq approximation, the material properties of each phase are constant, and it takes into account the effect of fluid density on buoyancy force.

The porous zone is considered to be isotropic and homogeneous, and expansion of the PCM in volume is not considered. The porous media approach, as reported by Sardari et al. [112] is employed to analyse the MF-based PCM system. The governing equations for the model are detailed below:

Continuity equation:

$$\frac{\partial \rho}{\partial t} + \nabla . \left(\rho_{pcm} \vec{V}_{pcm}\right) = 0 \tag{3.17}$$

Momentum equation:

X – dir.:

$$\frac{\rho_{pcm}}{\varepsilon}\frac{\partial u_{pcm}}{\partial t} + \frac{\rho_{pcm}}{\varepsilon^2}\left(\vec{V}_{pcm} . \nabla\right)u_{pcm} = -\frac{\partial P}{\partial x} + \frac{\mu_{pcm}}{\varepsilon}\left(\nabla^2 u_{pcm}\right) - \left(\frac{\mu_{pcm}}{M} + \frac{\rho_{pcm} C}{\sqrt{M}}\left|u_{pcm}\right|\right)u_{pcm} + S_x \tag{3.18}$$

Y – dir.:

$$\frac{\rho_{pcm}}{\varepsilon}\frac{\partial v_{pcm}}{\partial t} + \frac{\rho_{pcm}}{\varepsilon^2}\left(\vec{V}_{pcm} . \nabla\right)v_{pcm} = -\frac{\partial P}{\partial y} + \frac{\mu_{pcm}}{\varepsilon}\left(\nabla^2 v_{pcm}\right) - \left(\frac{\mu_{pcm}}{M} + \frac{\rho_{pcm} C}{\sqrt{M}}\left|v_{pcm}\right|\right)v_{pcm} + S_y + S_a \tag{3.19}$$

Z – dir.:

$$\frac{\rho_{pcm}}{\varepsilon}\frac{\partial w_{pcm}}{\partial t} + \frac{\rho_{pcm}}{\varepsilon^2}\left(\vec{V}_{pcm} . \nabla\right)w_{pcm} = -\frac{\partial P}{\partial z} + \frac{\mu_{pcm}}{\varepsilon}\left(\nabla^2 w_{pcm}\right) - \left(\frac{\mu_{pcm}}{M} + \frac{\rho_{pcm} C}{\sqrt{M}}\left|w_{pcm}\right|\right)w_{pcm} + S_z \tag{3.20}$$

Where $S_x, S_y, and\ S_z$ are source terms representing the mushy zone resistance, calculated as follows:

$$S_x = \frac{A_{mush}(1-\lambda)^2}{(\lambda^3 + 0.001)}\left(u_{pcm} - u_{pull}\right) \tag{3.21a}$$

$$S_y = \frac{A_{mush}(1-\lambda)^2}{(\lambda^3 + 0.001)}\left(v_{pcm} - v_{pull}\right) \quad (3.21b)$$

$$S_z = \frac{A_{mush}(1-\lambda)^2}{(\lambda^3 + 0.001)}\left(w_{pcm} - w_{pull}\right) \quad (3.21c)$$

$$S_a = \rho_{pcm} g\beta(T - T_{ref}) \quad (3.21d)$$

S_a represents the gravitational force on the PCM in the y direction due to buoyancy; A_{mush} defines the mushy zone and impacts both the suppression and melting behavior of the PCM. The value of A_{mush} can range from 10^4 to 10^6, and as recommended in many literatures [82], [87], [88], [92], [93], a value of 10^5 is selected. To prevent division by zero, a constant value of 0.001 is added to the denominator in Eqns. (3.21a-3.21c). The pull velocities u_{pull}, v_{pull} and w_{pull} are zero, as the solidified PCM is assumed to be stationary. The PCM is tracked using the melt fraction (λ), ranging from 0 (completely solid) to 1 (completely liquid) based on the temperature field:

$$\lambda = \begin{cases} 0 & (T < T_s) \\ \dfrac{T - T_s}{T_l - T_s} & (T_s < T < T_l) \\ 1 & (T > T_l) \end{cases} \quad (3.22)$$

Using the Darcy's law of damping [113], the effect of the porous material in the domain is marked by introducing source term on right hand side in the momentum equation:

$$\left(\frac{\mu_f}{M} + \frac{\rho_f C|\vec{V}|}{\sqrt{M}}\right)\vec{V} \quad (3.23)$$

The source term comprises the loss that occurs due to the viscous and inertial effect, whereas $\vec{V}$ denotes the magnitude of the velocity vector. In the context of laminar flow in porous media propelled by a pressure gradient, establishing a connection between the pressure gradient and velocity often involves the use of permeability. However, determining the permeability for natural convection in metal foam poses challenges due to the limited availability of relevant experimental data in the open literature. Because of the high porosity of the metal foams, most of the

studies [112, 114-117] use the permeability (M) and the inertia coefficient (C) using the following equations as formulated by Calmidi and Mahajan [118].

As explained by Calmidi and Mahajan, the equations 3.24-3.25 are valid for high porosity open cell metal foams having ligament diameter (d_l) between 0.0025-0.00050 m, pore diameter (d_p) between 0.00180-0.00402 m and pore density (ω) between 5-40. d_l and d_p are depicted in the Fig. 3.4.

$$M = 0.00073{d_p}^2(1-\varepsilon)^{-0.224}\left(\frac{d_l}{d_p}\right)^{-1.11} \quad (3.24)$$

$$C = 0.00212(1-\varepsilon)^{-0.132}\left(\frac{d_l}{d_p}\right)^{-1.63} \quad (3.25)$$

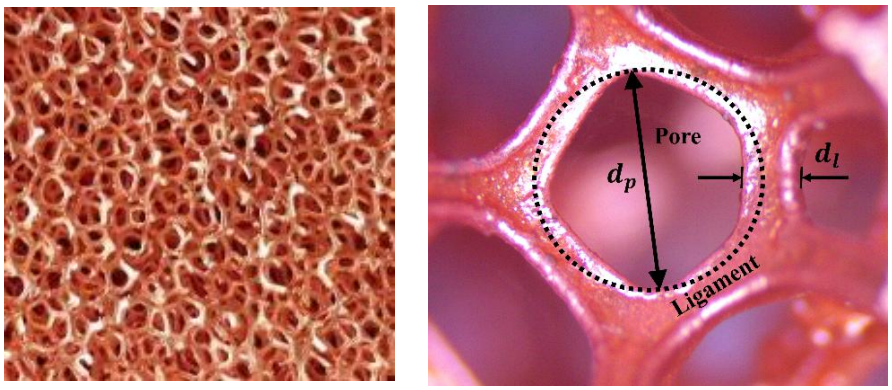

Figure 3.4: Open cell copper metal foam

Normally, the porosity, the pore size and the ligament diameter are the parameters used to describe the structure characteristics of porous media. These parameters are not independent parameters as explained by Calmidi and Mahajan [118]. The equations (3.26-3.27) have been widely adopted for open cell copper metal foams [112, 114-117].

Here, d_l and d_p is:

$$d_l = 1.18d_p\sqrt{\frac{1-\varepsilon}{3\pi}}\left(\frac{1}{1-e^{-(1-\varepsilon)/0.004}}\right) \quad (3.26)$$

$$d_p = 0.0254/\omega \quad (3.27)$$

The total enthalpy H, which includes sensible (h_s) and latent heat (ΔH) contribution:

$$H = h_s + \Delta H \tag{3.28}$$

$$h_s = \int_{T_{ref}}^{T} C_{p_{pcm}} dT \tag{3.29}$$

$$\Delta H = \lambda L \tag{3.30}$$

The present investigation adopts both approaches, i.e., the thermal equilibrium and thermal non-equilibrium to model heat transfer in the MF–PCM domain. In the case of the thermal equilibrium model, the temperature between the metal foam (MF) and the PCM is considered to be the same, and it is assumed that no heat transfer takes place between both domains. The energy equation for such a case is:

$$\frac{\partial(\varepsilon\rho_{pcm}C_{p_{pcm}}T_{pcm})}{\partial t} + \nabla.\left(\rho_{pcm}C_{p_{pcm}}\vec{V}_{pcm}T_{pcm}\right) = \nabla.\left(k_{eff}\nabla T_{pcm}\right) - S_L \tag{3.31}$$

Here, S_L is source term, in case of non-thermal equilibrium, the variation in temperature of the PCM and the MF is considered. Heat transfer between both the domains is contemplated, and a heat transfer coefficient is defined. The energy equation in the case of non-thermal equilibrium is defined as:

For PCM:

$$\frac{\partial(\varepsilon\rho_{pcm}C_{p_{pcm}}T_{pcm})}{\partial t} + \nabla.\left(\rho_{pcm}C_{p_{pcm}}\vec{V}_{pcm}T_{pcm}\right) = \nabla.\left(k_{eff}\nabla T_{pcm}\right) - S_L - h_{sf}A_{sf}(T_{pcm} - T_{mf}) \tag{3.32}$$

For metal foam:

$$(1-\varepsilon)\rho_{mf}C_{p_{mf}}\left(\frac{\partial T_{mf}}{\partial t}\right) = \nabla.(k_{eff}\nabla T_{mf}) - h_{sf}A_{sf}(T_{pcm} - T_{mf}) \tag{3.33}$$

The source term in the energy equation is:

$$S_L = \frac{\partial\varepsilon\rho_{pcm}\lambda L}{\partial t} + \nabla.\left(\rho_{pcm}\vec{V}_{pcm}\lambda L\right) \tag{3.34}$$

As discussed in Chapter 2, the metal foam and PCM, together form a composite system, and hence effective thermal conductivity needs to be defined. For the thermal equilibrium model, average thermal conductivity can be calculated as:

$$k_{eff} = (1-\varepsilon)k_s + \varepsilon k_f \tag{3.35}$$

While, for the case of thermal non-equilibrium model, thermal conductivity needs to be defined independently. To get the ETC of the MF-PCM composite system, the volume averaging technique can be employed. A host of studies are available where the effective thermal conductivity has been defined for MFs for various infiltration cases such as air, water and PCM. Dai et al. [63] corrected and extended the original model of Boomsma and Poulikakos [61], and ETC and is defined as:

$$k_{eff} = \frac{L_A+L_B+L_C+L_D}{\sqrt{2}(R_A+R_B+R_C+R_D)} \tag{3.36}$$

where

$$R_A = \frac{4\Theta L_t}{(2e^2+\pi\Theta(1-e))k_s+(4-2e^2-\pi\Theta(1-e))k_f} \tag{3.37a}$$

$$R_B = \frac{(e-2\Theta)\,L_t}{e^2k_s+(2-e^2)k_f} \tag{3.37b}$$

$$R_C = \frac{(\sqrt{2}-2e)L_t}{\sqrt{2}\pi\Theta^2k_s+(2-\sqrt{2}\pi\Theta^2)k_f} \tag{3.37c}$$

$$R_D = \frac{2eL_t}{e^2k_s+(4-e^2)k_f} \tag{3.37d}$$

$$\Theta = \sqrt{\frac{\sqrt{2}\left(2-\left(\frac{3\sqrt{2}}{4}\right)e^3-2\varepsilon\right)}{\pi(3-4\sqrt{2}e-e)}}, \text{with } e = 0.198 \tag{3.37e}$$

$$k_{fe} = k_e|k_{s_{=0}}\,,\; k_{se} = k_e|k_{f_{=0}} \tag{3.37f}$$

Here L_t is the total layer thickness. The Reynold number and the specific area is defined as the function of the porosity of the MFs:

$$R_{e_d} = \frac{\rho_{pcm}\sqrt{u^2+v^2}d_l}{\varepsilon\mu_{pcm}} \tag{3.38}$$

$$A_{s_f} = \frac{3\pi d_l(1-e^{-(1-e)/0.004})}{0.59{d_p}^2} \tag{3.39}$$

To establish heat transfer between MF and PCM, local heat transfer coefficient is defined considering laminar flow conditions over solid cylinders. The coefficient for interstitial heat transfer is [112, 114-117] [119]

$$h_{sf} = \begin{cases} \frac{0.76 {R_{e_d}}^{0.4} Pr^{0.37} k_{pcm}}{d_l} \text{ for } 0 < R_{e_d} \leq 40 \\ \frac{0.52 {R_{e_d}}^{0.5} Pr^{0.37} k_{pcm}}{d_l} \text{ for } 40 < R_{e_d} \leq 1000 \\ \frac{0.26 {R_{e_d}}^{0.4} Pr^{0.37} k_{pcm}}{d_l} \text{ for } 1000 < R_{e_d} \leq 200000 \end{cases} \quad (3.40)$$

Boundary Conditions

The boundary conditions for the system are set at an ambient temperature at 27 °C. The initial temperature of the system is uniform and equal to the ambient temperature. The specific boundary conditions across different interfaces are defined as follows [89, 91]:

- Between contact interface of battery and PCM:

$$-k_b \frac{\partial T}{\partial n} = -k_{pcm} \frac{\partial T}{\partial n} \quad (3.41)$$

These equations ensure continuity of heat flux across the interface.

- Boundary conditions at the battery, tabs and PCM exposed to the ambient environment:

$$-k_b \frac{\partial T}{\partial n} = h_b (T_b - T_{amb}) \quad (3.42)$$

$$-k_{tabs} \frac{\partial T}{\partial n} = h_{tabs} (T_{tabs} - T_{amb}) \quad (3.43)$$

$$-k_{pcm} \frac{\partial T}{\partial n} = h_{pcm} (T_{pcm} - T_{amb}) \quad (3.44)$$

where $\frac{\partial T}{\partial n}$ is the temperature gradient and heat transfer coefficient to the ambient environment $h_{surface}$ is taken as 5 W/(m^2.K) [93], [120].

Material selection, grid sensitivity and parameters

For this investigation, the phase change material PCM RT-35, with a peak melting temperature of 35 °C, high latent heat of fusion (160 kJ/kg)

and excellent thermal stability making it ideal for battery thermal management. Its melting temperature aligns with the optimum operating temperature range of lithium-ion batteries, ensuring effective thermal regulation and heat absorption during phase change. Additionally, RT-35 is non-toxic, has a long thermal cycle life, easily available and therefore has been recommended in many literatures [121-124] for battery thermal management systems. The material for positive tab and the negative tab is aluminium and copper, respectively.

It is required to get optimum grid size and time step to carry out the numerical study. For this, the grid and time tests for a LIB (2S1P) coupled with PCM are carried out for a discharge rate of 5C. The average temperature for the discharge of cells is analysed. Initially, the mesh with four different element sizes namely 2.5 mm, 2 mm, 1.6 mm and 1 mm having 77988, 106920, 587385 and 876388 elements, respectively are investigated for a time step (Δt) of 1 second. The deviation in the results is found to be less than 1% when the grid size is reduced to 1.6 mm from 2 mm; however, further reduction in the element size beyond 1.6 mm, no significant change in the results is observed in the analysis, with the significant increase in the computational time. Following this, two additional time steps of 2 second and 0.5 second are tested with the element size of 1.6 mm. Considering the reference conditions as an element size of 1.6 mm having 587385 elements and a time step of 0.5 seconds, it is found that the average deviation is 0.09% for time step of 2 second and 0.012% for 1 second. It should be noted that further refinement of the time step increases the computational time without any reasonable change in the results. Therefore, an element size of 1.6 mm and a time step of 1 second are selected for the present study.

To carry out the simulations, a pressure-based double precision solver was used with absolute velocity formulations to ensure accurate modeling of fluid flow. The transient time simulations were conducted to capture the dynamic behaviours of the system. Semi-Implicit Method

for Pressure-Linked Equations (SIMPLE) algorithm was employed to discretize the governing equations. The Pressure Staggering Option (PRESTO) and Quadratic Upstream Interpolation for Convective Kinetics (QUICK) schemes were implemented to solve momentum and energy equations, respectively. The following values of under-relaxation parameters were set to ensure numerical stability and convergence: pressure - 0.3, density - 0.5, body force - 0.5, momentum - 0.5, energy - 0.9, and scalars - 0.9. Convergence thresholds for continuity, momentum, and energy equations were set at 10^{-8}, 10^{-10}, and 10^{-10}, respectively. Each time step involved up to 500 iterations to achieve convergence, and the simulations were performed on ANSYS Fluent 2023R2 software using the high-performance computing (HPC) resources provided by the Digital Research Alliance of Canada (Compute Canada). Table 3.2.2 lists the material properties of the lithium-ion battery cell components, while Table 3.2.3 summarizes the thermophysical properties of the MF and PCM.

Table 3.2.2: Material properties of the Li-ion battery [103-104]

Details	Active material	Positive Tab (Aluminium)	Negative Tab (Copper)
Density [kg/m^3]	2092	2719	8978
Thermal conductivity [W/m-K]	0.97 (in-plane) 26.5 (cross-plane)	202.4	387.6
Specific heat [J/kg-K]	678	871	381
Electrical conductivity (σ_+) [S/m]	1190000	-	-
Electrical conductivity (σ_-) [S/m]	983000	-	-

Table 3.2.3: Thermophysical properties of the MF and PCM [112], [115]

Property	Metal foam	PCM (RT-35)
Material	Copper	Paraffin wax
Density (solid) [kg/m^3]	8978	860 (l), 770 (s)
Thermal conductivity [W/(m·K)]	380	0.2
Solidus temperature [K]	-	302
Liquidus temperature [K]	-	309
Specific heat [kJ/(kg·K)]	0.381	2
Latent heat [kJ/kg]	-	160
Thermal expansion coefficient [1/K]	-	0.0001
Viscosity [Pa.s]	-	0.0235

3.2.2 Validation of the numerical model

Validation of the cell model

The Li-ion batteries consist of several layers of negative, positive, and separator sheets; the overall cell properties can be calculated by taking the average properties of individual constituents. Because of stacked configuration of battery core, one needs to consider the interfacial phenomena of contact resistance at different interfaces such as porous-porous and porous-solid for estimation of effective thermal conductivity values; while, because the contact interfaces of polymer LIBs are wet due to electrolyte liquid, its effects here can be disregarded. Also, the same order of the thermal conductivities of electrolytes and polymer justifies this simplification; similar approach has been adopted by many authors [103-104, 110]

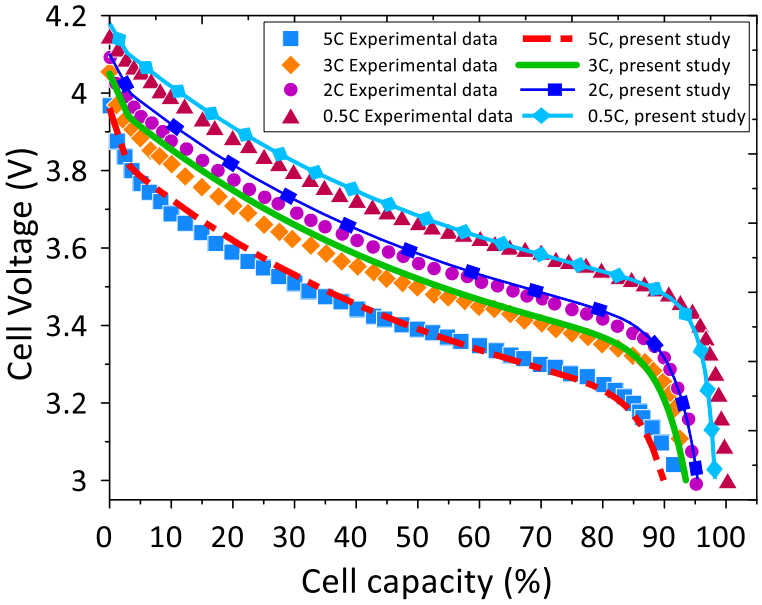

Figure 3.5: Comparison of battery voltage-time profile with the results of Taheri et al. [103]

The present cell model is validated using the experimental polarization test data of Taheri et al. [103] for various discharging rates, namely 5C, 3C, 2C and 0.5C. The average deviation between present simulations and the test data is found to be 5% and is depicted in Fig. 3.5. The temperature of the battery is validated using the existing experimental data of Fink et al. [125] and Liu et al. [126] as can be seen in Figs. 3.6(a-b), respectively. Fink et al. [125] and Liu et al. [126] have considered ePLB-C020, 20Ah battery cell in their experimental study and the same battery cell has been considered in the present investigation. Fink et al. [125] conducted experiments with the battery cell to compare two different battery models in their investigation. Fig. 3.6(a) depicts the temperature rise of the cell with respect to the various depths of discharge for two different discharge rates i.e., 5C and 3C. The battery cell was discharged to about 70% for 5C and 85% for 4C, while maintaining the cutoff conditions of 3V. Similarly, Fig. 3.6(b) presents the results from Liu et al. [126] for the temperature rise for different discharge time for 4C, 3C and 2C. It can be seen that the prediction of the current battery model matches well with the experimental test data.

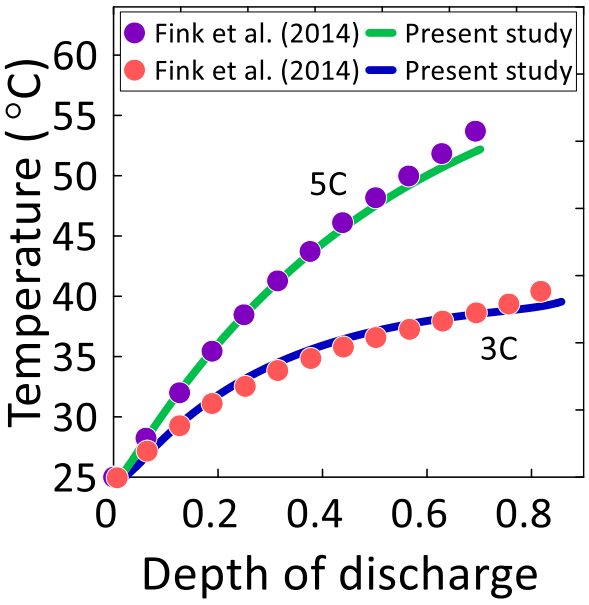

(a) Comparision with the results of Fink et al. [125]

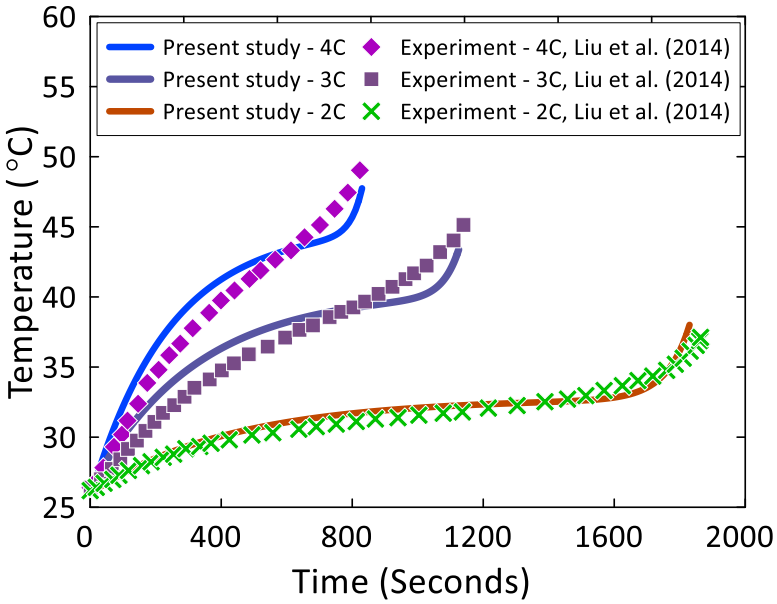

(b) Comparision with the results of Liu et al. [126]

Figure 3.6: Validation of the cell temperature

The observed average absolute deviation with the test data of Fink et al. [125] is found to be 2.49% and 1.9% for 5C and 4C, respectively. The observed average absolute deviation with the test data of Liu et al. [126] is found to be 4.2%, 3.9% and 1.8% for 4C, 3C, and 2C, respectively. The results suggest that the current numerical model aligns closely with the experimental results, demonstrating its accuracy in predicting temperatures under various discharging conditions.

Verification and validation of the MF-PCM model

The aim of the current study is to investigate the effectiveness of the PCM embedded with MF by using 3D geometrical model. In the present study, the model for melting of PCM embedded with metal foams is verified with the numerical investigation of Sardari et al. [112] and validated with the experimental study of Zhao et al. [127]. Sardari et al. [112] investigated a 3D model of a vertical container (15×2.5×2.5cm) having PCM (RT-35) embedded with copper MF of varying porosities (ε = 0.85, 0.9, 0.95) and pore densities (PPI = 10, 30, 50). A constant wall temperature of 373 K was applied at one face (heater wall), while the two side walls were treated with symmetry boundary conditions. The initial temperature of the geometry is set to 292K. The mushy zone constant A_m is chosen based on the sensitivity analysis to yield less than 0.5% deviation in melting time while comparing with the experimental results, resulting in a value of 10^5, consistent with the prior recommendations.

The authors [112] studied the effect of porosity, pore densities, equilibrium and non-equilibrium porous media models, multiple-segment cascaded metal foam and the effect of different heater location. The results are reproduced and verified to ensure the conformity of the present numerical model. The results are presented in Fig. 3.7 and Fig.3.8. The verified 3D model of the PCM embedded with the copper metal foam was then used to validate with the experimental results for Zhao et al. [127]. Zhao et al. [127] investigated the solidification and melting performance of PCM RT-58 saturated with copper metal foam (porosity = 0.95, PPI = 10). The rectangular copper foam having the dimensions of 200×120×25 mm and thermal conductivity of 350 W/m·K has been used. A heat flux of 1.6 kW/m^2 is supplied on the bottom side of the cavity with the help of a copper plate to maintain uniform heat flux conditions.

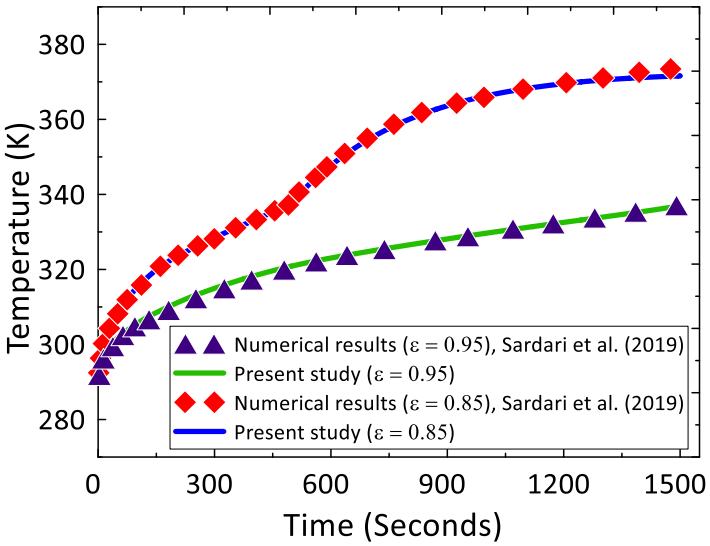

Figure 3.7: Validation of PCM domain temperature against Sardari et al. [112]

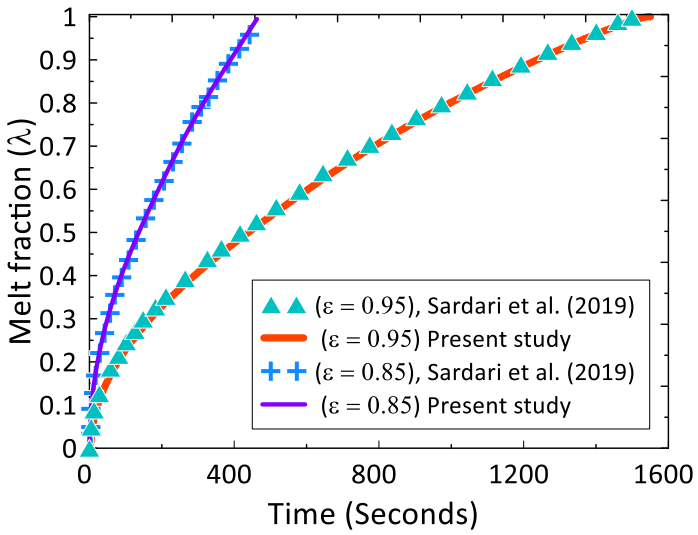

Figure 3.8: Analysis of melting of PCM with the study of Sardari et al. [112]

The temperature of the heater plate wall and at three different locations having a vertical distance of 8 mm, 16 mm, and 20 mm from the heater plate have been used for analysis. The present MF-PCM model is validated with the test data of Zhao et al. [127] by employing both thermal equilibrium and thermal non-equilibrium models and is shown in Fig. 3.9. The equilibrium model over predicts the test data both in the pre-melting and post-melting zones; while the non-equilibrium model under predicts the test data in the pre-melting region and over predicts the post melting region.

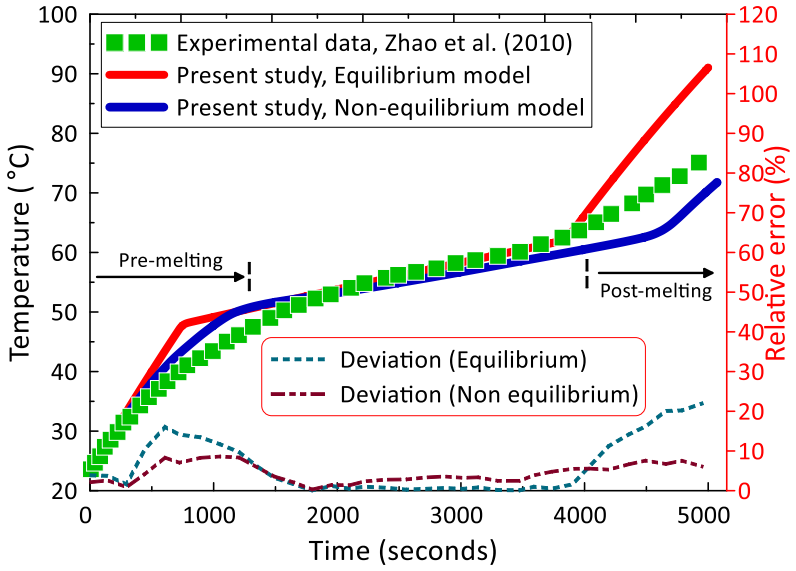

Figure 3.9: Validation of MF-PCM melting with the test data of Zhao et al. [127]

The average deviation is found to be 4.52% and 8.56% for non-thermal equilibrium and thermal equilibrium, respectively. The thermal non-equilibrium model was selected to carry out the simulation in the present study.

3.2.3 Result and discussion

Here, an effort has been made to examine the performance of the MF-PCM composite for thermal management of LIBs under rapid discharging and thermal abuse conditions. Rapid discharge of the cells occurs over a short duration, especially during acceleration of the EV; therefore, in situations where thermal control is critical, it is important to test the appropriate BTMS. Fig. 3.10 illustrates the configuration of battery pack for present study. This study simulates two different high discharge rates: "5C" and "4C". The expected discharge times for these rates are 12 minutes and 15 minutes, respectively. Initially, the 2S1P battery pack is studied and the minimum thickness of the PCM is determined; subsequently, the effect of various foam characteristics affecting the thermal performance are examined. The external, internal short circuit and profile tests are performed to examine the performance of MF-composite for abusive thermal conditions. Later, a 7S1P battery pack is simulated for rapid discharging at 5C.

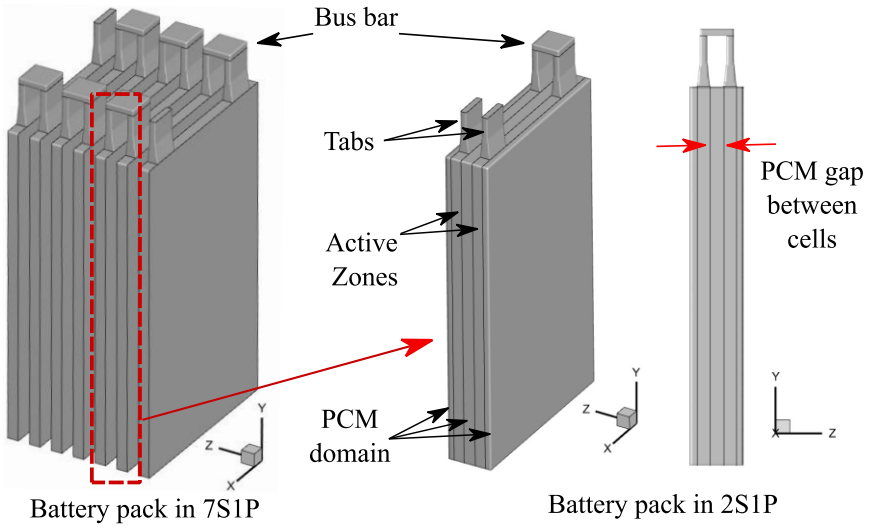

Figure 3.10: Schematic of the battery pack under investigation

Minimum thickness of the PCM

It is essential to determine the minimum thickness for the MF-PCM composite to achieve the desired temperature. Using a 2S1P configuration, rapid discharge rates of 5C and 4C are simulated with a discharge cutoff voltage value of 2.5 V and an initial temperature of 300 K under natural convection cooling condition (Fig.3.11(a-b)).

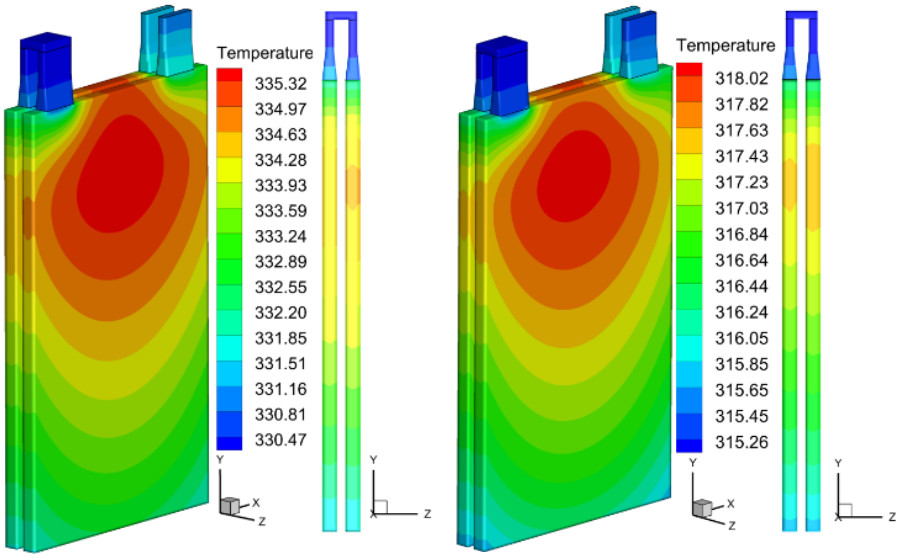

(a) Discharge rate 5C (b) Discharge rate 4C

Figure 3.11: Temperature distribution after complete discharge

The rise in temperature is significant in the cells; while lower temperature is obtained in tabs, which may be due to the more thermal conductivity of aluminium that is used in tabs. Tabs are employed in

prismatic Li-ion batteries to gather the current flow produced throughout the cell domain. Under natural convection cooling, temperature of the cells after complete discharge is found to be 334 K and 319 K for 5C and 4C, respectively. It may be noted that due to the accelerated reaction rate, more amount of heat is generated at 5C within shorter time period compared to 4C; therefore, the discharge rate of 5C is used to optimize the thickness of the PCM. Various PCM thickness values (4 mm–12 mm) are considered to determine the most suitable thickness.

Figure 3.12 reports the average temperature of cell after the complete discharge with only PCM. The average cell temperature is found to be 326.8 K, 316.36 K, 315.04 K, 314.97 K, and 314.82 K for the PCM thickness of 4, 6, 8, 10, and 12 mm, respectively. The average cell temperature is found to increase sharply towards the end of the discharge process; the rise in the temperature is associated with the depletion of the Li-ions in the carbon-based anode, which causes sudden decrease in the voltage (can be seen in Fig. 3.5). The abrupt voltage drop triggers additional irreversible heat generation from electrochemical reactions, further increasing the cell temperature.

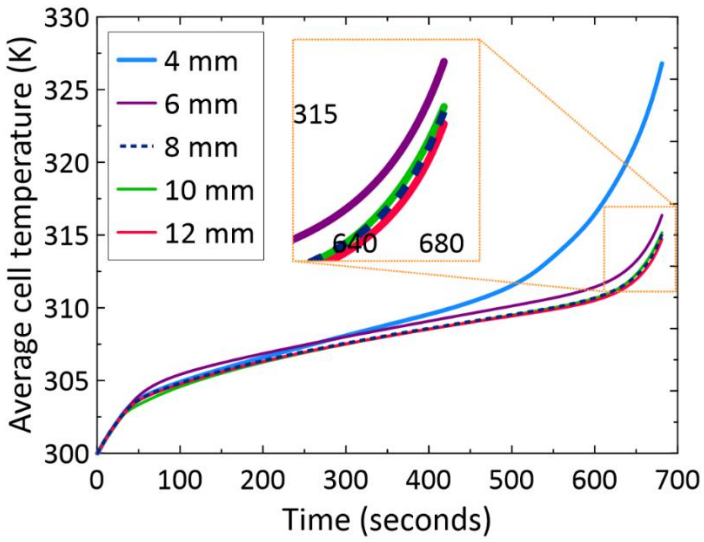

Figure 3.12: Effect of PCM thickness on average temperature

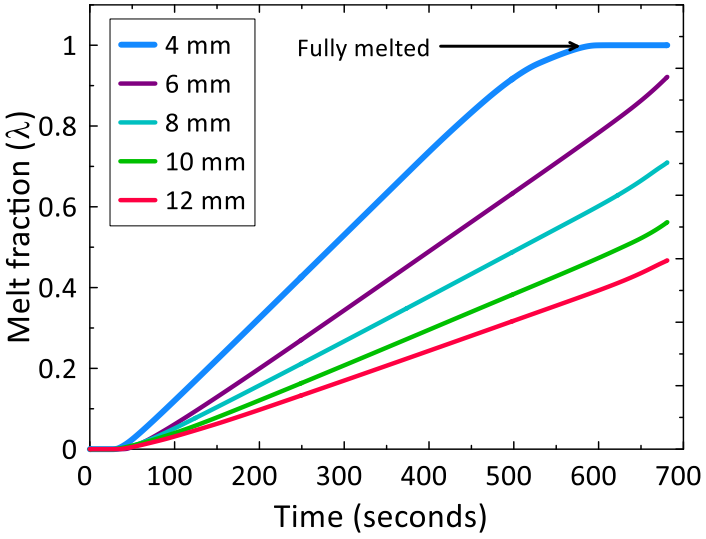

Figure 3.13: Effect of PCM thickness on melt fraction

The melt fraction in MF-PCM composite is found to be 100%, 92.1%, 69.7%, 56.18%, 46.71% for 4, 6, 8, 10 and 12 mm thickness, respectively, as reported in Fig. 3.13. The average cell temperature is found to decrease with the increase in the thickness, although the decrease in cell temperature is less significant with the increase in the thickness beyond 8 mm. It may be noted that with further increase in the PCM thickness, the energy density of the battery module will be reduced for a fixed space. Also, for the selected thickness of 8mm it can be seen from Fig. 3.13 that even after the battery is fully discharged, about 30% of the PCM remains solid (unmelted). Therefore, a PCM thickness of 8 mm is considered to carry out further investigations.

Rapid discharging of the battery pack by 5C and 4C

The MF is usually characterized by porosity, pore density (PPI) and thermal conductivity of the material. The porosity (ε) defines the amount of the void volume present in the defined volume and the PPI (pores per inch) defines the distribution of the pores for a fixed porosity. The effect of PPI on melting performance is not significant for lower thickness PCM, which may be due to the lower value of the Reynolds number of the liquid PCM that undergoes natural convection [112, 117]. Huang et al. [67] reported that for a fixed porosity, higher PPI reduces the mean

surface temperature. The authors recommended the value of the PPI as 30 for further investigation. In the present study, the PCM saturated in MF with varying porosities (ε = 0.80, 0.85, 0.90, 0.95 and 0.98) is analysed for a fixed PPI of 30. Fig. 3.14 illustrates average cell temperature after complete discharge by 5C. The average cell temperature after complete discharge is found to be 315.04 K, 314.09 K, 313.61 K, 313.17 K, 312.63 K, 312.96 K for pure PCM, MF-PCM (ε = 0.80), MF-PCM (ε = 0.85), MF-PCM (ε = 0.90), MF-PCM (ε = 0.95) and MF-PCM (ε = 0.98), respectively.

With increasing porosity (ε), the average temperature decreases up to ε = 0.95, beyond this value, the temperature tends to increase. For a lower value of ε, the MF-PCM composite exhibits higher average temperature; this may be due to the decrease in available PCM volume which lowers the heat absorption rate; nevertheless, MF provides more heat conduction path in the PCM domain. A similar observation was reported by [67], where the optimum performance of the MF embedded with PCM was obtained in the porosity range of 0.94-0.96. Fig. 3.15 depicts the peak temperature gradient in cell domain. During the discharge, the temperature gradient increases more sharply for pure PCM (PCM without MF).

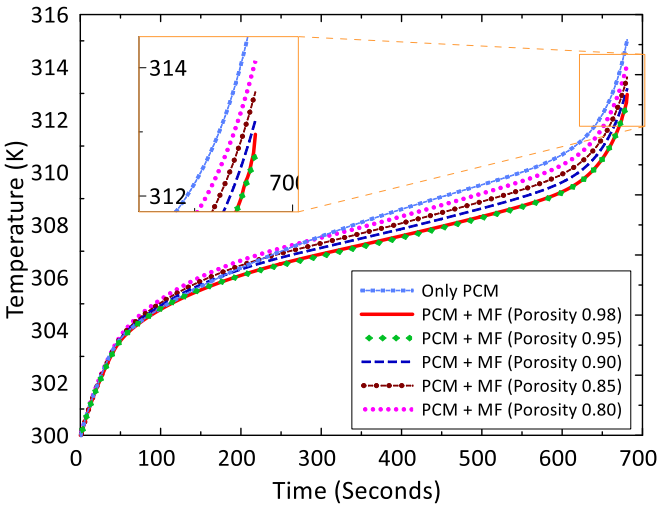

Figure 3.14: Effect of MF-PCM composite on the average cell temperature during 5C discharge

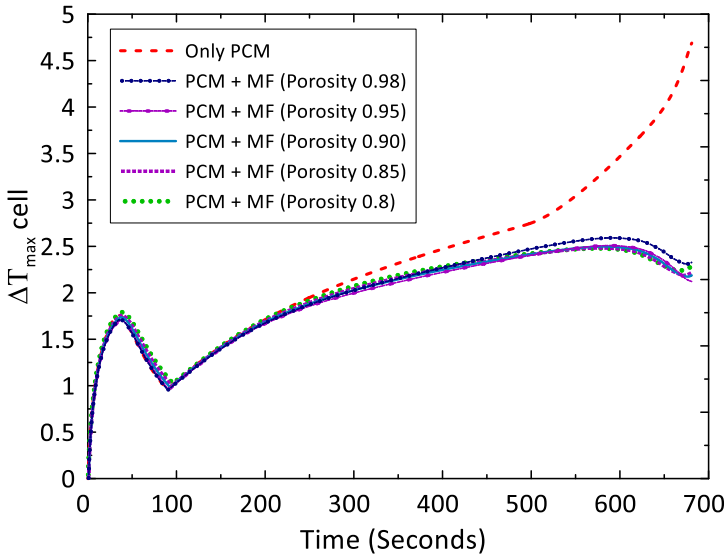

Figure 3.15: Effect of MF-PCM composite on the maximum temperature gradient during 5C discharge

This could be due to non-uniform melting of the PCM because of the delayed heat diffusion inside the domain due to the lower thermal conductivity of PCM [48]. In contrast, a uniform temperature gradient is obtained for MF-PCM composite; this may be due to the enhanced heat distribution inside the domain because of metal foam. Initially, the temperature gradient attains a peak value and subsequently decreases; this may be due to the delay in initiation of the melting of the PCM. This delay in the initiation of melting occurs due to enhancement in effective conduction in solid PCM that causes uniform temperature distribution. Another observation is the increase in the temperature gradient of the cell when only PCM (without MF) is used. During the rapid discharging, there is a higher and faster heat generation in the cell. The PCMs generally have low thermal conductivity and finite heat absorption rate, leading to slow spreading and diffusion of heat, causing localized heating and higher temperature gradients. To solve this problem, the highly conducting open cell porous metallic foams is added with PCM. The metallic ligaments in the metal foams provide an excellent thermal conducting path for the propagation and uniform spreading of heat.

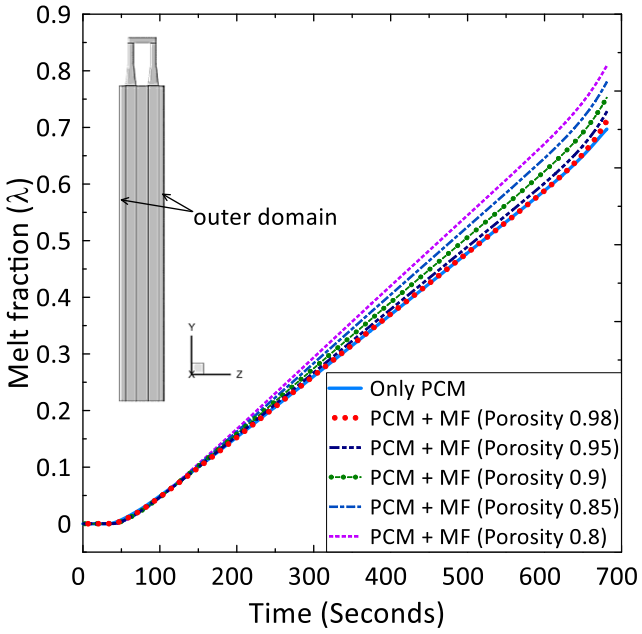

Figure 3.16: Analysis of melt fraction in the outer domain of PCM for 5C discharge rate

The addition of metallic foams increases the effective thermal conductivity of PCM, thereby increasing the heat diffusion and heat spreading rate in the PCM. As can be seen from the results, the rate of increase of maximum temperature gradient is decreased with PCM-MF composite compared to PCM alone. Figs. 3.16 and 3.17 depicts the melting performance of the PCM in the outer and center domain of LIB cells. The melting in the outer domain of the cells is presented in Fig. 3.16; the rate of melting of PCM is more for a lower value of porosity. The melting in outer domain is found to be 69.7%, 80.91%, 78.02%, 75.29%, 72.78%, 71.18% for pure PCM and MF-PCM with ε = 0.80, 0.85, 0.90, 0.95 and 0.98, respectively. For center domain (Fig. 3.17), the melt fraction is found to be 70.12% 85.5% 82.48%, 79.53%, 76.95%, 75.02% for pure PCM and MF-PCM with ε = 0.80, 0.85, 0.90, 0.95 and 0.98, respectively. With a reduction in ε, the effective conduction ratio increases while free convection decreases; this indicates that at lower value of ε, the available PCM is reduced, and rate of heat distribution is higher.

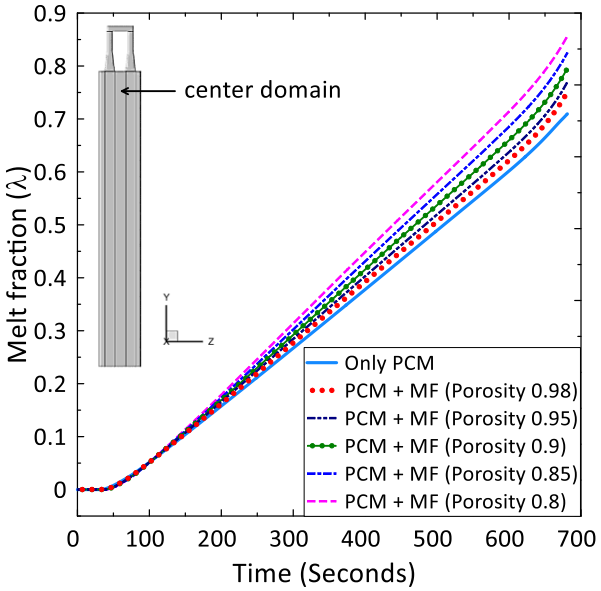

Figure 3.17: Analysis of melt fraction in the center domain of PCM for 5C discharge rate

Figs. 3.18(a-f) represent the temperature contours in the cell domain and MF-PCM domain during complete discharge of the cell by 5C. The first part of the figure depicts both the domains (cell and PCM), and the second part depicts the cell domain. For all cases, the peak temperature exists near the tab zone, the temperature gradually decreases in the bottom half of the LIB pack and the temperature gradient in the cell domain is found to remain below 5K. The melt contours of PCM during complete discharge of the cells are also presented in Fig. 3.19(a-f) for better visualization of the melting phenomena. The average cell temperature, the maximum temperature gradient, and the melt fractions for the discharge rate of 4C are investigated for various combinations of MF-PCM, considering a fixed gap of 8 mm between the cells, as shown in Figs. 3.20-3.23. For 4C discharge rate, a similar trend is observed as in case of 5C; the PCM effectively controls the cell temperature and average temperature of cell remains below 312 K. The best performance is observed in the case of MF-PCM ($\varepsilon = 0.95$). The peak temperature gradient remains in the optimum range, as can be seen in Fig. 3.21. The melting of the PCM is tracked for the outer and the center domain as can be seen in Fig. 3.22 and Fig. 3.23.

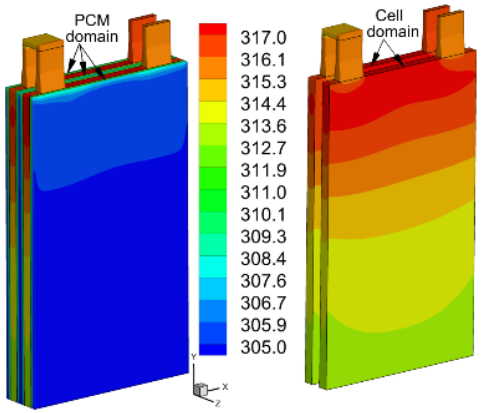

(a) Only PCM

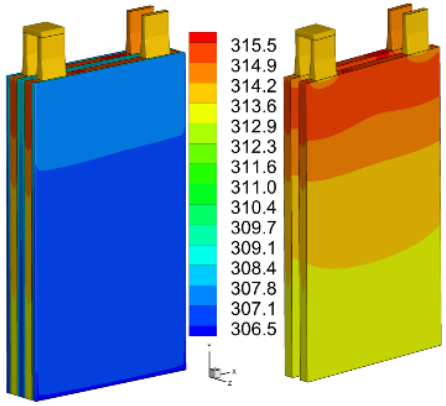

(b) MF-PCM (ε = 0.80)

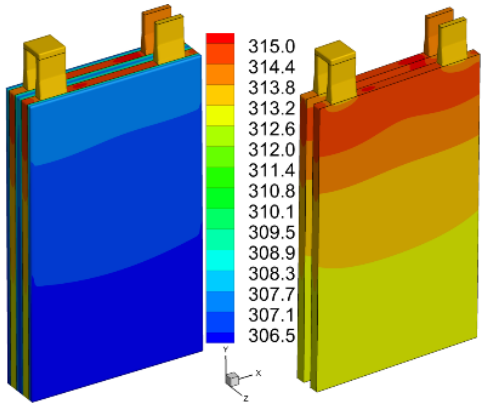

(c) MF-PCM (ε = 0.85)

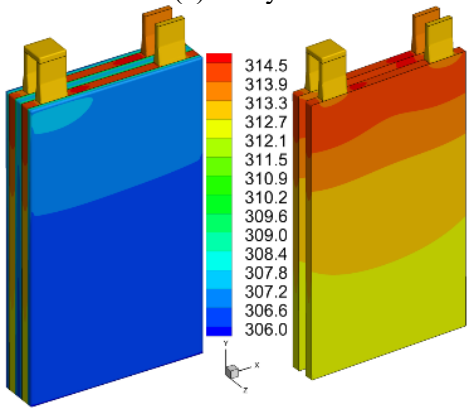

(d) MF-PCM (ε = 0.90)

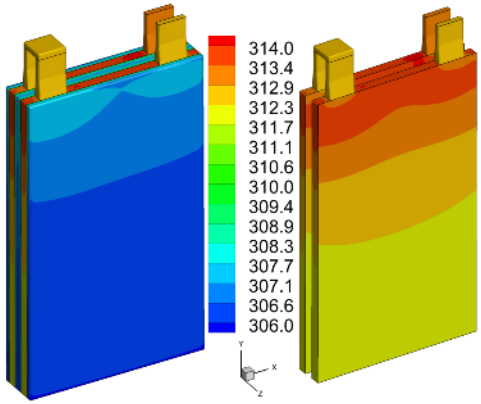

(e) MF-PCM (ε = 0.95)

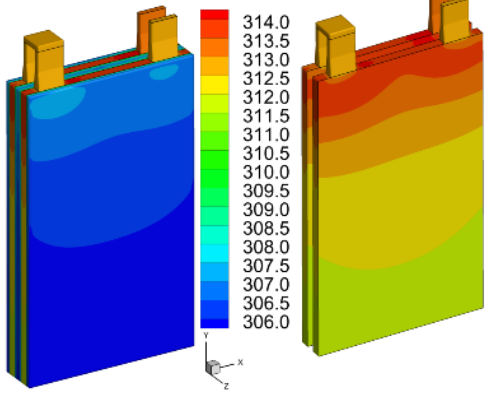

(f) MF-PCM (ε = 0.98)

Figure 3.18: Temperature (K) contours at the complete discharge of the cell by 5C

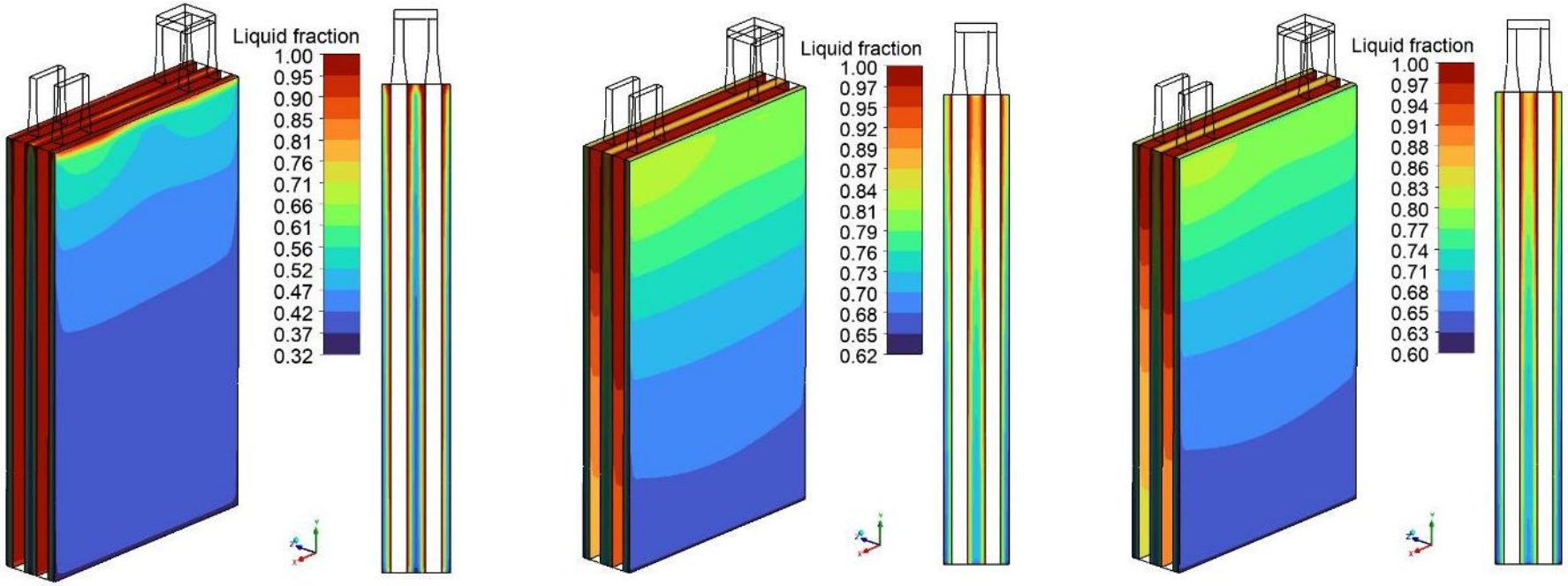

(a) Only PCM (b) MF-PCM (ε = 0.80) (c) MF-PCM (ε = 0.85)

Figure 3.19 (a-c): Melt contours after the complete discharge of the cell by 5C

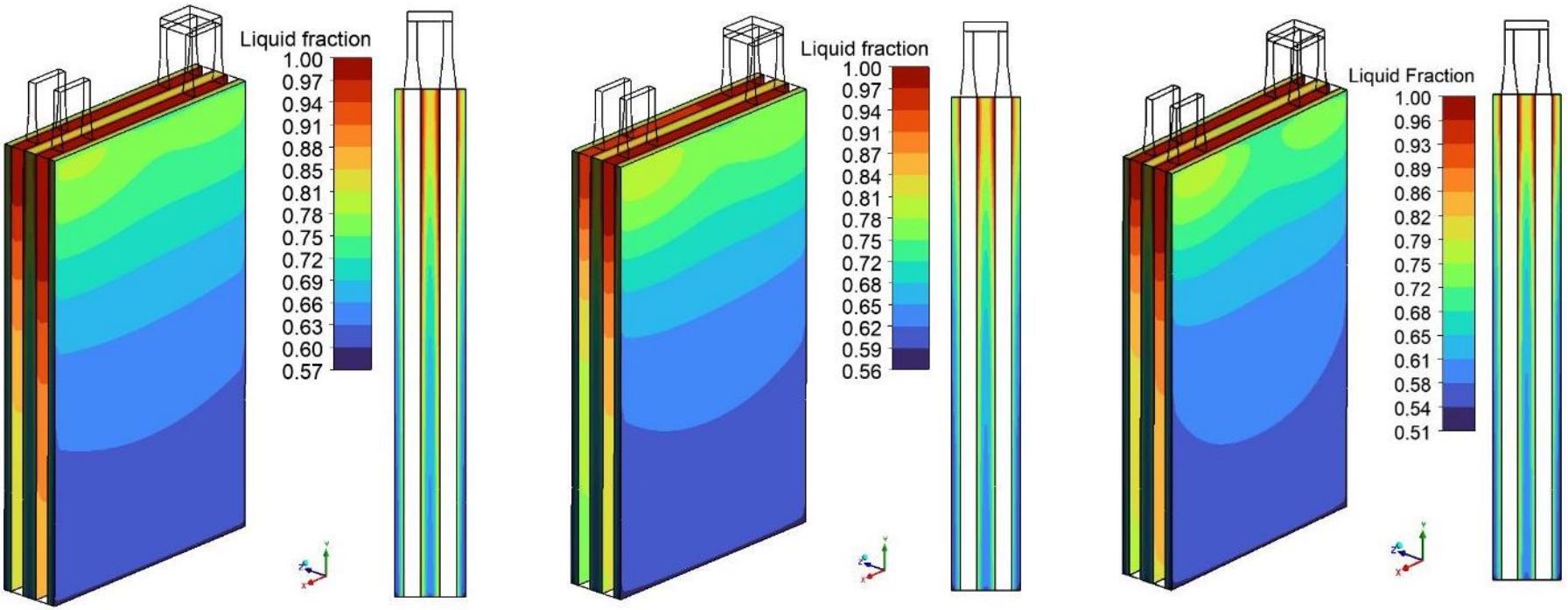

(d) MF-PCM (ε = 0.90) (e) MF-PCM (ε = 0.95) (f) MF-PCM (ε = 0.98)

Figure 3.19 (d-f): Melt contours after the complete discharge of the cell by 5C

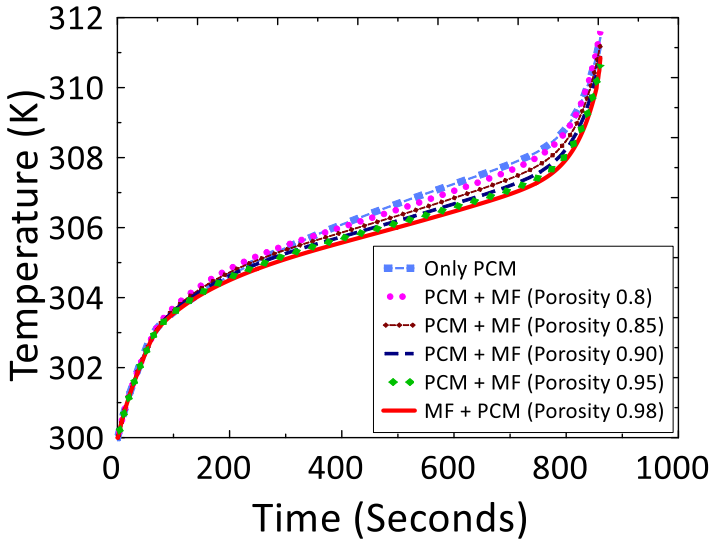

Figure 3.20: Average cell temperature using MF-PCM composite at 4C discharge rate

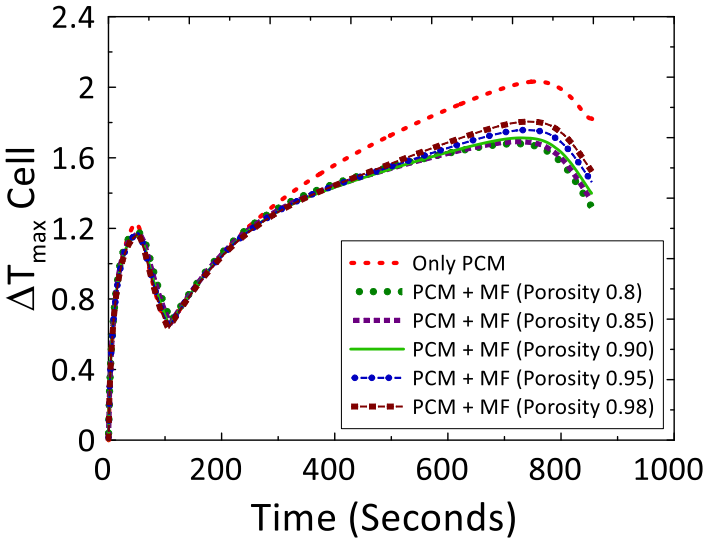

Figure 3.21: Maximum temperature gradient during 4C discharge rate

From Figs. 3.22 and 3.23, the melting in outer domain is 58.17%, 65.28%, 62.88%, 60.68%, 58.56%, 57.41%, while in center domain it is 60.0% 69.71% 67.07%, 64.62%, 62.29%, 60.99%, respectively for only PCM and MF-PCM with ε = 0.80, 0.85, 0.90, 0.95 and 0.98.

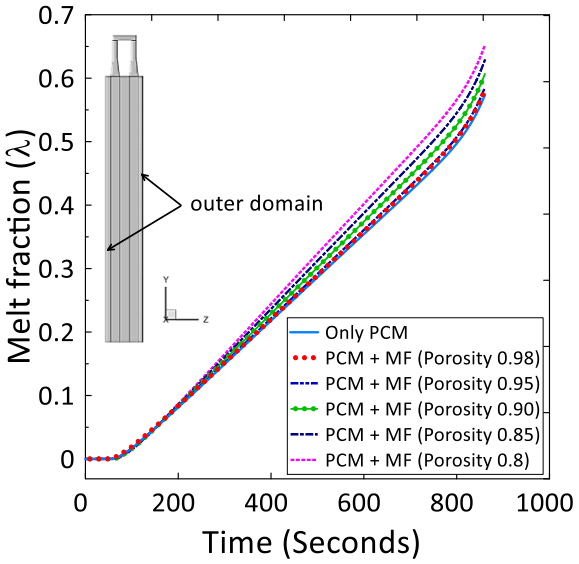

Figure 3.22: Melting in the outer domain of the PCM

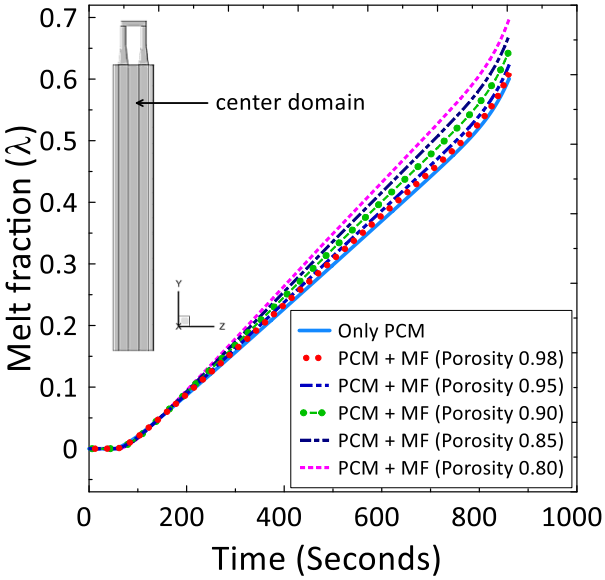

Figure 3.23: Melting in the center domain of the PCM

Fig. 3.24 (a-f) shows the temperature contours after the complete discharge of the cell for all the cases. Fig. 3.25 (a-f) illustrates the contours for the melting of the PCM for each case at the end of discharge of the cell.

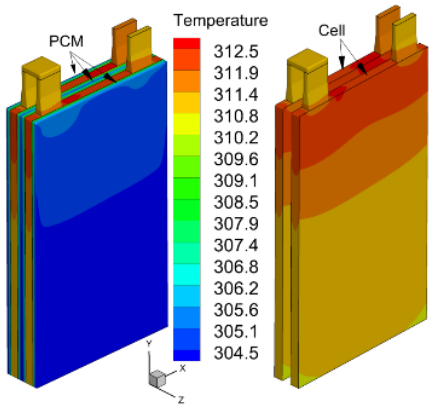

(a) Only PCM

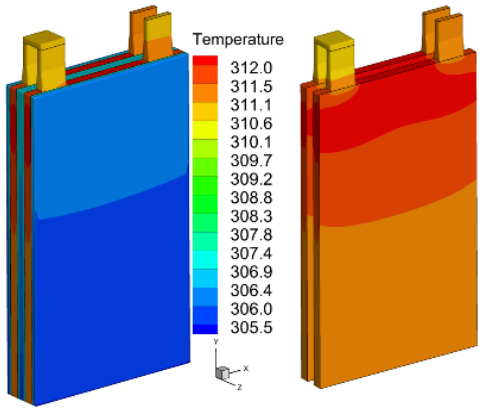

(b) MF-PCM (ε = 0.80)

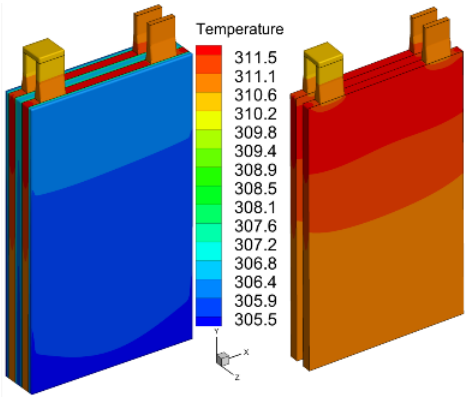

(c) MF-PCM (Ɛ = 0.85)

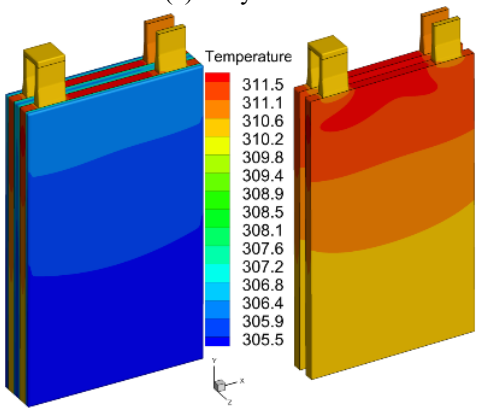

(d) MF-PCM (Ɛ = 0.90)

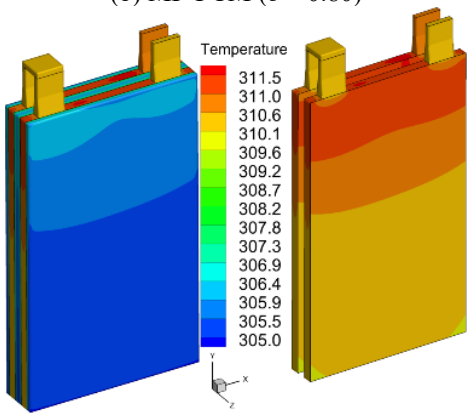

(e) MF-PCM (Ɛ = 0.95)

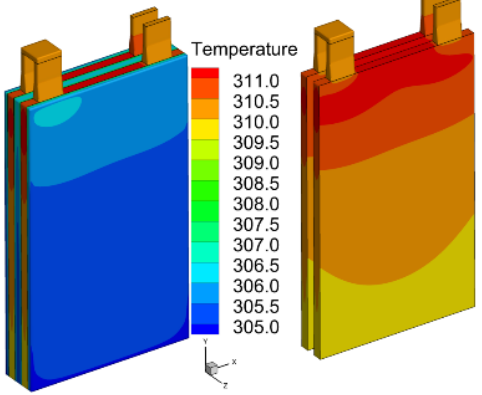

(f) MF-PCM (Ɛ = 0.98)

Figure 3.24: Temperature (K) after discharging the cells by 4C

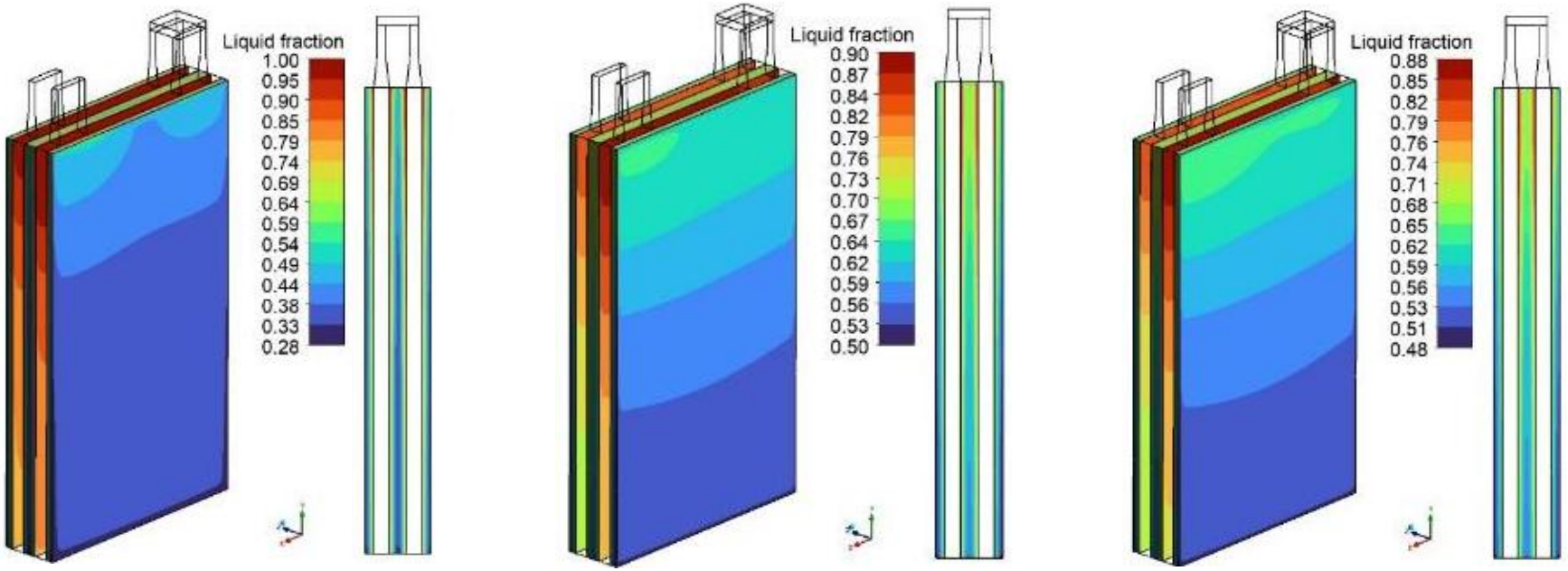

(a) Only PCM (b) PCM with MF (ε = 0.80) (c) PCM with MF (ε = 0.85)

Figure 3.25 (a-c): Melt contours after discharging the cells by 4C

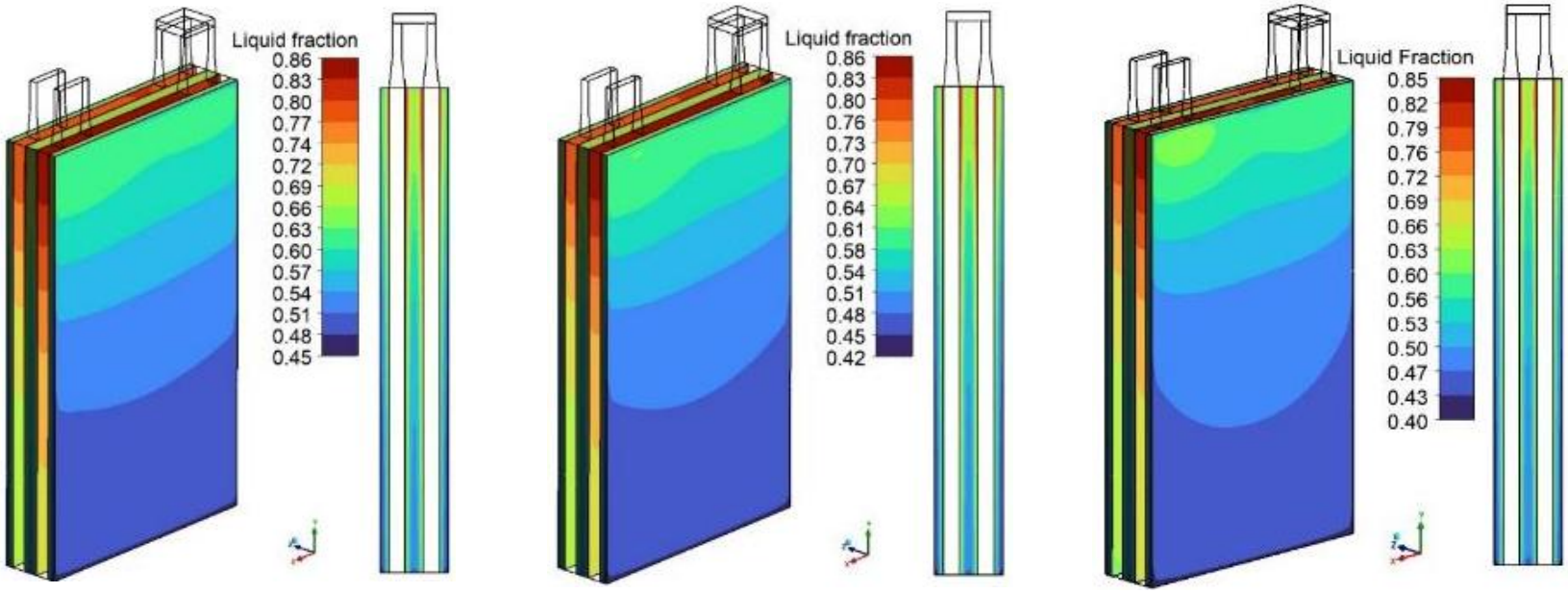

(d) PCM with MF (ε = 0.90) (e) PCM with MF (ε = 0.95) (f) PCM with MF (ε = 0.98)

Figure 3.25 (d-f): Melt contours after discharging the cells by 4C

Comparison of results for discharge rate of 4C and 5C

Figures 3.26 (a-d) depicts the comparative performance of MF-PCM (ε = 0.95) module for different discharge rates (5C and 4C). The average temperature rise at 5C and 4C discharge rates under different conditions such as natural convection, only PCM and MF–PCM (ε = 0.95) is shown in Figs. 3.26(a–b). The corresponding maximum temperature gradients are shown in Figs. 3.26(c–d).

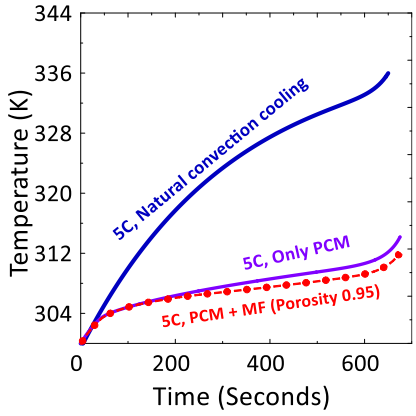

(a) Average cell temperature: 5C

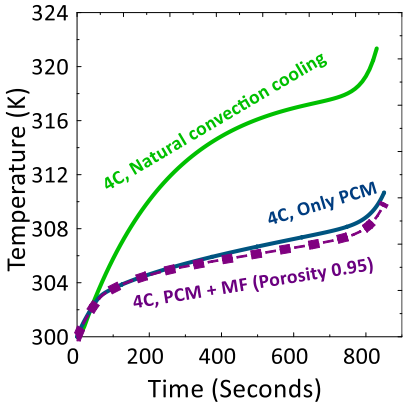

(b) Average cell temperature: 4C

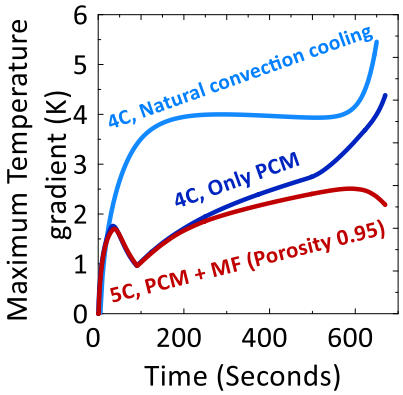

(c) Maximum temperature gradient at 5C

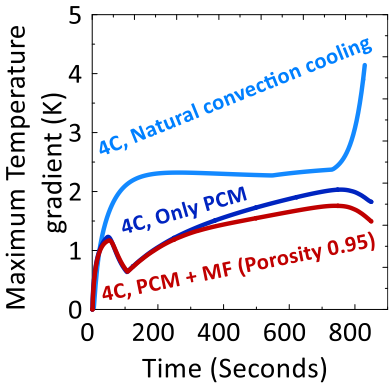

(d) Maximum temperature gradient at 4C

Figure 3.26: Comparative performance for 5C and 4C

A sharp temperature gradient is observed at the end of the discharge process, likely due to the sudden voltage drop. However, the MF-PCM composite effectively suppresses this maximum temperature gradient. Li et al. [104] used an active system consisting of a mini channel liquid cooled plate for thermal management of the EIG-ePLB C020 cell. The

comparative results for the current investigation and with the study of Li et al. [104] for a discharge rate of 5C are depicted in Fig. 3.27.

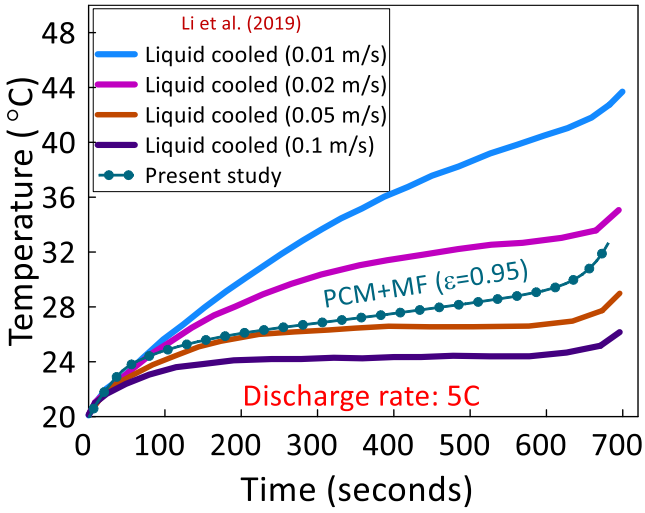

Figure 3.27: Comparison of performance of MF-PCM composite with active cooling system

It can be seen that the current MF-PCM configuration outperforms the active system at coolant velocities of 0.01 m/s and 0.02 m/s. However, for higher coolant velocities, the cold plate maintains a lower temperature in the cell. In the current configuration, a PCM thickness of 8 mm with MF (ε = 0.95) provides the best performance for rapid discharge conditions. The percentage reduction in the cell temperature can be calculated as:

$$\text{Temperature reduction (\%)} = \left|\frac{\Delta T_{\text{with TMS}} - \Delta T_{\text{without TMS}}}{\Delta T_{\text{without TMS}}}\right| \quad (3.45)$$

Here, $\Delta T_{with\,TMS}$ and $\Delta T_{without\,TMS}$ denote the temperature rise in the LIB with PCM/MF-PCM and natural convection, respectively. Table 3.2.4 summarizes the cooling performance of the applied phase change composites.

Table 3.2.4: Thermal performance of 2S1P configuration with natural convection, PCM and MF-PCM composite

Cases → Parameters ↓	No cooling		Only PCM		MF-PCM (ε = 0.98)		MF-PCM (ε = 0.95)		MF-PCM (ε = 0.90)		MF-PCM (ε = 0.85)		MF-PCM (ε = 0.80)	
	5C	4C	5C	4C	5C	4C	5C	4C	5C	4C	5C	4C	5C	4C
Average Temperature (after complete discharge) (K)	334.09	319	315.04	311.72	312.96	310.88	312.63	310.65	313.17	310.89	313.61	311.22	314.09	311.59
Reduction in temperature (%)	-	-	55.94	38.31	61.98	42.73	62.95	43.94	61.36	42.68	60.06	40.94	58.66	39
Maximum cell temperature (K)	335.60	319.97	317.79	312.62	314.47	311.64	314.02	311.53	314.60	311.72	315.06	312.02	315.56	312.37
Minimum cell temperature (K)	330.15	315.82	313.10	310.75	311.94	309.96	311.90	310.09	312.41	310.30	312.83	310.54	313.27	310.82
Maximum temperature gradient (K)	5.45	4.14	4.68	2.03	2.64	1.8	2.50	1.75	2.49	1.71	2.48	1.69	2.47	1.67
Average temperature gradient (K)	3.74	2.26	2.32	1.51	1.99	1.38	1.95	1.37	1.96	1.35	1.97	1.35	1.99	1.35
Average melt fraction of PCM (both the domains)	-	-	0.70	0.59	0.74	0.60	0.76	0.61	0.78	0.62	0.81	0.66	0.84	0.68

3.2.4 Short circuit and profile test

BTMS performance must be assessed under harsh thermal loading conditions like short circuit and profile tests. Though uncommon under normal operation, including them in the design phase can help prevent potential failures. In this section, the external, internal short circuit and the profile tests are simulated using the MF-PCM composite (ε = 0.95).

External short circuit test

In the external shorting conditions, the battery is simulated involving external shorting resistances (ESR) with no electric load condition. Fig. 3.28(a) depicts the temperature response of the battery with various values of ESR (0.002 Ω, 0.003 Ω, and 0.004 Ω). The resistance load connected to cell can be defined as [108]:

$$R_{load} = \frac{V_{tab}}{I_{tab}} \tag{3.46}$$

The stopping condition is set at 2.5 V; this value is used to the cut off simulation process. For a lower shorting resistance, current through the battery is higher and results in higher heat generation in the LIBs. The average temperatures for ESR values of 0.002 Ω, 0.003 Ω and 0.004 Ω are 367 K, 343 K and 329 K, respectively. The temperature above 360 K can be defined as the risky zone for the possible initiation of the thermal runaway issues in the cells. The sharp temperature rise for ESR = 0.002 Ω is likely due to insufficient PCM availability for effective heat absorption. This is evident from the melt front evolution over time for different ESR values (Fig. 3.28 (b)); for ESR = 0.002 Ω, the temperature increase is more pronounced, and the PCM completely melts by t=140 s. Figures 3.29(a-d) depicts the temperature and melt contours for the cell domain and PCM domain for ESR=0.002 Ω at two different time steps such as before the completion melting of PCM and at the end of shorting condition.

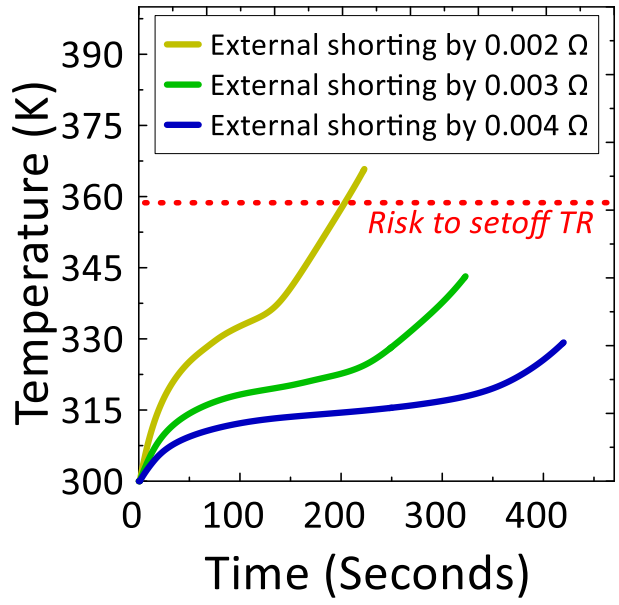

(a) Temperature rise

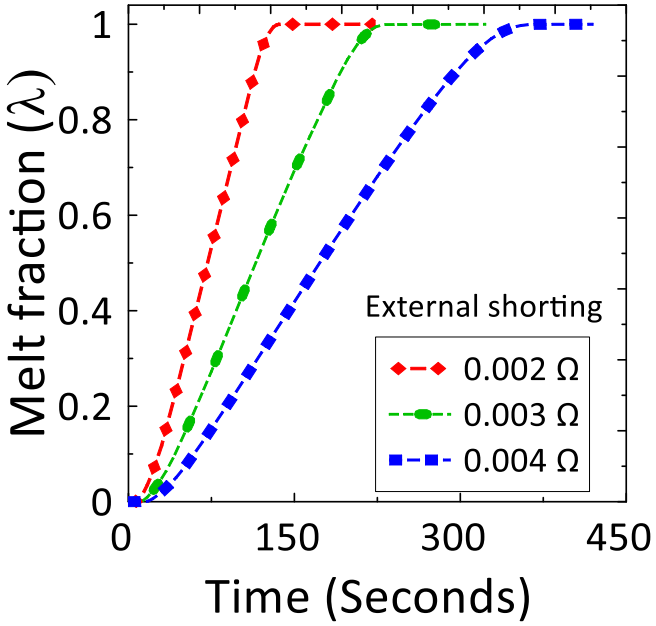

(b) Melt fraction

Figure 3.28: Temperature and Melt under external shorting of battery

It can be observed that the PCM is able to control the cell temperature below the risk zone as this condition indicates completion of melting process; while, at the end of the shorting process, the complete melting of PCM occurs and reports significant temperature hotspots. Therefore, one needs to adopt appropriate measures to ensure safe operating limits for LIBs.

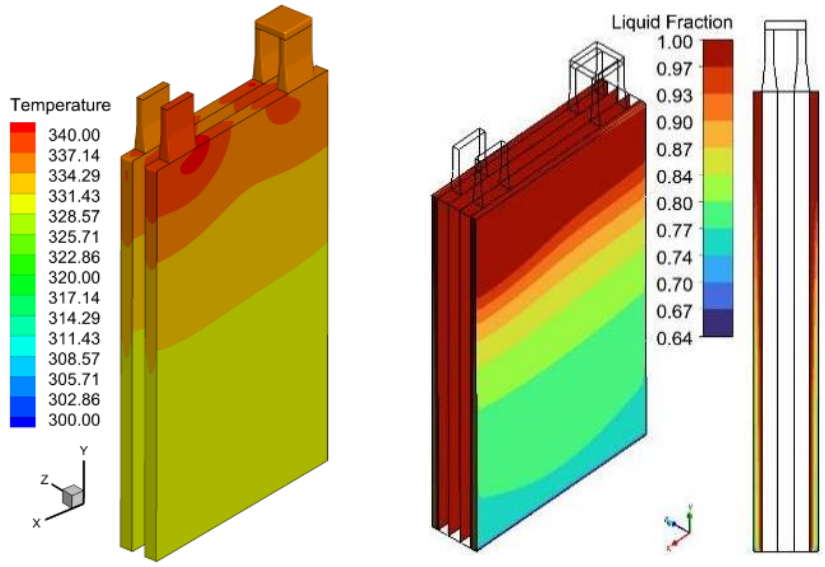

(a) Temperature at 100 seconds (b) Melt fraction at 100 seconds

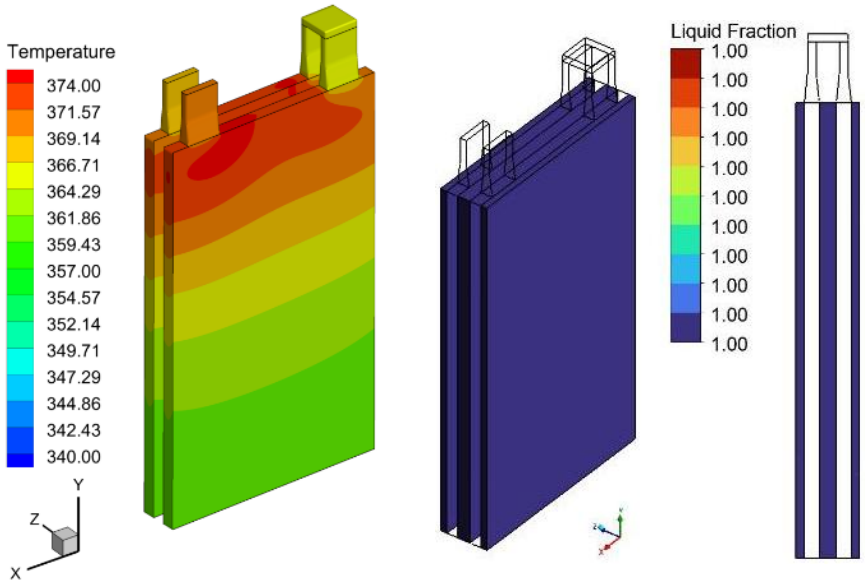

(c) Temperature at 223 seconds (d) Melt fraction at 223 seconds

Figure 3.29: Temperature contours for the External shot circuit tests

Internal short circuit test

An internal short is considered as one of the potential causes of thermal runaway in LIBs, usually occurs due to manufacturing flaws that include the sticking of conductive particles in the jelly roll/separator or wrinkles; very often, nail penetration tests are carried out in experiments to trigger the internal shorting in the battery. In the MSMD approach, the internal shorting in the cell can be triggered by assigning a smaller volume in the

cell with shorting resistance where the rise in the local temperature takes place. The transfer of short-current density, j_{short} and the subsequent heat generation under such condition can be estimated as [108]:

$$j_{short} = \left(\frac{\emptyset_+ - \emptyset_-}{r_c}\right) \tag{3.47}$$

$$\dot{q}_{short} = \frac{(\emptyset_+ - \emptyset_-)^2}{r_c} \tag{3.48}$$

The short circuit test is performed on cell-1 in the 2S1P configuration; the dimension of the patched volume is considered as 5mm×6mm×7.2mm (Fig. 30(a)). Two different internal shorting resistances (ISR) i.e., $0.5e^{-7}\Omega.m^3$ and $1e^{-7}\ \Omega.m^3$ with MF-PCM ($\varepsilon = 0.95$) are considered for the analysis by following the procedure reported in [108].

Fig. 3.30(b) shows the peak temperature for shorted zone and the average cell temperature. For smaller ISR (case 1), the temperature rise in the shorting zone is very sharp; this is due to the increase in the magnitude of the current. The average temperature of cell 1 is found to be 335.64 K and 324.7 K for case 1 and case 2, respectively. Figs. 3.31 depict the melt front propagation in the PCM domain coupled to cell-1 for case 1.

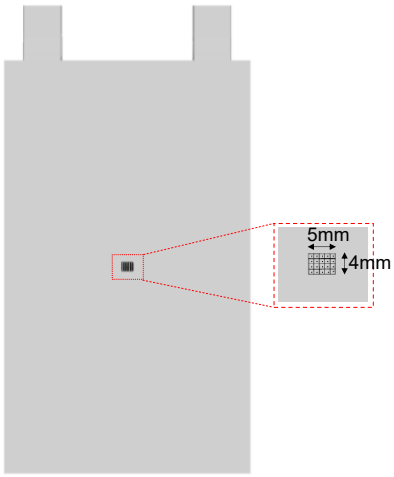

(a) Patched location for shorting

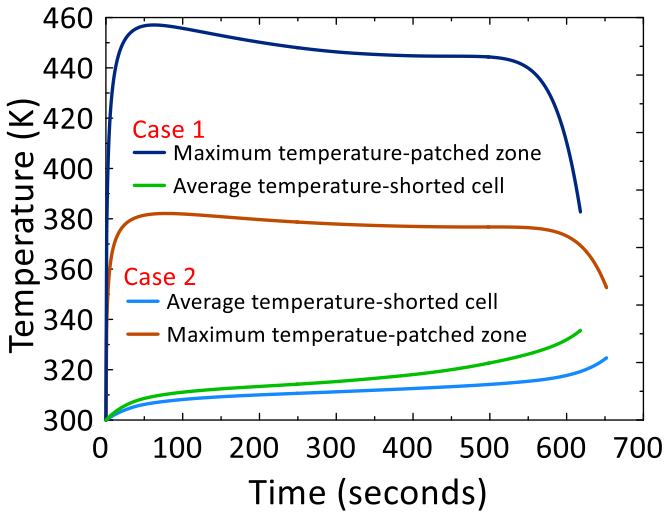

(b) Temperature response of the cell

Figure 3.30: Temperature response of the battery under internal shorting

The PCM melts rapidly near the shorting zone, while the local temperature rises sharply in the cell. For case 2, the melt front contours are presented in Figs. 3.32. Additionally, thermal runaway in one cell can spread and trigger thermal runaway in adjacent cells. The safety and reliability of the battery cell can be ensured during the design of the BTMS; in such a case, detailed investigation is needed to analyse the spread and subsequently mitigate the TR in Li-ion cells. Such investigations are currently not in the scope of the present study and therefore not discussed here.

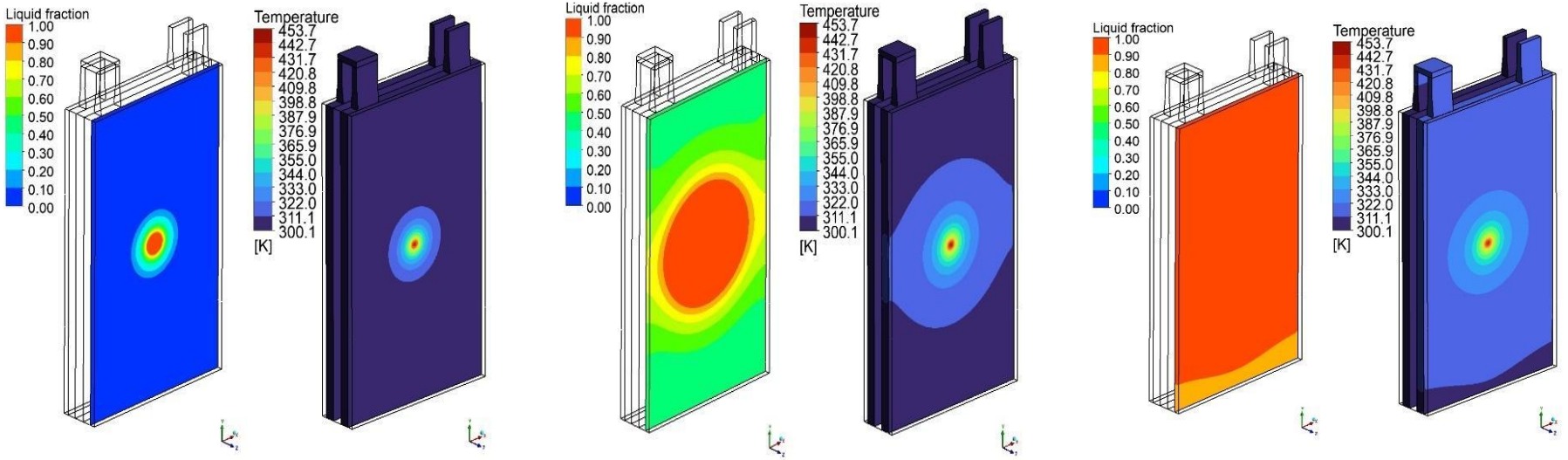

(a) Time 20 seconds (b) Time 200 seconds (c) Time 400 seconds

Figure 3.31: Melt and temperature contours for case I (ISR=0.5e^{-7}Ω.m^{3})

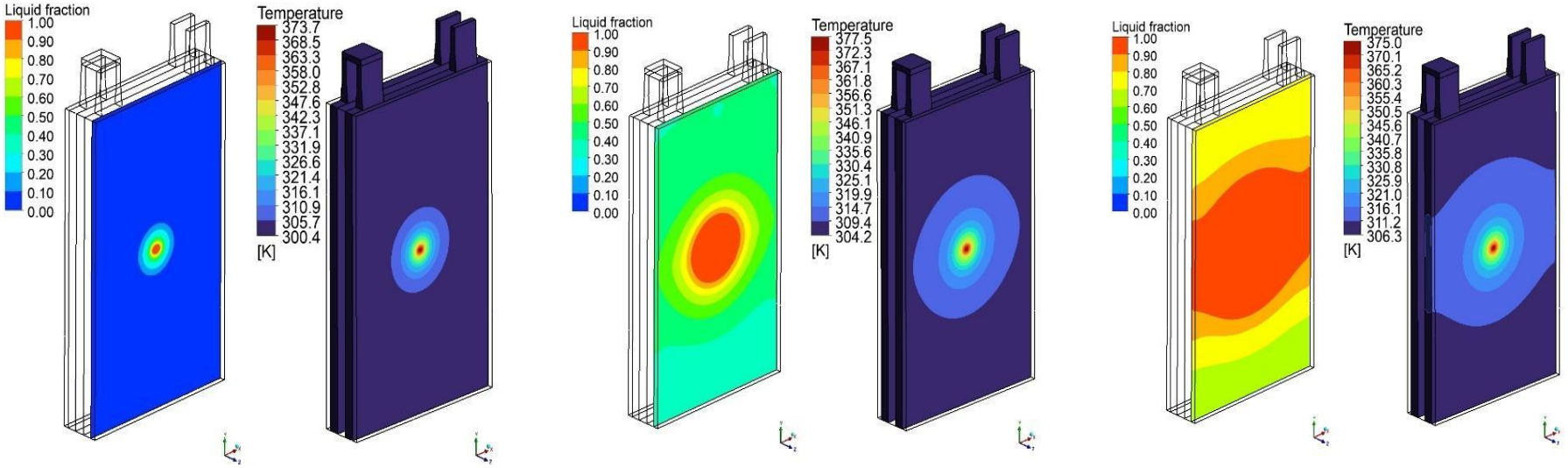

(a) Time 20 seconds (b) Time 200 seconds (c) Time 400 seconds

Figure 3.32: Melt and temperature contours for case II (ISR=1e^{-7}Ω.m3)

3.2.5 Dynamic charging-discharging test

Time varying constant current discharge

To test the optimized MF-PCM composite under dynamic loading conditions, a time schedule event is simulated in which the battery first discharges for 3 minutes by 5C, followed by repeated cycles of 1 minute of charging at 1C and 2 minutes of discharging at 5C.

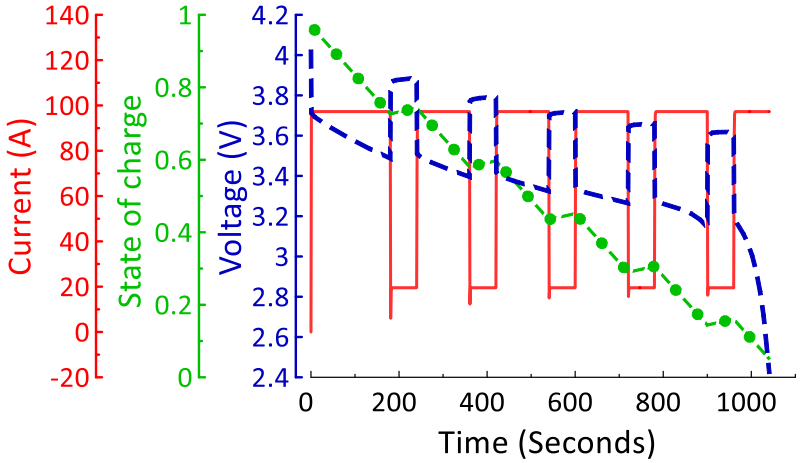

(a) Current, voltage and SOC profiles during the test

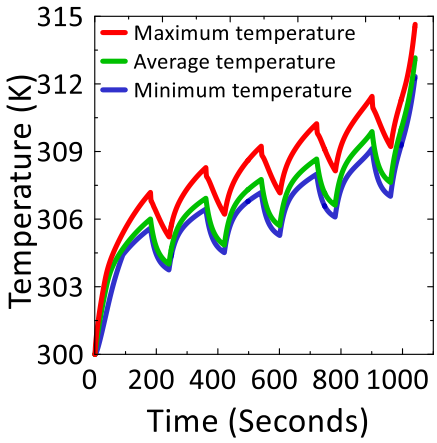

(b) Temperature of the cells

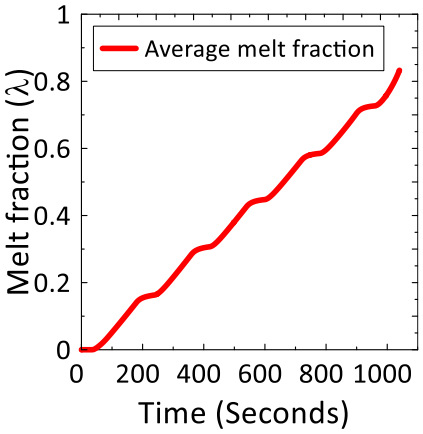

(c) Melt fraction

Figure 3.33: Dynamic profile tests of the cells

The simulation is carried out till the battery is completely discharged; Fig. 3.33(a) depicts the dynamic variation of current, voltage and SOC during the process. The average, maximum and minimum temperatures of the cell at the end of complete discharge are 313.13K, 314.64K and 312.3K, respectively, as depicted in Fig. 3.33(b). The melt fraction of the PCM at the end of discharge is 0.81 (Fig. 3.33(c)). The findings

indicate that the present modeling approach is suitable for forecasting transient temperature responses during dynamic loading.

Thermal performance under aggressive drive cycle

Worwood et al. [128], in their investigation, utilized an aggressive duty cycle for a high-performance EV developed using an electric sports car on racetracks varying in length and location. The C-rate data presented in [128] corresponds to a 200-second loop, where the maximum discharge and charge rates reach 8C and 2C, respectively. Using this data, a C-rate profile for four continuous loops of the aggressive duty cycle was generated and applied in the present study, as shown in Fig. 3.34(a). The lower voltage cutoff value at the end of the cycle is kept at 2.5V as can be seen from the voltage profile in Fig. 3.34(b). The SOC variation depicts that the battery pack is completely discharged at the end of the drive cycle (Fig. 3.34(c)). The temperature increase during the cycle, both without PCM case and with the current configuration of MF-PCM (porosity 0.95) is depicted in Fig. 3.35(a).

It is observed that the battery pack temperature at the end of cycle for without PCM is 341.3K and with MF-PCM is 310.90K. About 68% of the PCM gets completely melted at the end of the cycle and about 32% remains unmelted which has the potential to further absorb heat from the battery pack as illustrated in Fig. 3.35(b). This demonstrates the effectiveness of the MF-PCM in controlling cell temperature.

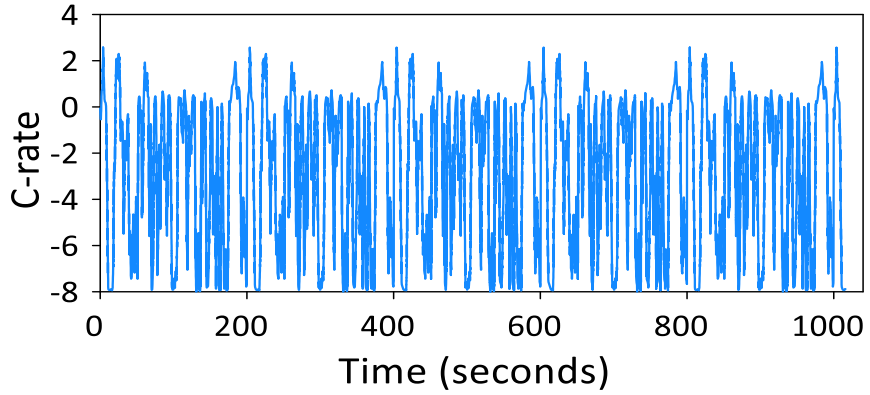

(a) C-rate profile for 4 continuous loops

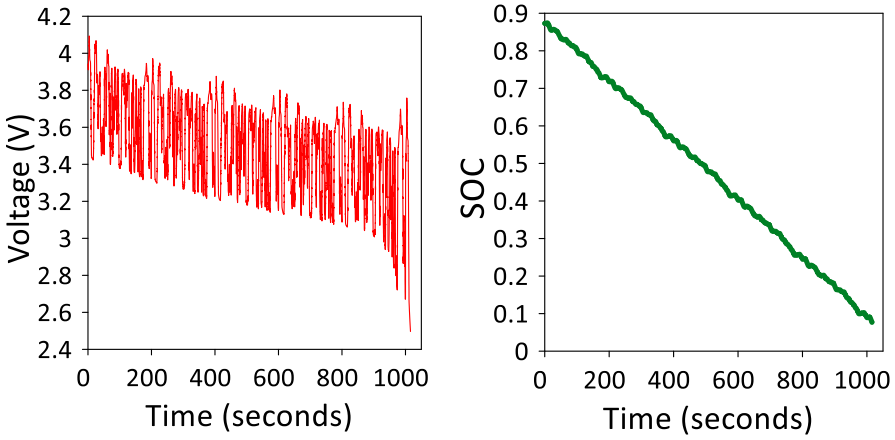

(b) Voltage profile (c) SOC profile

Figure 3.34: Battery characteristics during aggressive drive cycle

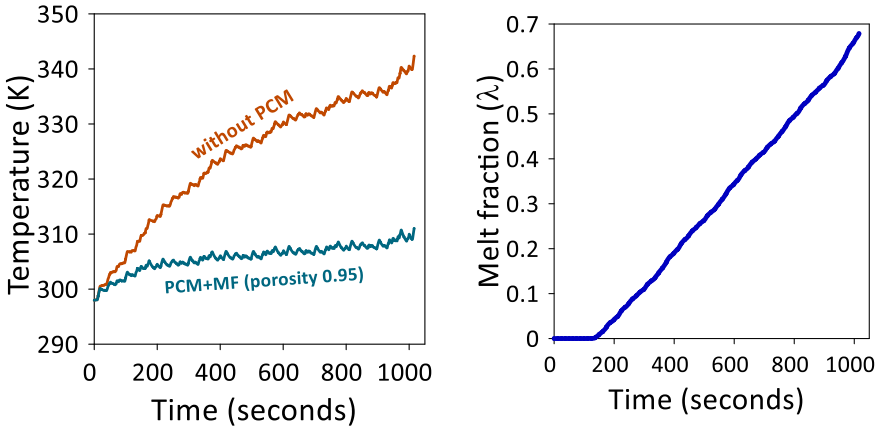

(a) Battery temperature (b) Melt fraction

Figure 3.35: Thermal performance of MF-PCM composite under the aggressive drive cycle

Thermal performance under realistic drive cycle

Fink et al. [125], in their study, utilized a realistic driving profile that included periods of discharging and charging. The current time data has been obtained based on the normal driving conditions for about 75 minutes. The C-rate profile is depicted in Fig. 3.36. This variation in the voltage (Fig. 3.37(a)) illustrates periods of charging and discharging. Clearly the temperature of the battery pack is lower in the first 2500 seconds and remains near 303K, as seen from Fig. 3.37(b). It is to be noted that the current battery modeling approach can be used to model highly dynamic charging-discharging conditions using the realistic driving cycle test data.

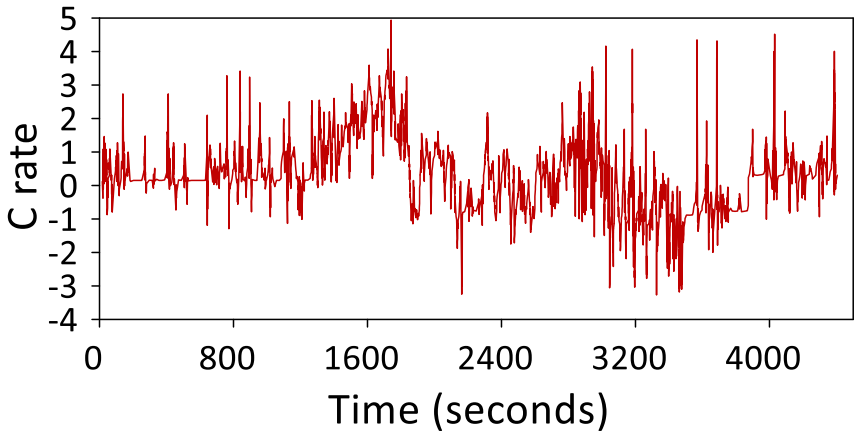

Figure 3.36: C rate for the realistic drive cycle

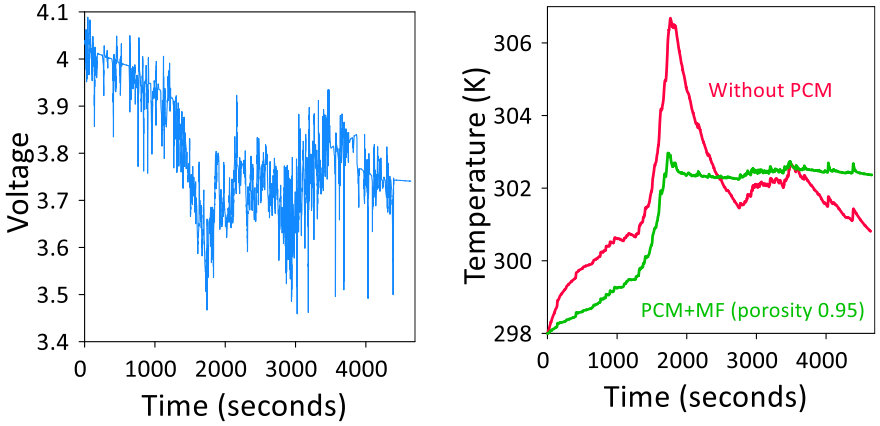

(a): Voltage profile (b) Average battery temperature

Figure 3.37: Thermal performance of MF-PCM composite under the realistic drive cycle

3.2.6 Battery pack (7S1P) simulations

Here, the battery module in 7S1P configuration is tested with MF-PCM ($\varepsilon = 0.95$) composite. The voltage of the pack is maintained as 26 V and the capacity remains 20 Ah due to the series configuration. PCM domain thickness is kept the same at 8 mm and a discharge rate of 5C is used. Fig. 3.38(a) shows the temperature hotspots after the complete discharge in the battery cell with cooling in the natural convective conditions. Fig. 3.38(b) shows the temperature distribution in both domains with the MF–PCM composite; a significant reduction in temperature and gradient is observed, with no hotspots appearing in the cell domain during or after complete discharge. The peak temperature is limited to 313.8K and the temperature gradient found to be less than 5K. Fig. 3.38(c) shows the information on PCM melting after the complete

discharge of the battery pack; a more uniform melting is observed, which may be due to the metal foam in the PCM domain.

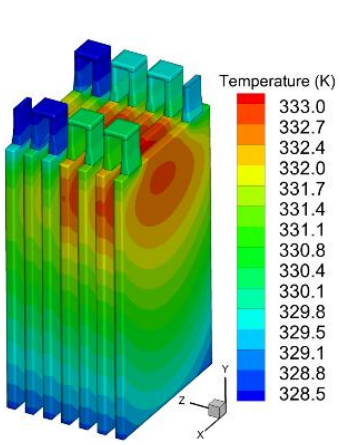

(a) Natural convection cooling

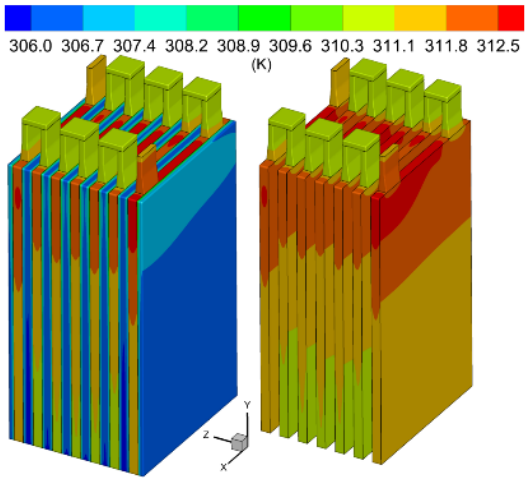

(b) MF-PCM enhanced Battery pack

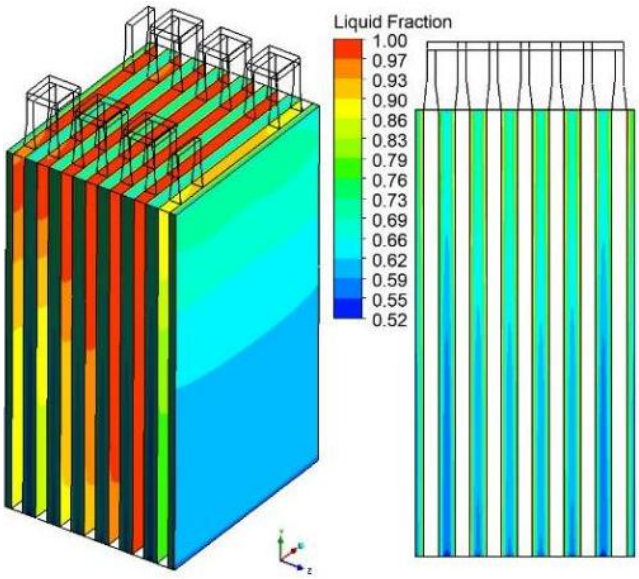

(c) Melt fraction for MF-PCM enhanced pack

Figure 3.38: Battery pack (7S1P) temperature contours after complete discharging by 5C

3.3 Enhanced Thermal Management System for Li-ion Batteries Using Phase Change Material and Liquid Cooling Under Realistic Driving Cycles

The risk of overheating remains a concern with PCM as it cannot absorb more heat once fully melted. To overcome this, hybrid cooling systems combining active and passive cooling techniques have been explored [129-130] integrating PCMs for heat absorption with active cooling to dissipate the stored heat, optimizing battery thermal management. Recent studies have also explored configurations that combine PCM with active cooling methods, seeking to enhance the effectiveness of BTMS. Despite advancements, several challenges remain, particularly in adapting these systems to real-world conditions where batteries experience dynamic and variable thermal loads such as urban stop-and-go traffic, highway cruising, and aggressive acceleration.

Most existing hybrid BTMS designs integrate liquid cooling structures and PCM layers separately between cells, increasing system size and complexity [131]. Some configurations place cooling channels at the bottom with PCM sandwiched between cells, significantly increasing the system's size, weight, and complexity, thus compromising practicality. Although structural optimizations like fin enhancements and cooling plate designs have been explored, their full potential for minimizing pumping power, reducing system weight, and maximizing PCM utilization is not fully realized. Often, these hybrid systems require continuous coolant flow to maintain performance, leading to higher energy consumption and a corresponding reduction in overall system efficiency, further limiting their practicality for real-world EV operations.

Addressing these challenges, this work introduces a novel hybrid BTMS for lithium-ion batteries, featuring a unique zig-zag cold plate with integrated cooling channels inside the PCM domain to enhance heat transfer. Using a 3S1P battery pack, four distinct cooling schemes are investigated: 1) natural air convection cooling, 2) PCM enhanced

passive cooling, 3) Active Cooling, using a liquid-cooled cold plate; 4) Hybrid Cooling, with PCM infused inside the cold plates. Two coolant flow strategies are examined: continuous cooling (CC), where coolant flows continuously during battery operation, and intermittent cooling, which adjusts coolant flow based on the PCM's melt state inside the cold plate. The system's performance is assessed under four realistic driving conditions [132], including the Supplemental Federal Test Procedure (SFTP-US06), Urban Dynamometer Driving Schedule (UDDS), Worldwide Harmonized Light Vehicles Test Procedure (WLTP-class-3), Highway Fuel Economy Test (HWFET), along with two constant current cycles with rapid discharge and charge rate of 5C/4C and 1C, respectively. The detailed thermal loading conditions have been tabulated in Table 3.3.1

3.3.1 Design concepts

Optimizing the weight and volume of the BTMS for EVs is crucial for maintaining vehicle efficiency and driving range. Ideally, the BTMS should not exceed 40% of the battery module's overall weight and volume to avoid significant impacts on performance [133]. The current design employs a hybrid cold plate that integrates PCM with strategically placed cooling channels between two (top and bottom) support plates, as shown in Figs. 3.39. Initially, a conventional serpentine cooling channel with two turns is selected, which is then improved by changing it to a zig-zag pattern with four turns. Two different cooling strategies are studied: continuous coolant flow (CC) and intermittent coolant flow (IC), where the coolant flow is controlled based on the melting state of the PCM. To maximize energy storage and release, the current study introduces a coolant flow decision-making algorithm based on the melt state of the PCM. The approach begins with no initial coolant flow, allowing the PCM to absorb the heat generated by the cells and undergo melting. Once 80% of the PCM is melted, coolant flow starts, absorbing heat from both the PCM and the cells. This continues until only 20% of the PCM remains melted, indicating about 80% of the PCM has solidified, then the coolant flow stops, and

the PCM absorbs heat until it reaches 80% melting again, repeating the cycle. These thresholds were selected to optimize PCM utilization while ensuring effective thermal management. The 80% threshold aims to maximize the passive heat storage capacity of the PCM without excessive melting, which could lead to a rapid decrease in its heat absorption capacity and compromise its effectiveness in managing peak thermal loads. On the other hand, the 20% threshold was chosen to ensure that the PCM has sufficient unmelted volume to provide additional passive cooling capacity when required. During the intermittent cooling, initiating the coolant flow too early (at lower melt fractions) would underutilize the PCM's latent heat capacity, reducing its overall contribution to temperature regulation. These chosen thresholds also help maintain a buffer of solid PCM for subsequent thermal cycles, providing robustness during fluctuating or extended thermal loads. In discussing heat flow dynamics, the heat generated by the battery cells is first transferred to the aluminium support plate and then to the PCM and cooling channel. The PCM absorbs heat initially as sensible heat until reaching its melting point, followed by latent heat absorption. During coolant flow, the coolant extracts heat from the PCM and aluminium plates, aiding in the restoration of the PCM's latent heat capacity. Simultaneously, heat is dissipated through natural air convection from the surfaces exposed to the environment. Fig. 3.39 elaborates the flow chart for the steps involved in this investigation.

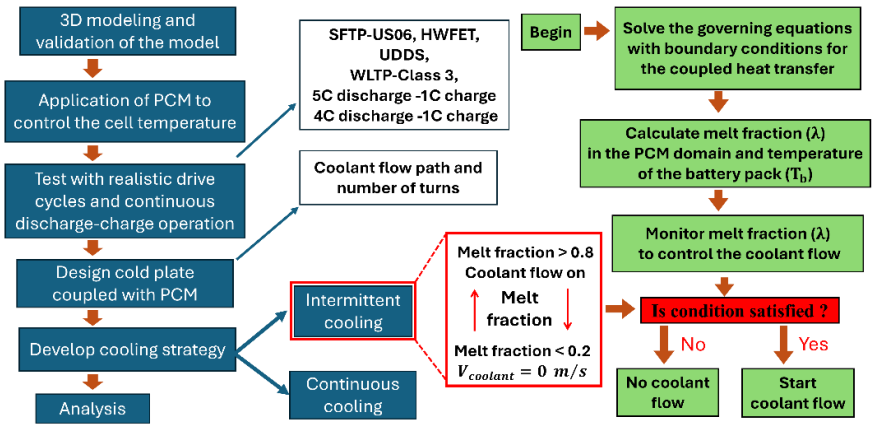

Figure 3.39: Investigation flow chart for hybrid system

Table 3.3.1: Description of the various thermal loading conditions

Type	Drive cycle	Description	Standard cycle time	Distance covered	Speed
Transient realistic driving cycles [132]	Urban Dynamometer Driving Schedule (UDDS) also known as LA4 (the city test)	The cycle simulates urban driving with frequent stops, slow accelerations, and low-speed cruising making it ideal for city traffic fuel efficiency, emissions, and performance testing.	23 minutes	11 miles	19.6 mph
	Highway Fuel Economy Driving Schedule (HWFET)	The steady cruising and low acceleration and deceleration make HWFET ideal for highway fuel economy testing at higher speeds.	12.75 minutes	10.26 miles	48.3-60 mph
	Supplemental FTP/US06	This driving cycle simulates aggressive driving with rapid acceleration, deacceleration and high-speed fluctuations to mimic performance in harsh real-world conditions.	10 minutes	8 miles	80.3 mph
	WLTP (Worldwide Harmonized Light Vehicles Test Procedure) - Class 3	This cycle includes a series of tests that simulate a mix of urban, suburban, and highway driving conditions, divided into four phases: low, medium, high, and extra-high speed. WLTP Class 3 provides a more accurate and realistic assessment for modern vehicles compared to previous test procedures.	30 minutes	14.45 miles	37-81 mph
Constant current charge-discharge cycles	4C-1C	Discharging by 4C followed by charging by 1C (No rest in between)	71.4 minutes	-	
	5C-1C	Discharging by 5C followed by charging by 1C (No rest in between)	67.7 minutes	-	

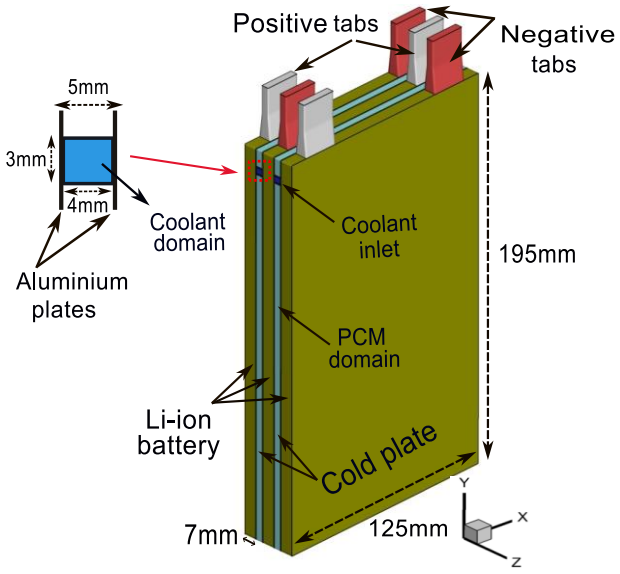

Figure 3.40(a): Geometry of the battery pack coupled with cold plate

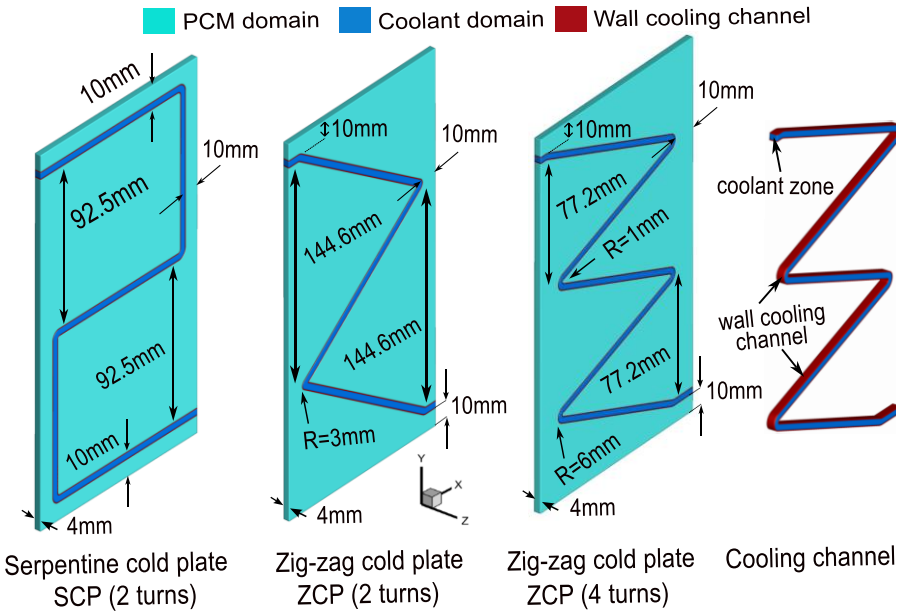

Figure 3.40(b): Various designs of cold plates

3.3.2 Geometry and design

The current hybrid thermal management system has been developed using the same prismatic lithium-ion cell (ePLB C020, EIG corporation, Korea). The geometry, configuration, and dimensions of the HBTMS are depicted in Fig. 3.40(a). The setup features a 3S1P battery configuration with virtual tab connections and incorporates two cold plates between

the cells. These cold plates include a cooling channel, PCM domain, and top and bottom plates. Fig. 3.40(b) illustrates three different hybrid cold plate designs: the serpentine cold plate (SCP) with two turns, and the zig-zag cold plate (ZCP) with two and four turns. Each cold plate has a total thickness of 5 mm, consisting of 1 mm for the top and bottom support plates combined, and 4 mm for the PCM domain. The cooling channel inside the PCM domain is positioned 10 mm away from the top, side, and bottom edges, with a 0.5 mm thick wall separating the coolant from the PCM. The variant without PCM has a serpentine configuration with two turns.

3.3.3 Governing equations

The cell model and Phase change material model

The ECM model, as discussed in the previous section 3.2.1, is used to simulate the transient behavior of the battery. However, the current hybrid system is designed by using pure PCM (without MF), therefore, the governing equation for the phase change model are discussed below.

Using the enthalpy-porosity method, the PCM domain is treated as a mushy zone with a liquid fraction (λ) ranging from 0 (solid) to 1 (liquid), enabling smooth phase transitions without explicitly tracking the interface. The PCM is considered incompressible and follows Newtonian behaviour in its liquid phase. Natural convection driven by density variations is modelled using the Boussinesq approximation, while volumetric expansion during phase change is neglected due to its minimal system-level impact. Thermal properties such as conductivity, density, and specific heat are defined separately for solid and liquid phases. The following equations govern heat transfer, phase transition, and convective flow in the PCM domain, incorporating resistance effects in the mushy region [89]:

Continuity equation:

$$\frac{\partial \rho}{\partial t} + \nabla . \left(\rho_{pcm} \vec{V}_{pcm}\right) = 0 \tag{3.49}$$

Momentum equation:

$$\text{X – dir.:}\quad \rho_{pcm}\frac{\partial u_{pcm}}{\partial t}+\rho_{pcm}\left(\vec{V}_{pcm}\,.\,\nabla\right)u_{pcm}=-\frac{\partial P}{\partial x}+\nabla.\left(\mu_{pcm}\nabla u_{pcm}\right)+S_x \tag{3.50}$$

$$\text{Y – dir.:}\quad \rho_{pcm}\frac{\partial v_{pcm}}{\partial t}+\rho_{pcm}\left(\vec{V}_{pcm}\,.\,\nabla\right)v_{pcm}=-\frac{\partial P}{\partial y}+\nabla.\left(\mu_{pcm}\nabla v_{pcm}\right)+S_y+S_a \tag{3.51}$$

$$\text{Z – dir.:}\quad \rho_{pcm}\frac{\partial w_{pcm}}{\partial t}+\rho_{pcm}\left(\vec{V}_{pcm}\,.\,\nabla\right)w_{pcm}=-\frac{\partial P}{\partial z}+\nabla.\left(\mu_{pcm}\nabla w_{pcm}\right)+S_z \tag{3.52}$$

Where $S_x, S_y, and\ S_z$ are source terms representing the mushy zone resistance, as discussed in the previous section:

$$S_x=\frac{A_{mush}(1-\lambda)^2}{(\lambda^3+0.001)}\left(u_{pcm}-u_{pull}\right) \tag{3.53}$$

$$S_y=\frac{A_{mush}(1-\lambda)^2}{(\lambda^3+0.001)}\left(v_{pcm}-v_{pull}\right) \tag{3.54}$$

$$S_z=\frac{A_{mush}(1-\lambda)^2}{(\lambda^3+0.001)}\left(w_{pcm}-w_{pull}\right) \tag{3.55}$$

$$S_a=\rho_{pcm}\vec{g}\,\beta(T-T_{ref}) \tag{3.56}$$

The PCM is tracked using the melt fraction (λ), ranging from 0 (completely solid) to 1 (completely liquid) based on the temperature field:

$$\lambda=\begin{Bmatrix}0 & (T<T_s)\\ \dfrac{T-T_s}{T_l-T_s} & (T_s<T<T_l)\\ 1 & (T>T_l)\end{Bmatrix} \tag{3.57}$$

Finally, the energy conservation equation for the PCM is expressed as:

$$\rho_{pcm}\frac{\partial H}{\partial t}+\nabla\left(\rho_{pcm}\vec{V}_{pcm}H\right)=\nabla\,.\left(k_{pcm}\nabla T_{pcm}\right) \tag{3.58}$$

Where H is the total entropy, which includes sensible (h_s) and latent heat (ΔH) contributions:

$$H=h_s+\Delta H \tag{3.59}$$

$$h_s=\int_{T_o}^{T}C_{p_{pcm}}dT,\text{where}\ \ \Delta H=\lambda L \tag{3.60}$$

Governing equation for coolant and cooling plate

For Coolant flow

Based on the conservation of mass, momentum, and energy, the governing equations for the liquid flow and heat transfer in the coolant and cold plate zone are [134]:

Continuity equation:

$$\nabla . \left(\rho_c \vec{V}_c\right) = 0 \tag{3.61}$$

Momentum equation (for laminar flow):

$$\rho_c \frac{\partial \vec{V}_c}{\partial t} + \rho_c \left(\vec{V}_c . \nabla\right) \vec{V}_c = -\nabla P + \nabla . \left(\mu_c \nabla \vec{V}_c\right) \tag{3.62}$$

Energy equation:

$$\rho_c C_{p_c} \frac{\partial T_c}{\partial t} + \nabla \left(\rho_c C_{p_c} \vec{V}_c T_c\right) = \nabla . \left(k_c \nabla T_c\right) \tag{3.63}$$

The above equation governs the thermal energy transport in the coolant, incorporating both convective and conductive heat transfer. The Reynolds number (*Re*) is calculated as:

$$Re = \frac{\rho_c V_c D_{eq}}{\mu_c} \tag{3.64}$$

Here, D_{eq} is the equivalent hydraulic diameter of the channel, V_c is coolant velocity, ρ_c coolant density and μ_c is viscosity. In this study, with a maximum velocity of coolant of 0.3 m/s, the resulting value of Re is less than 2000, indicating laminar flow conditions. The pumping power (P_{pump}) and the energy consumption (J) for the coolant can be calculated as:

$$P_{pump} = V_c A_{cs,inlet} \Delta P, \text{ where } \Delta P = P_{inlet} - P_{outlet} \tag{3.65}$$

$$J = \int_0^{t_{coolant\ flow}} P_{pump} dt \tag{3.66}$$

$A_{cs,inlet}$ is the cross-section area of coolant inlet.

For the Cooling plate:

$$\text{Energy equation:}\quad \rho_{cp} C_{p_{cp}} \frac{\partial T_{cp}}{\partial t} = \nabla . \left(k_{cp} \nabla T_{cp}\right) \tag{3.67}$$

This equation models the heat transfer in the top and bottom plates of the cooling system, where ρ_{cp}, $C_{p_{cp}}$, and k_{cp} represent the density, specific heat, and thermal conductivity of the cooling plate material, respectively.

Boundary conditions

The boundary conditions for the system are set with the ambient temperature at 27 °C. The initial temperatures of battery, coolant, PCM and aluminum plates are uniform and equal to the ambient temperature. The coolant inlet-outlet conditions are set to a velocity inlet at the entry, and pressure outlet at the exit. The specific boundary conditions across different interfaces are defined as follows [89], [91]:

- Between contact interface of cell and aluminum plate, aluminum plate and PCM:

$$-k_b \frac{\partial T}{\partial n} = -k_{cp} \frac{\partial T}{\partial n} \tag{3.68}$$

$$-k_{cp} \frac{\partial T}{\partial n} = -k_{pcm} \frac{\partial T}{\partial n} \tag{3.69}$$

These equations ensure continuity of heat flux across the interface.

- Contact interface between aluminum plate and coolant transfers heat through convection:

$$-k_{pcm} \frac{\partial T}{\partial n} = h_c \left(T_{cp,wall} - T_c\right) \tag{3.70}$$

- Boundary conditions at the cold plate, battery, and PCM exposed to the ambient environment:

$$-k_{cp} \frac{\partial T}{\partial n} = h_{cp} \left(T_{cp,wall} - T_{amb}\right) \tag{3.71}$$

$$-k_b \frac{\partial T}{\partial n} = h_b (T_b - T_{amb}) \tag{3.72}$$

$$-k_{pcm}\frac{\partial T}{\partial n} = h_{pcm}(T_{pcm} - T_{amb}) \quad (3.73)$$

where $\frac{\partial T}{\partial n}$ is the temperature gradient and like the previous case the heat transfer coefficient to the ambient environment $h_{surface}$ is taken as 5 W/(m^2.K).

3.3.4 Simulation setup

Material selection, grid analysis and numerical parameters

The thermophysical properties of the Li-ion cell and the PCM are provided in Tables 3.2.2 and 3.2.3 from previous section 3.2.1. In the present investigation, aluminium is used as the cold plate material, and water is selected as the cooling fluid. Their thermophysical properties are provided in Table 3.3.2.

Table 3.3.2: Material Properties for cold plate and coolant [89, 91]

Properties Materials	Density (kg/m^3)	Heat Capacity (kJ/kg.K)	Thermal Conductivity (W/m.K)	Viscosity (Pa.s)
Cold Plate (Aluminum)	2719	871	202.4	-
Coolant (Water)	997	4.18	0.59	8.90×10^{-4}

Further, optimizing the grid size and time step is crucial for achieving accurate and efficient simulations, minimizing computational time while ensuring precision. Grid and time-step analyses were performed for a discharge rate of 5C, with hybrid cold plate coupled with battery pack as per current configurations.

The generated mesh and grid analysis are presented in Fig. 3.41; at first, for a time step (Δt_{ts}) of 1second, five different mesh element sizes, 3 mm, 2 mm, 1 mm, 1 mm, 0.8 mm and 0.5 mm, having element count of 43,706, 100,643, 579,330, 1,010,460, and 2,024,184, respectively, were tested. The temperature and melt fraction are monitored, and results reported a deviation of less than 0.4% when reducing the grid size from 0.8 mm to 0.5 mm and plateaus after 0.8mm. Therefore, a grid size of

0.8 mm is selected for the cell domain and, to maintain the accuracy of results, the entire cold plate domain element size is kept at 0.5 mm. Four additional time steps (Δt_{ts}) of 5, 2, 0.5, and 0.25 seconds were tested. Taking 0.25 second as a baseline, the average deviation for time step of 1 second was 0.08% and for time step of 0.5 seconds was 0.01%.

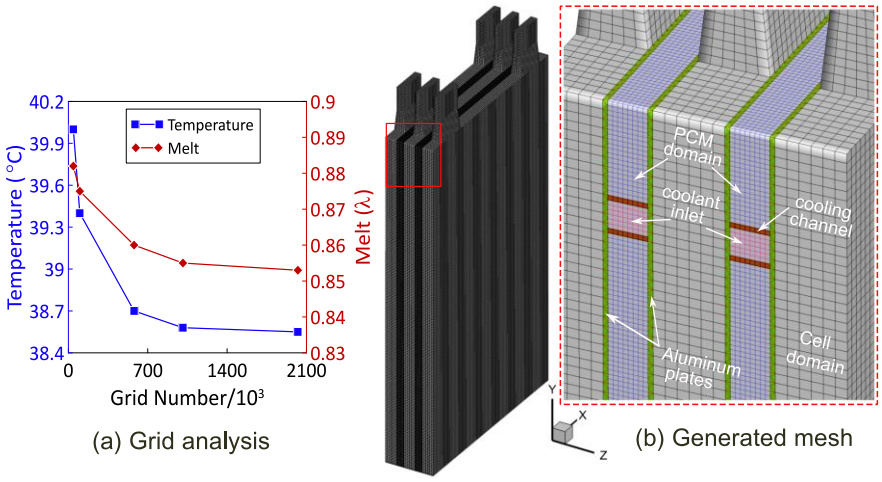

Figure 3.41: Grid analysis and mesh for the computational domain

Consequently, a time step of 0.5 seconds was selected for the simulations to balance computational efficiency and accuracy. Similar to previous case each time step involved up to 500 iterations to achieve convergence.

3.3.5 Validation of the numerical model

The validation of the numerical model is vital to establish its accuracy in simulating the thermal response of lithium-ion cells under various thermal loading conditions, including drive cycles and constant current cyclic operations, which are investigated in this study. The electrochemical–thermal behavior of the Li-ion cell under constant C-rate discharging has already been validated earlier in Section 3.2.2 using experimental data from Taheri et al. [103], Fink et al. [125], and Liu et al. [126] (Figs. 3.5-3.6). Building upon that, the present section extends the validation to hybrid configurations involving cold plates, PCM integration, and realistic drive cycles.

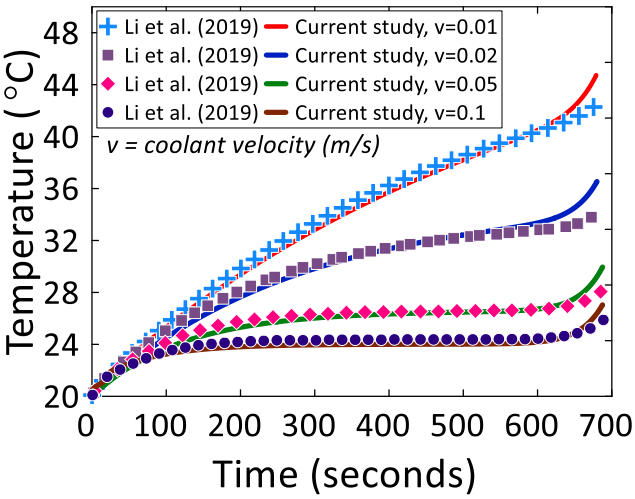

(a) Cold plate coupled with battery [104]

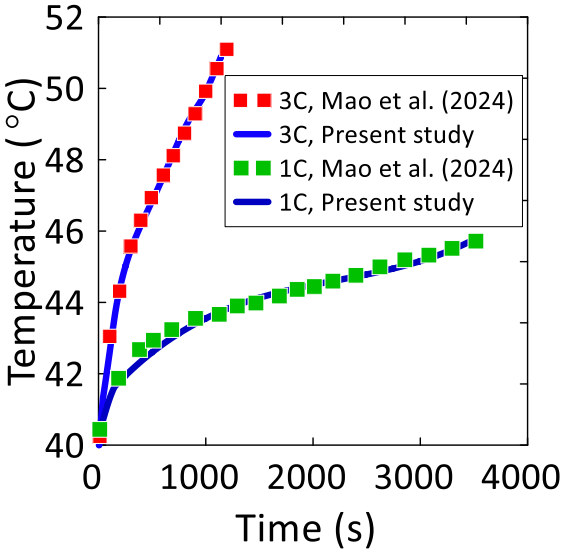

(b) Hybrid cold plate coupled with battery [135]

Figure 3.42: Validation of cell coupled with liquid and hybrid cooling

The thermal management with a channeled cold plate was studied and validated against the work of Li et al. [104], who studied a three channeled cold plate at a 5C discharge rate. Fig. 3.42(a) shows consistent results of the rise in cell temperature for a discharge rate of 5C for different coolant velocities, with an average deviation less than 5% compared to the numerical results of Li et al. [104]. Further, the numerical model for the cold plate integrated with PCM has been validated against the study by Mao et al. [135], as illustrated in Fig. 3.42(b). The comparison was conducted with a battery pack comprising

nine cells undergoing discharging by 3C and 1C. The results demonstrate excellent agreement between the current model and the reference data, with an average deviation of less than 3%

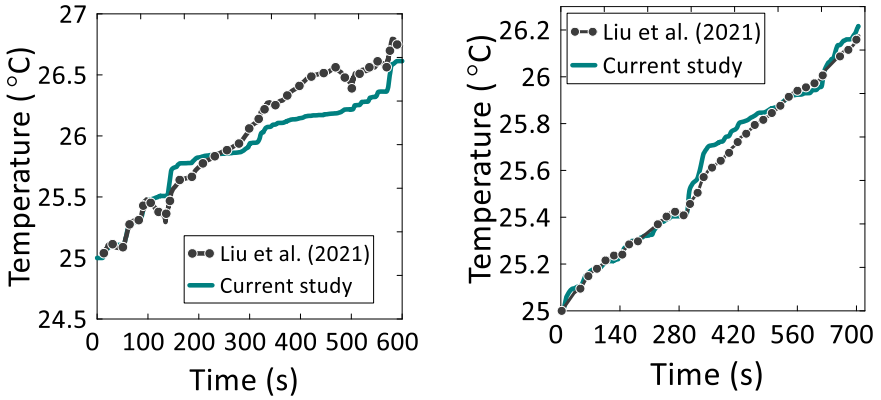

(a) Temperature response from a battery pack (360V/43.2 kWh) undergoing US06 drive cycle

(b) Temperature response from a battery pack (360V/43.2 kWh) undergoing HWFET drive cycle

Figure 3.43: Validation with the study of Liu et al. [132]

Finally, to simulate and validate realistic drive cycles, experimental data from Liu et al. [132], who used the same Li-ion cell and modeled an equivalent EV (Nissan Leaf 2018) in GT-SUITE, was used. Two different drive cycles, namely US-06 and HWFET are used to validate as these include distinct dynamic driving scenarios. From Fig. 3.43(a-b), results from the current numerical model match well with the experimental test data of [132] with average deviation of less than 3% for US-06 and HWFET drive cycle.

These validations across multiple scenarios show good agreement with various experimental comparisons, indicating the accuracy of the numerical simulations. The findings demonstrate that the model can effectively and accurately replicate the thermal behavior of the cell under a diverse range of thermal loading conditions, thereby being a powerful tool. Consequently, the developed numerical tool is crucial for the development and optimization of battery thermal management systems and is extended to more realistic cell operating conditions, discussed in Section 4.

3.3.6 Results and discussion

Realistic drive cycles

This study analyses the battery thermal management system using four distinct drive cycles: Supplemental Federal Test Procedure (US-06), Urban Dynamometer Driving Schedule (UDDS), Worldwide Harmonized Light Vehicles Test Procedure (WLTP-class 3), and Highway Fuel Economy Test (HWFET). Each cycle represents unique driving conditions, influencing the thermal behavior of the battery. The US-06 drive cycle, characterized by aggressive acceleration and high speeds, resulted in the highest temperature peaks among the cycles tested. The UDDS mimics city driving with frequent stops and starts, emphasizing thermal load during idle and acceleration phases. The WLTP-class 3 reflects a mix of urban and highway driving conditions. The HWFET focuses on steady-state highway driving. Initially, the system was optimized for the US-06 drive cycle due to its aggressive and demanding nature. Subsequently, the system was tested under the remaining thermal loading conditions to comprehensively evaluate its performance.

The US-06 drive cycle

US-06 drive cycle was developed to better represent the aggressive driving behaviour, including high-speed and high-acceleration conditions, and rapid speed fluctuations. Fig. 3.44(a) illustrates the variation in the voltage, current, and state of charge (SOC) during the drive cycle. The battery pack endures peak discharging currents reaching 250 A and charging currents up to 100 A. Typically, the drive cycle spans 600 seconds; however, here it is repeated until the SOC hits the discharge cutoff condition, extending the total cycle duration to approximately 1900 seconds. In the analysis of thermal management strategies for the battery pack, two cooling methods were initially evaluated: natural air convection and the application of a 4 mm-thick phase change material (PCM) sandwiched between aluminum plates

adjacent to the cells. The corresponding temperature and melt fraction results are shown in Figs. 3.44(b–c) and are further discussed.

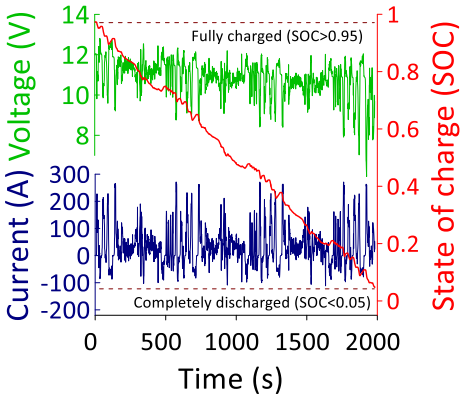

(a) Current, voltage and SOC for US06

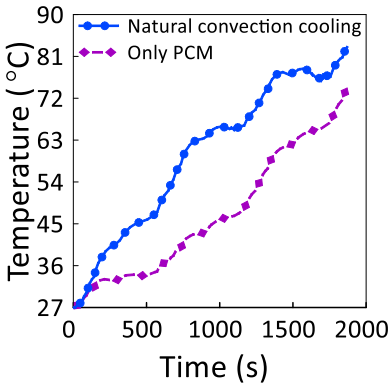

(b) Temperature rise in battery pack under natural convection and only PCM case

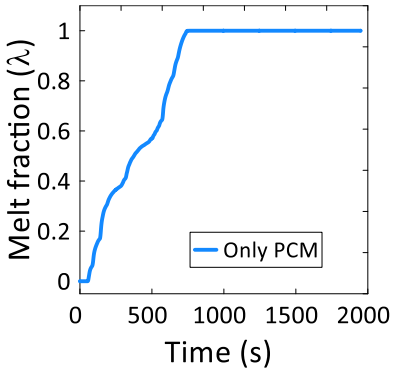

(c) Melt fraction of PCM for only PCM case

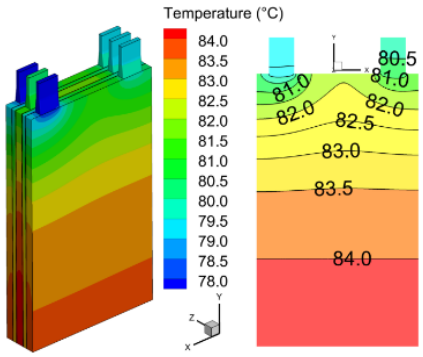

(d) Temperature contours for only PCM case

Figure 3.44: The response of the 3S1P battery pack for US06 drive cycle

Natural air convection cooling (NC): Under this passive cooling scenario, significant heat is generated in the battery pack, and the battery temperature reached the unsafe level, which could trigger thermal runaway in the cells. This temperature increase suggests that natural air convection alone is insufficient for dissipating the heat generated under aggressive drive cycle conditions, such as those simulated in the US-06 scenario.

PCM implementation: Introducing a 4 mm-thick PCM layer between aluminum plates improved thermal management significantly during the

initial phase. The PCM absorbed heat effectively until it melted, maintaining the battery temperature below 36 °C for the first 600 seconds. However, once most of the PCM melted (by 732 seconds), its cooling effect diminished, leading to a sharp increase in temperature. This suggests that while PCM is effective in delaying temperature rise, it struggles to manage heat throughout longer drive cycles. It should be noted that increasing the volume of the PCM is not a viable solution due the limited space available in the battery compartment and low thermal conductivity of the PCM.

Temperature contours analysis: As shown in Fig. 3.44(d), temperature contours at the end of the cycle reveal how the heat distribution varies with using standalone PCM. The contours indicate that even with PCM, certain areas within the battery pack approach high temperatures, nearing the unsafe zone. The use of standalone PCM, while beneficial in delaying the onset of high temperatures, proves inadequate for maintaining safe temperature levels throughout extended or particularly demanding driving conditions. Further enhancements or hybrid cooling solutions must be considered to optimize thermal management in electric vehicle battery packs.

Serpentine cold plate with and without PCM using Continuous and Intermittent cooling

In this subsection, the efficacy of a serpentine cold plate (SCP) with and without PCM, employing both continuous (CC) and intermittent cooling (IC) strategies has been examined. The coolant velocity is set to 0.2 m/s for both the cases. In terms of performance analysis for different cooling configurations, Fig. 3.45(a) illustrates the temperature rise of the battery pack for SCP with and without PCM. Fig. 3.45(b) reports the melt fraction, and Fig. 3.45(c) depicts the temperature of the coolant at the outlet of the cold plate. Overall, the setup with a hybrid cold plate using CC demonstrated the most effective cooling with the lowest battery temperature, followed by the SCP without PCM using CC, and finally the hybrid SCP using IC.

In the hybrid SCP with CC, the PCM directly absorbs heat from the cells while the coolant simultaneously extracts heat from both the PCM and the cells. This dual-action maintains lower battery temperatures throughout the cycle. Conversely, the SCP configuration without PCM, under CC, results in higher coolant exit temperatures (Fig. 3.45(c)) due to the lack of PCM, leading to greater battery temperature fluctuations as heat is absorbed solely through sensible heat transfer. For IC with hybrid SCP, the coolant flow is initially paused, allowing PCM to absorb heat until 80% of the it gets melted, approximately 1500 seconds into the cycle (see Fig. 3.45(d)).

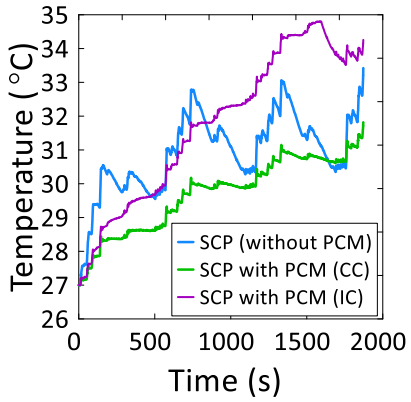

(a) Temperature rise with serpentine cold plate

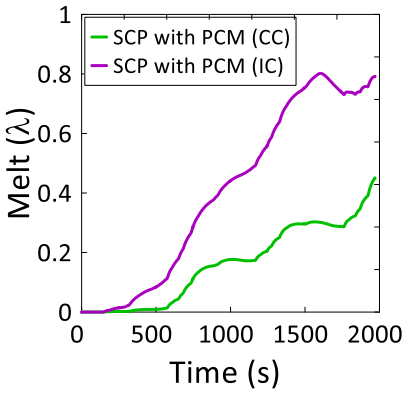

(b) Melting of the PCM

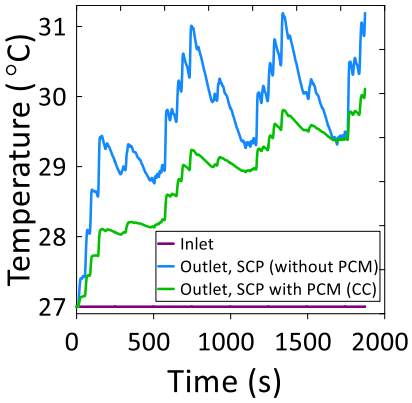

(c) Coolant outlet temperature

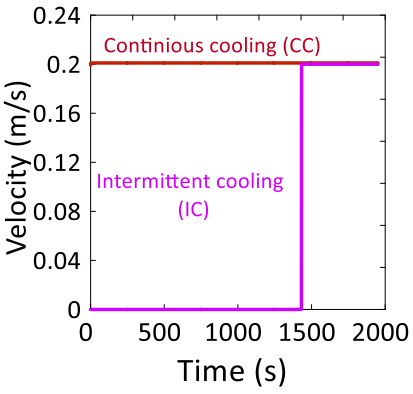

(d) Duration of coolant flow

Figure 3.45: Analysis for serpentine cold plate with/without PCM using continuous/intermittent cooling strategy for US06 drive cycle

Upon reaching this melt percentage, coolant flow resumes, thus reducing battery temperatures as depicted in Fig. 3.45(a). During the entire drive cycle, the reported maximum temperature with SCP without

PCM, SCP with PCM (CC) and SCP with PCM (IC) are 33.4 °C, 34.8 °C and 32.5 °C, respectively.

Figure 3.46 illustrates the temperature contours and the PCM melt fractions at the end of the cycle. In CC, even though the average PCM melt is below 50% at the end of the cycle, there is significant localized melting in areas distant from the cooling channels, indicating uneven heat distribution. The PCM located closest to the coolant starts to solidify initially, with the solidification front advancing towards the area where the melt puddle is concentrated. However, PCM's low thermal conductivity inhibits its rapid solidification, allowing for localized melting, potentially creating temperature hotspots within the battery.

For IC, the delay in coolant flow until 80% of the PCM melted allows substantial heat absorption by the PCM but also suggests that PCM alone may not effectively manage heat without the coolant flow, especially over extended periods. Further, despite variations in cooling strategy, the location of temperature hotspots remained consistent due to the uniform placement and design of the serpentine cooling channels. This observation has led to a redesign of the cooling channels to a zig-zag pattern, enhancing mixing and heat transfer within the PCM domain to better manage thermal gradients and hotspots. The section below discusses the performance comparison of ZCP and SCP using the intermittent cooling strategy.

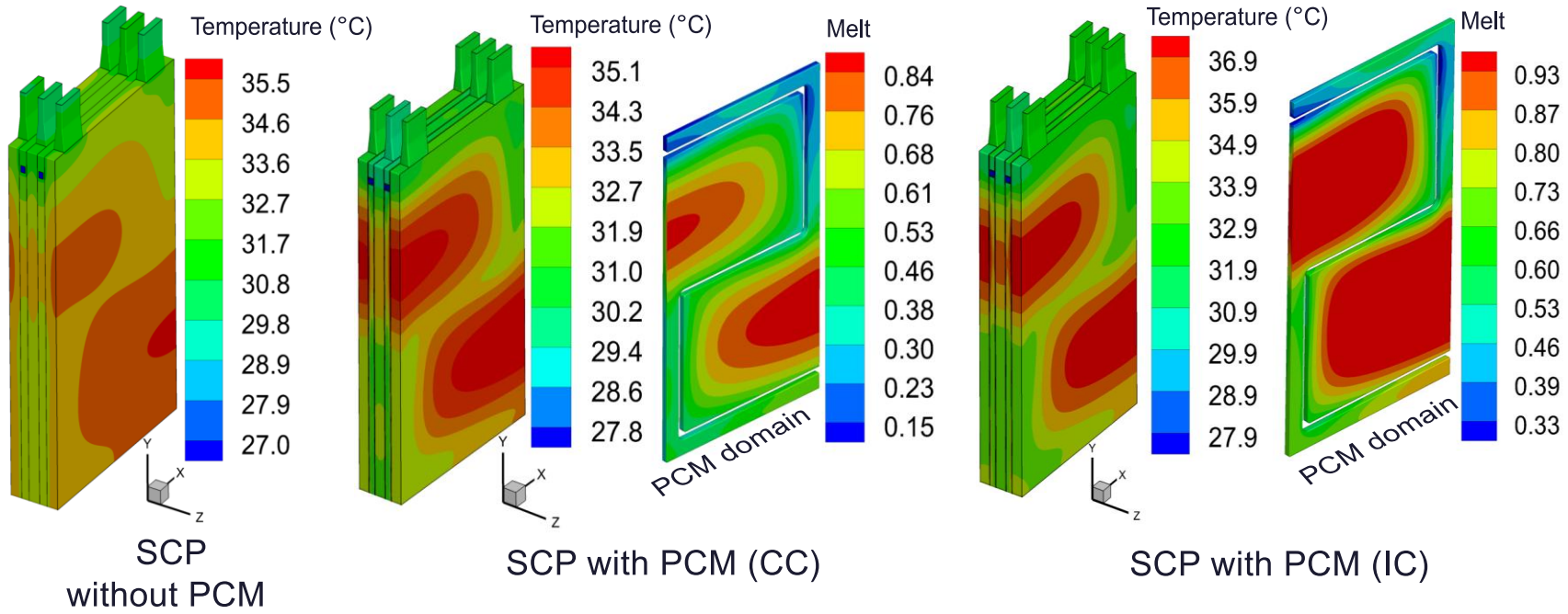

Figure 3.46: Temperature and Melt contours for US06 using serpentine cold plate with/without PCM using continuous/intermittent cooling

Comparative analysis between Zig-Zag and Serpentine cold plates using Intermittent cooling

Zig-zag cold plates (ZCP) with two and four turns have been specifically designed to optimize heat transfer within the PCM domain. Utilizing IC strategy, the comparative performance of ZCP and SCP is analysed. Fig. 3.47(a) details the battery temperature, Fig. 3.47(b) depicts PCM melting rates, and Fig. 3.47(c-d) show temperature contours. For SCP, ZCP with two turns, and ZCP with four turns, PCM reaches an 80% melt threshold in 1592, 960, and 932 seconds respectively, with corresponding battery temperatures of 34.87 °C, 35.06 °C, and 35.2 °C. This rapid melting in ZCPs indicates superior heat transfer efficiency. Upon coolant activation, the temperatures decrease to 33.57 °C for SCP, 32.8 °C for ZCP with two turns, and 32.1 °C for ZCP with four turns, with melt fractions of 0.73, 0.54, and 0.40, respectively. The zig-zag design demonstrates enhanced thermal management, particularly as the number of turns increases, promoting quicker PCM solidification. Temperature contours from Fig. 3.48(a) at 900 s without coolant flow, and Fig. 3.48(b) at the end of the cycle with coolant flow, further support these results.

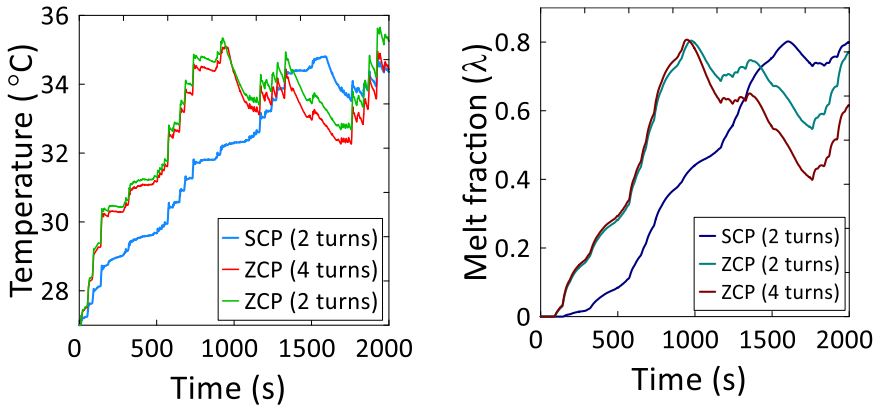

(a) Temperature rise for SCP and ZCPs

(b) Melting of PCM for SCP and ZCPs

Figure 3.47: Analysis for Zig-zag cold plate for US06 drive cycles

These contours are presented in both 3D views of the entire battery pack and 2D views (x-y plane) through a mid-plane slice of the middle cell.

Initially, SCP may seem to perform better when coolant is not flowing, exhibiting a lower peak battery temperature by 2.1 °C.

However, as the cycle progresses, the ZCP with four turns displays the lowest overall temperature and gradient. The SCP shows a significant temperature gradient and two large hotspots in the PCM domain. As the channel design transitions from serpentine to zig-zag with an increasing number of turns, the temperature gradient and hotspot area decrease. Increasing the number of cooling channels enhances the surface area for heat exchange between the coolant and PCM, enabling more efficient heat removal from the battery cells. This configuration also ensures a more uniform coolant flow distribution, which reduces localized hotspots and minimizes temperature gradients.

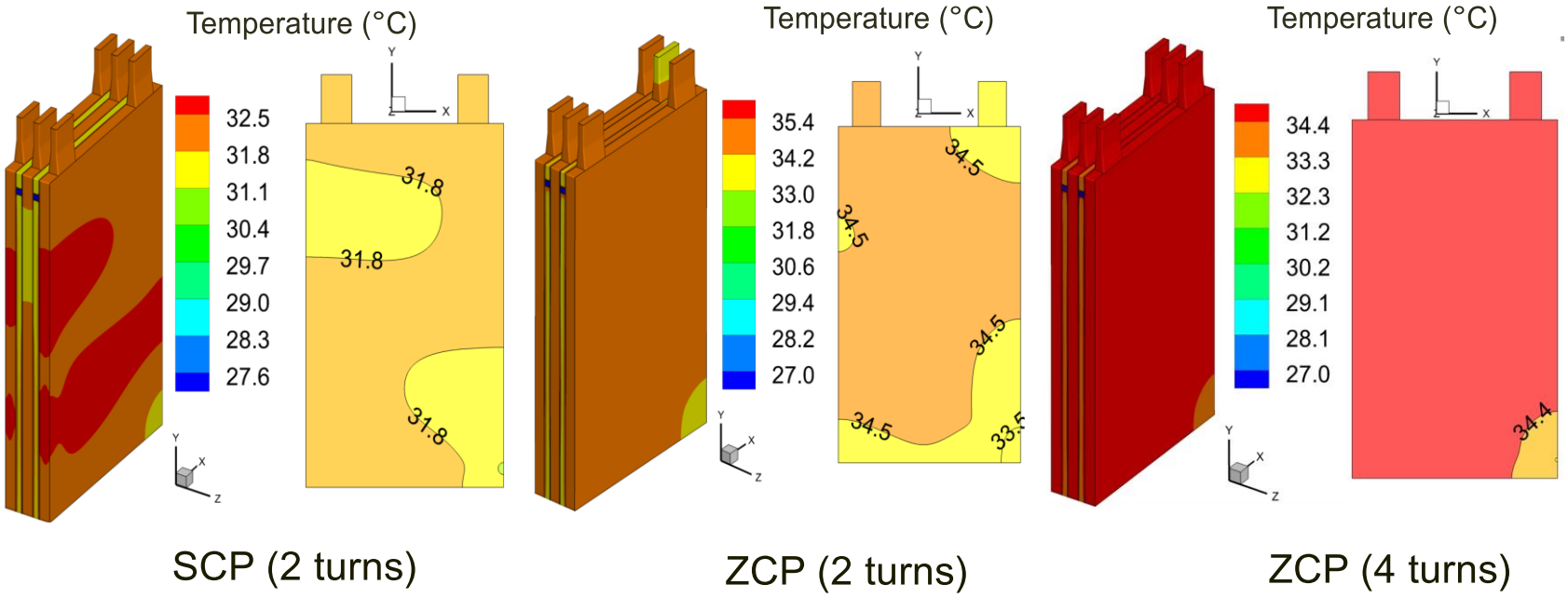

Temperature contours at 900 seconds

Figure 3.48 (a): Analysis for Zig-zag cold plate for US06 drive cycles

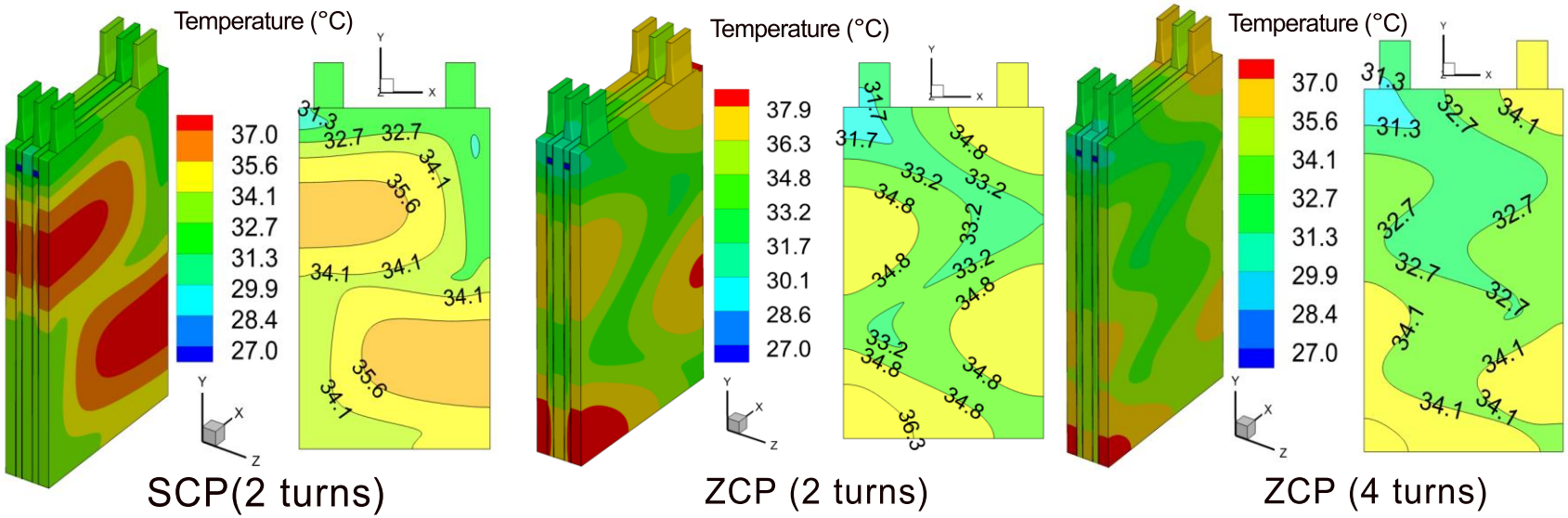

Temperature contours at the end of drive cycle

Figure 3.48 (b): Analysis for Zig-zag cold plate for US06 drive cycles

Fig. 3.49 illustrates the internal dynamics, displaying velocity vectors, streamlines, and melt fractions in the cold plates when there is no coolant flow in the system (900 s). The visualization utilizes several planes along the x-z axis for velocity vectors and a mid-plane along the x-y axis for streamlines. The PCM melt fraction in the ZCP is approximately 1.7 times higher than in the SCP, indicating that the zig-zag channel shape enhances melting and heat transfer. This superior efficiency can be attributed to several factors; firstly, the zig-zag pattern induces greater turbulence within the coolant flow and leads to enhanced convective heat transfer. Secondly, the increased surface area provided by the zig-zag design facilitates more extensive and effective heat exchange. Thirdly, the ZCP design promotes a more uniform distribution of coolant, which significantly reduces thermal gradients and minimizes hotspots across the battery pack. Finally, this design also accelerates the phase change processes of the PCM, enabling quicker melting and solidification, which is pivotal for optimal thermal management. This is further supported by the velocity vector plot, which shows strong convection currents within the PCM domain of the ZCP, promoting more effective intermixing and heat distribution. Given these advantages the ZCP with four turns is selected for further investigation, promising enhanced thermal regulation and efficiency.

Effect of inlet coolant flow velocity for ZCP with Intermittent cooling

To evaluate the impact of inlet coolant velocity, additional flow velocities of 0.1 m/s, 0.3 m/s, and 0.4 m/s were investigated with the coolant inlet temperature maintained at 27 °C across all cases. Fig. 3.50(a-c) depicts the temperature of the battery pack, melting rate of the PCM, and the maximum temperature gradient (ΔT) within the battery. ΔT is defined as the difference between the maximum and minimum temperature inside the cell domain. Before the onset of the coolant flow, i.e., until 80% of the PCM gets melted, the battery temperature, melt fraction, and temperature gradient remained consistent across all velocities.

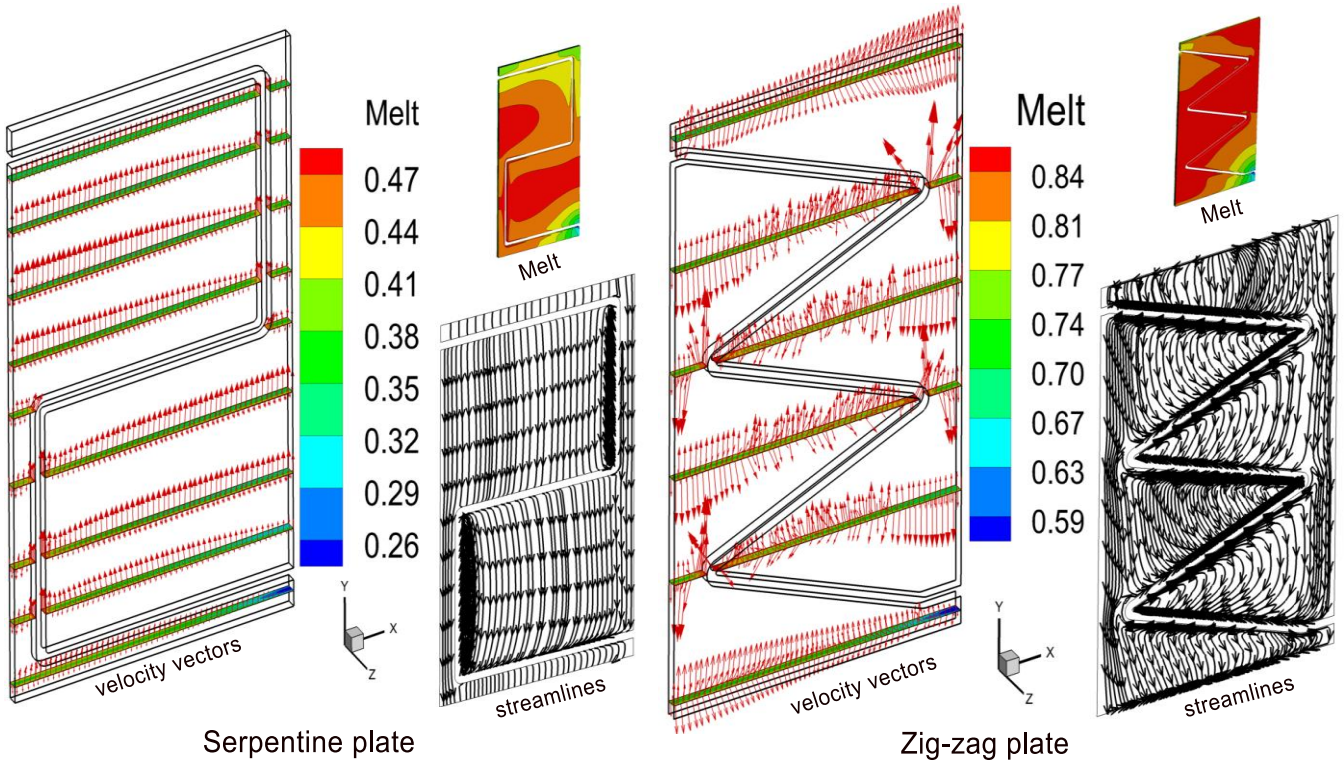

Figure 3.49: Velocity vectors, streamlines and PCM melting analysis

This is expected, as there is no coolant flow during this regime, and these parameters remain unaffected. At 930 seconds, coolant flow started, resulting in a decline in both battery temperature and PCM melt fraction, with the rate of change proportional to the flow velocity. The lowest battery temperature of 32.6 °C, 31.22 °C, 30.2 °C and 30.1 °C is reported for a coolant flow velocity of 0.1 m/s, 0.2 m/s, 0.3 m/s and 0.4 m/s, respectively. This shows that increasing the coolant flow velocity enhances convective heat transfer resulting in a lower battery temperature.

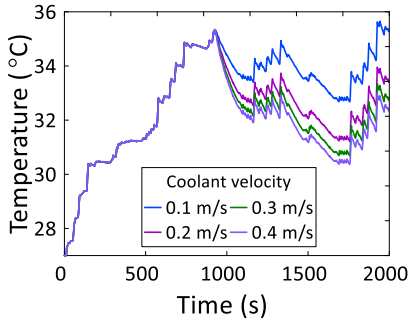

(a) Effect of coolant velocity on battery temperature

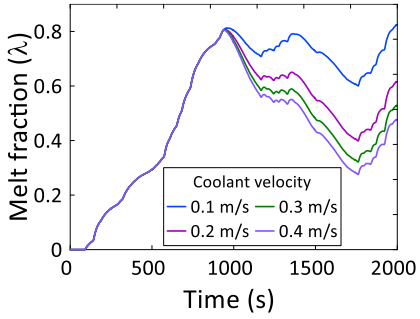

(b) Variation in the melt fraction with coolant velocity

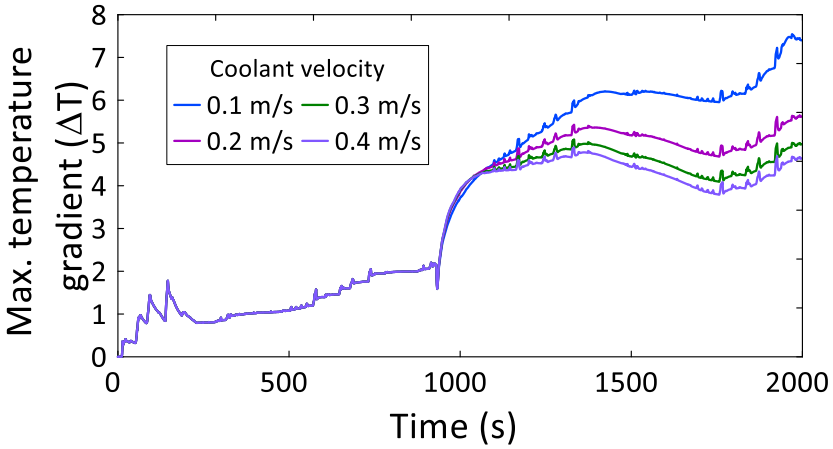

(c) Effect on the maximum temperature gradient with coolant velocity

Figure 3.50: Effect of coolant flow velocity for Zig-zag cold plate (4 turns) with intermittent cooling

During periods without coolant flow, the temperature gradient stayed below the critical 5 °C threshold. However, upon the initiation of coolant flow, the gradient increased temporarily. This increase can be attributed to the rapid heat removal from cells and PCM adjacent to the cooling

channel walls, leading to localized temperature drops and thus a temporary spike in the temperature gradient. The low thermal conductivity of the PCM initially hampers the heat diffusion, but as coolant flow continues, the temperature gradient decreases and stabilizes. At the end of the drive cycle, an increase in gradient is noted, likely due to high demand during this phase. Compared with an inlet velocity of 0.2 m/s, the temperature gradient remains less than 5 °C for flow velocity of 0.3 m/s and 0.4 m/s, and the average battery temperature is lower by 0.48 °C and 0.78 °C for the entire coolant flow duration. Therefore, for further investigation, the coolant flow velocity of 0.3 m/s is chosen, instead of 0.2 m/s, for intermittent cooling (IC) strategy.

Effect of coolant inlet temperature for ZCP with Intermittent cooling

To assess the impact of lowering the coolant inlet temperature on the intermittent cooling strategy, additional temperatures of 20 °C and 15 °C were evaluated. Fig. 3.51 (a-c) illustrates the battery temperature, PCM melt fraction, and maximum temperature gradient, respectively. Results indicate that a decrease in coolant inlet temperature enhances the rate of heat transfer, leading to a rapid decline in both battery temperature and PCM melt fraction. However, the delayed initiation of flow combined with the low coolant temperature introduces a higher temperature gradient in the system.

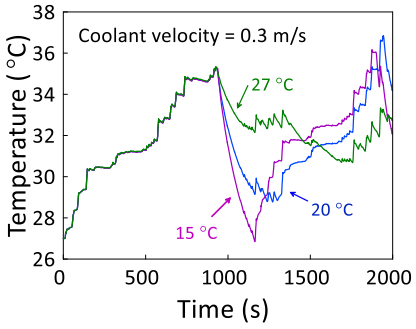

(a) Effect on battery temperature

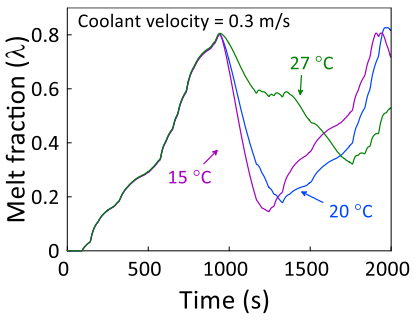

(b) Effect on melting of PCM

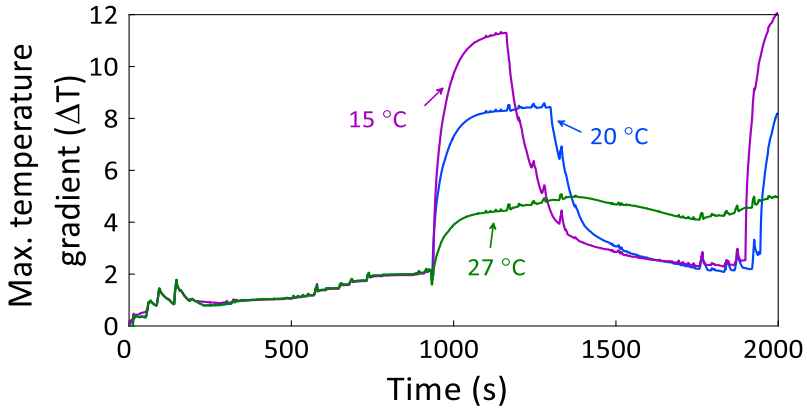

(c) Variation in the maximum temperature gradient with inlet coolant temperature

Figure 3.51: Effect of inlet coolant temperature for Zig-zag cold plate (4 turns) with intermittent cooling (IC)

Fig. 3.52(a) depicts the duration of coolant flow at different inlet temperatures. At 15 °C, the melt fraction swiftly drops from 0.8 to 0.2 within 228 seconds, and the average battery temperature decreases from 35.12 °C to 26.84 °C. Subsequently, the coolant flow is shut off due to the operational parameters ($V_{coolant} = 0\ as\ \lambda < 0.2$), and both temperature and melt fraction begin to rise again. Despite the quick reduction in PCM melt fraction, the maximum temperature gradient remains elevated and does not stabilize due to the premature cutoff of coolant flow. This results in a significant temperature disparity between the cell regions close to the cooling channels and those farther away. A similar pattern is observed with a coolant temperature of 20 °C; however, this effect is not replicated at the standard inlet temperature of 27 °C, where the flow does not cease prematurely, allowing for a more uniform temperature distribution within the cell domain. Consequently, using excessively low coolant temperatures in this intermittent cooling configuration is not advisable due to the unstable temperature gradients it induces. Fig. 3.52(b-c) displays the temperature contours at the end of the US-06 cycle for both intermittent and continuous cooling scenarios using the zig-zag cold plate.

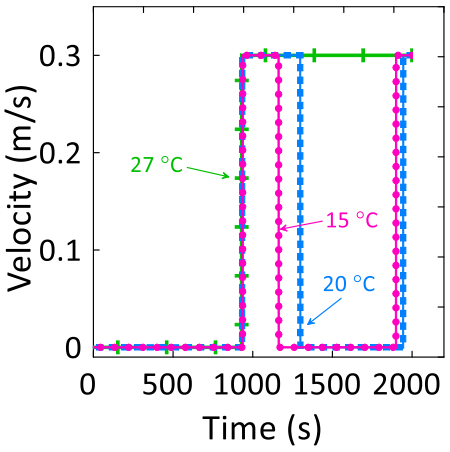

(a) Coolant flow duration at different inlet temperatures

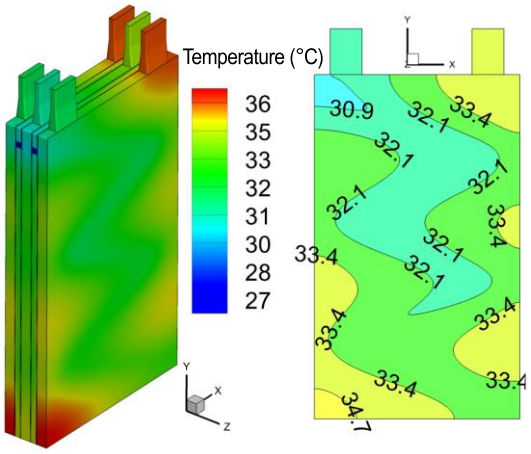

(b) Intermittent cooling (IC)

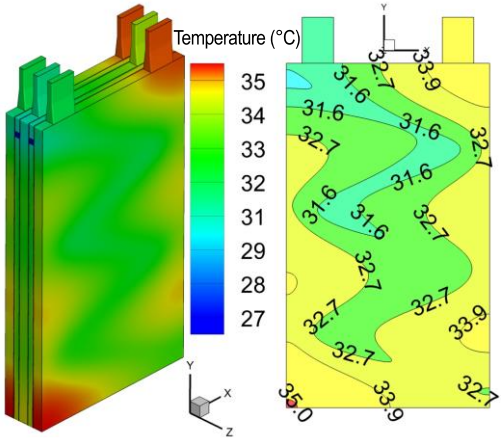

(c) Continuous cooling (CC)

Figure 3.52: Analysis of coolant flow duration and temperature contours

Based on these observations, for continuous cooling, the coolant flow velocity is maintained at 0.2 m/s, while for intermittent cooling, it is set at 0.3 m/s with an inlet temperature of 27 °C for both strategies. Although the temperature and temperature gradient are lower in CC

compared to IC, it is noteworthy that during IC, the coolant flows for only 57.2% of the cycle time. Despite this reduced engagement, the battery temperature and gradient remain within the optimum range, demonstrating the efficiency of the intermittent cooling strategy.

Analysis for WLTP, HWFET and UDDS drive cycles

The WLTP Class 3 driving cycle offers a comprehensive representation of real-world driving conditions, encompassing urban, suburban, and highway segments. The first half of the WLTP cycle and the entirety of the UDDS simulate urban conditions, characterized by frequent start-stop actions and moderate currents generally below 50A. In contrast, the latter half of the WLTP cycle features highway driving scenarios, including hard accelerations where currents range from 100A to 150A, indicative of rapid speed increases and overtaking maneuvers. The HWFET cycle, simulating smoother highway driving, exhibits fewer harsh accelerations and maintains currents mostly below 50A, except during brief periods of hard deceleration and subsequent acceleration around 300 seconds. Fig. 3.53 (a-c) displays various parameters such as voltage, current, SOC, battery temperature, and PCM melt fraction across different profiles of the WLTP drive cycle.

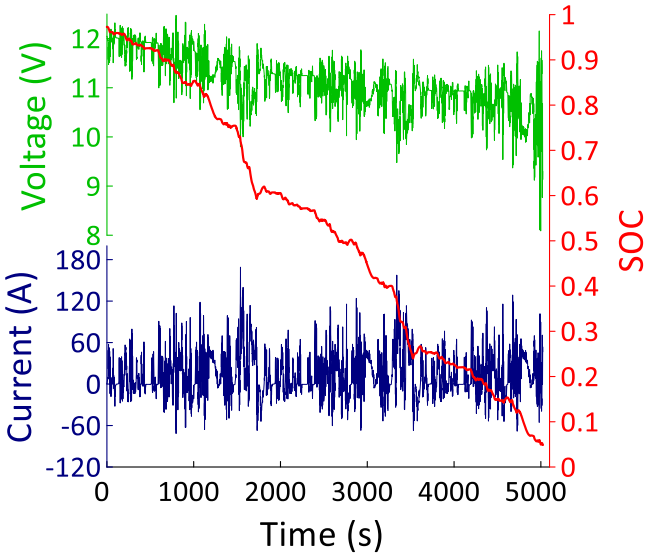

Figure 3.53 (a): Current, voltage and SOC profile (WLTP drive cycle)

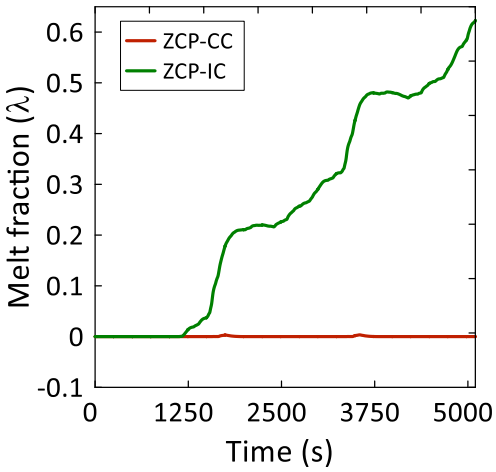

(b) Melting of PCM

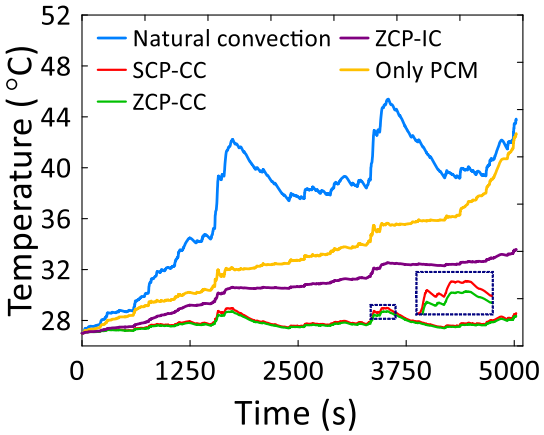

(c) Temperature of the battery pack using different cooling configurations

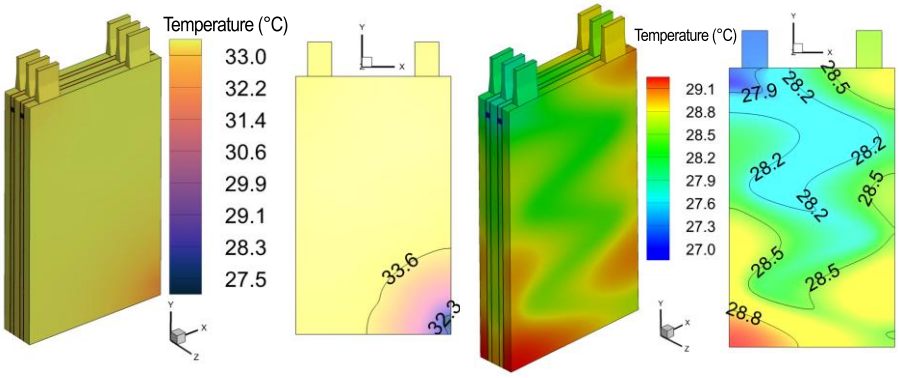

(d) Temperature contour for IC (e) Temperature contour for CC

Figure 3.53 (b-e): Analysis for WLTP drive cycle

The standard WLTP cycle completes in 1800 seconds, but here, it is extended till the SOC falls below 5%, totaling 5108 seconds. Fig. 3.53(b) shows the PCM melt percentages for ZCP with CC and ZCP

with IC. For ZCP-IC, a melting of 68.2% is observed, whereas ZCP-CC shows negligible PCM melt. Temperature analyses (Fig. 3.53(c)) reveal that natural air convection leads to the highest battery temperature peak at 45.39 °C, followed by PCM alone, where the temperature rises to a maximum of 42.68 °C once the PCM is fully melted. Comparatively, the temperatures for ZCP-IC, ZCP-CC, and SCP-CC are significantly lower at 33.71 °C, 28.72 °C, and 29.59 °C, respectively, demonstrating superior thermal management. Fig. 3.53(d-e) illustrating the temperature contours for ZCP-IC and ZCP-CC at the end of cycle show excellent temperature control, confirming the efficacy of hybrid ZCP configurations over SCP in maintaining optimal thermal gradients. The HWFET and UDDS drive cycles, detailed in Fig. 3.54 and Fig. 3.55, last 3200 seconds and 7000 seconds, respectively. For HWFET, the maximum temperatures for natural air convection, only PCM, ZCP-IC, ZCP-CC, and SCP-CC configurations are 41.33 °C, 34.39 °C, 32.24 °C, 28.24 °C, and 28.76 °C, respectively. For UDDS, corresponding temperatures are 36 °C, 35.15 °C, 30.65 °C, 27.66 °C, and 27.98 °C.

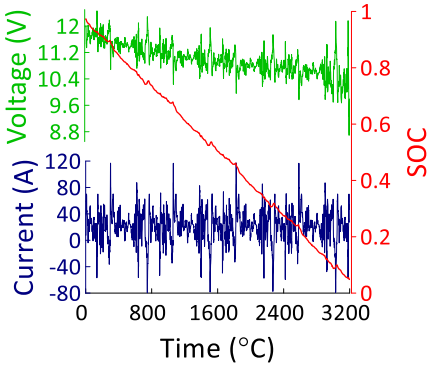

(a) Current, voltage and SOC profile

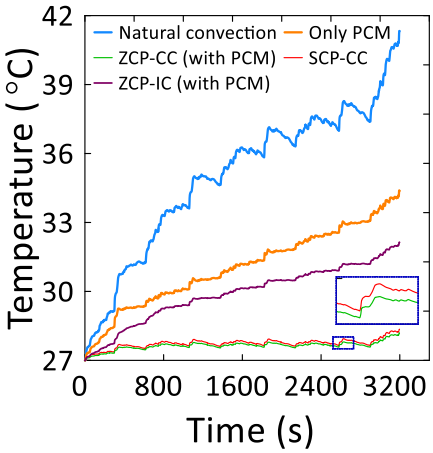

(b) Battery temperature under various cooling schemes

PCM melting for HWFET and UDDS in the PCM-only setup is 74.2% and 85% respectively, and 39.9% and 22.9% for ZCP-IC, with negligible melting in ZCP-CC for both cycles.

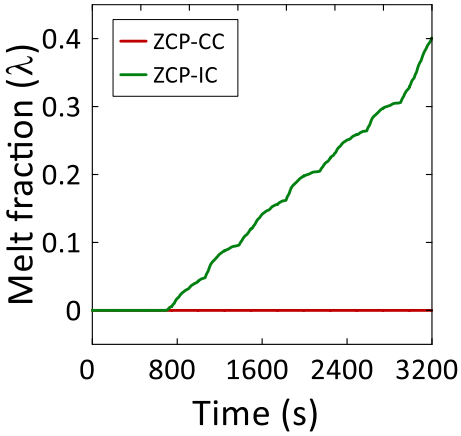

(c) Melting of the PCM

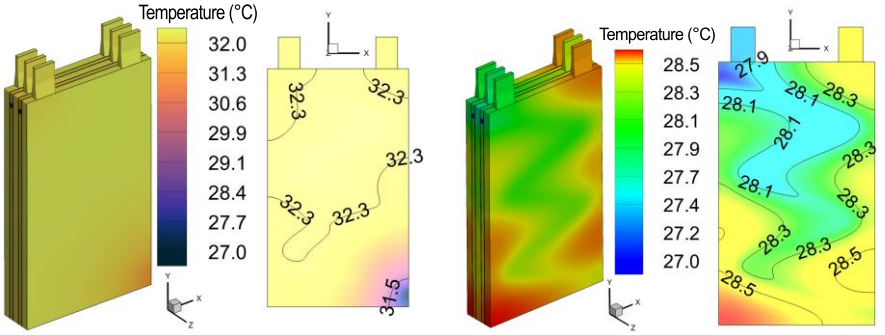

(d) Temperature contour with IC (e) Temperature contour with CC

Figure 3.54: Analysis for HWFET drive cycle

The temperature contours reveal effective management of temperature and temperature gradient for both cases, illustrating an outstanding performance of the current HBTMS across diverse driving conditions.

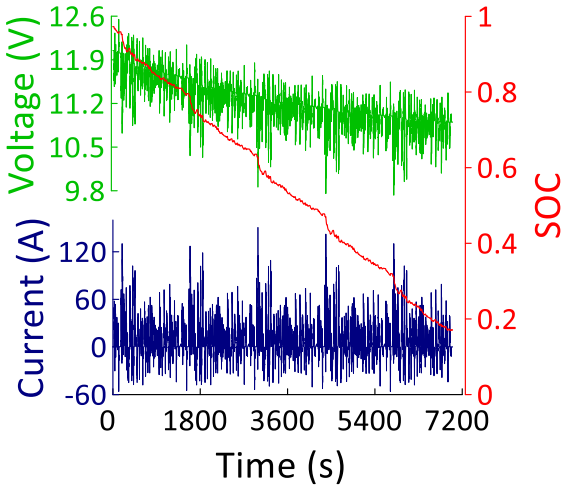

(a) Current, voltage and SOC profile

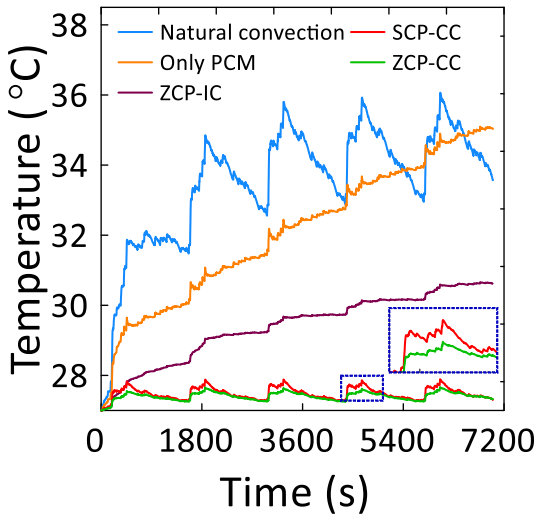

(b) Battery temperature under various cooling schemes

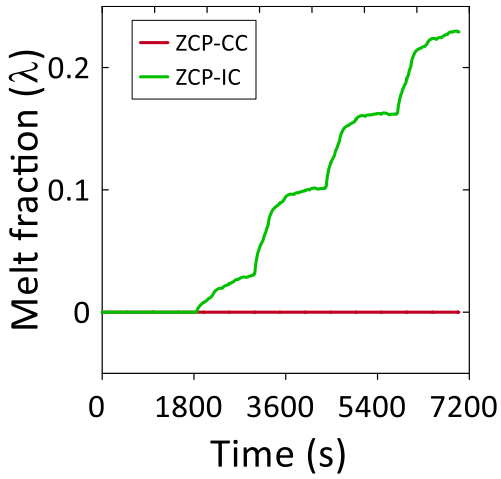

(c) Melting of PCM

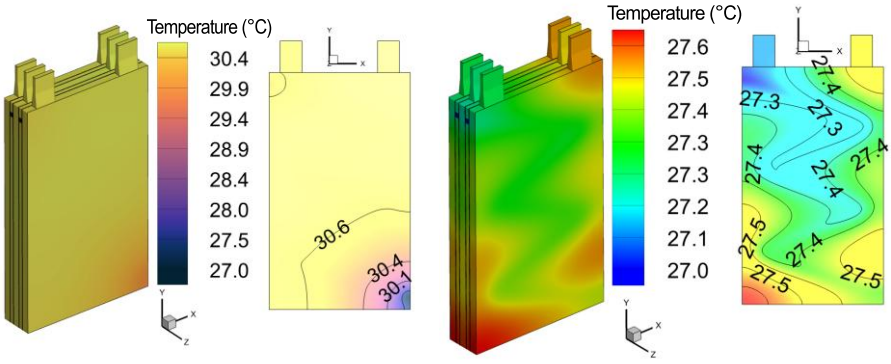

(d) Temperature contours with IC

(e) Temperature contours with CC

Figure 3.55: Analysis for UDDS drive cycle

Continuous discharge charge cycles

The 5C discharge and 1C charge cycles

This study further evaluates the thermal performance of various cooling strategies during constant current rapid discharge and charge cycles. The discharge rates of 5C and 4C, and a charge rate of 1C are used. Each cycle initiates with a rapid discharge at the specified 'C' rate, continuing until reaching the discharge cut-off (2.5V per cell), immediately followed by charge to a cut-off of 4.1V per cell, without any intervening rest period.

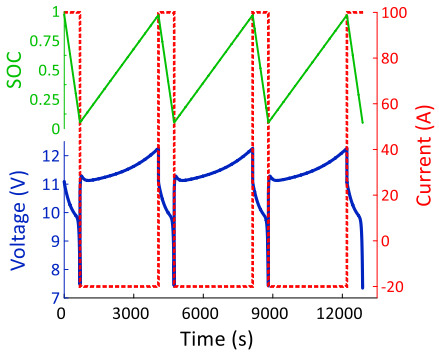

(a) Current, voltage and SOC profile

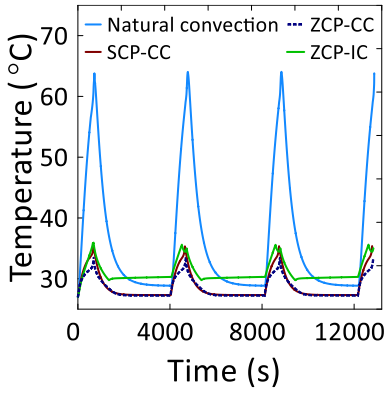

(b) Battery pack under various cooling schemes

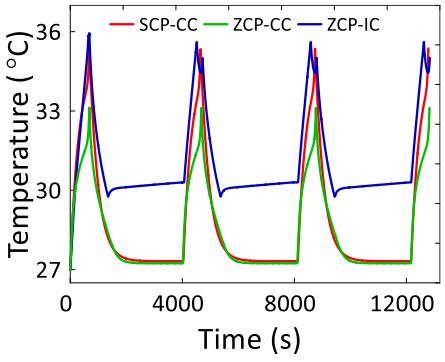

(c) Battery temperature for different cold plates

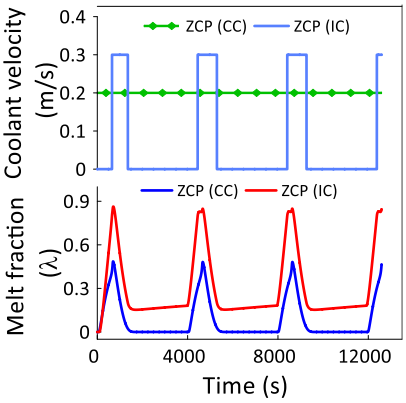

(d) Melting of PCM and coolant flow analysis

Figure 3.56: Analysis for 5C-1C discharge-charge cycles

This discharge-charge process is executed three times consecutively, ending with a final discharge that marks the end of the cycle. A 5C

discharge takes approximately 680 seconds and a 1C charge takes 3388 seconds, resulting in a total operational time of 12,800 seconds. The current, voltage, and the SOC profile during the cycle are shown in Fig. 3.56(a), demonstrating a linear SOC due to the constant current of 100A during discharge and 20A during charge. A significant amount of heat is generated during the rapid discharge, raising the battery temperature considerably compared to the charging periods. Fig. 3.56(b) depicts the battery temperature rise, with the recorded peak temperatures of 62.5 °C for natural air convection, 33.12 °C for hybrid ZCP with CC, 35.9 °C for hybrid ZCP with IC, and 35.4 °C for SCP with CC. Fig. 3.56(c) further details the comparison between SCP (without PCM) and hybrid ZCP with CC and IC.

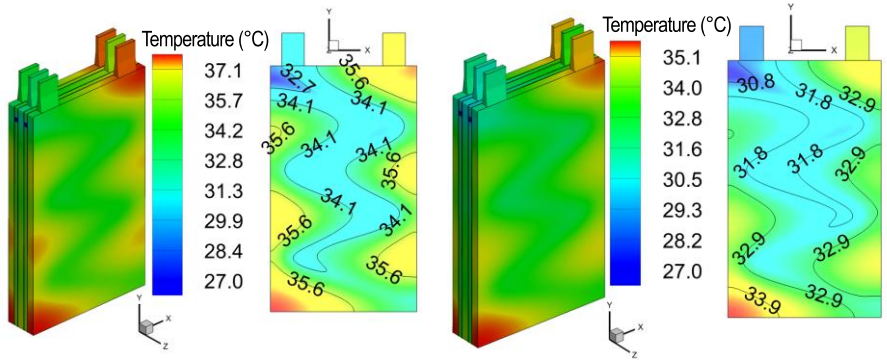

(a) Using intermittent cooling (b) Using continuous cooling

Figure 3.57: Temperature contours at the end of 5C-1C cycle

With CC, the battery temperature during charging nearly returns to ambient conditions. In contrast, with intermittent cooling, once the coolant flow begins, both the battery temperature and PCM melt fraction decrease. The coolant flow stops when only 20% of the PCM remains liquid, at which point the battery temperature is 29.76 °C. The residual PCM maintains this temperature, which gradually increases during the charging period, reaching 30.34 °C by the end of charge. Therefore, at the start of the second discharge cycle, the battery temperature is 30.34 °C, about 3.34 °C higher than ambient, and it reaches 35 °C at the end of the second discharge.

Fig. 3.56(d) reveals the variation in PCM melt fraction and coolant flow duration for different coolant velocities. For ZCP-IC, the melt fraction oscillates between 86.3% and 15.6%, while for ZCP-CC, it ranges from 48.5% to a full solidification at 0% during the charging phase. Temperature contours confirm that the peak temperature at the end of the first discharge cycle with IC strategy is only about 3 °C higher than with CC, while maintaining a temperature gradient of less than 5 °C throughout the entire cycle. The total coolant flow duration for the complete cycle for ZCP-(IC) is 2616 seconds, which is about 20.43% of the total cycle time. Fig. 3.57(a-b) illustrates the exceptional temperature management achieved with both cooling strategies at the end of the discharge. These observations suggest that the intermittent cooling strategy using a hybrid cold plate could be very useful in maintaining the battery temperature by wishfully utilizing the PCM and coolant ultimately leading to save cost and weight.

The 4C discharge and 1C charge cycles

The time for complete discharge for 4C discharge rate is 854 seconds and the total cycle time is 12424 seconds. During the 4C discharge cycles, the rise in battery temperature is less severe compared to the 5C cycles because decreases current demand and rate of electrochemical reactions. Fig. 3.58(a) presents the variation in current, voltage, and SOC of the battery pack, while the corresponding temperature rise is detailed in Fig. 3.58(b-c). The maximum reported temperatures are 55.7 °C for natural air convection, 30.81 °C for ZCP-CC, 35.3 °C for ZCP-IC, and 33.2 °C for SCP-CC. It is to be noted that the peak temperatures for ZCP-CC and ZCP-IC are lower by 24.8 °C and 20.4 °C, respectively, compared to the natural convection scenario. From Fig. 3.58(c), for the case of ZCP-IC, approximately 62% of the PCM melts by the end of the first discharge cycle, causing a 6 °C temperature increase and leading to 33 °C battery temperature.

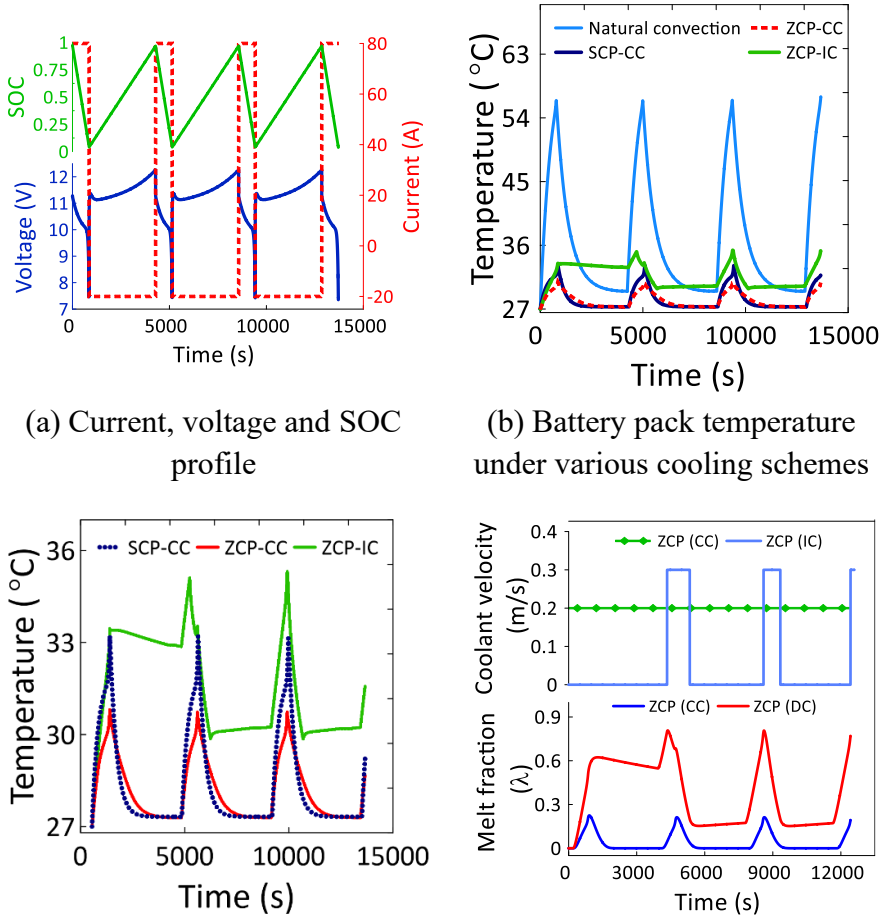

(a) Current, voltage and SOC profile

(b) Battery pack temperature under various cooling schemes

(c) Battery pack temperature for different cold plates

(d) Melting of PCM and coolant flow analysis

Figure 3.58: Analysis for 4C-1C discharge-charge cycles

Since the melt fraction remains less than 80%, there is no coolant flow during the first discharge. This is followed by the charging period and then the second discharge where the melt fraction exceeds 80%, triggering the coolant flow. The onset of coolant flow and the melt fraction plot have been illustrated in Fig. 3.58(d); the maximum melt fraction for IC is 80.7% and for CC is 22.4%. Clearly, the performance of the hybrid zig-zag cold plate in CC is superior to that of the SCP, reducing the peak average temperature by 2.39 °C (Fig. 3.58(c)), stating the enhanced performance of ZCP over the SCP. Temperature contours at the end of the first discharge are shown in Fig. 3.59(a-b), demonstrating effective thermal management.

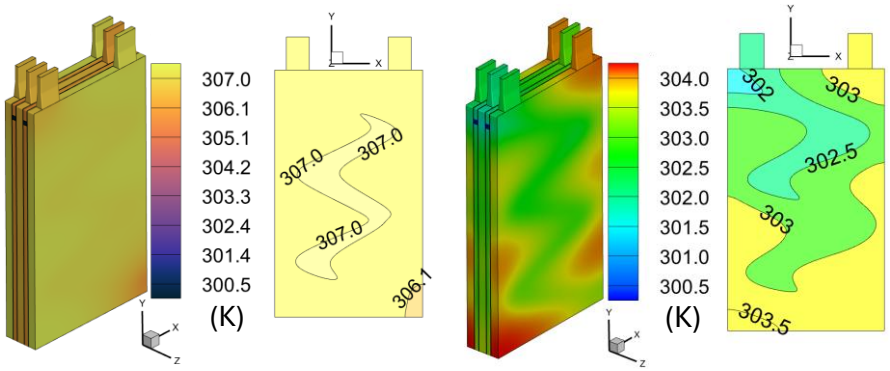

(a) Temperature contours using the intermittent cooling strategy

(b) Temperature contours using continuous cooling strategy

Figure 3.59: Temperature contours at the end of 4C-1C cycle

Table 3.3.3 and Table 3.3.4 summarize the battery temperature, PCM melt fraction, and coolant flow under various thermal loads and cooling strategies employed in this study. The reduction in temperature rise for cooling strategy is calculated as:

$$Temperature\ reduction\ (\%) = \left|\frac{\Delta T_{with\ TMS} - \Delta T_{without\ TMS}}{\Delta T_{without\ TMS}}\right| \times 100 \quad (3.74)$$

Table 3.3.3: Thermal performance of various cold plates under realistic drive cycles

Cases →	US06				WLTP				UDDS				HWFET			
Parameters ↓	NC	SCP (CC)	ZCP (CC)	ZCP IC	NC	SCP (CC)	ZCP CC	ZCP IC	NC	SCP (CC)	ZCP CC	ZCP IC	NC	SCP (CC)	ZCP CC	ZCP IC
T_{max} (°C)	83	33.4	32.2	35.6	45.7	29.5	29.1	32.9	36.1	27.8	27.6	30.8	41.5	28.9	28.7	32.4
T_{avg} (°C)	62	30.9	30.1	32	37.3	28	27.7	30.2	33.5	27.4	27.2	29.2	35	27.8	27.6	29.9
% Reduction (T_{avg})	-	88.5	90.8	84.7	-	86.6	88.7	68.4	-	91.2	93.4	58.2	-	90	92.5	63.7
ΔT_{max} (°C)	2.2	2.8	4.1	4.8	3.8	1.3	1.1	1.7	1.8	0.46	0.4	1	1.6	1.09	1.1	1.4
ΔT_{avg} (°C)	0.9	1.4	3	2.6	0.9	0.6	0.54	1	0.8	0.17	0.15	0.7	0.7	0.49	0.6	0.8
λ_{max}	-	-	0.53	0.8	-	-	0	0.62	-	-	0	0.22	-	-	0	0.4
λ_{avg}	-	-	0.21	0.43	-	-	0	0.25	-	-	0	0.08	-	-	0	0.14
% of coolant flow duration for entire cycle time	-	100	100	57.2	-	100	100	0	-	100	100	0	-	100	100	0

Here, NC: Natural air convection cooling, SCP: Serpentine cold plate (2 turns, without PCM), ZCP: hybrid Zig-zag cold plate (4 turns), CC: continuous cooling, IC: Intermittent cooling

Table 3.3.4: Thermal performance of various cold plates under cyclic operations

Cases →	4C-1C				5C-1C			
Parameters ↓	NC	SCP (CC)	ZCP CC	ZCP IC	NC	SCP (CC)	ZCP CC	ZCP IC
T_{max} (°C)	56	33.2	31.8	35.7	62	36.4	33.4	36.9
T_{avg} (°C)	38.2	28.5	28.3	31.5	40.8	29.2	29.1	31.7
% Reduction in T_{avg}	-	86.5	88.7	82.7	-	88.8	90.6	85.8
ΔT_{max} (°C)	6.8	2.5	2.8	4.1	8.1	3.4	4.4	4.72
ΔT_{avg} (°C)	4.9	0.5	1.2	1.8	5.5	0.8	1.38	1.9
λ_{max}	-	-	0.2	0.8	-	-	0.48	0.86
λ_{avg}	-	-	0	0.3	-	-	0.08	0.29
% of coolant flow duration for entire cycle time	-	100	100	13.9	-	100	100	20.4

Here, NC: Natural air convection cooling, SCP: Serpentine cold plate (2 turns, without PCM), ZCP: hybrid Zig-zag cold plate (4 turns), CC: continuous cooling, IC: Intermittent cooling

Additionally, the total power consumption and coolant flow duration for each drive cycle using different cold plates and cooling strategies are presented in Fig. 3.60. The bar charts illustrate the total coolant flow time, while the line plot indicates the total energy consumed for pumping the coolant.

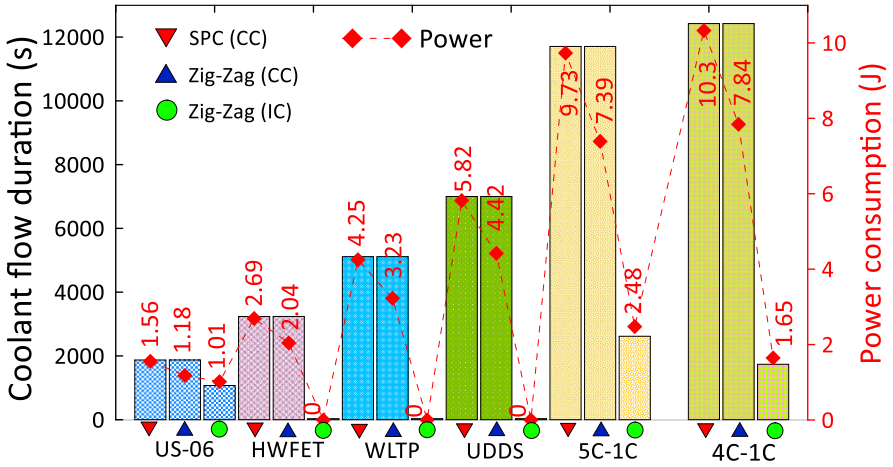

Figure 3.60: Coolant flow duration and total power consumption for all the cases

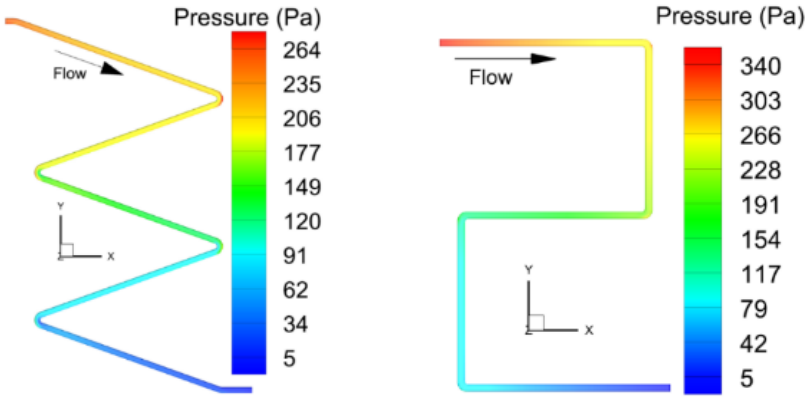

(a) Ziz-zag 4 turns (b) Serpentine 2 terns

Figure 3.61: Pressure contours for various coolant flow design

For CC cases, the total coolant flow duration equals the total cycle time, whereas in IC, it varies based on the melting and solidification of PCM. As expected, power consumption is directly proportional to the coolant flow duration; however, the required pumping power also depends on the design of the cold plate. Fig. 3.61 demonstrates the pressure drop in the serpentine and the zig-zag cold plate. The SCP with two turns exhibits a higher pressure drop compared to the ZCP with four turns,

resulting in greater pumping power requirements for the SCP. In all drive cycle cases, the ZCP offers lower pumping power demands while delivering better thermal performance than the SCP. In addition, significant power savings can be achieved using the intermittent cooling strategy.

Another advantage of the hybrid ZCP is its reduced weight compared to the conventional SCP without PCM. To illustrate these benefits, a simple cost analysis is conducted using the 4C-1C discharge-charge cycle:

(a) Savings in running cost from using zig-zag a cold plate: As shown in Fig. 3.60, a total energy consumption of 10.3 J is required using SCP, whereas 1.65J is required using the ZCP with IC strategy. Thus, for the entire duration of the cycle (12424 seconds), the ZCP saves 8.65 J, which is 83.9% less from the energy required from SCP while maintaining the battery pack in the optimum temperature range. Assuming a usage of EV consisting of 400 cold plates and operating for 50 hours/week, the energy savings can be up to 2.6 MJ per year.

(b) Savings from reduction in weight by hybrid cold plate: The mass of the SCP used in this study is 368 grams, and the mass of the hybrid ZCP is 173 grams, about 52.9% lighter than the former. Although the total volume of both the cold plates is same, the reduced weight in the hybrid cold plate can be attributed to the low density of the PCM, which is contributing to about 74% of the total cold plate volume.

3.4 Conclusion

The present chapter reports the performance analysis of two configurations of battery thermal management systems: a passive system based on metal foam–phase change material (MF–PCM) composites, and a hybrid system integrating PCM with liquid cooling.

Both cell-level and battery pack-level behaviours are investigated under a variety of operating conditions, including steady-state, transient, and extreme thermal environments. The results from each study are discussed below.

In the first study, a detailed three-dimensional (3D) thermal analysis has been carried out to analyse the effect of various thermal loading scenarios, including steady, dynamic conditions, thermal abuse conditions (internal and external shorting), realistic EV drive cycles, PCM thickness and porosity values on the thermal performance. The PCM module with 8 mm thickness is found to maintain safe temperatures during 5C discharging of a 20 Ah prismatic cell. The temperature rise is found to reduce by 56% compared to natural convection cooling by employing MF-PCM composite with a porosity value of 0.95; this configuration maintains a peak temperature of 313.8 K and a temperature gradient below 5 K for scaled 7S1P modules. Also, for both aggressive and normal driving cycles, the MF–PCM system is found to regulate the cell temperature, with substantial PCM melting and minimal thermal deviation.

In the second part of the study, the previous analysis has been extended that consider a hybrid system, involving liquid-cooled plate with PCM under continuous and melt-fraction-triggered intermittent cooling strategies. The hybrid configuration with 4-turn zig-zag channel has been evaluated under four standardized EV drive cycles (HWFET, WLTP, UDDS, US-06) and two rapid charge–discharge profiles (5C–1C and 4C–1C). Although the PCM is able to absorb transient heat loads, its thermal buffering capacity deteriorates with continuous melting, necessitating supplementary cooling. The hybrid system minimizes the cell temperature, reduces thermal gradients, and enhances PCM phase transitions while reducing system weight by 52.9%. Under intermittent cooling, the system is found to achieve energy savings of 83.9%, 76.7%, and 34.7% for 4C–1C, 5C–1C, and US-06 cycles, respectively, and eliminates the need for coolant flow entirely in WLTP, UDDS, and HWFET cycles. The thermal performance is found to

improve with the increase in the coolant flow velocity and reduction in the inlet temperature; for instance, in the US-06 cycle, with the increase in the flow velocity from 0.2 m/s to 0.3 m/s, the reduction in peak temperature and temperature gradient is found to 1.1 °C, and 0.84 °C, respectively. However, in low-diffusive PCMs, initial temperature gradients may temporarily rise before stabilizing during continued cooling.

These studies highlight the efficacy of MF–PCM and hybrid PCM–liquid systems in providing robust, efficient, and adaptable thermal management solutions for high-performance LIB modules. The developed 3D model integrates phase-change dynamics with conjugate heat transfer to capture both transient and steady behaviours under realistic discharge–charge conditions. Compared to natural convection, the MF–PCM configuration with 8 mm PCM and 0.95 porosity achieves nearly a 56% reduction in peak temperature, while the hybrid PCM–liquid system maintains the cell temperature within 5–6 °C of ambient and can save up to 84% coolant energy under intermittent cooling. These results demonstrate the enhanced heat-dissipation capability and operational efficiency achieved through the proposed configurations. Compared to existing MF–PCM and hybrid cooling studies reported in the literature, the present model shows measurable improvements in temperature reduction, melting uniformity, and energy-saving potential. The use of metal foams and optimized PCM thickness provides higher thermal-conductivity enhancement than conventional PCM-only systems, while the hybrid configuration also exhibits greater coolant-energy savings than typical continuous-flow liquid plates. Together, these findings position the present work as an advancement over earlier studies and provide clear design guidance for the practical implementation of advanced battery thermal management systems.

Chapter 4

Optimizing battery thermal management with phase change materials: Influence of thickness, ambient conditions, and material selection

4.1 General background

Phase change materials (PCMs) have been extensively utilized in thermal management systems due to their ability to absorb and store substantial amounts of heat at nearly constant temperature during phase transition. More recently, PCMs have been employed in passive cooling strategies for lithium-ion battery systems to regulate temperature rise during high-power operations; these systems are found to offer energy-efficient, silent, and compact thermal regulation compared to conventional air or liquid cooling methods. Numerous studies report different methods to integrate PCM into battery thermal management systems (BTMS), including selection of suitable PCM types, thermal conductivity enhancement using metal foams or additives, and the optimization of container or enclosure geometries; however, these studies mostly consider isolated design parameters under constrained conditions and assume a single PCM material, fixed discharge rates, or uniform ambient environments. Such approaches, while informative, do not fully address the complex thermal dynamics encountered in practical scenarios, where environmental conditions and battery loading vary significantly.

In practical applications, PCM performance is governed not only by its intrinsic properties (e.g., latent heat, melting point, and thermal conductivity) but also by external parameters such as ambient temperature and convective heat transfer at the system boundary. These factors affect heat accumulation, latent heat utilization, and the rate of solidification/recharging of the PCM during duty cycles. Inadequate alignment between PCM properties and operating conditions may result in thermal saturation, inefficient phase transition, or localized

overheating, which may reduce the efficiency of the system. Therefore, a systematic study needs to be carried out to analyse the performance of the thermal management module by incorporating various parameters such as PCM thickness, external convective heat transfer coefficients, ambient temperature, and PCM types for different thermal loads.

This chapter aims to address various key challenges by employing both experimental and numerical investigation. Initially, tests are conducted using a commercial cylindrical Li-ion cell (Samsung 18650-25R) to record the surface temperature evolution under different discharge rates and validate the baseline thermal response. Based on the test data, a numerical model has been developed to systematically analyse the effects of critical design and environmental parameters. The study focuses on identifying the optimal PCM layer thickness, PCM filling volume, system performance for a wide range of ambient temperatures, and the influence of external convective heat transfer coefficients on the performance. Furthermore, five commercially available PCM types are analysed, and their performance is compared to determine material suitability under varying thermal loads.

4.2 Methodology

4.2.1 Experimental investigation

The schematic of the experimental setup is shown in Fig. 4.1. It comprises a battery charger/discharger, a data acquisition system for thermal and electrical measurements, a commercial Li-ion cell (test specimen), and a computer for real-time monitoring and data processing. The lithium-ion battery is SAMSUNG (model: 18650-25R, form factor: cylindrical) with a capacity of 2.5 Ah [136-137]. The cell has a diameter of 18 mm and a height of 65 mm; the detailed specifications are listed in Table 4.1. For charging and discharging operations, a programmable DC power supply (BK PRECISION, USA, model 9115) and a DC electronic load (BK PRECISION, USA, model 8510B) were employed. The power supply provides a voltage/current range of 0–60 V and 0–60 A, while the electronic load operates up to 120 V and 120 A. Additionally, a

battery internal resistance tester (HIOKI, Japan, model BT3562A) was used to measure the internal resistance and open-circuit voltage of the cell. A photographic view of the experimental facility is presented in Fig. 4.2.

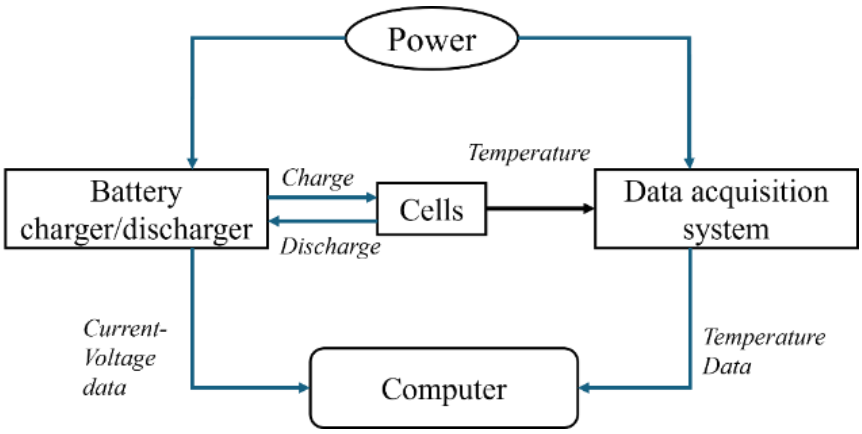

Figure 4.1: Schematic layout of the experimental facility

Table 4.1: Specification of 18650 Li-ion cell [136-137]

Parameter	Value
Make and model	Samsung 18650-25R
Dimensions	Height: 64.85 ± 0.15 mm, Diameter: 18.33 ± 0.07 mm
Capacity	2500 mAh
Nominal voltage	3.6V
Charge (CC-CV)	1.25A, 4.20V,125mA cut-off
Rapid charge (CC-CV)	4A, 4.20V, 100mA cut-off
Max. discharge rate (continuous/pulsed)	20A/35A
Discharge cut-off voltage	2.5V
Weight	45gms

The insulating sleeve of the 18650 Li-ion battery cell was carefully removed to allow direct attachment of thermocouples and a heat flux sensor to the cell surface, as illustrated in Fig. 4.3. Pre-calibrated K-type (Chromel–Alumel) thermocouples were used to record the cell's surface

temperatures, with calibration performed according to ASTM standards over a range of 0 °C to 100 °C [138-139]

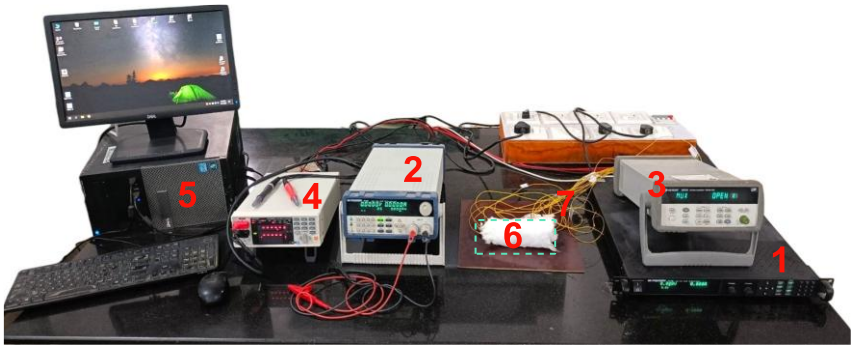

1: Power supply 2: Electronic load 3: Data logger 4: Battery resistance tester
5: Computer 6: Cell with insulation 7: Thermocouples

Figure 4.2: Photographic view of experimental test facility

Four thermocouples were affixed along the axial length of the cell to capture distributed temperature data. A flexible heat flux sensor (15 mm × 30 mm, model FHF05-02, Hukseflux, Netherlands) was also used to measure surface heat flux and temperature. The sensor has a sensitivity of 3×10^{-6} V/(W/m²), and the recorded voltage readings were used to calculate the surface heat flux values.

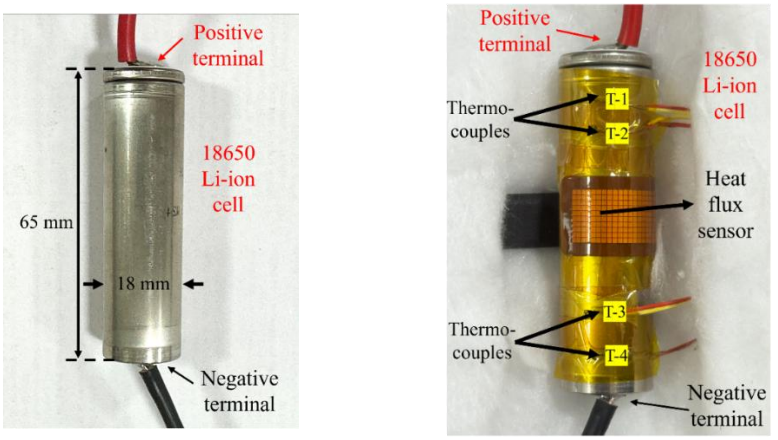

(a) The 18650 Li-ion cell

(b) Cell attached with thermocouples and heat flux sensor

Figure 4.3: The Li-ion cell under investigation

The sensor was centrally positioned along the lateral surface of the cylindrical cell and secured using thermal conductive paste (HM 501, thermal conductivity = 1.5 W/m.K) to ensure proper thermal contact and minimize interface resistance. The sensor covered an area of 450 mm²,

approximately 12% of the cell's lateral surface area. In addition to measuring surface heat flux, the sensor contains an integrated T-type thermocouple, providing an additional temperature reading at the center of the cell. Thus, a total of five surface temperature measurements were recorded along the length of the cell. The average of these five readings was used to determine the overall temperature rise of the cell during discharge. Data from the heat flux sensor and the thermocouples are recorded every 4 seconds using a data acquisition system (Keysight Technologies USA, Agilent 34972A). All experiments were conducted in ambient room temperature conditions.

The battery was charged using the Constant Current–Constant Voltage (CC-CV) method. During the charging process, the cell was initially charged at a specified "C" rate until the voltage reached 4.2 V and then maintained at 4.2 V until the current drops to C/10. Following full charge, the battery rested for 90 minutes before discharging at a specified C-rate (at a constant current) to a cutoff voltage of 2.5V. After completing a discharge cycle, the battery rested for 3 hours to ensure thermal and electrochemical equilibrium with ambient conditions before the next experiment. Each set of experiment is completed three times to ensure experimental repeatability and reliability.

Instrument uncertainties were carefully considered to ensure reliable and accurate measurements. Current and voltage readings were verified using a standard, calibrated multimeter, thereby minimizing any instrument-induced error. The electronic DC power supply utilized in the experiments possesses an uncertainty of 0.01% + 5 mV for voltage measurements and 0.1% + 10 mA for current measurements, while the electronic load introduces an uncertainty of approximately 0.05%. Additionally, preliminary tests with a battery tester confirmed that the selected cells exhibited less than a 1% difference in open-circuit voltage, ensuring consistency and reproducibility in the experimental data. The transient voltage-capacity response and temperature rise data recorded during the discharge cycles were used to validate the numerical model developed in this study.

4.2.2 Numerical modeling

The cell model

The thermal performance of LIBs is primarily influenced by heat generation during electrochemical reactions, which varies with discharge rates and ambient conditions. As discussed in chapter 3, the Multiscale Multi-Domain (MSMD) model is used to simulate the thermal and electrochemical behaviour of lithium-ion batteries. This framework effectively captures the electrochemical heating processes within the battery by solving for localized temperature variations and heat generation dynamics. The conservation equations for energy and current fluxes are given below [108, 124, 139-140]:

$$\frac{\partial \rho_b C_{p_b} T_b}{\partial t} = \nabla.(k_b \nabla T_b) + \sigma_+ |\nabla \varphi_+|^2 + \sigma_- |\nabla \varphi_-|^2 + \dot{q}_{ECh} + \dot{q}_{short} + \dot{q}_{abuse} \quad (4.1)$$

$$\nabla.(\sigma_+ \nabla \varphi_+) = -(j_{ECh} - j_{short}) \quad (4.2)$$

$$\nabla.(\sigma_- \nabla \varphi_-) = j_{ECh} - j_{short} \quad (4.3)$$

Equation (4.1) accounts for temperature changes due to heat generation and thermal conduction in the battery, while Eqns. 4.2-4.3 govern the current flux conservation in the positive and negative electrodes. In this formulation, $\sigma_+ |\nabla \varphi_+|^2 + \sigma_- |\nabla \varphi_-|^2$ represents heat generation due to the ohmic heating in the positive and negative electrode, $\dot{q}_{ECh}$ is the heat due to the electrochemical reactions, and the last two terms account for the shorting or thermal abuse conditions. ρ_b, C_{p_b}, T_b, k_b represent the battery's density, specific heat capacity, temperature, and thermal conductivity, respectively. σ_+ and σ_- denote the electrical conductivities of the positive and negative electrodes, while φ_+ and φ_- correspond to the electric phase potentials.

Calculations for j_{ECh} and $\dot{q}_{ECh}$ are performed using the coupled electrochemical sub-model within this framework. To enhance computational efficiency, the NTGK electrochemical sub-model is seamlessly integrated into the current approach [106]. The NTGK model is a semi-empirical approach that incorporates experimentally derived

parameters, allowing it to couple electrochemical and thermal effects effectively. It is widely adopted for computationally efficient electrochemical-thermal simulations, providing continuous distributions of temperature, voltage, and depth of discharge (DOD).

For the NTGK model, the electrochemical heat generation ($\dot{q}_{ECh}$) and the volume current transfer rate (j_{ECh}) are given by [108, 139-140]:

$$\dot{q}_{ECh} = j_{ECh}\left[U - (\varphi_+ - \varphi_-) - T\frac{dU}{dT}\right] \tag{4.4}$$

$$j_{ECh} = \frac{Q_{nom}}{Q_{ref}Vol}Y[U - (\varphi_+ - \varphi_-)] \tag{4.5}$$

Here, U and Y are model parameters that depend on the depth of discharge (DOD). The DOD is determined using Eq. (4.6), where Q_{nom} denotes the nominal capacity of the battery, Q_{ref} is the reference battery capacity, and Vol represents its volume. For a given battery, its voltage-current relationship can be experimentally obtained, and U and Y are estimated by fitting the experimental data [124], [137]. These parameters are expressed in Eqs. (4.7) and (4.8), where C_1 and are C_2 correction constants, and a_n and b_n (with n = 0 to 5) are the fitting coefficients derived from experimental curve fitting [108, 139-140]:

$$DOD = \frac{Vol}{3600Q_{nom}}\int_0^t jdt \tag{4.6}$$

$$U = \left(\sum_{n=0}^{5} a_n(DOD)^n\right) - C_2(T - T_{ref}) \tag{4.7}$$

$$Y = \left(\sum_{n=0}^{5} b_n(DOD)^n\right) * \exp\left[-C_1\left(\frac{1}{T} - \frac{1}{T_{ref}}\right)\right] \tag{4.8}$$

Finally, the energy conservation equation is expressed as:

$$\frac{\partial \rho_b C_{p_b} T}{\partial t} - \nabla.(k_b \nabla T) = \sigma_+|\nabla\varphi_+|^2 + \sigma_-|\nabla\varphi_-|^2 + j_{ECH}[U - (\varphi_+ - \varphi_-) - T\frac{dU}{dT}] \tag{4.9}$$

The PCM model

The PCM modeling approach, including the enthalpy-porosity method and related assumptions, has been discussed in detail in Chapter 3, Section 3.3.3. The governing equations that describe heat transfer, phase transition, and convective flow within the PCM domain, including the mushy zone resistance, are as follows [124]:

Continuity equation:

$$\frac{\partial \rho}{\partial t} + \nabla . \left(\rho_{pcm} \vec{V}_{pcm}\right) = 0 \tag{4.10}$$

Momentum equations:

$$\text{X – dir.:} \quad \rho_{pcm} \frac{\partial u_{pcm}}{\partial t} + \rho_{pcm}\left(\vec{V}_{pcm} . \nabla\right) u_{pcm} = -\frac{\partial P}{\partial x} + \nabla . \left(\mu_{pcm} \nabla u_{pcm}\right) + S_x \tag{4.11}$$

$$\text{Y – dir.:} \quad \rho_{pcm} \frac{\partial v_{pcm}}{\partial t} + \rho_{pcm}\left(\vec{V}_{pcm} . \nabla\right) v_{pcm} = -\frac{\partial P}{\partial y} + \nabla . \left(\mu_{pcm} \nabla v_{pcm}\right) + S_y + S_a \tag{4.12}$$

$$\text{Z – dir.:} \quad \rho_{pcm} \frac{\partial w_{pcm}}{\partial t} + \rho_{pcm}\left(\vec{V}_{pcm} . \nabla\right) w_{pcm} = -\frac{\partial P}{\partial z} + \nabla . \left(\mu_{pcm} \nabla w_{pcm}\right) + S_z \tag{4.13}$$

Where $S_x, S_y, and\ S_z$ are source terms representing the mushy zone resistance, calculated as follows:

$$S_x = \frac{A_{mush}(1-\lambda)^2}{(\lambda^3 + 0.001)}\left(u_{pcm} - u_{pull}\right) \tag{4.14}$$

$$S_y = \frac{A_{mush}(1-\lambda)^2}{(\lambda^3 + 0.001)}\left(v_{pcm} - v_{pull}\right) \tag{4.15}$$

$$S_z = \frac{A_{mush}(1-\lambda)^2}{(\lambda^3 + 0.001)}\left(w_{pcm} - w_{pull}\right) \tag{4.16}$$

$$S_a = \rho_{pcm} g\, \beta (T - T_{ref}) \tag{4.17}$$

As previously discussed in Chapter 3, Section 3.3.3, the source terms in the PCM model account for buoyancy (S_a), mushy zone resistance

(A_{mush}), and melt fraction (λ) evolution. A_{mush} is set to 10^5, as recommended in literature and pull velocities are neglected by assuming stationary solid PCM. A small constant (0.001) is added in the denominator to avoid division by zero. The melt fraction (λ) is defined as:

$$\lambda = \begin{cases} 0 & (T < T_s) \\ \dfrac{T - T_s}{T_l - T_s} & (T_s < T < T_l) \\ 1 & (T > T_l) \end{cases} \tag{4.18}$$

Finally, the energy conservation equation for the PCM is expressed as:

$$\rho_{pcm} \frac{\partial H}{\partial t} + \nabla\left(\rho_{pcm} \vec{V}_{pcm} H\right) = \nabla \cdot \left(k_{pcm} \nabla T_{pcm}\right), \tag{4.19}$$

where H is the total enthalpy, which includes sensible (h_s) and latent heat (ΔH) contributions:

$$H = h_s + \Delta H, \tag{4.20}$$

$$h_s = \int_{T_o}^{T} C_{p_{pcm}} dT, \qquad \Delta H = \lambda L \tag{4.21}$$

This model effectively captures the PCM's behaviour under different thermal conditions, offering precise predictions of its response to operational heat loads within the thermal management system.

Boundary conditions

The initial condition sets the system temperature at $T(x,y,z) = T_o$, where T_o = 27 °C at t = unless stated otherwise. The following boundary conditions were defined to accurately simulate the heat transfer dynamics for the system:

- Battery and PCM Interface: Thermal continuity holds with

$$-k_b \frac{\partial T}{\partial n} = -k_{pcm} \frac{\partial T}{\partial n} \tag{4.22}$$

- Battery exposed to the environment: Convective BC yields

$$-k_b \frac{\partial T}{\partial n} = h_{surface}\left(T_{b,wall} - T_{amb}\right) \quad (4.23)$$

- PCM exposed to the environment: similar convective condition holds

$$-k_{PCM} \frac{\partial T}{\partial n} = h_{surface}\left(T_{PCM,wall} - T_{amb}\right). \quad (4.24)$$

Here, k_b and k_{pcm} are the thermal conductivities of the battery and PCM, respectively, while T_b and T_{PCM} represent their corresponding temperatures. The convective heat transfer coefficient ($h_{surface}$), between the PCM and the ambient and between the battery and the ambient, is assumed to be 5 W/m²K unless specified otherwise. The battery material properties [67, 140-141], PCM properties [124] and fitted coefficients (a_n and b_n) [110, 141-142] are summarized in Table 4.2, Table 4.3 and Table 4.3, respectively.

Table 4.2: Material properties for the Li-ion cell [67, 140-141]

Properties	Battery (Active zone)	Positive tab (Aluminium)	Negative tab (Copper)
Density (kg/m^3)	1200	2719	8978
Heat capacity (kJ/kg.K)	1700	871	381
Thermal conductivity (W/m.K)	0.413 (Radial) 3 (Tangential/Axial)	202.4	387.6
Electrical conductivity (S/m) σ_+ σ_-	1190000 983000	-	-

Table 4.3: Properties of the PCM [112, 124]

Property	RT-24	RT-35	RT-38	RT-42	RT-47
Density (kg/m^3)	770	770	750	760	770
Heat capacity (kJ/kg.K)	2	2	2	2	2
Thermal conductivity (W/m.K)	0.2	0.2	0.2	0.2	0.2
Viscosity (Pa.s)	0.02	0.02	0.02	0.02	0.02
Latent heat (kJ/kg)	160	160	170	165	160
Solidus temperature (K)	294	304	307	311	314
Liquidus temperature (K)	298	309	312	316	321
Volume expansion (%)	12.5	12.5	12.5	12.5	12

Table 4.4: Fitted coefficients for the 18650 Li-ion cells

a_0	a_1	a_2	a_3	a_4	a_5
4.12	0.1648	-8.03	18.363	-12.577	0
b_0	b_1	b_2	b_3	b_4	b_5
1168.59	-8928	52504.6	-136231	158531.7	-67548.5

Numerical parameters and grid analysis

The governing equations were solved using a double-precision solver to enhance numerical accuracy. Pressure-velocity coupling was performed using the Semi-Implicit Method for Pressure-Linked Equations (SIMPLE) algorithm, pressure discretization was carried out with the Pressure Staggering Option (PRESTO) scheme, and the Quadratic Upstream Interpolation for Convective Kinematics (QUICK) scheme was used for momentum and energy discretization. Each time step underwent up to 500 iterations to ensure full convergence before proceeding. Convergence criteria were set at 10^{-8}, 10^{-10}, and 10^{-10} for continuity, momentum, and energy, respectively. All the simulations were performed on ANSYS Fluent 2023R2 software using the high-performance computing (HPC) resources provided by the Digital

Research Alliance of Canada (Compute Canada), leveraging parallel processing capabilities to optimize computational efficiency.

To balance computational efficiency and numerical accuracy, grid independence and time-step sensitivity analyses were performed for the battery pack model at a 5C discharge rate. The objective was to identify an optimal mesh resolution that maintains solution fidelity while minimizing computational cost. Key thermal and numerical parameters, including maximum battery temperature and Courant number stability, were evaluated. Figure 4.4 presents the results of the grid sensitivity study, along with the mesh layout for the simulation domain. A range of mesh sizes, from 3 mm to 0.5 mm, was tested, corresponding to element counts ranging from 12,971 to 1,820,047. Initial simulations were conducted using a fixed time step of 2 seconds.

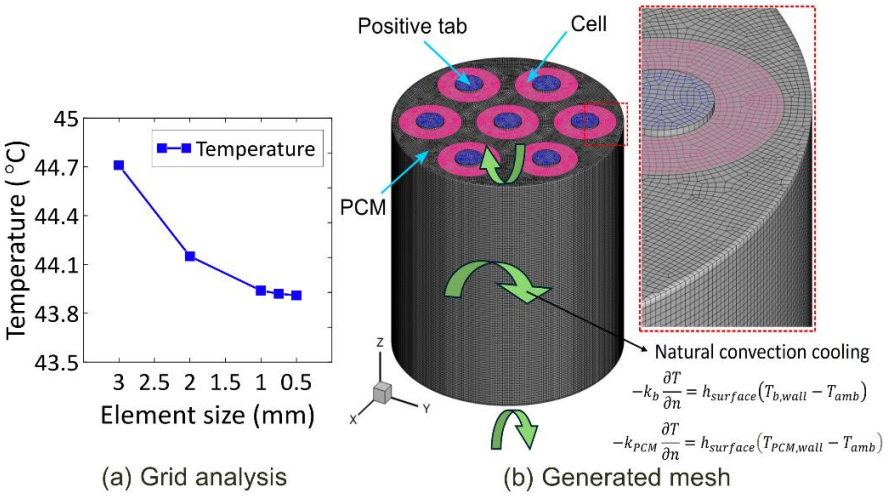

Figure 4.4: Generated mesh for the simulation setup

Reducing the element size from 2 mm to 1 mm yielded a temperature difference under 0.48%, while further refinement to 0.75 mm produced only a 0.08% difference. No significant improvement was observed with a 0.5 mm mesh, confirming that 0.75 mm provides sufficient spatial resolution for accurate simulation results. For the time-step sensitivity analysis, six time steps, 5, 4, 3, 1, 0.5, and 0.25 seconds, were evaluated. Maximum battery temperature ranged from 61.67 °C to 60.98 °C, with deviations of 0.2% for 1s and 0.1% for 0.5s, relative to the reference

time step of 0.25s. Based on these results, a time step of 0.5 seconds was selected for all subsequent simulations, as it provides a suitable trade-off between accuracy and computational cost. The maximum Courant number remained below 1 for the selected mesh and time step, confirming the numerical stability of the simulation setup.

Validation of numerical model and heat generation

Figure 4.5 compares the results for the experimental temperature measurements of the cell with the numerical simulations at three distinct discharge rates: 4C, 3C, and 2C. Higher C-rates correspond to faster discharges with greater heat generation and shorter durations. After each discharge cycle in the experiments, the cell was allowed to passively cool down by natural convection until it reached ambient conditions. The experiments were conducted under ambient conditions, with room temperature maintained at approximately 25 °C throughout the testing period. The numerical model was validated against both phases of the thermal cycle: the initial temperature rise during discharge and the subsequent cooldown period. The validation demonstrates good agreement between simulation and experimental results, with average temperature deviations of 4.10%, 2.45%, and 1.75% for the 4C, 3C, and 2C discharge rates, respectively.

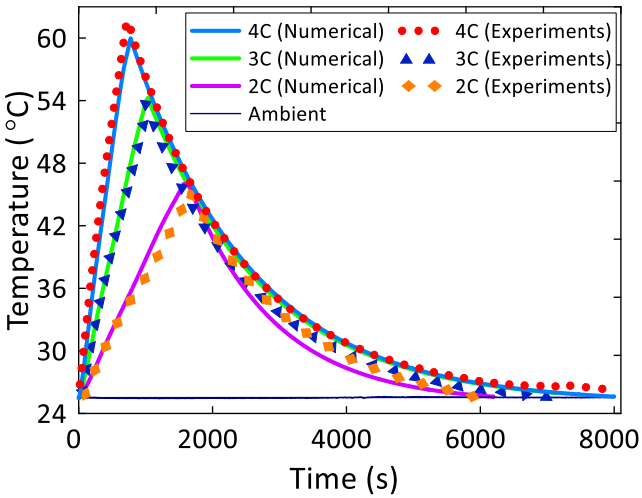

Figure 4.5: Validation of battery model with the experimental test data

These results show that the battery model captures the thermal behaviour of the cell with increasing accuracy as the discharge rate decreases. Figure 4.6 (i-ii) presents a comprehensive validation of the developed PCM-based thermal model against both experimental and numerical reference studies reported by Sun et al. [72] and Patel et al. [143], respectively. Sun et al. [72] analyzed the thermal performance of a cylindrical 26650 Li-ion battery integrated with paraffin wax-based PCM (OP44E), embedded with fins and a nylon outer casing. Their study examined various fin configurations and their effects on controlling battery temperature and promoting uniform melting of the PCM. Subsequently, Patel et al. [143] replicated Sun's experimental configuration [72] numerically and reported a 6–7% deviation in battery temperature from experimental results. For consistency, the present case adopts the same experimental configuration: a battery with four straight longitudinal fins (1 mm thickness), without an additional cylindrical ring, and a uniform heat generation rate of 10 W.

As shown in Figure 4.6(a), the current model shows close agreement of temperature evolution with both prior experimental and numerical results , with an average deviation of about 3.4% from the experimental data, indicating improved predictive accuracy. Figure 4.6(b) illustrates the modelled geometry of the battery–fin–PCM assembly corresponding to the specific test case from Sun et al., [72] and also compares the temperature distribution and PCM melt fraction contours from the current simulation at a representative time step of 1200 seconds, illustrating similar thermal behaviour and melting progression to that observed in the referenced study. This strong agreement in both temperature predictions and melting behaviour confirms the accuracy of the current model, which is therefore used for subsequent thermal performance analysis presented in this work.

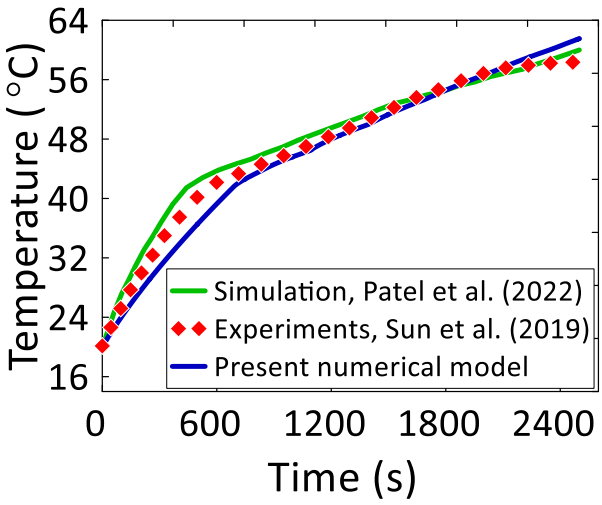

(a) Comparison of cell temperature

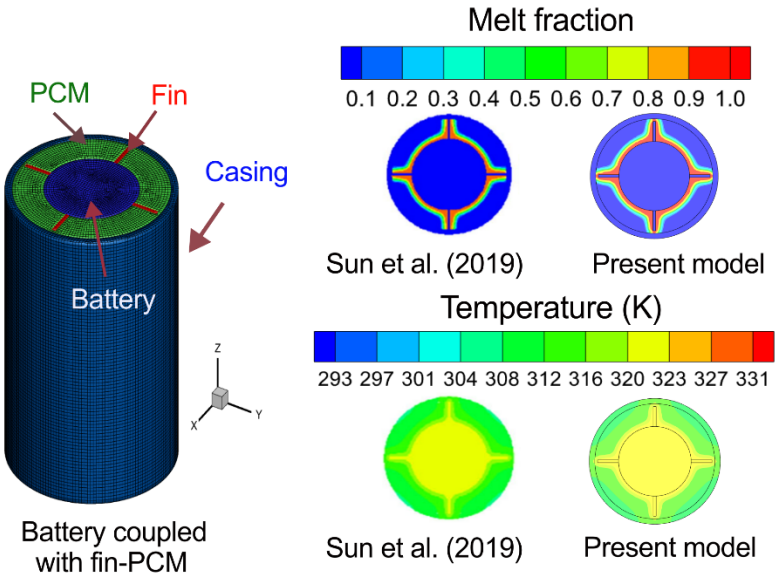

(b) Geometric configuration and thermal response contours

Figure 4.6: Validation of the cell-PCM model with the literature

Figure 4.7(a) illustrates the surface heat flux profiles measured using the heat flux sensor affixed directly to the cell surface during discharge at different C-rates. As observed, the heat flux gradually increases throughout the discharge process and peaks near the end of the cycle. A clear trend is evident: higher discharge rates lead to greater heat release from the cell surface. The peak surface heat flux values recorded were 414.38 W/m² at 4C, 294.5 W/m² at 3C, and 181 W/m² at 2C. Figure

4.7(b) presents the corresponding volumetric heat generation predicted by the NTGK model in ANSYS Fluent.

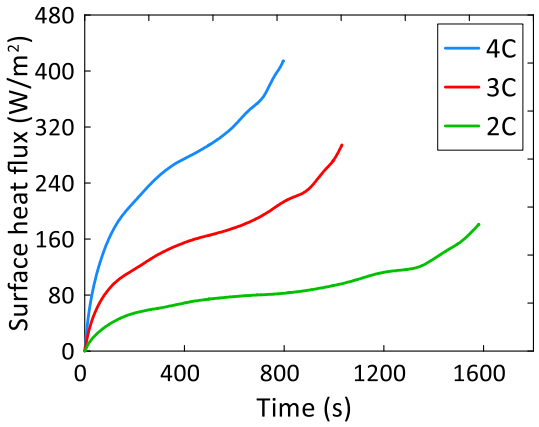

(a) Surface heat flux

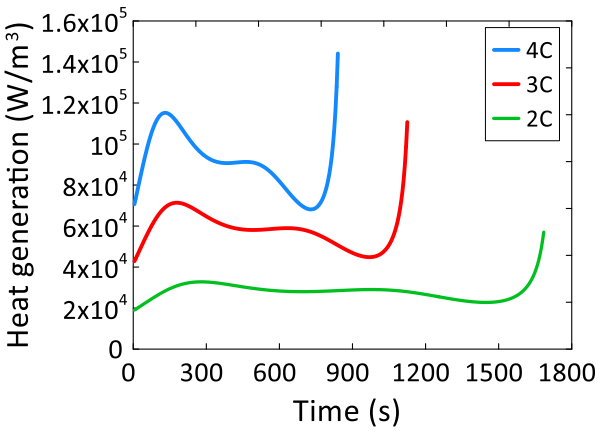

(b) Volumetric heat generation in the cell

Figure 4.7: Heat generation in the cell

This model accounts for both irreversible and reversible heat and captures internal thermal behaviour realistically. The peak volumetric heat generation values predicted by the model were approximately 145,000 W/m³ at 4C, 105,000 W/m³ at 3C, and 62,000 W/m³ at 2C. The volumetric heat generation during discharge shows a non-linear trend, especially at higher C-rates. It starts high, then gradually drops, and rises sharply again near the end of the cycle. This pattern results from changes in internal resistance and state of charge during discharge. At the beginning, the cell is cold, and higher polarization losses lead to greater heat generation. As the cell heats up, internal resistance decreases, so the heat generation drops. Toward the end of discharge, as the SOC

decreases, fewer lithium ions are available to sustain the electrochemical reactions. This leads to an increase in internal resistance and voltage drop, resulting in a sharp rise in heat generation.

4.3 Results and discussion

4.3.1 Effect of PCM thickness on the thermal performance of PBTMS at various discharge rates

The study varied the PCM thickness between the cells from 1 mm to 7 mm to analyse its impact on average battery temperature, maximum temperature gradient, and the amount of melting of the PCM across discharge rates ranging from 2C to 5C. To initiate the analysis, RT-35 was selected as the reference phase change material due to its well-established suitability for battery thermal management. With a melting point near 35 °C, it aligns closely with the optimal operating range of Li-ion cells, enabling effective thermal regulation during discharge. RT-35 also offers a high latent heat capacity (~160 kJ/kg), excellent thermal stability, and is non-toxic, commercially available, and widely recommended in the literature, making it an ideal baseline for evaluating PCM thickness and comparative performance. Table 5 summarizes the simulation results, including the maximum and average battery temperature, maximum temperature gradient, and PCM melt fraction across various PCM thicknesses and discharge rates.

5C and 4C discharge rate

From Figs. 4.8 and 4.9, it is observed that a consistent decrease in maximum battery temperature is observed as PCM thickness increases, demonstrating the PCM's heat absorption capacity and its ability to regulate thermal peaks effectively. At 5C discharge, the maximum battery temperature drops from 60.45 °C (1 mm) to 42.45 °C (7 mm) as reported in Fig. 4.8(a), while at 4C discharge, it decreases from 54 °C (1 mm) to 41.5 °C (7 mm) as reported in Fig. 4.9(a). This reduction highlights the role of PCM in delaying temperature rise by absorbing and storing heat through latent heat mechanisms. The melt fraction trend follows a similar pattern as maximum battery temperature, indicating

higher PCM utilization in thinner layers but greater thermal stability with thicker PCM. At 5C discharge, the melt fraction reduces from 90% (1 mm) to 44% (7 mm), while at 4C discharge, it drops from 86.3% (1 mm) to 36.8% (7 mm) as depicted in Figs. 4.8(b) and 4.9(b), respectively. This confirms that thinner PCM layers saturate quickly, leading to reduced thermal regulation capacity, whereas thicker layers absorb more heat over time but remain partially melted, improving long-term stability while reducing PCM utilization efficiency.

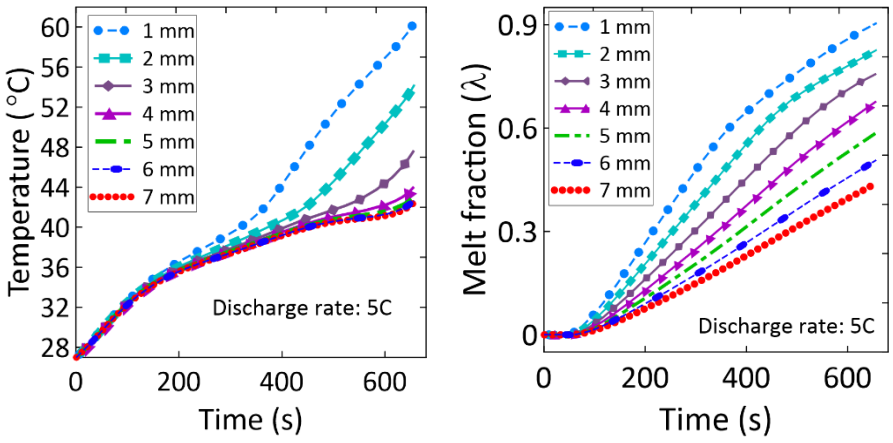

(a) Average battery temperature (b) PCM melt fraction

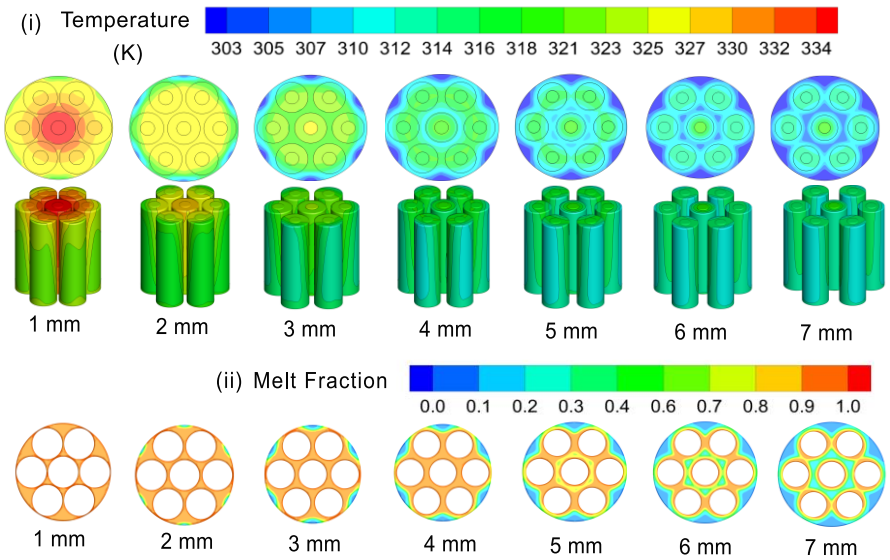

(c) Temperature and melt contours at the end of discharge

Figure 4.8: Effect of PCM thickness at 5C discharge rate

Interestingly, the maximum temperature gradient decreases from 6.2 °C (at 1 mm) to 4.8 °C (at 4 mm) at 5C discharge, then increases to 7.5 °C (at 7 mm). A similar trend is observed at 4C discharge, where it drops from 4.6 °C (at 1 mm) to 3.6 °C (at 4 mm) before rising to 5.2 °C (at 7 mm). The temperature contours (Figs. 4.8(c)(i) and 4.9(c)(i)), which illustrate the combined cells with PCM (top view) and the bottom isometric (3D) view for the cells with the PCM domain hidden, reveal that at lower PCM thicknesses (1–2 mm), significant heating occurs in the central region.

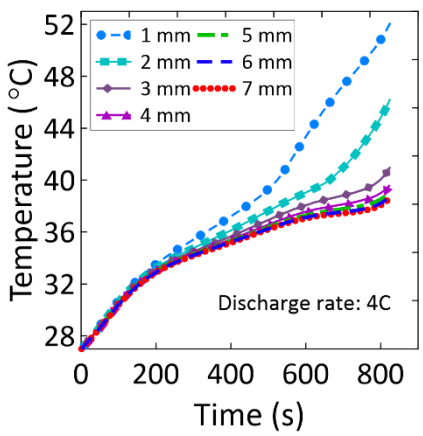

(a) Average battery temperature

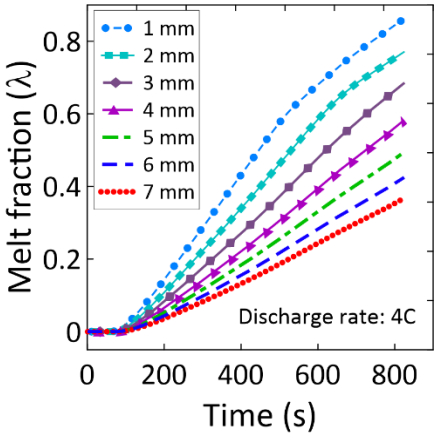

(b) PCM melt fraction

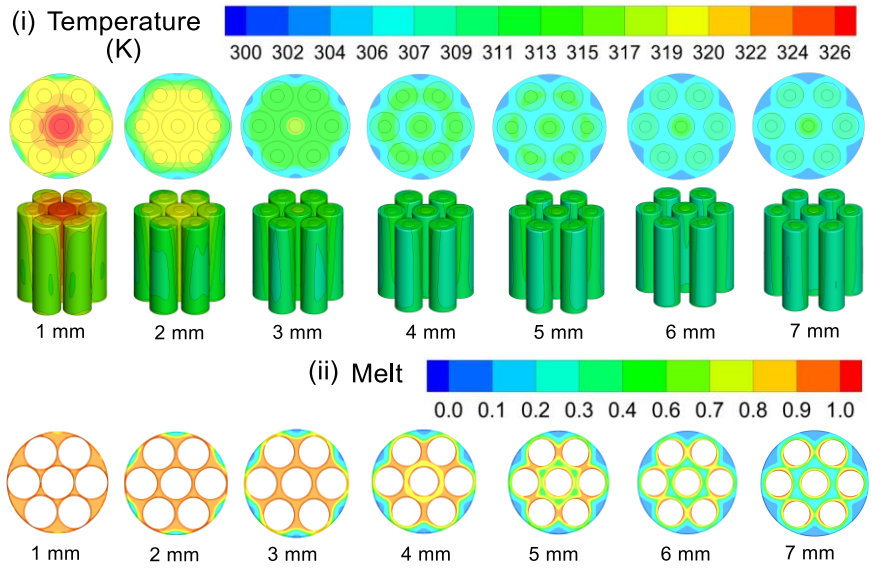

(c) Temperature and melt contours at the end of discharge (4C)

Figure 4.9: Effect of PCM thickness at 4C discharge rate

This is due to intense heat generation from closely packed cylindrical cells, where limited PCM volume restricts effective heat absorption, leading to localized temperature spikes and non-uniform cooling As PCM thickness increases (3–7 mm), the overall battery temperature decreases, leading to more uniform cooling throughout the pack. Similarly, the melt fraction contours (Figs. 4.8(c)(ii) and 4.9(c)(ii)) show that at 1–2 mm PCM thickness, near-complete melting occurs in the central region, indicating rapid saturation and loss of cooling efficiency. In contrast, thicker PCM layers (3–7 mm) exhibit progressively lower melt fractions, suggesting better heat absorption without complete saturation. However, at 6–7 mm, melting becomes localized near the battery surface, reducing overall PCM utilization. Thus, while thicker PCM layers enhance stability, excessive thickness introduces localized heat retention, diminishing cooling efficiency.

3C and 2C discharge rates

For 3C and 2C discharge rates, a consistent trend is observed, where increasing PCM thickness reduces maximum battery temperature but decreases PCM utilization. From Fig. 4.10(a), at 3C discharge (1106 s), battery temperatures progressively decrease from 43.64 °C (at 1 mm) to 35.4 °C (at 7 mm), while temperature gradients initially decrease till 4 mm (2.89 °C) before slightly increasing.

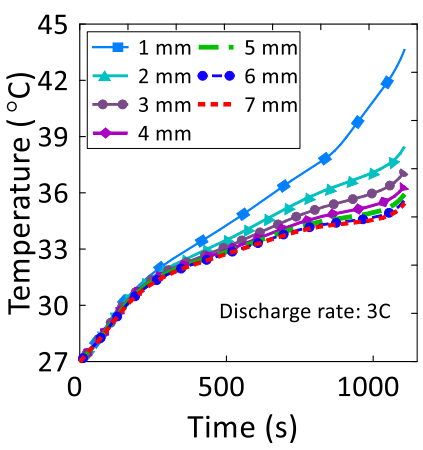

(a) Battery temperature for 3C

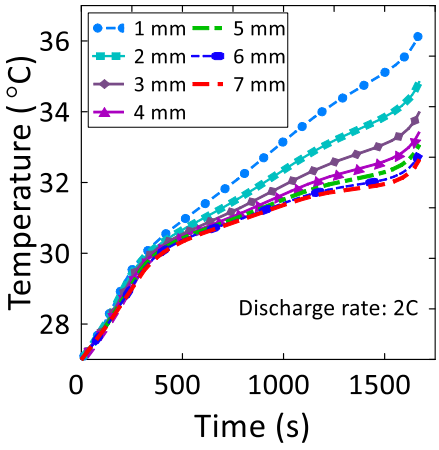

(b) Battery temperature for 2C

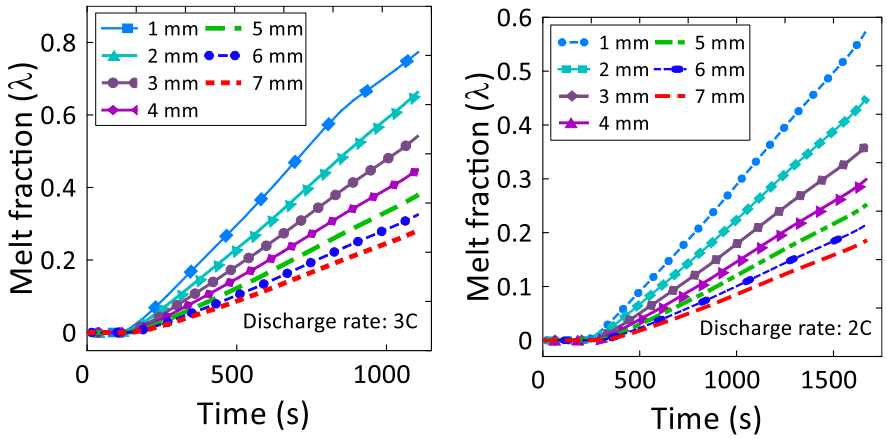

(c) Melt fraction during 3C (d) Melt fraction during 2C

Figure 4.10: Battery temperature and Melt fraction for 3C and 2C discharge rate

As can be seen from Fig. 4.10(c), the PCM melt fraction declines from 77.4% (at 1 mm) to 28.1% (at 7 mm), indicating reduced utilization with increased thickness. From Fig. 4.10(b), at 2C discharge (1672 s), a similar pattern emerges, with temperatures decreasing from 36.21 °C (at 1 mm) to 32.6 °C (at 7 mm), and minimal variation in temperature gradients (1.58 °C–1.69 °C) due to lower heat loads.

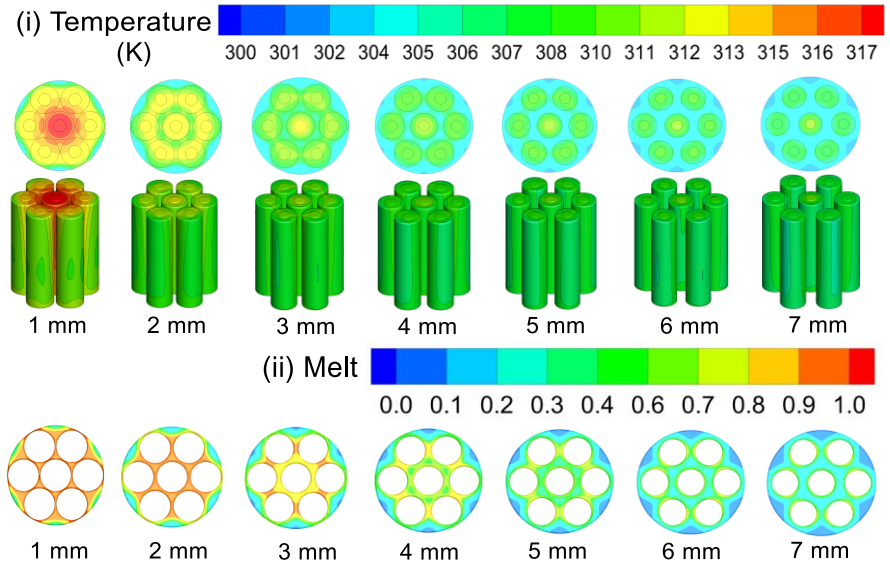

Figure 4.11 (a): Temperature and melt contours for 3C discharge rate

As can be seen Fig. 4.10(d), the PCM melt fraction for 2C discharge steadily decreases from 57.6% (at 1 mm) to 18.5% (at 7 mm), indicating again the trend of higher utilization in thinner layers but enhanced stability in thicker layers. The temperature and melt fraction contours (Figs. 4.11(a)(i-ii) and 4.11(b)(i-ii)) illustrate the distribution of heat and phase change behaviour at the end of 3C and 2C discharge, respectively. The detailed values of key parameters for each PCM thickness at various discharge rates are presented in Table 4.5.

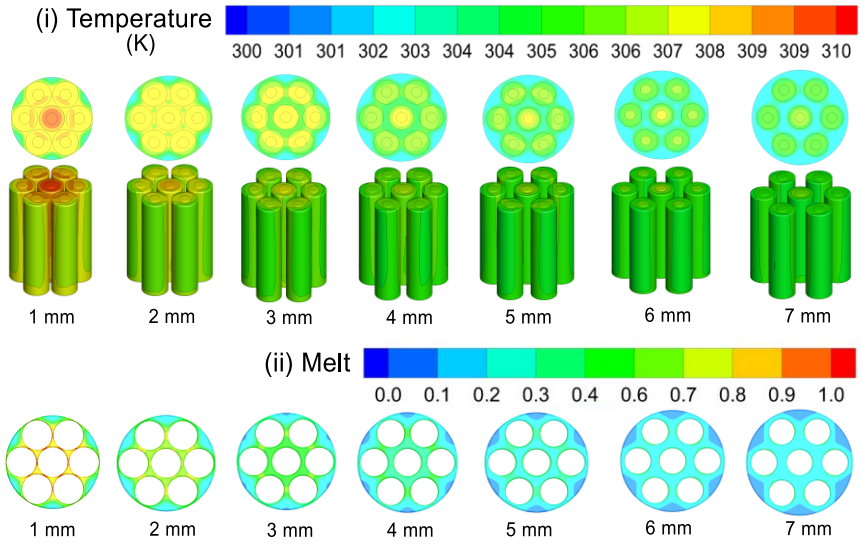

Figure 4.11 (b): Temperature and melt contours for 2C discharge rate

Key observations

The observed data shows that increasing PCM thickness significantly reduces the maximum battery temperature up to 4 mm, beyond which the rate of reduction slows down. This behaviour is governed by two key thermal mechanisms. First, as PCM thickness increases, the latent heat absorption capacity of PCM also increases, allowing efficient heat storage and dissipation before the material reaches full saturation. This phase change process effectively prevents excessive temperature buildup, leading to a sharp initial drop in battery temperature. However, beyond 4 mm, additional PCM volume does not proportionally enhance cooling performance due to the low thermal conductivity of PCM.

Table 4.5: Thermal performance under different thermal loading scenarios

Cases →	5C					4C					3C					2C				
PCM Thickness ↓	T_{max} (°C)	T_{avg} (°C)	ΔT_{max} (°C)	λ_{max}	λ_{avg}	T_{max} (°C)	T_{avg} (°C)	ΔT_{max} (°C)	λ_{max}	λ_{avg}	T_{max} (°C)	T_{avg} (°C)	ΔT_{max} (°C)	λ_{max}	λ_{avg}	T_{max} (°C)	T_{avg} (°C)	ΔT_{max} (°C)	λ_{max}	λ_{avg}
1 mm	62.9	60.4	6.2	0.90	0.47	54	52.1	4.6	0.86	0.42	44.8	43.6	3	0.77	0.35	37	36.2	1.6	0.57	0.23
2 mm	56.2	54.2	5.4	0.82	0.41	47.7	46.2	4.3	0.77	0.36	39.9	38.4	2.9	0.66	0.28	35.6	34.8	1.5	0.45	0.18
3 mm	50.3	47.6	4.9	0.75	0.35	43.2	41.1	3.9	0.68	0.29	38.7	37.1	2.8	0.54	0.22	34.8	33.9	1.5	0.36	0.14
4 mm	47.4	44	4.8	0.66	0.29	42.3	39.6	3.6	0.58	0.24	38	36.3	3	0.44	0.18	34.2	33.4	1.62	0.29	0.11
5 mm	46.8	43	5.9	0.58	0.25	41.9	39.1	4.1	0.49	0.20	37.6	35.9	3.15	0.37	0.15	33.9	33	1.65	0.25	0.09
6 mm	46.6	42.3	7	0.50	0.21	41.6	38.7	4.8	0.42	0.17	37.3	35.5	3.2	0.32	0.13	33.7	32.7	1.7	0.21	0.08
7 mm	46.4	42.4	7.5	0.44	0.18	41.5	38.6	5.2	0.36	0.15	37.2	35.4	3.3	0.28	0.11	33.5	32.6	1.72	0.18	0.07

Since heat travels through a thicker PCM layer before dissipating, thermal resistance increases, slowing heat transfer and resulting in localized heat accumulation near the battery surface rather than efficient dissipation. A similar trend is observed in temperature gradient behaviour, which initially decreases with increasing PCM thickness, improving thermal uniformity. The additional PCM helps distribute heat more evenly, preventing localized overheating and ensuring better cooling performance up to 4 mm thickness. However, beyond this point, thermal resistance further increases, restricting heat dissipation to the outer PCM layers. This leads to localized hotspots near the battery surface while the outer PCM remains underutilized, causing temperature differentials to rise. As a result, beyond 4 mm, the temperature gradient begins to rise rather than decrease, indicating a decline in heat dissipation efficiency

4.3.2 Selection of the PCM thickness

Figure 4.12 (a) and Fig. 4.12 (b) summarizes the results for the effect of PCM thickness (1-7 mm) on the temperature of the battery pack and melt fraction of the PCM at the end of the discharge, respectively. The data corresponding to zero PCM thickness is for the cells undergoing natural convection cooling without any PCM applied. For 5C discharge rate, incremental increases in PCM thickness (by 1 mm) significantly reduce the battery pack's temperature by 6.23 °C from 1 mm to 2 mm, 6.5 °C from 2 mm to 3 mm, 3.6 °C from 3 mm to 4 mm. However, further increase in the thickness beyond 4 mm decreases the temperature by less than 1 °C, and the PCM utilization remains less than 60% for the thickness above 4mm. Similarly, for 4C discharge rate, adding 1mm of thickness in steps decreases the temperature by 11.58 °C (11.5%), 5.90 °C (11.32%), 5.23 °C (11.1%), 1.39 °C (3.4%) till 4 mm and then the decreases are less than 1°C with further increase in thickness. Similar trend of results has been observed for 3C and 2C discharge rates. Beyond the 4 mm threshold, the reduction in maximum battery temperature

begins to plateau, indicating a shift in the dominant thermal phenomena of the system.

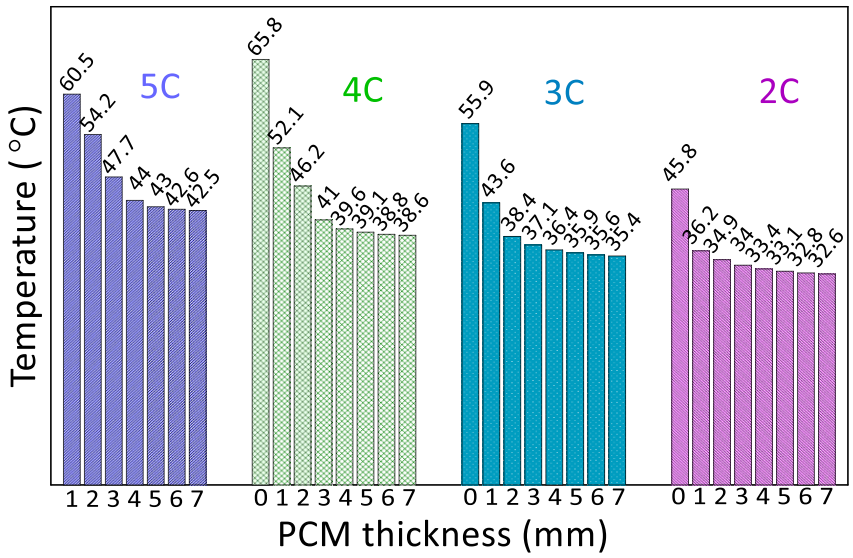

(a) Battery temperature

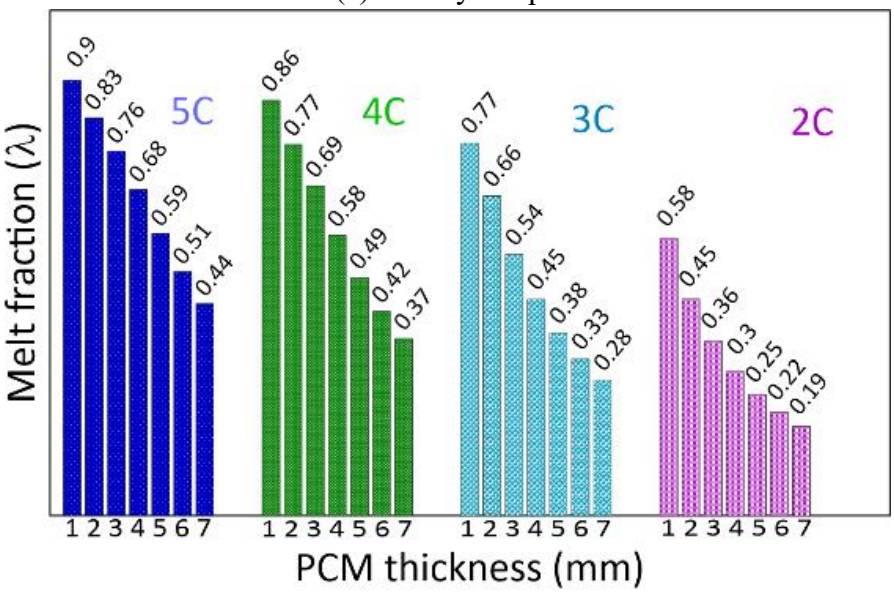

(b) Melt fraction

Figure 4.12: Temperature and melt fraction for various thickness at the end of discharge

At lower PCM thicknesses, latent heat absorption during the phase change process plays a major role in regulating cell temperature, as a substantial amount of heat is stored at nearly constant temperature during melting. However, as PCM thickness increases, the layer adjacent to the battery surface melts early in the discharge cycle, and any additional heat must travel through the already-melted PCM to reach the outer, still-solid regions. Given the inherently low thermal

conductivity of typical PCMs, this long conduction path introduces significant thermal resistance, thereby reducing the overall heat transfer rate and slowing the progression of melting in the remaining PCM volume. As a result, the additional PCM volume beyond 4 mm does not proportionally enhance cooling performance. Instead, heat begins to accumulate near the battery surface, while the outer PCM remains underutilized, leading to rising thermal gradients and localized overheating. This is further supported by melt fraction data, which shows that PCM utilization drops below 60% for thicknesses greater than 4 mm, indicating that only the inner PCM layer actively contributes to thermal regulation. The outer layers remain largely solid due to insufficient heat transfer, limiting their effectiveness. Moreover, the thicker PCM layer forms a thermal barrier to the ambient, diminishing convective heat dissipation and further reducing overall cooling efficiency. These combined effects lead to diminishing temperature reduction benefits, as reflected in the data where increasing the PCM thickness beyond 4 mm results in additional temperature drops of less than 1 °C.

Therefore, to further investigate on the optimum value of the PCM thickness, two key parameters are defined namely Normalized Peak battery Temperature (Ψ) and Normalized Battery Temperature gradient (Ψ^*) [44]:

$$\Psi = \frac{T_{max_i} - T_{max_n}}{T_{max_1} - T_{max_n}} \tag{4.13}$$

$$\Psi^* = \frac{\Delta T_i - \Delta T_1}{\Delta T_n - \Delta T_1} \tag{4.14}$$

here, i varies from 1 mm to 7 mm thickness of PCM and n corresponds to the maximum temperature at the highest value of thickness i.e. 7 mm. Figure 4.13 (a-b) depicts the intersection of the two curves for discharge rate of 5C and 4C, respectively, representing a balance between the two parameters encompassing the temperature and gradient. The intersection for the two discharge rates also lies between 3 mm to 4 mm.

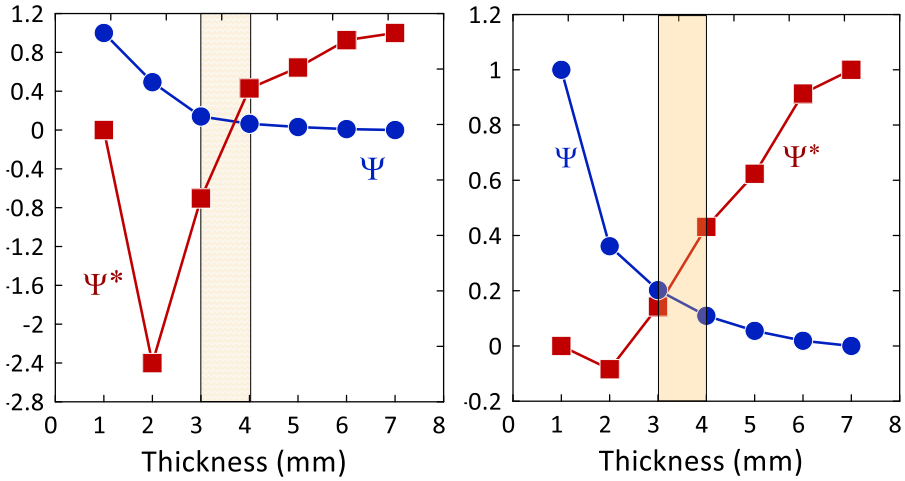

(a) Normalized peak temperature and gradient for 5C

(b) Normalized peak temperature and gradient for 4C

Figure 4.13: Normalized temperature and temperature gradient

Therefore, a higher thickness value i.e., 4 mm is taken as the minimum PCM thickness for this configuration; a similar approach has been used by previous researchers [44]. Additionally, the thermal response time (δ) is defined as the time taken by the cell to transition from 90% of its peak surface temperature to the maximum temperature during end of discharge. This parameter helps evaluate how effectively different PCM configurations moderate rapid temperature rise near peak heating conditions. Figure 4.14 illustrates the thermal response times for PCM thicknesses of 3 mm, 4 mm, and 5 mm, while Table 4.6 provides a detailed tabulation of response times at 5C and 4C discharge rates, highlighting the impact of thickness variations on thermal regulation efficiency.

At 5C discharge rate, increasing PCM thickness from 3 mm (δ =101 seconds) to 4 mm (δ = 251 seconds) extends the thermal response time by 148.5%, while further increasing to 5 mm (δ = 291 seconds) results in only a 15.9% delay, indicating diminishing benefits. Similarly, at 4C discharge, increasing thickness from 3 mm (δ = 328 seconds) to 4 mm (δ = 406 seconds) provides an additional 23.8% response time, whereas extending to 5 mm (δ = 439 seconds) adds just 8.14%, reinforcing the trend of diminishing returns beyond 4 mm.

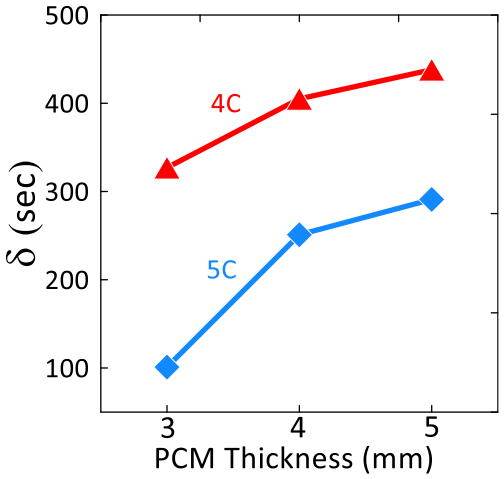

Figure 4.14: Thermal response time (δ)

Table 4.6: Thermal response time (δ) using various PCM thickness

Discharge rate	Thermal response time with the increase in the PCM thickness					
	3 mm	4 mm	% rise	4 mm	5 mm	% rise
5C	101 s	251 s	148.5	251 s	291	15.9
4C	328 s	406 s	23.8	406 s	439 s	8.14

Based on the results, a 4 mm PCM thickness is selected as the reference configuration, as it provides a favourable balance between thermal performance and material efficiency. This thickness offers significant peak temperature reduction, reduced thermal gradients, and effective PCM utilization, while avoiding the drawbacks associated with excessive PCM volume, such as increased thermal resistance and uneven heat dissipation. Beyond this threshold, further increases in thickness yield diminishing returns, with additional PCM contributing little to temperature control and instead leading to localized overheating near the battery surface. It is important to emphasize that the 4 mm value is not considered universally optimal for all PCM types or ambient conditions. Rather, it is selected based on observed performance using RT-35 at a nominal ambient temperature of 27 °C, serving as a consistent reference point for comparative evaluation of other PCMs and environmental scenarios presented in the following sections.

4.3.3 Effect of ambient temperature and different PCMs

Based on the selected 4 mm PCM thickness, the thermal performance of five different (RT-24, RT-35, RT-38, RT-42, and RT-47; each with varying melting temperature ranges and thermal properties) under various ambient temperatures (20 °C, 27 °C, 40 °C, and 50 °C) is investigated to simulate a range of operating conditions.

The results in Fig. 4.15(a-d) highlight the impact of different PCMs on the thermal performance of the battery pack for 5C and 4C discharge rates at an ambient temperature of 20 °C.

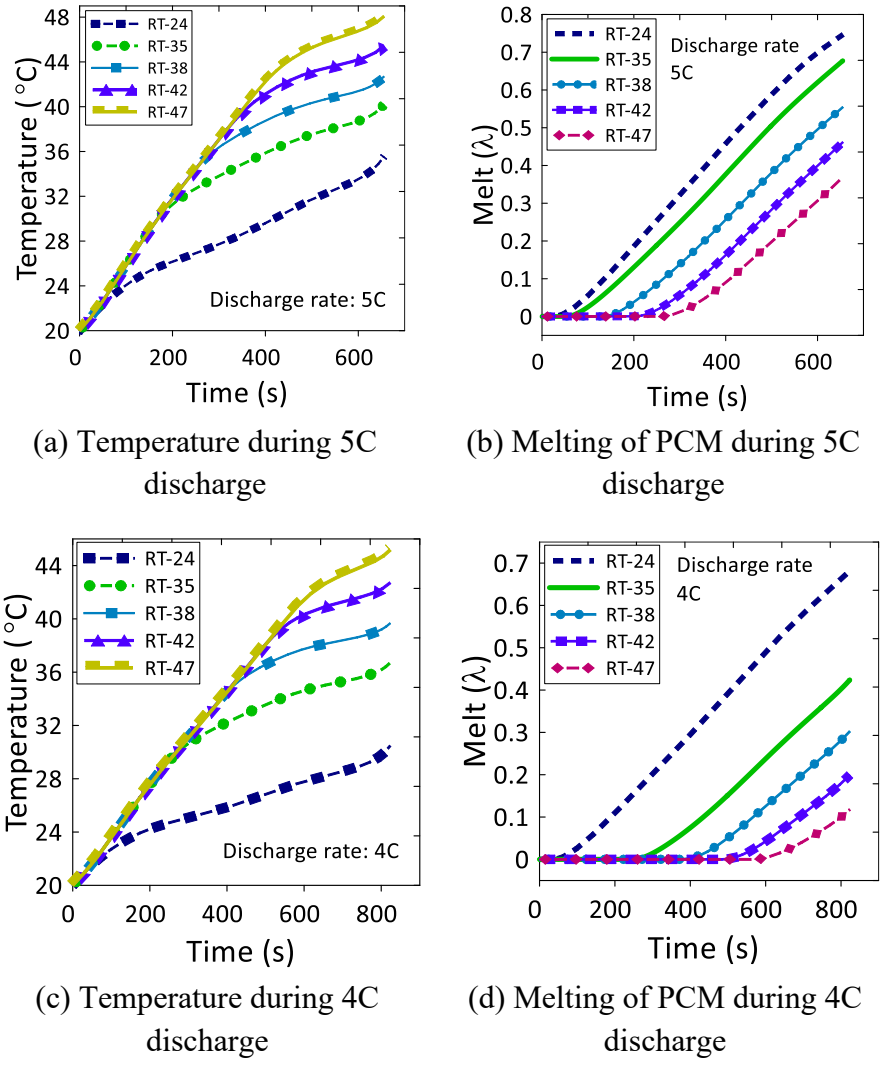

(a) Temperature during 5C discharge

(b) Melting of PCM during 5C discharge

(c) Temperature during 4C discharge

(d) Melting of PCM during 4C discharge

Figure 4.15: Effect of various PCMs on battery temperature and melt fraction at 20 °C

For the 5C discharge rate, PCMs with lower melting point, RT-24, exhibit superior thermal performance with peak temperatures of 35.53 °C, and high melt fractions of 74.6%. This indicates effective heat absorption due to their ability to fully utilize the phase change process. In contrast, PCMs with higher melting points, including RT-42 and RT-47, result in elevated peak temperatures of 45.47 °C and 48.14 °C, with melt fractions dropping to 32.9% and 24.1%, demonstrating reduced heat absorption efficiency under these conditions. For PCMs RT-35 and RT-38, the maximum temperature is 42.5 °C and 44.8 °C with melt fraction of 54% and 42.7%, respectively. Similarly, for the 4C discharge rate, RT-24 achieves the lowest peak temperature (30.46 °C) and the highest melt fraction (68.1%), with increase in battery temperature and decrease in melt fraction with increasing PCM melting range, where RT-47 leads to higher peak temperatures of 45.23 °C and lower melt fractions of 11.9%, indicating inadequate phase change utilization at this discharge rate. RT-35 maintain relatively low peak temperatures of 36.73 °C with melt fractions of 42.4%. Before reaching the onset temperature of melting, the temperature rise during the sensible heating period is linear and coincides for each PCM type due to similar thermal properties. At ambient of 20 °C, all the PCMs have above onset melting temperature and the PCM starting earliest phase change (RT-24 in this case) reports the lowest temperature and maximum utilization.

Fig. 4.16 depicts the results for ambient temperature of 27 °C, the performance of the PCMs shows significant variation for both 5C and 4C discharge rates. For the 5C discharge rate, the peak temperatures recorded were 60.07 °C, 44.02 °C, 44.59 °C, 47.07 °C, and 49.74 °C for RT-24, RT-35, RT-38, RT-42, and RT-47, respectively. Corresponding melt fractions were 1, 0.677, 0.555, 0.462, and 0.371. RT-24 exhibited the poorest thermal regulation due to complete saturation, whereas RT-35 provided a balance of lower peak temperatures and moderate PCM utilization. Higher melting point PCMs (RT-42 and RT-47) resulted in higher peak temperatures and lower melt fractions, demonstrating reduced effectiveness under this condition.

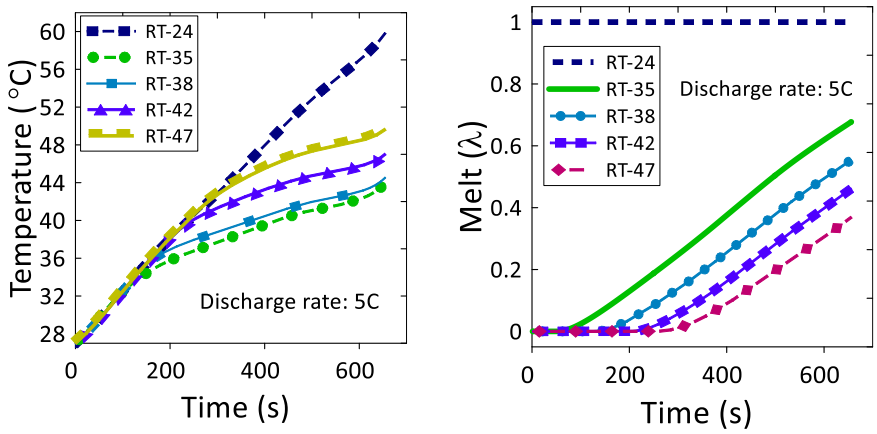

(a) Temperature during 5C discharge

(b) Melting of PCM during 5C discharge

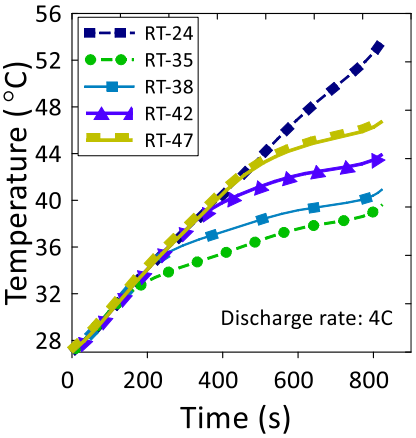

(c) Temperature during 4C discharge

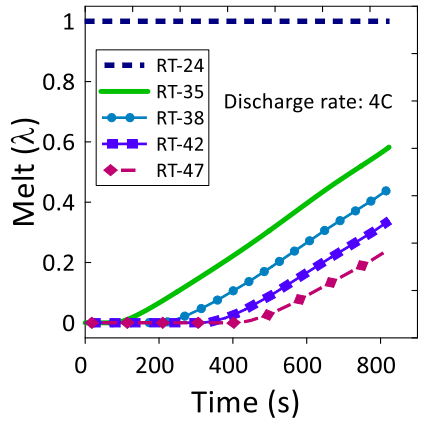

(d) Melting of PCM during 4C discharge

Figure 4.16: Effect of various PCMs on battery temperature and melt fraction at 27 °C

For the 4C discharge rate, the trends were consistent, with RT-24 showing a peak temperature of 53.79 °C and a melt fraction of 1. RT-35 achieved peak temperatures of 39.6 °C and melt fractions of 0.5826, respectively, maintaining the best balance between thermal regulation and utilization. Meanwhile, RT-42 and RT-47 exhibited peak temperatures of 43.98 °C and 46.84 °C and lower melt fractions of 0.34 and 0.24, reflecting their limited utilization. These results suggest that PCMs with moderate melting points, such as RT-35, for which the melting temperature range is in the optimum temperature range of

battery modules, are more effective under moderate ambient conditions like 27 °C.

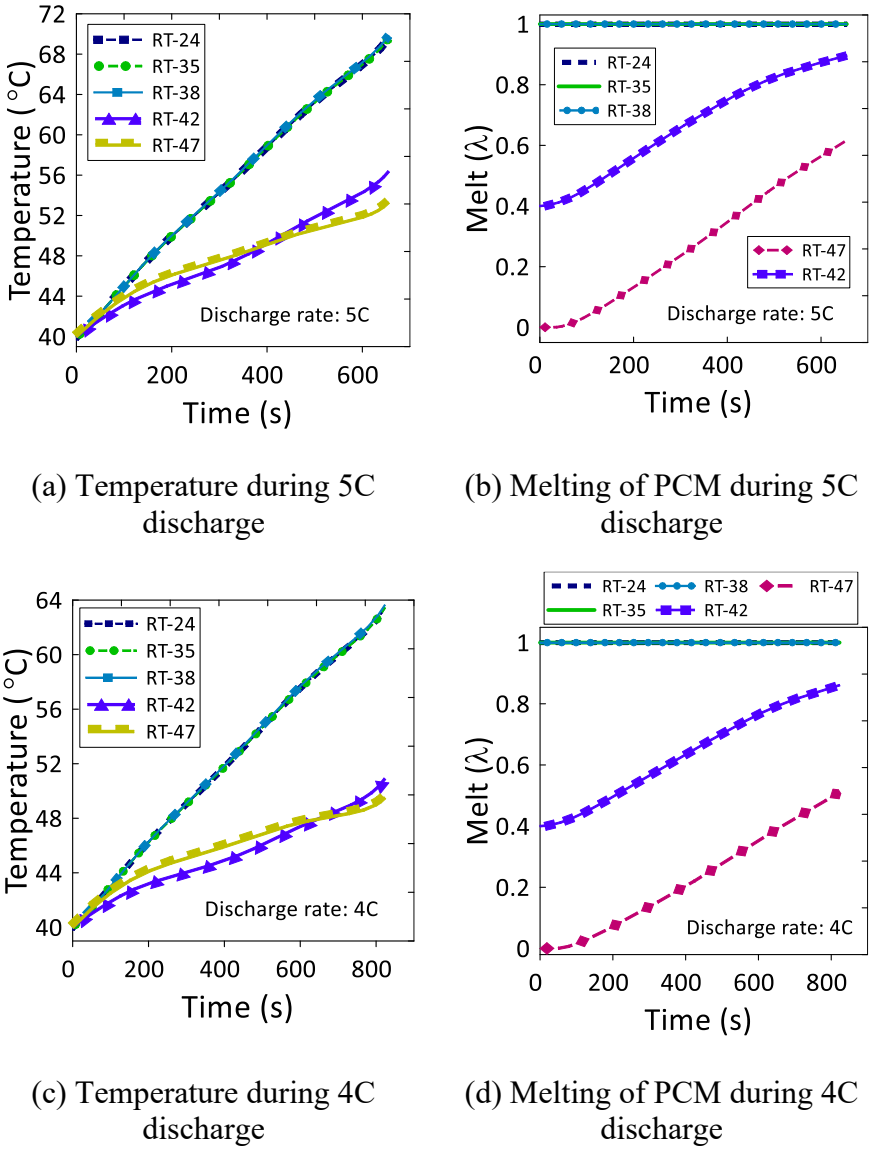

(a) Temperature during 5C discharge

(b) Melting of PCM during 5C discharge

(c) Temperature during 4C discharge

(d) Melting of PCM during 4C discharge

Figure 4.17: Effect of various PCMs on battery temperature and melt fraction at 40 °C

At elevated ambient temperatures of 40 °C (Fig. 4.17), the performance of PCMs is strongly influenced by their melting points. For the 40 °C ambient, PCMs with melting points below this temperature (RT-24, RT-35, and RT-38) reached complete saturation during both 5C and 4C discharge rates, resulting in uniformly high peak temperatures of 69.88 °C (5C) and 63.7 °C (4C).

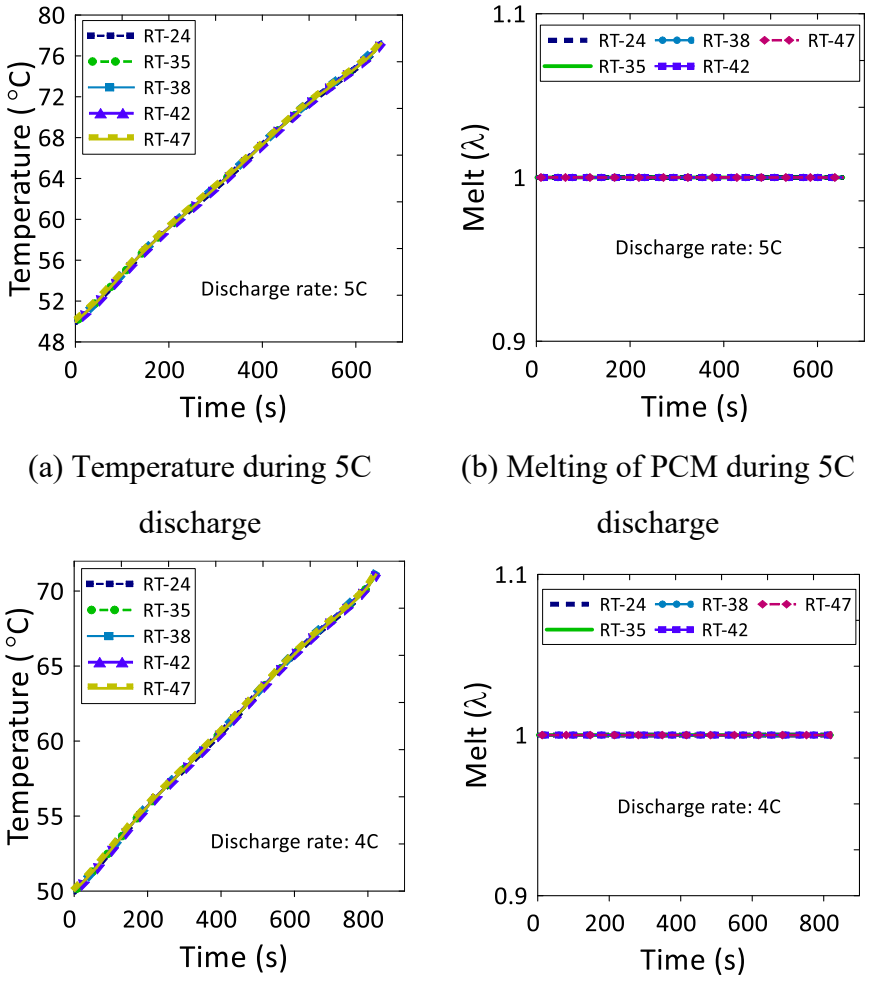

(a) Temperature during 5C discharge

(b) Melting of PCM during 5C discharge

(c) Temperature during 4C discharge

(d) Melting of PCM during 4C discharge

Figure 4.18: Effect of various PCMs on battery temperature and melt fraction at 50 °C

In contrast, higher melting point PCMs, RT-42 and RT-47, demonstrated better thermal regulation, achieving peak temperatures of 56.55 °C and 53.38 °C (5C) and 51.02 °C and 49.58 °C (4C), with reduced melt fractions of 0.89 and 0.61 (5C) and 0.86 and 0.515 (4C), respectively. The effect of different PCMs at an elevated ambient temperature of 50 °C is detailed in Fig. 4.18. These results indicate that at such high ambient temperatures, the PCM alone is unable to sufficiently regulate the thermal load, regardless of its melting point. These findings indicate that PCMs with moderate melting points, like RT-35, are more effective in maintaining optimal thermal conditions,

particularly under moderate ambient temperatures. This suggests the importance of selecting a PCM with a melting point that aligns well with the expected operating temperature range of the battery modules for efficient thermal management.

4.3.4 Effect of PCM volume

This section analyses the effect of varying PCM volume fractions (0%, 33%, 66%, and 100%) within a fixed 4 mm inter-cell spacing on the maximum battery temperature and temperature gradient across discharge rates ranging from 2C to 5C. As shown in Figs. 4.19(a–c), increasing PCM volume significantly lowers peak battery temperature and improves temperature uniformity. At 5C discharge, the peak temperature drops to 42.92 °C with 100% PCM. Similar reductions are observed at 4C (from 65.82 °C to 38.66 °C), 3C (from 57.74 °C to 35.59 °C), and 2C (from 48.28 °C to 32.93 °C). These improvements occur because larger PCM volumes can absorb more heat during phase change and delay saturation, maintaining better temperature control over longer discharge durations. Melt fraction data supports this trend. At lower fill levels (33%), the PCM saturates quickly, reducing its ability to continue absorbing heat. In contrast, higher volumes (66% and 100%) sustain cooling for longer periods. Temperature gradients also follow a similar pattern; at 4C, the gradient reduces from 23.19 °C (33% PCM) to 4.48 °C (100% PCM), with comparable improvements seen at 3C and 2C. Lower PCM volumes result in uneven cooling, as regions in contact with PCM stay cooler while uncovered areas heat up more rapidly. Temperature contour plots at 3C discharge (Fig. 4.19(c)) further illustrate this behaviour. PCM-covered regions remain significantly cooler, while uncovered zones develop hotspots. This uneven temperature distribution highlights the importance of ensuring sufficient PCM coverage to achieve uniform cooling and minimize localized overheating.

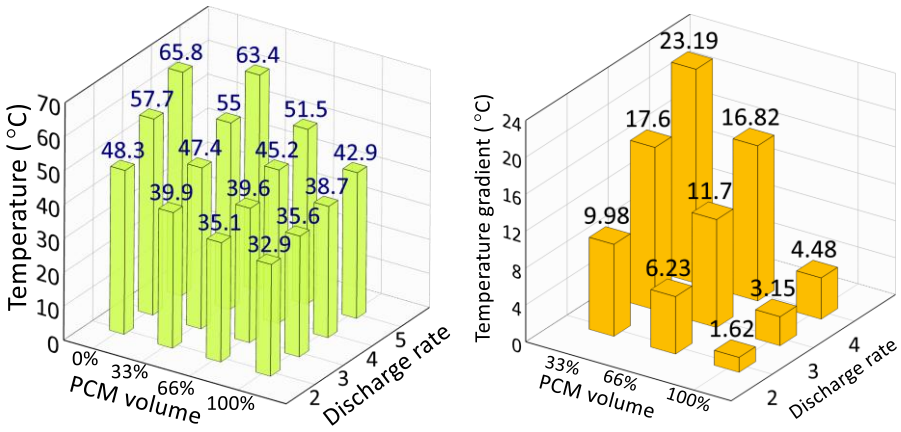

(a) Battery temperature

(b) Maximum temperature gradient

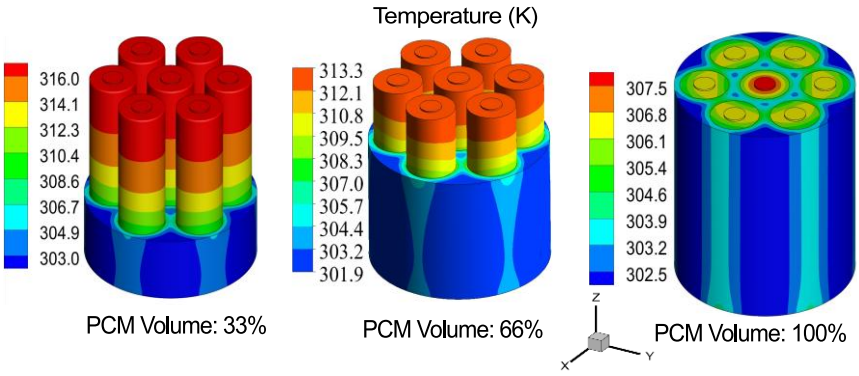

(c) Temperature contours at different PCM filling volume

Figure 4.19: Effect of PCM filling volume

4.3.5 Effect of heat transfer coefficient

The ambient heat transfer coefficient plays a crucial role in determining the cooling efficiency of passive thermal management systems, as it directly influences heat dissipation to the surroundings. Therefore, this section investigates the impact of varying ambient heat transfer coefficients ($h_{surface}$) on the thermal performance of the system under discharge conditions (5C, 4C, and 3C), followed immediately by charging at 1C. The room operating temperature conditions of 27 °C and PCM RT-35 have been used for the analysis. The tested $h_{surface}$ values (5, 10, 15, and 20 W/m²K) significantly influence the battery temperatures, temperature gradient and PCM utilization, as shown in Figs. 4.20-4.25.

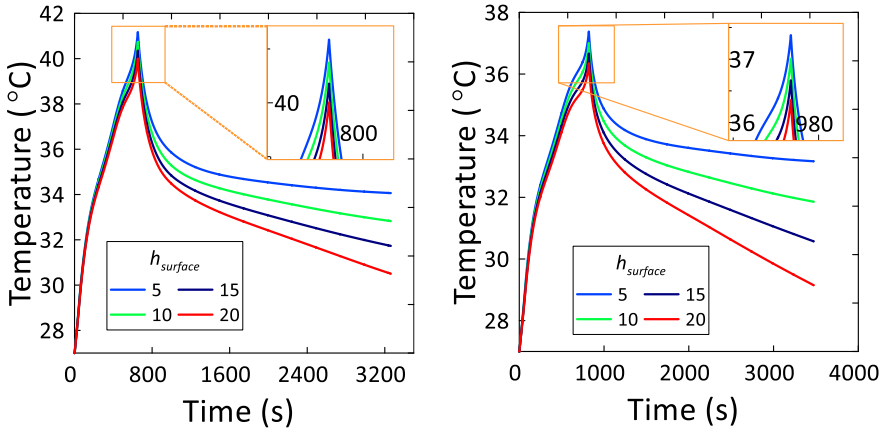

(a) Temperature response during 5C discharge-1C charge with $h_{surface}$

(b) Temperature response during 4C discharge-1C charge with $h_{surface}$

Figure 4.20: Effect of heat transfer coefficient

From Fig. 4.20(a-b), for the 5C-1C discharge-charge scenario, the battery temperature at the end of discharge decreased from 41.17 °C ($h_{surface}$=5 W/m²K) to 40 °C ($h_{surface}$=20 W/m²K), a drop of about 2.84%, while the end-of-charge temperatures dropped from 34 °C to 30.45 °C which is about 10.44%. Similarly, for 4C-1C case, the battery discharge temperature decreases from 37.33°C to 36.3°C (2.75%), and at the end of charge from 33.16 °C to 29.15 °C (12.09%) as $h_{surface}$ increased from 5 to 20 W/m²K. This observation illustrates that increasing the heat transfer coefficient do not contribute significantly to reduce the battery temperature, especially during rapid discharging conditions when compared to the standard charging; this could be due to the following possible reasons. First, during rapid discharging, the heat generation within the battery is much higher due to the increased current and the substantial heat generation within a short duration overwhelms the cooling capacity, minimizing the relative impact of an increased heat transfer coefficient. Second, during charging the slower and prolonged cycle with lower heat generation and longer duration allow the increased heat transfer coefficient to have a more pronounced impact. Interestingly, the effect of heat transfer coefficient on the maximum temperature gradient of the cell was opposite, and an increased temperature gradient is seen for higher $h_{surface}$ values.

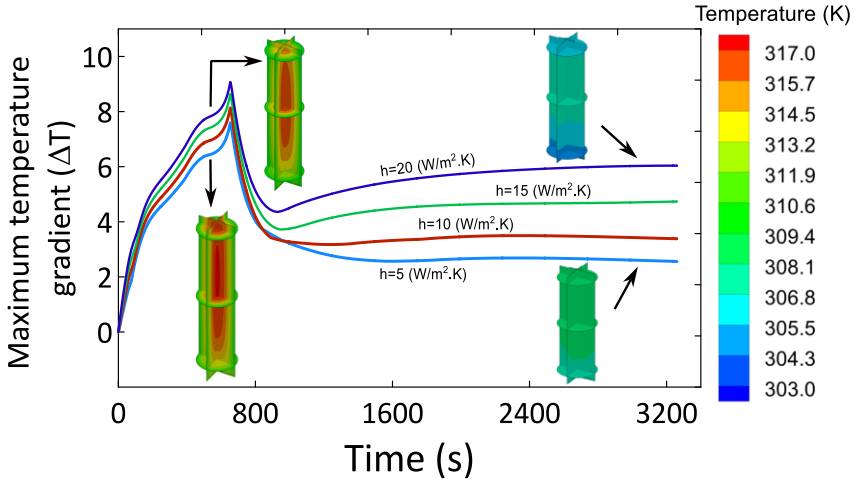

Figure 4.21: Maximum temperature gradient during 5C discharge-1C charge with $h_{surface}$

Fig. 4.21 and Fig. 4.22 depicts the variation in the maximum temperature gradient throughout the discharge and charge cycles, 5C-1C and 4C-1C, respectively. It can be observed that up to $h_{surface} = 10\,W/m^2K$, the temperature gradient increases during the rapid discharge and then decreases and stabilizes during the charge, whereas for higher $h_{surface}$, after the discharge the temperature gradient first decreases followed by an increase and then stabilizes as the charging progresses.

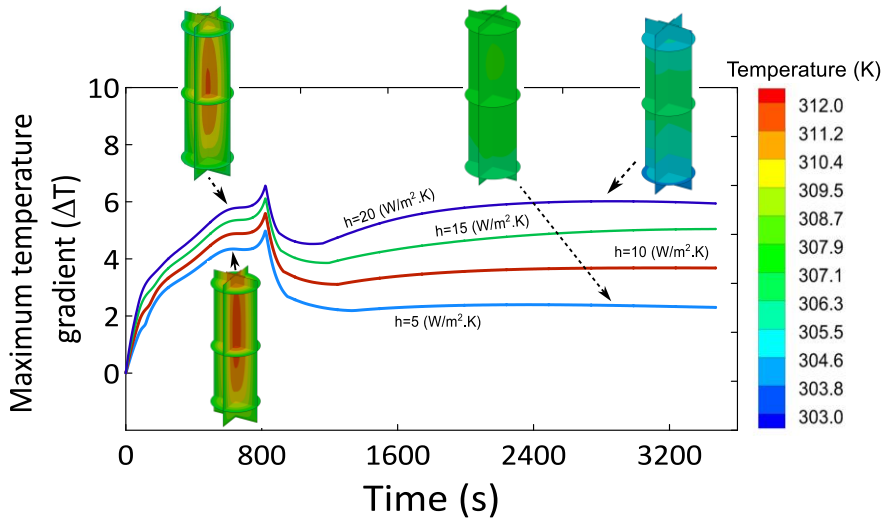

Figure 4.22: Maximum temperature gradient during 4C discharge-1C charge with $h_{surface}$

The underlying explanation is as follows: during the rapid discharging the heat generation rate is much more pronounced in comparison to the heat rejection from the peripheral surface area of the cell (which is surrounded by the PCM) and from the top and bottom surface area of the cell (which is exposed to the environment), in addition, the lower radial thermal conductivity of the cylindrical cell further limits the heat transfer, leading the core of the cell at a high temperature compared to the exposed boundary. As the charging begins, the rate of heat generation decreases (leading to decrease in core cell temperature) and with the continuous rate of heat rejection from the cell boundary a balanced state is reached stabilizing the temperature gradient while overall reducing the temperature of the cell. For higher heat transfer coefficients, there is a more pronounced heat loss from the battery's top and bottom surfaces. This increased heat dissipation leads to a cooler exterior compared to the core, creating a substantial core-to-boundary temperature differential. As a result, as the charging progresses, the temperature gradient initially decreases due to the cooler boundaries but then increases as the core remains relatively hotter for a longer period. This observation is further supported by the temperature contours of the centremost cell depicted at different time and heat transfer coefficients values. These contours show how different heat transfer coefficients affect the cell's temperature distribution over time, demonstrating the decrease and subsequent increase in temperature gradient as the charging progress under higher $h_{surface}$.

Fig. 4.23(a-b) presents the changes in PCM melt fractions for 5C-1C and 4C-1C cases. For 5C-1C scenario: At the end of discharge, the PCM melt fraction decreases from 0.61 to 0.52 (recovery of 14.75%), and at the end of charge from 0.66 to 0.19 (recovery of 71.21%), demonstrating that higher $h_{surface}$ values helps to restores the capacity of PCM to absorb more heat and improves the heat transfer between the PCM and environment.

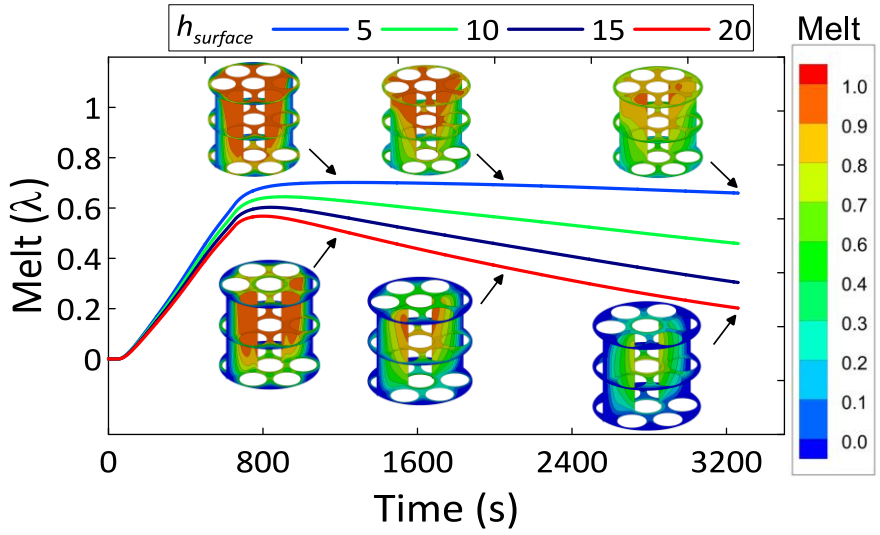

(a) 5C discharge – 1C charge

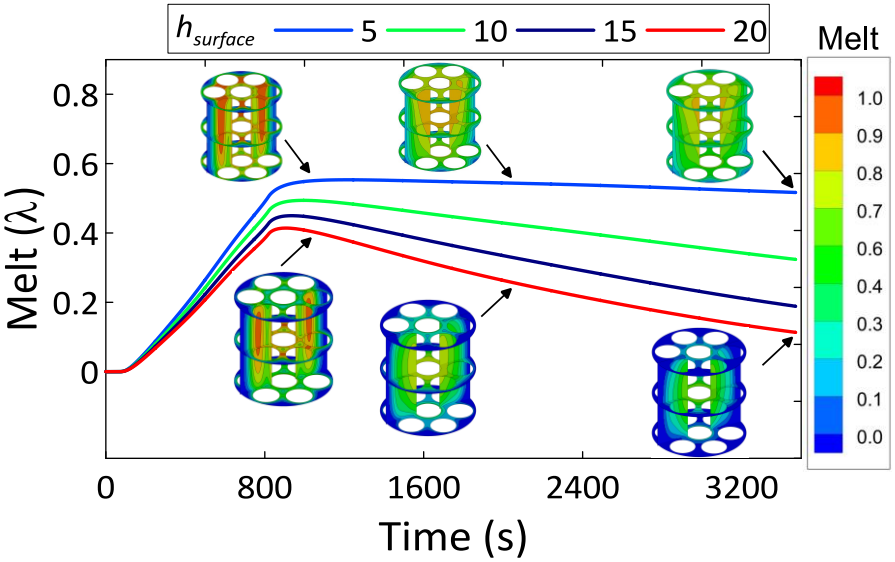

(b) 4C discharge – 1C charge

Figure 4.23: Variation in melt fraction variation during discharge – charge with $h_{surface}$

Similar improvements were observed for the 4C-1C scenario the PCM melt fractions dropped from 0.51 to 0.4 (recovery of 21.56%) at the end of discharge, and from 0.52 to 0.11 (recovery of 78.84%) at the end of charge, highlighting the enhanced cooling effect with higher $h_{surface}$. The effect of heat transfer coefficient variation is much more pronounced on the recovery of the PCM in comparison to the reduction in temperature because of the heat loss associated with the latent of PCM.

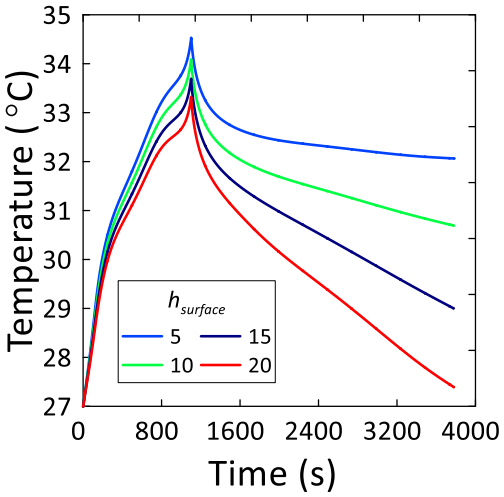

Figure 4.24: Temperature response during 3C discharge-1C charge with $h_{surface}$

For the 3C-1C scenario, Fig. 4.24 and Fig. 4.25 reveals that the battery temperatures at the end of discharge were 34.44 °C, 33.98 °C, 33.58 °C, and 33.2 °C for h=5, 10, 15, and 20 W/m²K, respectively, and at the end of charge, temperatures decreased from 32.06 °C to 27.39 °C. PCM melt fractions followed a similar trend, decreasing from 0.36 to 0.24 at the end of discharge and from 0.36 to 0.04 at the end of charge. The temperature gradient follows the similar behaviour, with pronounced valued at higher heat transfer coefficients.

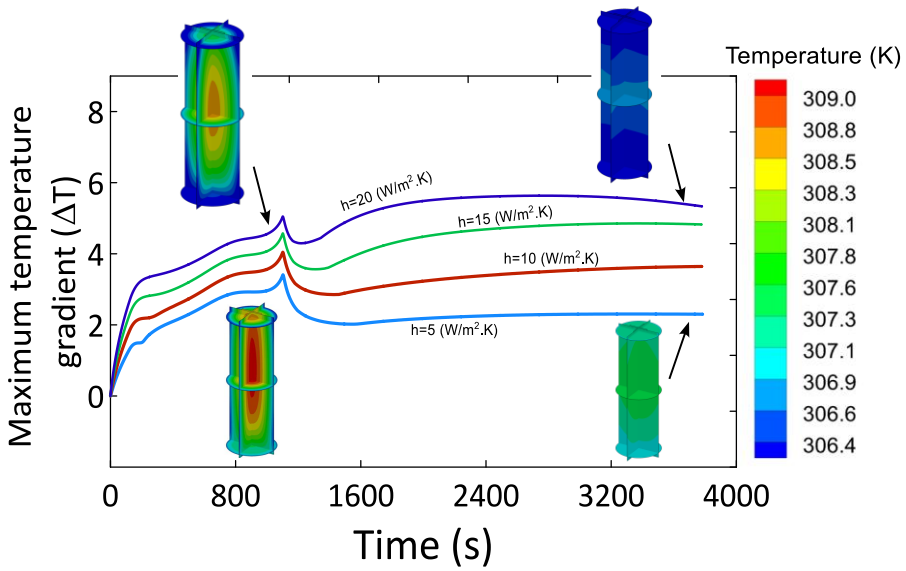

(a) Maximum temperature gradient

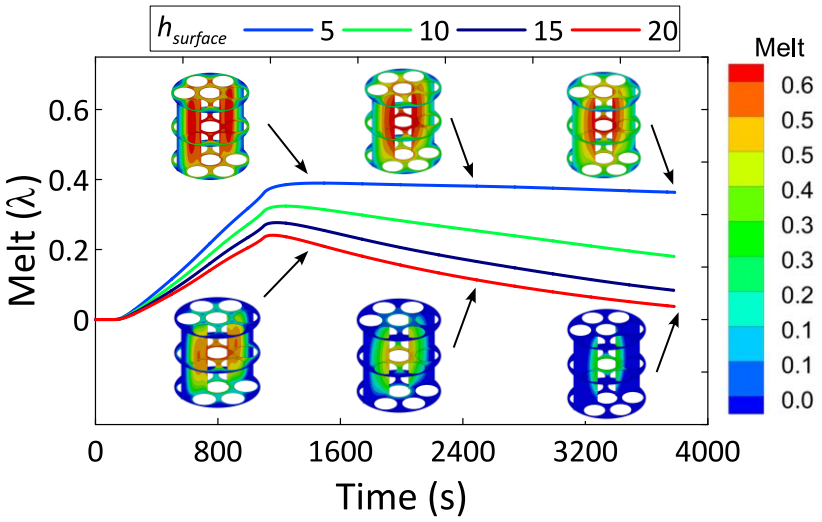

(b) Melt fraction

Figure 4.25: Maximum temperature gradient and melt fraction for various $h_{surface}$ during 3C discharge – 1C charge

4.4 Conclusion

This chapter reports a comprehensive analysis of a battery thermal management system (BTMS) involving PCM behaviour, discharge parameters, and environmental conditions for a fixed seven-cell module configuration. The effects of PCM thickness, discharge rates, ambient temperatures, convective heat transfer coefficients, and PCM volume fraction on the performance of BTMS are analysed systematically to understand their influence on thermal regulation, material utilization, and cooling efficiency; the details are elaborated below.

It is observed that the PCM RT-35, at an ambient temperature of 27 °C and 4 mm thickness, exhibits the best trade-off between thermal performance and material efficiency, reducing the maximum battery temperature by up to 24.12 °C during a 4C discharge. While increasing the thickness improves thermal buffering, it also introduces diminishing returns due to greater thermal resistance and underutilization of the outer PCM layers. Also, it is noted that the PCM filling volume plays a significant role in the performance; with an increase in the fill ratio from 33% to 100%, battery temperatures and temperature gradients are found to reduce, which improves the temperature uniformity. However, higher

PCM volumes introduce trade-offs in weight and packaging, reinforcing the need for design-specific volume selection.

In addition to this, PCM material selection depends on the ambient temperature. At moderate conditions, RT-35 exhibits superior performance, while RT-24 and RT-47 exhibit the best performance at lower and higher ambient temperatures, respectively. At higher temperatures (> 50 °C), all PCMs reach near-total saturation, which indicates the need for hybrid cooling approaches. It is observed that the battery peak temperature decreases with an increase in the external convective heat transfer coefficient, especially during the charging phase, due to enhanced surface cooling. However, this also leads to lower PCM melt fractions at the end of discharge, as faster cooling causes more heat energy to dissipate before it can be stored in the PCM.

The study highlights the combined influence of PCM type, thickness, filling volume, ambient temperature, and convective heat-transfer coefficient on the overall thermal performance of cylindrical-cell modules. The optimized RT-35 PCM at 4 mm thickness provides the best balance between cooling efficiency and added weight, reducing the maximum cell temperature by 24.12 °C during 4C discharge, while 100% PCM fill volume further enhances temperature uniformity with acceptable trade-offs in mass and packaging. These results establish design-specific guidelines for PCM-based cooling systems operating under varied thermal environments. In comparison with previously reported PCM-based cooling studies, the optimized configuration presented here achieves greater temperature reduction and more uniform thermal distribution under high-rate discharge conditions. The findings also reveal a clearer dependence on ambient temperature and fill volume, illustrating conditions under which PCM-only systems become insufficient and hybrid strategies are required. Overall, this chapter provides updated, practical insight for the design and deployment of lightweight, efficient PCM-based thermal management solutions.

Chapter 5

Conclusions and Scope of Future Work

The present dissertation presents theoretical, numerical and experimental investigations on PCM-based passive and hybrid thermal management systems for electric vehicle battery modules. These studies include the development of a theoretical model to estimate the effective thermal conductivity of open-cell coated metal foams saturated with fluid or PCM, and the performance analysis of both PCM-based passive and PCM-based hybrid thermal management systems under various operating conditions. The key outcomes of the present dissertation are summarized, and the conclusions are highlighted in this chapter.

In this dissertation, initially, a theoretical model is developed to estimate the effective thermal conductivity (ETC) of open-cell coated metal foams (MFs) saturated with fluid or PCMs, considering the effects of ligament shape, node geometry, ligament orientation, foam geometry, coating thickness, and material properties. A 3-D computational fluid dynamics (CFD) model is also developed to analyse the effect of parameters such as PCM thickness, discharge rate, and metal foam porosity on the performance of BTMS under steady, transient, and realistic driving conditions. Also, efforts have been made to analyse the performance of hybrid battery thermal management system (BTMS) involving PCM with a lightweight, liquid-cooled cold plate under both continuous and melt-fraction-triggered intermittent cooling strategies for different drive cycles (HWFET, WLTP, UDDS, and US-06) with cyclic charging/discharging scenarios (4C–1C and 5C–1C). Additionally, the effects of PCM type (RT-24, RT-35, RT-38, RT-42, RT-47) and discharge rates (2C–5C) on the performance of a passive PCM-based BTMS for cylindrical (18650) lithium-ion cells are investigated through both numerical and experimental methods. The significant findings from the present investigation are elaborated below:

5.1 Theoretical model for effective thermal conductivity of open cell coated metal foams saturated with fluid/Phase change material

In this chapter, a theoretical model has been proposed to evaluate the effective thermal conductivity (ETC) of open-cell coated metal foams (MFs) saturated with fluid or phase change materials (PCMs). The model considers realistic three-dimensional geometric characteristics based on tetrakaidecahedron unit cell structures. The effects of ligament shape, node geometry, ligament orientation, foam geometry, coating thickness, and material properties on the ETC have been analysed, and the model is validated with available test data. The key outcomes of the study are detailed below.

- Model M-2 (hexagonal cell with concave triprism ligaments and pyramidal nodes) achieves average deviations of <3% for nickel and <2% for copper compared to test data, making it more reliable than existing 2D models and alternative 3D geometries.
- For graphene-coated foams, M-2 exhibits deviations of only 2.36% (nickel) and 1.25% (copper), compared to 12.27% and 4.85% for M-1, and 7.33% and 1.27% for M-3, respectively
- Increasing the dimensionless coating thickness β_2 from 0.0004 to 0.008 results in an ETC enhancement from 10.83% to 226.07%, demonstrating that coating thickness has the most significant impact on conductivity enhancement across all porosity ranges
- For thermal conductivity ratios of Kg/Ks = 2 to 15, ETC improves by up to 37.72% at high porosity (ε_o = 0.98), confirming that higher coating conductivity enhances solid conduction, particularly in foams with large pore volumes
- When the thermal conductivity ratio increases from 10 to 30, the ETC enhancement rises to 135.16% at high porosity, indicating that high-conductivity PCMs or fluids are particularly effective in porous structures with reduced solid content

5.2 Numerical investigation of passive and hybrid battery thermal management using metal foam–PCM and liquid-assisted PCM systems

5.2.1 Analysis of Li-ion battery under high discharge rate embedded with metal foam phase change composite.

In this chapter, a three-dimensional (3-D) computational fluid dynamics (CFD) model is proposed to analyse the thermal performance of MF-PCM composites integrated with a commercial prismatic lithium-ion battery. The effects of various parameters, including PCM thickness, discharge rate, and metal foam porosity, are analysed under steady, transient, and realistic driving conditions. The key outcomes of the study are detailed below.

- A minimum PCM thickness of 8 mm is found to be optimal for 20 Ah prismatic cells under 5C discharge, reducing the average temperature from 334 K (no PCM) to 315.04 K, with diminishing returns beyond this point
- MF-PCM Outperforms Pure PCM: At porosity $\varepsilon = 0.95$, the MF-PCM composite lowers the temperature rise by up to 56% compared to natural convection-only cooling. Average discharge temperatures reach 312.63 K (5C) and 310.65 K (4C) for 2S1P configurations
- In external short circuit tests, peak average temperatures rise to 367 K, 343 K, and 329 K for ESR values of 0.002, 0.003, and 0.004 Ω, respectively. Internal short circuit cases (ISR = 0.5×10^{-7} Ω·m³ and 1×10^{-7} Ω·m³) lead to average cell temperatures of 335.64 K and 324.7 K, respectively
- Aggressive Drive Cycle Performance: Under back-to-back aggressive cycles, the MF-PCM system limits battery temperature to 310.9 K, while 68% of the PCM melts, leaving residual thermal capacity for additional load buffering
- Realistic Drive Cycle Thermal Response: During a 75-minute urban driving cycle with mixed charging-discharging, the

battery temperature remains around 303 K, with negligible PCM melting, confirming the system's robustness under moderate real-world conditions

5.2.2 Enhanced thermal management system for Li-ion batteries using phase change material and liquid cooling under realistic driving cycles

In this chapter, a hybrid battery thermal management system (BTMS) combining phase change material (PCM) and a lightweight liquid-cooled plate is analysed under both continuous and melt-fraction-triggered intermittent cooling strategies using numerical simulations. The performance of the hybrid BTMS is evaluated under realistic drive cycles, including the Highway Fuel Economy Test (HWFET), Worldwide Harmonized Light Vehicles Test Procedure (WLTP), Urban Dynamometer Driving Schedule (UDDS), and Supplemental Federal Test Procedure (US-06), as well as under different cold plate configurations and rapid cyclic charge/discharge conditions (4C–1C and 5C–1C). The key outcomes of the study are elaborated below.

- Design Efficiency: The zig-zag cold plate with four turns improves convective heat transfer, reduces hotspots, and enhances PCM phase transitions. The hybrid system is 52.9% lighter than traditional SCP-based cold plates of equal volume.
- Energy Savings: Intermittent cooling strategy (IC) with ZCP reduces coolant energy consumption by 83.9% in 4C–1C cycles and 76.7% in 5C–1C cycles. Coolant usage dropped to as low as 13.9% of total cycle time.
- Realistic Drive Cycle Performance: In WLTP, HWFET, and UDDS cycles, the PCM absorbed sufficient heat without requiring coolant activation, achieving 100% pumping energy savings, with peak temperatures below 34 °C and gradients <5 °C.

- Optimal Operating Parameters: Increasing coolant velocity (0.2 → 0.3 m/s) and maintaining inlet temperature at 27 °C reduces peak temperature (from 33.5 °C to 32.4 °C) and temperature gradient (from 5.64 °C to 4.8 °C) during aggressive US-06 cycling.
- Thermal Uniformity and Stability: The ZCP design promotes more uniform temperature distribution, supports faster PCM solidification, and minimizes local thermal gradients, thereby improving overall system reliability for repeated dynamic thermal loads.

5.3 Optimizing battery thermal management with phase change materials: Influence of thickness, ambient conditions, and material selection

In this chapter, the performance of a PCM-based battery thermal management system for cylindrical (18650) lithium-ion cells is analysed through both experimental and numerical investigations. The effects of various discharge rates (2C–5C) and different PCMs (RT-24, RT-35, RT-38, RT-42, RT-47) on thermal performance have been analysed. The key outcomes of the study are detailed below.

- Optimal PCM Thickness: A 4 mm layer of RT-35 PCM offered the best trade-off between cooling effectiveness, material utilization, and weight. Beyond this, diminishing returns were observed due to increased thermal resistance and hotspot formation.
- Effect of Discharge Rate: Higher discharge rates significantly increased heat generation. At 5C, the 4 mm PCM layer reduced cell temperature from 60.45 °C (for 1 mm PCM thickness) to 44.02 °C, with the melt fraction dropping to 67.7%, showing efficient energy absorption but nearing saturation limits.
- Ambient Temperature and Material Selection: RT-35 was most effective at moderate ambient temperatures. RT-24 and RT-47

were more effective in cold and hot environments, respectively. All PCMs exhibited saturation beyond 50 °C, underlining the limits of passive cooling.

- Heat Transfer Coefficient Impact: Increasing $h_{surface}$ from 5 to 20 W/m².K improved PCM solidification and restored over 80% of melt fraction. However, this enhancement came with increased thermal gradients within the PCM, indicating the need to balance external cooling with the risk of uneven internal thermal gradients.

5.4 Scope of future work

It has been observed that due to their multiple advantages, PCMs can be employed to develop thermal management modules for cooling a wide range of thermal devices, including battery modules. These thermal management systems offer several benefits, such as regulating temperature, delaying or preventing thermal runaway, and reducing temperature gradients within battery modules. Although PCM-based thermal management systems offer significant advantages, further research is required to address several remaining challenges; these are detailed below.

- The long-term thermal cycling behaviour of PCMs, including phase change hysteresis, subcooling, and degradation over time needs to be analysed; as these effects can significantly influence latent heat storage capacity and thermal reliability in practical applications.
- Research should focus on enhancing the thermal conductivity and structural stability of PCMs through composites incorporating expanded graphite, graphene, or nano-fillers. Additionally, the use of solid–solid PCMs should be explored, as they offer improved form stability and eliminate leakage risks during phase transitions.

- PCM-based BTMSs should be tested under realistic, time-varying drive cycles and fluctuating ambient conditions to assess their effectiveness and long-term reliability.
- Further studies are needed on smart BTMS frameworks that incorporate sensor-based monitoring of temperature and PCM melt fraction, enabling real-time control of active or passive cooling and optimizing thermal load distribution under dynamic conditions.

References

[1] International Energy Agency (IEA), “Net Zero by 2050 - A Roadmap for the Global Energy Sector,” Paris, May 2021. Accessed: Apr. 15, 2025. [Online]. Available: https://www.iea.org/reports/net-zero-by-2050

[2] D. Gielen, F. Boshell, D. Saygin, M. D. Bazilian, N. Wagner, and R. Gorini, “The role of renewable energy in the global energy transformation,” *Energy Strategy Reviews*, vol. 24, pp. 38–50, Apr. 2019, doi: 10.1016/j.esr.2019.01.006.

[3] M. S. Hossain *et al.*, “Narrowing fossil fuel consumption in the Indian road transport sector towards reaching carbon neutrality,” *Energy Policy*, vol. 172, Jan. 2023, doi: 10.1016/j.enpol.2022.113330.

[4] X. Wang, X. Dong, Z. Zhang, and Y. Wang, “Transportation carbon reduction technologies: A review of fundamentals, application, and performance,” Dec. 01, 2024, *KeAi Communications Co.* doi: 10.1016/j.jtte.2024.11.001.

[5] Indian Brand Equity Foundation (IBEF), “Electric Vehicle,” The Indian EV market is forecasted to expand from US$ 3.21 billion in 2022 to US$ 113.99 billion by 2029, with a 66.52% CAGR. (IBEF). Accessed: Apr. 15, 2025. [Online]. Available: https://www.ibef.org/industry/electric-vehicle

[6] M. Shahjalal *et al.*, “A review of thermal management for Li-ion batteries: Prospects, challenges, and issues,” Jul. 01, 2021, *Elsevier Ltd*. doi: 10.1016/j.est.2021.102518.

[7] M. M. Amer, M. A. Shouman, M. S. Salem, A. M. Kannan, and A. M. Hamed, “Advances in thermal management systems for Li-Ion batteries: A review,” Aug. 01, 2024, *Elsevier Ltd*. doi: 10.1016/j.tsep.2024.102714.

[8] J. Ma *et al.*, “The 2021 battery technology roadmap,” *J Phys D Appl Phys*, vol. 54, no. 18, 2021, doi: 10.1088/1361-6463/abd353.

[9] D. Deng, “Li-ion batteries: Basics, progress, and challenges,” Sep. 01, 2015, *John Wiley and Sons Ltd*. doi: 10.1002/ese3.95.

[10] M. Li, J. Lu, Z. Chen, and K. Amine, “30 Years of Lithium-Ion Batteries,” *Advanced Materials*, vol. 30, no. 33, pp. 1–24, 2018, doi: 10.1002/adma.201800561.

[11] J. B. Goodenough and K. S. Park, “The Li-ion rechargeable battery: A perspective,” Jan. 30, 2013. doi: 10.1021/ja3091438.

[12] S. Babu Sanker and R. Baby, “Phase change material based thermal management of lithium ion batteries: A review on thermal performance of various thermal conductivity enhancers,” *J Energy Storage*, vol. 50, no. September 2021, p. 104606, 2022, doi: 10.1016/j.est.2022.104606.

[13] S. Kharabati and S. Saedodin, “A systematic review of thermal management techniques for electric vehicle batteries,” Jan. 01, 2024, *Elsevier Ltd*. doi: 10.1016/j.est.2023.109586.

[14] X. Han *et al.*, “A review on the key issues of the lithium ion battery degradation among the whole life cycle,” Aug. 01, 2019, *Elsevier B.V.* doi: 10.1016/j.etran.2019.100005.

[15] D. Bernardi, E. Pawlikowski, and J. Newman, “Bernardi1985,” vol. 132, no. 1, 1970.

[16] R. Srinivasan, A. Carson Baisden, B. G. Carkhuff, and M. H. Butler, “The five modes of heat generation in a Li-ion cell under discharge,” *J Power Sources*, vol. 262, pp. 93–103, Sep. 2014, doi: 10.1016/j.jpowsour.2014.03.062.

[17] A. G. Olabi *et al.*, “Battery thermal management systems: Recent progress and challenges,” *International Journal of Thermofluids*,

vol. 15, no. June, p. 100171, 2022, doi: 10.1016/j.ijft.2022.100171.

[18] G. Liu, M. Ouyang, L. Lu, J. Li, and X. Han, “Analysis of the heat generation of lithium-ion battery during charging and discharging considering different influencing factors,” in *Journal of Thermal Analysis and Calorimetry*, Kluwer Academic Publishers, 2014, pp. 1001–1010. doi: 10.1007/s10973-013-3599-9.

[19] D. Velumani and A. Bansal, “Thermal Behavior of Lithium- and Sodium-Ion Batteries: A Review on Heat Generation, Battery Degradation, Thermal Runway - Perspective and Future Directions,” Dec. 01, 2022, *American Chemical Society*. doi: 10.1021/acs.energyfuels.2c02889.

[20] S. S. Zhang, K. Xu, and T. R. Jow, “Charge and discharge characteristics of a commercial LiCoO2-based 18650 Li-ion battery,” *J Power Sources*, vol. 160, no. 2 SPEC. ISS., pp. 1403–1409, Oct. 2006, doi: 10.1016/j.jpowsour.2006.03.037.

[21] S. Tippmann, D. Walper, L. Balboa, B. Spier, and W. G. Bessler, “Low-temperature charging of lithium-ion cells part I: Electrochemical modeling and experimental investigation of degradation behavior,” *J Power Sources*, vol. 252, pp. 305–316, Apr. 2014, doi: 10.1016/j.jpowsour.2013.12.022.

[22] G. Nagasubramanian, “Electrical characteristics of 18650 Li-ion cells at low temperatures,” *J Appl Electrochem*, vol. 31, no. 1, pp. 99–104, 2001, doi: 10.1023/A:1004113825283.

[23] M. Alipour, E. Esen, A. R. Varzeghani, and R. Kizilel, “Performance of high capacity Li-ion pouch cells over wide range of operating temperatures and discharge rates,” *Journal of Electroanalytical Chemistry*, vol. 860, Mar. 2020, doi: 10.1016/j.jelechem.2020.113903.

[24] P. Ramadass, B. Haran, R. White, and B. N. Popov, “Capacity fade of Sony 18650 cells cycled at elevated temperatures: Part I. Cycling performance,” *J Power Sources*, vol. 112, no. 2, pp. 606–613, 2002, doi: 10.1016/S0378-7753(02)00474-3.

[25] H. Togun *et al.*, “A comprehensive review of battery thermal management systems for electric vehicles: Enhancing performance, sustainability, and future trends,” Jan. 06, 2025, *Elsevier Ltd*. doi: 10.1016/j.ijhydene.2024.11.093.

[26] G. Zhao, X. Wang, M. Negnevitsky, and H. Zhang, “A review of air-cooling battery thermal management systems for electric and hybrid electric vehicles,” Jul. 31, 2021, *Elsevier B.V.* doi: 10.1016/j.jpowsour.2021.230001.

[27] F. Zhang, L. Zhai, L. Zhang, M. Yi, B. Du, and S. Li, “A novel hybrid battery thermal management system with fins added on and between liquid cooling channels in composite phase change materials,” *Appl Therm Eng*, vol. 207, May 2022, doi: 10.1016/j.applthermaleng.2022.118198.

[28] P. Qin, M. Liao, D. Zhang, Y. Liu, J. Sun, and Q. Wang, “Experimental and numerical study on a novel hybrid battery thermal management system integrated forced-air convection and phase change material,” *Energy Convers Manag*, vol. 195, pp. 1371–1381, Sep. 2019, doi: 10.1016/j.enconman.2019.05.084.

[29] S. Lee, U. Han, and H. Lee, “Development of a hybrid battery thermal management system coupled with phase change material under fast charging conditions,” *Energy Convers Manag*, vol. 268, Sep. 2022, doi: 10.1016/j.enconman.2022.116015.

[30] Y. Yang, L. Chen, L. Yang, and X. Du, “Numerical study of combined air and phase change cooling for lithium-ion battery during dynamic cycles,” *International Journal of Thermal Sciences*, vol. 165, no. October 2020, p. 106968, 2021, doi: 10.1016/j.ijthermalsci.2021.106968.

[31] M. Li, S. Ma, H. Jin, R. Wang, and Y. Jiang, “Performance analysis of liquid cooling battery thermal management system in different cooling cases,” *J Energy Storage*, vol. 72, Nov. 2023, doi: 10.1016/j.est.2023.108651.

[32] Y. Huo, Z. Rao, X. Liu, and J. Zhao, “Investigation of power battery thermal management by using mini-channel cold plate,” *Energy Convers Manag*, vol. 89, pp. 387–395, 2015, doi: 10.1016/j.enconman.2014.10.015.

[33] W. Yang, F. Zhou, H. Zhou, Q. Wang, and J. Kong, “Thermal performance of cylindrical lithium-ion battery thermal management system integrated with mini-channel liquid cooling and air cooling,” *Appl Therm Eng*, vol. 175, Jul. 2020, doi: 10.1016/j.applthermaleng.2020.115331.

[34] X. Li, D. Zhou, G. Zhang, C. Wang, R. Lin, and Z. Zhong, “Experimental investigation of the thermal performance of silicon cold plate for battery thermal management system,” *Appl Therm Eng*, vol. 155, pp. 331–340, Jun. 2019, doi: 10.1016/j.applthermaleng.2019.04.007.

[35] H. Wang, T. Tao, J. Xu, X. Mei, X. Liu, and P. Gou, “Cooling capacity of a novel modular liquid-cooled battery thermal management system for cylindrical lithium ion batteries,” *Appl Therm Eng*, vol. 178, Sep. 2020, doi: 10.1016/j.applthermaleng.2020.115591.

[36] D. Zhao, Z. Lei, and C. An, “Research on battery thermal management system based on liquid cooling plate with honeycomb-like flow channel,” *Appl Therm Eng*, vol. 218, Jan. 2023, doi: 10.1016/j.applthermaleng.2022.119324.

[37] K. Chen, Y. Chen, M. Song, and S. Wang, “Multi-parameter structure design of parallel mini-channel cold plate for battery thermal management,” *Int J Energy Res*, vol. 44, no. 6, pp. 4321–4334, May 2020, doi: 10.1002/er.5200.

[38] K. Pielichowska and K. Pielichowski, “Phase change materials for thermal energy storage,” 2014, *Elsevier Ltd*. doi: 10.1016/j.pmatsci.2014.03.005.

[39] K. Du, J. Calautit, Z. Wang, Y. Wu, and H. Liu, “A review of the applications of phase change materials in cooling, heating and power generation in different temperature ranges,” Jun. 15, 2018, *Elsevier Ltd*. doi: 10.1016/j.apenergy.2018.03.005.

[40] M. M. Kenisarin, “Thermophysical properties of some organic phase change materials for latent heat storage. A review,” *Solar Energy*, vol. 107, pp. 553–575, 2014, doi: 10.1016/j.solener.2014.05.001.

[41] M. Hussain, M. K. Khan, and M. Pathak, “Thermal analysis of phase change material encapsulated li-ion battery pack using multi-scale multi-dimensional framework,” *J Energy Storage*, vol. 65, Aug. 2023, doi: 10.1016/j.est.2023.107290.

[42] R. Zhao, J. Gu, and J. Liu, “Optimization of a phase change material based internal cooling system for cylindrical Li-ion battery pack and a hybrid cooling design,” *Energy*, vol. 135, pp. 811–822, 2017, doi: 10.1016/j.energy.2017.06.168.

[43] W. Wu, S. Xie, W. Zhang, R. Ma, J. Yang, and Z. Rao, “Role of natural convection and battery arrangement for phase change material based battery thermal management unit,” *J Energy Storage*, vol. 52, Aug. 2022, doi: 10.1016/j.est.2022.104820.

[44] S. Vashisht and D. Rakshit, “Unravelling the impact of PCM thickness: Passive thermal management for INR18650 Li-ion cells across discharge rates,” *Thermal Science and Engineering Progress*, vol. 53, Aug. 2024, doi: 10.1016/j.tsep.2024.102758.

[45] L. Fan and J. M. Khodadadi, “Thermal conductivity enhancement of phase change materials for thermal energy storage: A review,” Jan. 2011. doi: 10.1016/j.rser.2010.08.007.

[46] M. G. Kibria *et al.*, “A Review on Composite Phase Change Materials and Fins-Based Li-Ion Battery Thermal Management Systems with Design Perspectives and Future Outlooks,” Aug. 01, 2024, *American Chemical Society*. doi: 10.1021/acs.energyfuels.4c02062.

[47] S. L. Tariq, H. M. Ali, M. A. Akram, M. M. Janjua, and M. Ahmadlouydarab, “Nanoparticles enhanced phase change materials (NePCMs)-A recent review,” *Appl Therm Eng*, vol. 176, no. April, p. 115305, 2020, doi: 10.1016/j.applthermaleng.2020.115305.

[48] M. M. Heyhat, S. Mousavi, and M. Siavashi, “Battery thermal management with thermal energy storage composites of PCM, metal foam, fin and nanoparticle,” *J Energy Storage*, vol. 28, no. September 2019, p. 101235, 2020, doi: 10.1016/j.est.2020.101235.

[49] A. M. Elshaer, A. M. A. Soliman, M. Kassab, S. Mori, and A. A. Hawwash, “Experimental investigations on copper foam/PCM composite-based thermal control hardware (TCH) using foam samples with different pore sizes under intermittent thermal conditions,” *J Energy Storage*, vol. 72, Nov. 2023, doi: 10.1016/j.est.2023.108320.

[50] M. T. Pettes, H. Ji, R. S. Ruoff, and L. Shi, “Thermal transport in three-dimensional foam architectures of few-layer graphene and ultrathin graphite,” *Nano Lett*, vol. 12, no. 6, pp. 2959–2964, 2012, doi: 10.1021/nl300662q.

[51] A. Hussain, C. Y. Tso, and C. Y. H. Chao, “Experimental investigation of a passive thermal management system for high-powered lithium ion batteries using nickel foam-paraffin composite,” *Energy*, vol. 115, pp. 209–218, 2016, doi: 10.1016/j.energy.2016.09.008.

[52] V. V. Calmidi and R. L. Mahajan, “The effective thermal conductivity of high porosity fibrous metal foams,” *J Heat Transfer*, vol. 121, no. 2, pp. 466–471, 1999, doi: 10.1115/1.2826001.

[53] A. Bhattacharya, V. V. Calmidi, and R. L. Mahajan, “Thermophysical properties of high porosity metal foams,” *Int J Heat Mass Transf*, vol. 45, no. 5, pp. 1017–1031, 2002, doi: 10.1016/S0017-9310(01)00220-4.

[54] K. Lafdi, M. Almajali, and O. Huzayyin, “Thermal properties of copper-coated carbon foams,” *Carbon N Y*, vol. 47, no. 11, pp. 2620–2626, 2009, doi: 10.1016/j.carbon.2009.05.014.

[55] K. C. Chan, C. Y. Tso, A. Hussain, and C. Y. H. Chao, “A theoretical model for the effective thermal conductivity of graphene coated metal foams,” *Appl Therm Eng*, vol. 161, no. July, p. 114112, 2019, doi: 10.1016/j.applthermaleng.2019.114112.

[56] J. W. Paek, B. H. Kang, S. Y. Kim, and J. M. Hyun, “Effective thermal conductivity and permeability of aluminum foam materials,” *Int J Thermophys*, vol. 21, no. 2, pp. 453–464, 2000, doi: 10.1023/A:1006643815323.

[57] G. N. Dul’nev, “Heat transfer through solid disperse systems,” *Journal of Engineering Physics*, vol. 9, no. 3, pp. 275–279, 1965, doi: 10.1007/BF00828349.

[58] D. Edouard, “The Effective Thermal Conductivity for ‘“Slim”’ and ‘“Fat”’ Foams,” *AIChE Journal*, vol. 57, no. 6, pp. 1646–1651, 2011, doi: 10.1002/aic.

[59] A. Zenner and D. Edouard, “Revised cubic model for theoretical estimation of effective thermal conductivity of metal foams,” *Appl Therm Eng*, vol. 113, pp. 1313–1318, 2017, doi: 10.1016/j.applthermaleng.2016.11.129.

[60] R. M. Sullivan, L. J. Ghosn, and B. A. Lerch, “A general tetrakaidecahedron model for open-celled foams,” *Int J Solids Struct*, vol. 45, no. 6, pp. 1754–1765, 2008, doi: 10.1016/j.ijsolstr.2007.10.028.

[61] K. Boomsma and D. Poulikakos, “On the effective thermal conductivity of a three-dimensionally structured fluid-saturated metal foam,” *Int J Heat Mass Transf*, vol. 44, no. 4, pp. 827–836, 2001, doi: 10.1016/S0017-9310(00)00123-X.

[62] K. Boomsma and D. Poulikakos, “Erratum: On the effective thermal conductivity of a three-dimensionally structured fluid-saturated metal foam (International Journal of Heat and Mass Transfer (2001) 44 (827-836)),” *Int J Heat Mass Transf*, vol. 54, no. 1–3, pp. 746–748, 2011, doi: 10.1016/j.ijheatmasstransfer.2010.08.023.

[63] Z. Dai, K. Nawaz, Y. G. Park, J. Bock, and A. M. Jacobi, “Correcting and extending the Boomsma-Poulikakos effective thermal conductivity model for three-dimensional, fluid-saturated metal foams,” *International Communications in Heat and Mass Transfer*, vol. 37, no. 6, pp. 575–580, 2010, doi: 10.1016/j.icheatmasstransfer.2010.01.015.

[64] H. Yang, M. Zhao, Z. L. Gu, L. W. Jin, and J. C. Chai, “A further discussion on the effective thermal conductivity of metal foam: An improved model,” *Int J Heat Mass Transf*, vol. 86, pp. 207–211, 2015, doi: 10.1016/j.ijheatmasstransfer.2015.03.001.

[65] Y. Yao, H. Wu, and Z. Liu, “A new prediction model for the effective thermal conductivity of high porosity open-cell metal foams,” *International Journal of Thermal Sciences*, vol. 97, pp. 56–67, 2015, doi: 10.1016/j.ijthermalsci.2015.06.008.

[66] D. Wu and C. Huang, “Thermal conductivity model of open-cell foam suitable for wide span of porosities,” *Int J Heat Mass*

Transf, vol. 130, pp. 1075–1086, 2019, doi: 10.1016/j.ijheatmasstransfer.2018.11.016.

[67] R. Huang, Z. Li, W. Hong, Q. Wu, and X. Yu, "Experimental and numerical study of PCM thermophysical parameters on lithium-ion battery thermal management," *Energy Reports*, vol. 6, pp. 8–19, 2020, doi: 10.1016/j.egyr.2019.09.060.

[68] M. Alipanah and X. Li, "Numerical studies of lithium-ion battery thermal management systems using phase change materials and metal foams," *Int J Heat Mass Transf*, vol. 102, pp. 1159–1168, 2016, doi: 10.1016/j.ijheatmasstransfer.2016.07.010.

[69] W. Q. Li, Z. G. Qu, Y. L. He, and Y. B. Tao, "Experimental study of a passive thermal management system for high-powered lithium ion batteries using porous metal foam saturated with phase change materials," *J Power Sources*, vol. 255, pp. 9–15, 2014, doi: 10.1016/j.jpowsour.2014.01.006.

[70] D. Barnes and X. Li, "Battery thermal management using phase change material-metal foam composite materials at various environmental temperatures," *Nutr Today*, vol. 17, no. 2, pp. 1–7, 2020, doi: 10.1115/1.4045326.

[71] B. Kurşun, E. Toklu, F. Polat, and M. Balta, "The effect of outer container geometry on the thermal management of lithium-ion batteries with a combination of phase change material and metal foam," *J Energy Storage*, vol. 80, Mar. 2024, doi: 10.1016/j.est.2023.110227.

[72] Z. Sun, R. Fan, F. Yan, T. Zhou, and N. Zheng, "Thermal management of the lithium-ion battery by the composite PCM-Fin structures," *Int J Heat Mass Transf*, vol. 145, Dec. 2019, doi: 10.1016/j.ijheatmasstransfer.2019.118739.

[73] Z. Sun, R. Fan, and N. Zheng, "Thermal management of a simulated battery with the compound use of phase change material and fins: Experimental and numerical investigations,"

International Journal of Thermal Sciences, vol. 165, Jul. 2021, doi: 10.1016/j.ijthermalsci.2021.106945.

[74] V. G. Choudhari, A. S. Dhoble, and S. Panchal, "Numerical analysis of different fin structures in phase change material module for battery thermal management system and its optimization," *Int J Heat Mass Transf*, vol. 163, Dec. 2020, doi: 10.1016/j.ijheatmasstransfer.2020.120434.

[75] V. G. Choudhari, A. S. Dhoble, S. Panchal, M. Fowler, and R. Fraser, "Numerical investigation on thermal behaviour of 5 × 5 cell configured battery pack using phase change material and fin structure layout," *J Energy Storage*, vol. 43, Nov. 2021, doi: 10.1016/j.est.2021.103234.

[76] S. Ambekar, P. Rath, and A. Bhattacharya, "A novel PCM and TCE based thermal management of battery module," *Thermal Science and Engineering Progress*, vol. 29, Mar. 2022, doi: 10.1016/j.tsep.2022.101196.

[77] P. Zare, N. Perera, J. Lahr, and R. Hasan, "A novel thermal management system for cylindrical lithium-ion batteries using internal-external fin-enhanced phase change material," *Appl Therm Eng*, vol. 238, Feb. 2024, doi: 10.1016/j.applthermaleng.2023.121985.

[78] Y. Li *et al.*, "A novel petal-type battery thermal management system with dual phase change materials," *Int J Heat Mass Transf*, vol. 207, Jun. 2023, doi: 10.1016/j.ijheatmasstransfer.2023.123989.

[79] J. Weng, D. Ouyang, X. Yang, M. Chen, G. Zhang, and J. Wang, "Optimization of the internal fin in a phase-change-material module for battery thermal management," *Appl Therm Eng*, vol. 167, Feb. 2020, doi: 10.1016/j.applthermaleng.2019.114698.

[80] A. R. Bais, D. G. Subhedar, and S. Panchal, "Critical thickness of nano-enhanced RT-42 paraffin based battery thermal

management system for electric vehicles: A numerical study," *J Energy Storage*, vol. 52, Aug. 2022, doi: 10.1016/j.est.2022.104757.

[81] R. Akula and C. Balaji, "Thermal management of 18650 Li-ion battery using novel fins–PCM–EG composite heat sinks," *Appl Energy*, vol. 316, Jun. 2022, doi: 10.1016/j.apenergy.2022.119048.

[82] S. Mousavi, M. Siavashi, and A. Zadehkabir, "A new design for hybrid cooling of Li-ion battery pack utilizing PCM and mini channel cold plates," *Appl Therm Eng*, vol. 197, Oct. 2021, doi: 10.1016/j.applthermaleng.2021.117398.

[83] W. Yang, F. Zhou, Y. Liu, S. Xu, and X. Chen, "Thermal performance of honeycomb-like battery thermal management system with bionic liquid mini-channel and phase change materials for cylindrical lithium-ion battery," *Appl Therm Eng*, vol. 188, no. November 2020, 2021, doi: 10.1016/j.applthermaleng.2021.116649.

[84] M. Akbarzadeh, T. Kalogiannis, L. Jin, D. Karimi, J. Van Mierlo, and M. Berecibar, "Experimental and numerical thermal analysis of a lithium-ion battery module based on a novel liquid cooling plate embedded with phase change material," *J Energy Storage*, vol. 50, no. April, p. 104673, 2022, doi: 10.1016/j.est.2022.104673.

[85] Q. Xu, Y. Xie, X. Li, L. Li, K. Zheng, and S. Bei, "Cycle performance analysis of hybrid battery thermal management system coupling phase change material with liquid cooling for lithium-ion battery module operated at high C-rates," *Energy*, vol. 308, Nov. 2024, doi: 10.1016/j.energy.2024.132847.

[86] J. Zheng *et al.*, "A novel thermal management system combining phase change material with wavy cold plate for lithium-ion battery pack under high ambient temperature and rapid

discharging," *Appl Therm Eng*, vol. 245, May 2024, doi: 10.1016/j.applthermaleng.2024.122803.

[87] Y. Wang, T. Gao, L. Zhou, J. Gong, and J. Li, "A parametric study of a hybrid battery thermal management system that couples PCM with wavy microchannel cold plate," *Appl Therm Eng*, vol. 219, Jan. 2023, doi: 10.1016/j.applthermaleng.2022.119625.

[88] Y. Liu *et al.*, "Numerical simulations on hybrid thermal management of mini-channel cold plate and PCM for lithium-ion batteries," *Appl Therm Eng*, vol. 250, Aug. 2024, doi: 10.1016/j.applthermaleng.2024.123475.

[89] S. Lee, H. Lee, Y. J. Jun, and H. Lee, "Hybrid battery thermal management system coupled with paraffin/copper foam composite phase change material," *Appl Energy*, vol. 353, Jan. 2024, doi: 10.1016/j.apenergy.2023.122043.

[90] Z. An, W. Gao, J. Zhang, H. Liu, and Z. Gao, "Bionic capillary/honeycomb hybrid lithium-ion battery thermal management system for electric vehicle," *Appl Therm Eng*, vol. 242, Apr. 2024, doi: 10.1016/j.applthermaleng.2024.122444.

[91] Z. Liu, G. Xu, Y. Xia, and S. Tian, "Numerical study of thermal management of pouch lithium-ion battery based on composite liquid-cooled phase change materials with honeycomb structure," *J Energy Storage*, vol. 70, Oct. 2023, doi: 10.1016/j.est.2023.108001.

[92] H. Yang, M. Li, Z. Wang, and B. Ma, "A compact and lightweight hybrid liquid cooling system coupling with Z-type cold plates and PCM composite for battery thermal management," *Energy*, vol. 263, Jan. 2023, doi: 10.1016/j.energy.2022.126026.

[93] C. Qiu, B. Kong, Y. Zou, R. Zheng, and H. Shi, "Multi-Objective Optimization with PCM integration and delayed cooling strategy

for high-rate discharge applications," *Int J Heat Mass Transf*, vol. 218, Jan. 2024, doi: 10.1016/j.ijheatmasstransfer.2023.124763.

[94] A. Amiri and K. Vafai, "Analysis of dispersion effects and non-thermal equilibrium, non-Darcian, variable porosity incompressible flow through porous media," *Int J Heat Mass Transf*, vol. 37, no. 6, pp. 939–954, 1994, doi: 10.1016/0017-9310(94)90219-4.

[95] C. L. Tien and M. L. Hunt, "Boundary-layer flow and heat transfer in porous beds," *Chemical Engineering and Processing*, vol. 21, no. 2, pp. 53–63, 1987, doi: 10.1016/0255-2701(87)80007-7.

[96] S. Kanaun and O. Tkachenko, "Effective conductive properties of open-cell foams," *Int J Eng Sci*, vol. 46, no. 6, pp. 551–571, 2008, doi: 10.1016/j.ijengsci.2008.01.012.

[97] M. S. Phanikumar and R. L. Mahajan, "HT in foams, Phanikumar and Mahajan 2002," vol. 45, pp. 3781–3793, 2002.

[98] E. N. Schmierer and A. Razani, "Self-consistent open-celled metal foam model for thermal applications," *J Heat Transfer*, vol. 128, no. 11, pp. 1194–1203, 2006, doi: 10.1115/1.2352787.

[99] E. Sadeghi, S. Hsieh, and M. Bahrami, "Thermal conductivity and contact resistance of metal foams," *J Phys D Appl Phys*, vol. 44, no. 12, 2011, doi: 10.1088/0022-3727/44/12/125406.

[100] R. Dyga and S. Witczak, "Investigation of effective thermal conductivity aluminum foams," *Procedia Eng*, vol. 42, no. August, pp. 1088–1099, 2012, doi: 10.1016/j.proeng.2012.07.500.

[101] X. H. Yang, J. X. Bai, H. Bin Yan, J. J. Kuang, T. J. Lu, and T. Kim, "An Analytical Unit Cell Model for the Effective Thermal Conductivity of High Porosity Open-Cell Metal Foams," *Transp*

Porous Media, vol. 102, no. 3, pp. 403–426, 2014, doi: 10.1007/s11242-014-0281-z.

[102] X. Xiao, P. Zhang, and M. Li, "Effective thermal conductivity of open-cell metal foams impregnated with pure paraffin for latent heat storage," *International Journal of Thermal Sciences*, vol. 81, no. 1, pp. 94–105, 2014, doi: 10.1016/j.ijthermalsci.2014.03.006.

[103] P. Taheri and M. Bahrami, "Temperature Rise in Prismatic Polymer Lithium-Ion Batteries: An Analytic Approach," *SAE Int J Passeng Cars Electron Electr Syst*, vol. 5, no. 1, pp. 164–176, 2012, doi: 10.4271/2012-01-0334.

[104] Y. Li, Z. Zhou, and W. T. Wu, "Three-dimensional thermal modeling of Li-ion battery cell and 50 V Li-ion battery pack cooled by mini-channel cold plate," *Appl Therm Eng*, vol. 147, pp. 829–840, Jan. 2019, doi: 10.1016/j.applthermaleng.2018.11.009.

[105] M. Chen and G. A. Rincón-Mora, "Accurate electrical battery model capable of predicting runtime and I-V performance," *IEEE Transactions on Energy Conversion*, vol. 21, no. 2, pp. 504–511, 2006, doi: 10.1109/TEC.2006.874229.

[106] K. H. Kwon, C. B. Shin, T. H. Kang, and C. S. Kim, "A two-dimensional modeling of a lithium-polymer battery," *J Power Sources*, vol. 163, no. 1 SPEC. ISS., pp. 151–157, 2006, doi: 10.1016/j.jpowsour.2006.03.012.

[107] M. Doyle, T. F. Fuller, and J. Newman, "Modeling of Galvanostatic Charge and Discharge," *J Electrochem Soc*, vol. 140, no. 6, pp. 1526–1533, 1993.

[108] Ansys Fluent Theory Guide, *Ansys Fluent Theory Guide*, vol. 15317, no. November. ANSYS, 2021. [Online]. Available: http://scholar.google.com/scholar?hl=en&btnG=Search&q=intitle:ANSYS+FLUENT+Theory+Guide#0

[109] L. Cai and R. E. White, “Mathematical modeling of a lithium ion battery with thermal effects in COMSOL Inc. Multiphysics (MP) software,” *J Power Sources*, vol. 196, no. 14, pp. 5985–5989, Jul. 2011, doi: 10.1016/j.jpowsour.2011.03.017.

[110] H. Zhang, C. Li, R. Zhang, Y. Lin, and H. Fang, “Thermal analysis of a 6s4p Lithium-ion battery pack cooled by cold plates based on a multi-domain modeling framework,” *Appl Therm Eng*, vol. 173, Jun. 2020, doi: 10.1016/j.applthermaleng.2020.115216.

[111] V. R. Voller and C. Prakash, “A fixed grid numerical modelling methodology for convection-diffusion mushy region phase-change problems,” *Int J Heat Mass Transf*, vol. 30, no. 8, pp. 1709–1719, 1987, doi: 10.1016/0017-9310(87)90317-6.

[112] P. T. Sardari, H. I. Mohammed, D. Giddings, G. S. walker, M. Gillott, and D. Grant, “Numerical study of a multiple-segment metal foam-PCM latent heat storage unit: Effect of porosity, pore density and location of heat source,” *Energy*, vol. 189, p. 116108, 2019, doi: 10.1016/j.energy.2019.116108.

[113] S. Whitaker, *The Method of Volume Averaging*, vol. 13. in Theory and Applications of Transport in Porous Media, vol. 13. Dordrecht: Springer Netherlands, 1999. doi: 10.1007/978-94-017-3389-2.

[114] M. Esapour, A. Hamzehnezhad, A. A. Rabienataj Darzi, and M. Jourabian, “Melting and solidification of PCM embedded in porous metal foam in horizontal multi-tube heat storage system,” *Energy Convers Manag*, vol. 171, no. May, pp. 398–410, 2018, doi: 10.1016/j.enconman.2018.05.086.

[115] B. Buonomo, O. Manca, S. Nardini, and R. E. Plomitallo, “Numerical Investigation on Shell and Tube Latent Thermal Energy Storage Partially Filled With Metal Foam and Corrugated Internal Tube,” *Proceedings of ASME 2022 Heat Transfer*

Summer Conference, HT 2022, vol. 03003, 2022, doi: 10.1115/HT2022-81806.

[116] S. M. Borhani, M. J. Hosseini, R. Pakrouh, A. A. Ranjbar, and A. Nourian, "Performance enhancement of a thermoelectric harvester with a PCM/Metal foam composite," *Renew Energy*, vol. 168, pp. 1122–1140, 2021, doi: 10.1016/j.renene.2021.01.020.

[117] Z. Liu, Y. Yao, and H. Wu, "Numerical modeling for solid-liquid phase change phenomena in porous media: Shell-and-tube type latent heat thermal energy storage," *Appl Energy*, vol. 112, pp. 1222–1232, 2013, doi: 10.1016/j.apenergy.2013.02.022.

[118] V. V. Calmidi and R. L. Mahajan, "Forced convection in high porosity metal foams," *J Heat Transfer*, vol. 122, no. 3, pp. 557–565, 2000, doi: 10.1115/1.1287793.

[119] A. Žukauskas, "Heat Transfer from Tubes in Crossflow," *Adv Heat Transf*, vol. 8, no. C, pp. 93–160, Jan. 1972, doi: 10.1016/S0065-2717(08)70038-8.

[120] W. Zhang, Z. Liang, W. Wu, G. Ling, and R. Ma, "Design and optimization of a hybrid battery thermal management system for electric vehicle based on surrogate model," *Int J Heat Mass Transf*, vol. 174, Aug. 2021, doi: 10.1016/j.ijheatmasstransfer.2021.121318.

[121] I. Kumar Lokhande and N. Tiwari, "A numerical investigation of novel segmented PCM blocks filled with different phase change material cooling for Lithium-Ion battery," *Appl Therm Eng*, vol. 252, Sep. 2024, doi: 10.1016/j.applthermaleng.2024.123673.

[122] S. Sudhakaran, M. Terese, Y. Mohan, A. D. Thampi, and S. Rani, "Influence of various parameters on the cooling performance of battery thermal management systems based on phase change materials," *Appl Therm Eng*, vol. 222, Mar. 2023, doi: 10.1016/j.applthermaleng.2022.119936.

[123] J. Ren *et al.*, “Battery thermal management system by employing different phase change materials with SWCNT nanoparticles to obtain better battery cooling performance,” *Case Studies in Thermal Engineering*, vol. 61, Sep. 2024, doi: 10.1016/j.csite.2024.104987.

[124] H. Wang *et al.*, “Investigation of the thermal management potential of phase change material for lithium-ion battery,” *Appl Therm Eng*, vol. 236, Jan. 2024, doi: 10.1016/j.applthermaleng.2023.121590.

[125] C. Fink and B. Kaltenegger, “Electrothermal and Electrochemical Modeling of Lithium-ion Batteries: 3D Simulation with Experimental Validation,” *ECS Trans*, vol. 61, no. 27, pp. 105–124, Oct. 2014, doi: 10.1149/06127.0105ecst.

[126] Y. Liu, Y. G. Liao, and M.-C. Lai, “Transient Temperature Distributions on Lithium-Ion Polymer SLI Battery,” *Vehicles*, vol. 1, no. 1, pp. 127–137, 2019, doi: 10.3390/vehicles1010008.

[127] C. Y. Zhao, W. Lu, and Y. Tian, “Heat transfer enhancement for thermal energy storage using metal foams embedded within phase change materials (PCMs),” *Solar Energy*, vol. 84, no. 8, pp. 1402–1412, 2010, doi: 10.1016/j.solener.2010.04.022.

[128] D. Worwood *et al.*, “Thermal analysis of a lithium-ion pouch cell under aggressive automotive duty cycles with minimal cooling,” *IET Conference Publications*, no. CP691, pp. 1–6, 2016, doi: 10.1049/cp.2016.1255.

[129] J. R. Patel and M. K. Rathod, “Recent developments in the passive and hybrid thermal management techniques of lithium-ion batteries,” *J Power Sources*, vol. 480, no. July, p. 228820, 2020, doi: 10.1016/j.jpowsour.2020.228820.

[130] G. Murali, G. S. N. Sravya, J. Jaya, and V. Naga Vamsi, “A review on hybrid thermal management of battery packs and it’s cooling performance by enhanced PCM,” *Renewable and*

Sustainable Energy Reviews, vol. 150, p. 111513, 2021, doi: 10.1016/j.rser.2021.111513.

[131] M. M. Khan, M. Alkhedher, M. Ramadan, and M. Ghazal, "Hybrid PCM-based thermal management for lithium-ion batteries: Trends and challenges," Dec. 01, 2023, *Elsevier Ltd*. doi: 10.1016/j.est.2023.108775.

[132] Y. Liu, Y. G. Liao, and M. C. Lai, "Temperature variations of a lithium-ion polymer battery cell during electric vehicle driving cycles," in *2021 IEEE Transportation Electrification Conference and Expo, ITEC 2021*, Institute of Electrical and Electronics Engineers Inc., Jun. 2021, pp. 34–39. doi: 10.1109/ITEC51675.2021.9490120.

[133] J. Lin, X. Liu, S. Li, C. Zhang, and S. Yang, "A review on recent progress, challenges and perspective of battery thermal management system," Mar. 01, 2021, *Elsevier Ltd*. doi: 10.1016/j.ijheatmasstransfer.2020.120834.

[134] W. Zuo, D. Li, Q. Li, Q. Cheng, and Y. Huang, "Effects of intermittent pulsating flow on the performance of multi-channel cold plate in electric vehicle lithium-ion battery pack," *Energy*, vol. 294, May 2024, doi: 10.1016/j.energy.2024.130832.

[135] Y. Wang, Y. Wang, T. He, and N. Mao, "A numerical study on a hybrid battery thermal management system based on PCM and wavy microchannel liquid cooling," *Renew Energy*, vol. 235, Nov. 2024, doi: 10.1016/j.renene.2024.121273.

[136] J. Zhu *et al.*, "Investigation of capacity fade for 18650-type lithium-ion batteries cycled in different state of charge (SoC) ranges," *J Power Sources*, vol. 489, Mar. 2021, doi: 10.1016/j.jpowsour.2020.229422.

[137] K. I. Alsharif *et al.*, "A Coupled Thermo-Mechanical Dynamic Characterization of Cylindrical Batteries," *IEEE Access*, vol. 10, pp. 51708–51722, 2022, doi: 10.1109/ACCESS.2022.3173640.

[138] J. Holman, *Experimental methods for engineers eighth edition*. 2021. Accessed: Dec. 16, 2024. [Online]. Available: http://debracollege.dspaces.org/handle/123456789/560

[139] N. Napa, M. K. Agrawal, and B. Tamma, "Design of novel thermal management system for Li-ion battery module using metal matrix based passive cooling method," *J Energy Storage*, vol. 73, Dec. 2023, doi: 10.1016/j.est.2023.109119.

[140] U. Moralı, "Computational modeling and statistical evaluation of thermal behavior of cylindrical lithium-ion battery," *J Energy Storage*, vol. 55, Nov. 2022, doi: 10.1016/j.est.2022.105376.

[141] K. Kumar, J. Sarkar, and S. S. Mondal, "Analysis of ternary hybrid nanofluid in microchannel-cooled cylindrical Li-ion battery pack using multi-scale multi-domain framework," *Appl Energy*, vol. 355, Feb. 2024, doi: 10.1016/j.apenergy.2023.122241.

[142] U. Seong Kim, J. Yi, C. B. Shin, T. Han, and S. Park, "Modeling the Dependence of the Discharge Behavior of a Lithium-Ion Battery on the Environmental Temperature," *J Electrochem Soc*, vol. 158, no. 5, p. A611, 2011, doi: 10.1149/1.3565179.

[143] J. R. Patel and M. K. Rathod, "Phase change material selection using simulation-oriented optimization to improve the thermal performance of lithium-ion battery," *J Energy Storage*, vol. 49, May 2022, doi: 10.1016/j.est.2022.103974.

Appendix I

Experimental Uncertainty

In experimental studies, uncertainties arise due to limitations in instrumentation, measurement procedures, and environmental factors. These uncertainties in various parameters need to be quantified to assess the reliability of test data and validation of numerical models. In the present experimental study, temperature, voltage and current are measured by using pre-calibrated instruments. This section discusses the errors involved with the measured parameters and the uncertainties associated with calculated parameter (Power).

Theoretical background: If a measured quantity y is a function of n independent variables $x_1, x_2, x_3, x_4, \ldots\ldots x_n$, then the combined standard uncertainty u_y can be estimated using the Taylor Series method also known as the method of propagation of uncertainty [1]:

$$u_y{}^2 = \left(\frac{\partial y}{\partial x_1}\right)^2 u_{x_1}{}^2 + \left(\frac{\partial y}{\partial x_2}\right)^2 u_{x_2}{}^2 + \cdots \left(\frac{\partial y}{\partial x_n}\right)^2 u_{x_n}{}^2$$

Temperature: Here, temperature measurements are carried out using K-type thermocouples (Chromel–Alumel), 1/36 SWG with Teflon insulation. The thermocouples are fixed directly to the surface of 18650 cylindrical lithium-ion cells using Kapton tape. Data acquisition (Agilent 34972A) system records the temperature readings at a sampling interval of four seconds. The thermocouples are factory-calibrated and verified for accuracy over a temperature range of 0°C to 100°C.

Voltage and current: Voltage and currents are measured during the charging and discharging phases by employing high-precision programmable instruments. During the charging phase, the BK Precision 9115 Programmable DC Power Supply is used to supply controlled voltage and current to the battery. The instrument offers a voltage accuracy of ±(0.01% of reading + 5 mV) and a current accuracy of ±(0.1% of reading + 10 mA). For the discharging phase, the BK

Precision 8510B Programmable DC Electronic Load is employed to draw current from the battery while maintaining accurate voltage and current tracking. This device provides the same level of measurement accuracy, i.e. voltage ± (0.05% + 10 mV) and current ± (0.1% + 10 mA).

Uncertainty during discharge:

For the Li-ion cell (Samsung 18650-25R) capacity of 2.5Ah and nominal voltage of 3.7V that undergoes discharge at 5C.

$$\text{Current} = 5 \times 2.5 = 12 \text{ A} \quad \text{(I.1)}$$

$$\text{Voltage: } 3.7 \text{ V} \quad \text{(I.2)}$$

$$\text{Power} = (\text{VI}) = 12 \times 3.7 = 46.25 \text{ W} \quad \text{(I.3)}$$

Instrument Voltage uncertainty:

$$u_v = 0.05\% \times 3.7 + 0.005 = 0.01185 \text{ V} \quad \text{(I.4)}$$

Instrument Current uncertainty:

$$u_I = 0.1\% \times 12.5 + 0.01 = 0.0225 \text{ A} \quad \text{(I.5)}$$

Estimated instrument power uncertainty:

$$u_p = \sqrt{((I \times u_v)^2 + (V \times u_I)^2)} \quad \text{(I.6)}$$

$$u_p = \sqrt{((0.148125)^2 + (0.08325)^2)} \quad \text{(I.7)}$$

$$u_p = 0.170 \text{ W} \quad \text{(I.8)}$$

$$\frac{u_p}{P} X100 = \frac{0.170}{46.25} X100 = \pm 0.37\% \quad \text{(I.9)}$$

Uncertainty during temperature measurement:

- Thermocouple accuracy (u_{sensor}) : ± 0.4 °C
- Repeatability uncertainty ($u_{experiments}$) : ± 0.3 °C
- Reference temperature: 50 °C

$$u_T = \sqrt{\left((u_{sensor})^2 + \left(u_{experiments}\right)^2\right)} \quad \text{(I.10)}$$

$$u_T = \sqrt{(0.16 + 0.09)} \quad \text{(I.11)}$$

$$u_T = 0.5\ °C \tag{I.12}$$

Relative Uncertainty

$$\frac{u_T}{T} X100 = \frac{0.5}{50} X100 = 1\% \tag{I.13}$$

[1] “Uncertainty of measurement-Part 3: Guide to the expression of uncertainty in measurement (GUM:1995, 98-3:2008(E)),” 2008. Accessed: Feb. 20, 2021. [Online]. Available: https://www.iso.org/standard/50461.html

Appendix II

Specifications of the Instruments

S.No	Items	Description
(1)	Battery charger (Programmable DC power supply)	BK PRECISION 9115B Output: 0–80 V, 0–60 A, up to 1200 W Resolution: 1 mV / 1 mA Voltage accuracy: ±(0.05% + 10 mV) Current accuracy: ±(0.1% + 10 mA) 
(2)	Battery discharger (Programmable DC electronic load)	BK PRECISION 8510B Voltage range: 0.1–80 V, Current range: 0–30 A Accuracy: ±(0.05% + LSD) LSD: least significant digit Modes: CC, CV, CR, CP 

(3)	Internal Resistance Tester	HIOKI BT3562A Measurement range (Resistance): 0.1 μΩ to 3000 Ω Measurement range (Voltage): 0 to 60 V DC 
(4)	Data acquisition system (data logger)	AGILENT 34972-A 
(5)	Heat flux sensor	Hukseflux, model FHF05-02, Sensor type: Differential thermopile Sensitivity: 3×10^{-6} V/(W/m²) Sensor area: 15 mm × 30 mm Response time (95%): < 5 seconds 

(6)	Thermocouples	K type, 1/36 SWG with Teflon coating 
(7)	Stereo zoom trinocular microscope	Switzerland Dewinter-ZOOMSTAR-IV 

List of Publication

(Part of present dissertation)

International Journals

1) **V. Saxena**, S.K. Sahu, S.I. Kundalwal, P.A. Tsai. Enhanced thermal management system for Li-ion batteries using phase change material and liquid cooling under realistic driving cycles. Energy 318, 2025, 134759, https://doi.org/10.1016/j.energy.2025.134759 , **IF: 9.4**

2) **V. Saxena**, A. Sharma, R. Kothari, S.K. Sahu, S.I. Kundalwal. Analysis of Li-ion battery under high discharge rate embedded with metal foam phase change composite: A numerical study. Journal of Energy Storage 84, 2024, 110752, https://doi.org/10.1016/j.est.2024.110752 , **IF: 9.8**

3) **V. Saxena**, R Kothari, A Kumar, S K Sahu, S I Kundalwal, A theoretical model for effective thermal conductivity of open-cell-coated metal foams saturated with fluid/phase change material. Int J Energy Res, 2022,1–24, https://doi.org/10.1002/er.8190 , **IF: 4.2**

4) **V. Saxena,** S.K. Sahu, S.I. Kundalwal, P.A. Tsai. Optimizing Battery Thermal Management with Phase Change Materials: Influence of Thickness, Ambient Conditions, and Material Selection. Journal of Energy Storage, Volume 132, Part A, 1 October 2025, 117657, https://doi.org/10.1016/j.est.2025.117657, **IF: 9.8**

International conferences

1) **V. Saxena**, A. Sharma, S.K. Sahu, S.I. Kundalwal, Critical thickness of the phase change material (RT-42) for temperature management of 18650 Li-ion cell undergoing rapid discharging, Proceedings of the 9th International and 49th National Conference on Fluid Mechanics and Fluid Power (FMFP), December 14-16, 2022, IIT Roorkee, India

2) **V. Saxena**, A. Kumar, H. Ziniwal, G. Nagar, S. K. Sahu, S. I. Kundalwal, Thermal Performance Analysis of Cross Finned Heat Sinks using Nano-Enhanced Phase Change Material, Proceedings of the 9th International and 49th National Conference on Fluid Mechanics and Fluid Power (FMFP), December 14-16, 2022, IIT Roorkee, India

3) **V. Saxena,** A. Luthra, P.P. Dutta, S.K. Sahu, S.I. Kundalwal, Experimental Investigation on Phase Change Material enhanced Pin Finned Heat Sinks for Thermal Management Applications, Proceedings of 8th International Conference on Advances in Energy Research (ICAER-2022), July 7-9, 2022, IIT Bombay, India

4) **V. Saxena,** A. Kumar, A. Sharma, S.K. Sahu, S.I. Kundalwal. Thermal Analysis of a Li-Ion Battery Coupled with Phase Change Material (RT-35) filled with Copper Metal Foam. ASME POWER 2022, Pittsburgh, USA. https://doi.org/10.1115/POWER2022-86263

5) **V Saxena**, H Dey, A Kumar, A Sharma, S K Sahu, S I Kundalwal, Numerical investigation of Phase Change Material Enhanced Li-ion Battery Pack using the Dual Potential Multi-Scale Multi-Dimensional (MSMD) Approach, Proceedings of the 26th National and 4th International Heat and Mass Transfer Conference (IHMTC-ASTFE 2021), 2021, DOI: 10.1615/IHMTC-2021.2290

6) **V Saxena**, R Kothari, S K Sahu, S I Kundalwal, An analytical approach for predicting the effective thermal conductivity of coated metal Foam infiltrated with Phase change material, Proceedings of the 26th National and 4th International Heat and Mass Transfer Conference (IHMTC-ASTFE 2021), DOI: 10.1615/IHMTC-2021.3080.

7) **V Saxena**, R Kothari, A Kumar, S K Sahu, S I Kundalwal, Theoretical Modelling for Effective Thermal Conductivity of Open-Cell Infiltrated Metal Foams, Proceedings of the 15th International Conference on Heat Transfer, Fluid Mechanics and Thermodynamics (ATE-HEFAT 2021), July 25-28, 2021.

List of Publication

(Apart of present dissertation)

International Journals

1) Sharma A, Kothari R, **Saxena V**, Sahu SK. Numerical analysis of the combined influence of fin shape and location on constrained melting of phase change materials in a spherical capsule with double fins. *Heat Transfer*. 2025; 54: 904-940. doi:10.1002/htj.23196

2) Dutta PP, **Saxena V**, Kumar A, Sahu SK, Investigation of finned heat sinks with PEG-6000/EG and PEG-6000/MWCNT composite phase change material for thermal management application, Journal of Energy Storage, Volume 70, 2023, 108057, ISSN 2352-152X, https://doi.org/10.1016/j.est.2023.108057

3) Kumar A., Kothari R., **Saxena V**, Sahu SK, Kundalwal SI, Experimental investigation on paraffin wax-based heat sinks with cross plate fin arrangement for cooling of electronic components. J Therm Anal Calorim 147, 9487–9504 (2022). https://doi.org/10.1007/s10973-022-11223-9

International Conferences

1) Chourasia H, Saxena V, Mistry K, Bansal A, Sinha P, Sahu SK, Experimental Investigation of Cooling Performance of Phase Change Materials With 18650 Lithium-ion Battery, Proceedings of

the 28th National and 6th International Heat and Mass Transfer Conference (IHMTC-ASTFE 2021), December 9-12, 2025

2) Sharma A, Joshi J, **Saxena V**, Sahu SK, Influence of double fin shape on constrained melting of PCM in a spherical capsule: A numerical study, Proceedings of the 9th International and 49th National Conference on Fluid Mechanics and Fluid Power (FMFP) December 14-16, 2022, IIT Roorkee, Roorkee-247667, Uttarakhand, India

3) Datta PP, **Saxena V**, Sahu SK, Thermal performance analysis of phase change material-based plate finned heat sinks for thermal management applications, Proceedings of 8th International Conference on Advances in Energy Research (ICAER-2022), July 7-9, 2022, IIT Bombay, India

4) Sharma A, **Saxena V**, Sahu SK, Kundalwal SI, Effect of Fin Shape on Constraint Melting of PCM in a Spherical Enclosure for Latent Heat Storage: A Numerical Study, Proceedings of the ASME 2022, POWER-2022 Conference, July 18 – 19, 2022, Omni William Penn in Pittsburgh, Pennsylvania, USA. https://doi.org/10.1115/POWER2022-86314

5) Sharma A, Kothari R, **Saxena V**, Sahu SK, Effect of fin location on constrained melting heat transfer of phase change material in a spherical capsule: A numerical study, Proceedings of the 26th National and 4th International Heat and Mass Transfer Conference (IHMTC-ASTFE 2021), December 17-20, 2021. DOI: 10.1615/IHMTC-2021.2760

6) Kumar A, Singh AK, Chitre AA, Kothari R, **Saxena V**, Sahu SK, Kundalwal SI, Thermal performance of PCM based heat sink with solid and hollow fins for thermal management of electronics, Proceedings of the 26th National and 4th International Heat and

Mass Transfer Conference (IHMTC-ASTFE 2021), December 17-20, 2021. DOI: 10.1615/IHMTC-2021.2130

7) Sutradhar J, Kothari R, **Saxena V,** Sahu SK, Investigation of Solidification of Nano enhanced Phase change material considering Volumetric Shrinkage: An Analytical Approach, Proceedings of the 15th International Conference on Heat Transfer, Fluid Mechanics and Thermodynamics (ATE-HEFAT 2021), July 25-28, 2021.

Award and scholarships

- Prime Minister's Research Fellowship (PMRF) – Awarded the prestigious PMRF by the Ministry of Education, Government of India, to pursue doctoral research at IIT Indore.

- Overseas Visiting Doctoral Fellowship (OVDF) – Selected for the highly competitive OVDF program by the Anusandhan National Research Foundation (ANRF), Government of India, to conduct a 12-month collaborative doctoral research work at the University of Alberta, Canada. This has provided an opportunity to work under the supervision of Dr. Peichun Amy Tsai, Professor, Department of Mechanical Engineering, University of Alberta, Canada.